Universiteit Gent
Faculteit Toegepaste Wetenschappen
Vakgroep Informatietechnologie

Multigolflengtelasers voor WDM-netwerken

Theorie, ontwerp en realisatie door hybride integratie

Multiwavelength lasers for WDM-networks

Theory, design and realisation by hybrid integration

Dries Van Thourhout

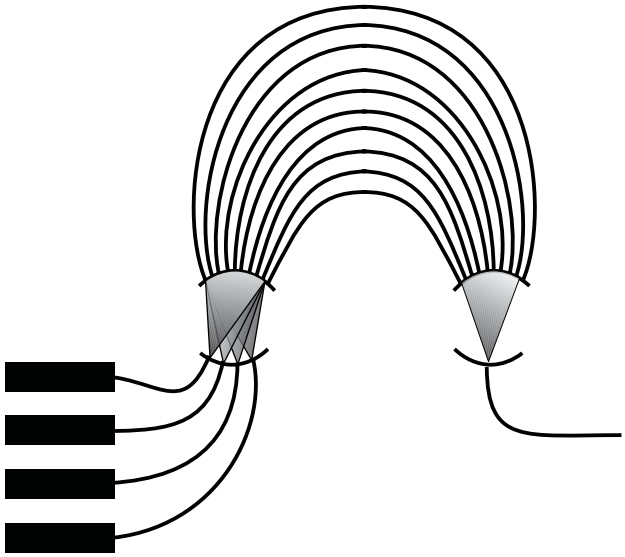

Proefschrift tot het bekomen van de graad van
Doctor in de Toegepaste Wetenschappen
Elektrotechniek
Academiejaar 1999-2000

Promotor:

Prof. Dr. Ir. Roel Baets	Universiteit Gent, vakgroep Informatietechnologie

Examencommisie:

Prof. Dr. Ir. Daniel Dezutter	Universiteit Gent, vakgroep Informatietechnologie
Prof. Dr. Ir. Meint Smit	Technische Universiteit Delft, Nederland
Dr. Ir. Anne Talneau,	CNRS, France
Prof. Dr. Ir. André Van Calster	Universiteit Gent, vakgroep elektronica en informatiesystemen
Prof. Dr. Ir. Paul Lagasse	Universiteit Gent, vakgroep Informatietechnologie
Prof. Dr. Ir. Peter Van Daele	Universiteit Gent, vakgroep Informatietechnologie
Prof. Dr. Ir. Geert Morthier	Universiteit Gent, vakgroep Informatietechnologie
Dr. Ir. Ingrid Moerman	Universiteit Gent, vakgroep Informatietechnologie

Universiteit Gent

Faculteit van de Toegepaste Wetenschappen

Vakgroep Informatietechnologie

Sint-Pietersnieuwstraat 41

B-9000 Gent

Tel. +32 9 264 33 16

Fax. +32 9 264 35 93

Dit werk kwam tot stand in het kader van een specialisatiebeurs toegekend door het IWT (Vlaams instituut voor de bevordering van het wetenschappelijk - technologisch onderzoek in de industrie).

Voorwoord

Een multigolflengtelaser maken. Vier maanden literatuurstudie, twee maanden ontwerp, drie maanden fabricage en dan nog twee maanden karakterisatie. En klaar is kees. Dacht ik. Lang geleden. Het bleek iets ingewikkelder te zijn dan dat. Er bleken vooral veel meer mensen bij nodig te zijn dan ik verwacht had. Ik wil dit voorwoord dan ook aangrijpen om hen hartelijk te bedanken voor hun hulp bij de voltooiing van dit werk.

Eerst en vooral was (en is) er natuurlijk mijn promotor, professor Roel Baets, die ik wil bedanken voor de steun en het vertrouwen bij het tot stand komen van dit werk. Bovendien moet ik mijn respect uitdrukken voor zijn intellectuele capaciteiten, zijn vermogen om - ondanks de vele verschillende projecten - specifieke problemen toch heel snel te doorzien en zijn kunst om de juiste (de lastige) vraag te stellen. Het belangrijkste was misschien echter z'n voorkeur voor het "niet-begane" pad en de moed om dat te blijven aanmoedigen, ook na eventuele initiële mislukkingen. Zonder deze ingesteldheid hadden we het hybride koppelen van InP-chips waarschijnlijk al opgegeven na de eerste week sukkelen, twee jaar verder blijkt dat dat jammer geweest zou zijn.

Professor Lagasse moet ik danken, voor "het werk achter de schermen" dat er voor gezorgd heeft dat de vakgroep is wat hij is: een alsmaar uitbreidende groep van gemotiveerde mensen waar het leuk is om werken en waar het onderzoek de link met de realiteit niet uit het oog verliest. Ik wil bovendien eveneens de bereidwilligheid waarmee ook de andere leden van de vakgroep dit werk gesteund hebben benadrukken. Meer in het bijzonder denk ik dan aan Dr. Ingrid Moerman, Professor Peter Van Daele, Professor Piet Demeester en Professor Daniel De Zutter, de eerste drie voor de ondersteuning op technologisch vlak, Professor De Zutter voor de hulp bij de tocht door de facultaire reglementen. Ook Professor Geert Morthier en Professor Bart Dhoedt moet ik natuurlijk bedanken, Geert voor de hulp bij het theoretische werk, Bart eerder voor de psychologische ondersteuning.

De leden van mijn jury en in het bijzonder Dr. Talneau van CRNS, Professor Smit van de Technische Universiteit Delft en Professor Van Calster wil ik bedanken voor de betoonde interesse en de interessante vragen. Professor Smit moet ik, samen met Professor Groen en Dr. Xaveer Leijtens bovendien bedanken voor de jarenlange samenwerking in het kader van het BLISS en APEX-project en voor het realiseren van een hele reeks Phased-Array chips.

De twee mensen die waarschijnlijk het nauwst betrokken waren bij de realisatie van de multigolflengtelaser zijn Tom en An. Tom werkt(e) natuurlijk vooral aan de monolithische integratie maar ik denk dat ook zijn bijdrage aan de hybride PAL niet te onderschatten is en ik kon me geen betere steunpilaar in het groeikamp voorstellen. Ik hoop dan ook van ganser harte dat één dezer dagen een selectief gegroeide PAL het wereldnieuws haalt. En alhoewel ik natuurlijk ook alle mensen moet bedanken die voorstelden om eens Pritt te gebruiken om mijn chips aan elkaar te plakken, denk ik dat toch vooral Ans deskundige keuze van geschikte epoxies verantwoordelijk was voor het slagen van het hybride integratieproces.

Bovendien was het niet onbelangrijk om iemand te hebben die - als alle moed me in de schoenen (of nog dieper) was gezonken - toch nog eens wilde proberen met wat meer lijm of wat ander licht.

Jan en Mathias moet ik danken voor het overnemen van het plakwerk toen ik dit boekje begon te schrijven. Misschien zijn ze er zelf van overtuigd dat ze maar wat aangemodderd hebben maar het was door hun werk dat we er uiteindelijk toch nog in geslaagd zijn om de APEX-module af te krijgen. En wie weet komt er ooit nog wel een hybride regenerator of een geplakte isolator.

Bij de realisatie van de module zelf zijn nog heel wat andere mensen betrokken geweest - soms had ik het gevoel dat ik alleen maar een koerier was die de verschillende onderdelen van de ene persoon naar de andere moest dragen. Zo waren er Koen en Luc voor het coaten en het bonden, Steven voor de processing, Jan voor het zagen en Eddy, Luc en Marc voor de realisatie van diverse onderdelen van de opstelling. Bedankt allemaal.

Ook aan de thesisstudenten die ik de voorbije jaren mocht begeleiden - Geert, An, Filip, Joeri, Brice, Pieter, Jan, Bart en Matthias denk ik met plezier terug. Hun ambetante vragen hebben me meer geleerd dan ze zelf waarschijnlijk vermoedden.

Ik zou ook mijn diverse bureaugenoten en collega's willen danken en succes wensen met hun eigen werk maar ik durf het echt niet aan om daarbij namen te gaan noemen. Die ene die ik vergeet zou veel te boos zijn.

Tenslotte moet ik natuurlijk mijn vrienden van scouts en elders, mijn familie en broers en alle andere mensen die nog altijd niet geloven dat ik "echt werk", bedanken omdat ze me zo nu en dan konden terughalen uit "de wondere wereld der wetenschap" en me met de voeten op de grond hielden. 't Is ook altijd plezant als er weer iemand meer is die weet dat ze tegenwoordig verschillende "kleurtjes" gebruiken om de telefoons van hier naar Amerika te sturen.

Ik heb dit voorwoord aangevat met te zeggen dat dit werk er zonder mijn promotor waarschijnlijk niet zou zijn. Wel, zonder mijn ouders zou het er zeker niet zijn. Ik wil ze dan ook van harte bedanken voor de constante ondersteuning en motivering, voor de vele kansen die ze me hebben geboden en voor de rust waarmee ze het allemaal overschouwden.

Gent, 9 Mei 2000

Dries.

Deel 1

Nederlandse samenvatting

INHOUDSTAFEL

Part 2

English text

SUMMARY

CHAPTER 1

GENERAL INTRODUCTION

CHAPTER 2

COMPUTER AIDED DESIGN TOOLS FOR INTEGRATED PHOTONIC CIRCUITS

CHAPTER 3

THEORETICAL ANALYSIS OF PHASED-ARRAY MULTI-WAVELENGTH LASERS

CHAPTER 4

DESIGN, FABRICATION AND CHARACTERISATION OF SUB-COMPONENTS FOR THE PHASED-ARRAY LASER

CHAPTER 5

DEVELOPMENT OF HYBRIDLY COUPLED PHASED-ARRAY MULTI-WAVELENGTH LASERS

CHAPTER 6

DEVELOPMENT OF A HYBRID INTEGRATION TECHNOLOGY FOR MULTI-WAVELENGTH PHASED-ARRAY LASERS

CHAPTER 7

SUMMARY AND CONCLUSIONS

INHOUDSTAFEL

Hoofdstuk 1

Algemene inleiding

In moderne optische telecommunicatie netwerken lijkt het gebruik van golflengtemultiplexering (WDM - wavelength division multiplexing) voorgoed doorgebroken te zijn. Door meerdere golflengtekanalen (4 tot 80) te gebruiken om informatie door het netwerk te sturen kan de capaciteit drastisch verhoogd worden, gebruik makend van de bestaande glasvezelinfrastructuur. Tot nu toe wordt deze techniek (WDM) vooral gebruikt om de capaciteit van punt-tot-punt verbindingen te verhogen. Meer en meer echter is er de tendens om volledig optisch gerouteerde netwerken te gaan ontwikkelen waarbij de golflengte gebruikt wordt om het licht door het netwerk te routeren.

De optische bronnen vormen een belangrijk onderdeel van deze netwerken. Meestal worden daarbij drie verschillende groepen onderscheiden:

- Discrete lasers met vaste golflengte: dit is de optie die nu over het algemeen wordt gebruikt.
- Afstembare lasers: kunnen een volledige reeks discrete reservelasers vervangen
- Multigolflengtelasers: genereren meerdere golflengtekanalen tegelijk

Het doel van dit werk was het ontwerpen en realiseren van een multigolflengtelaser door de integratie van een passieve demultiplexer en een versterkerrij binnen één optische caviteit. In paragraaf 1.1 van dit hoofdstuk wordt het werkingsprincipe van zo'n laser besproken. In de volgende paragrafen bespreken we kort waarom een Phased-Array demultiplexer gebruikt werd (paragraaf 1.2) en introduceren we de bij het ontwerp beoogde specificaties (paragraaf 1.3).

Het tweede deel van dit hoofdstuk geeft een overzicht van recent gepubliceerde multigolflengtelasers en in het derde deel worden zowel de monolithische als de hybride integratietechnologie die gebruikt werden in het kader van dit werk ingeleid. Als besluit wordt het doel van dit werk besproken en wordt een kort overzicht van de inhoud van de thesis en de belangrijkste verwezenlijkingen gegeven.

1 Multigolflengtelasers: werkingsprincipe en algemeen ontwerp

1.1 Werkingsprincipe

Het belangrijkste voordeel van multigolflengtelasers is dat meerdere golflengtekanalen in één gemeenschappelijke uitgangsgolfgeleider worden gekoppeld. Daardoor kan zowel het aantal kritische vezel-chipkoppelingen als het totaal aantal componenten sterk worden verminderd. Ze kunnen gebruikt worden als golflengteafstembare laser, bijvoorbeeld in reconfigureerbare add-drop knooppunten van een optisch gerouteerd WDM-netwerk, maar ook

als echte multigolflengtelaser waarbij meerdere kanalen tegelijk worden aangestuurd, bijvoorbeeld ter vervanging van een volledige rij van discrete lasers.

We kunnen twee verschillende types multigolflengtelaser onderscheiden: de kortecaviteitslasers en de langecaviteitslasers. Het eerste type wordt gevormd door het integreren van een rij van discrete lasers - meestal DFB- of DBR-lasers - met een passieve koppelaar op één chip. Dit type lasers heeft een hoge modulatiebandbreedte en opereert betrouwbaar in een enkele longitudinale mode. Het kan echter moeilijk zijn om een voldoende nauwkeurige kanaalspatiëring te realiseren en de koppelaar heeft meestal hoge intrinsieke verliezen.

Langecaviteitslasers worden gevormd door integratie van een versterkerrij en een passieve multiplexer binnen één optische caviteit, gevormd door de gekliefde facetten van de chip. Als één van de versterkers aangeschakeld wordt, wordt de versterkte spontane emissie gegenereerd door deze versterker gefilterd door de multiplexer. Door reflectie aan het facet ontstaat een golflengteselectieve terugkoppeling naar de versterker. Als de winst van de versterker voldoende groot is om de caviteitsverliezen te compenseren treedt laserwerking op, bij een frequentie bepaald door de multiplexer. Als een andere versterker aangeschakeld wordt, zal ook dit kanaal laserwerking vertonen, maar bij een verschillende frequentie. De kanaalspatiëring is bepaald door de multiplexer en is meestal heel precies. De lange caviteit kan echter de modulatiebandbreedte gevoelig beperken.

1.2 Keuze van de Phased-Array als demultiplexer

In de literatuur zijn verschillende types geïntegreerde optische demultiplexers voorgesteld. De belangrijkste zijn de traliedemultiplexer, de Phased-Array demultiplexer en de uitgebreide Mach-Zehnder interferometer demultiplexer. Traliedemultiplexers gebruiken een geëtst diffractierooster als golflengteselectief element. Ze kunnen een nauwkeurige kanaalspatiëring hebben maar de verliezen zijn relatief hoog en het etsen van het diffractierooster is niet eenvoudig. In Phased-Array demultiplexers doet een golfgeleiderrij met lineair toenemende lengte dienst als dispersief element (zie ook hoofdstuk 2). Hun fabricage vereist geen bijkomende processingstappen en ze kunnen heel lage verliezen hebben. Ook uitgebreide Mach-Zehnder interferometer demultiplexers maken slechts gebruik van een standaardgolfgeleidertechnologie maar hun werking is nogal gevoelig voor kleine fasefouten.

Vanwege deze voordelen, eenvoudige fabricage, lage verliezen en hoge tolerantie voor processingfouten, werd gekozen voor de Phased-Array demultiplexer voor het realiseren van de multigolflengtelaser. Bovendien konden we, in het kader van een Europees ACTS-project, een beroep doen op de ervaring van één van de partners (Technische Universiteit Delft) bij het ontwerp en de realisatie van deze demultiplexers.

1.3 Vooropgestelde specificaties

In de context van twee Europese projecten (BLISS & APEX) werden een reeks generieke specificaties voor multigolflengtelasers vooropgesteld. Er werd daarbij uitgegaan van een vier-

kanaalslaser met een kanaalspatiëring van 400 GHz. De beoogde modulatiebandbreedte was 620 MHz.

Voor praktische WDM-netwerken wordt meestal aan een veel hoger aantal kanalen en een kleinere kanaalspatiëring gedacht. Bovendien is het in dat geval belangrijk dat een voldoende hoog uitgangsvermogen geleverd wordt (afhankelijk van de toepassing kan dit variëren van 1 tot 100 mW).

2 Multigolflengtelasers: state-of-the-art

2.1 Kortecaviteitslasers

Zoals beschreven in paragraaf 1.1, worden deze lasers gevormd door integratie van een rij discrete lasers met een passieve koppelaar. Meestal wordt daarvoor een sterkoppelaar of een cascade van Y-juncties gebruikt, die beide een hoog intrinsiek verlies hebben. Als het aantal golflengtekanalen toeneemt kan het daarom zinvol zijn om een Phased-Array multiplexer te gebruiken als koppelaar.

Voordelen van kortecaviteitslasers:

- Zowel DFB- als DBR-lasers hebben een hoge modulatiebandbreedte.
- Het is mogelijk om per kanaal een aparte modulator te integreren.
- Door hun afstembaarheid hebben DBR-laserrijen een grotere flexibiliteit.
- Beperking van de benodigde uitrusting: één temperatuurcontroller, één isolator, …

Nadelen van kortecaviteitslasers:

- Moeilijk te fabriceren tralies met kleine periode noodzakelijk
- Intrinsiek 1/N loss wanneer een sterkoppelaar gebruikt wordt (N is daarbij het aantal kanalen)
- Het is moeilijk de gewenste nauwkeurigheid voor de kanaalspatiëring te realiseren
- Het golflengteselectief filter bevindt zich in het actieve gebied: dit resulteert in een drift van de laserfrequentie bij opwarming van de laser of bij verandering van de winst. Bovendien wordt over de leeftijd van een DFB-laser typisch een golflengteverschuiving van 0.1 nm waargenomen, wat externe golflengtecontrole noodzakelijk maakt.
- Als DBR-lasers gebruikt worden, moet het licht geëxtraheerd worden langs de kant van het golflengteselectieve rooster. Dit maakt dat een compromis moet worden gevonden tussen een goede onderdrukking van zijmodes en het maximaliseren van het uitgangsvermogen.
- DBR-lasers vereisen extra controle

2.2 Langecaviteitslasers

De eerste demonstraties van langecaviteitsmultigolflengtelasers waren niet meer dan een uitbreiding van de klassieke afstembare lasers met extern diffractierooster. Ze werden opgebouwd door een versterkerrij en een bulk diffractierooster te combineren binnen één caviteit. Dergelijke lasers vereisen echter een uiterst stabiele opstelling. Om dit probleem te omzeilen werd voorgesteld om het diffractierooster monolithisch te integreren met de versterkerrij. Zo'n component werd voor het eerst gerealiseerd in 1992. De nauwkeurigheid op de kanaalspatiëring was veel beter dan de waarden die typisch gemeten worden voor de in de vorige paragraaf besproken kortecaviteitslasers maar de overige werkingskarakteristieken waren niet zo goed: de drempelstroom was hoger dan 300 mA en de onderdrukking van de zijmodes en van de ASE-ruis was heel beperkt.

In 1993 werd de eerste component gepresenteerd waarbij gebruik gemaakt werd van een Phased-Array demultiplexer. Voor deze component werd de Phased-Array doormidden gekliefd, resulterend in een laser met een caviteitslengte van 7 mm, een drempelstroom van 37 mA en een maximaal uitgangsvermogen van 0.7 mW. Simultane werking van meerdere kanalen was echter nog niet mogelijk.

Sindsdien zijn door verschillende onderzoeksgroepen Phased-Array lasers gepresenteerd. Daarbij werden verschillende technieken gebruikt voor het integreren van de passieve golfgeleiders met de actieve golfgeleiders.

2.3 Werkingskarakteristieken van Phased-Array multigolflengtelasers

2.3.1 Aantal kanalen

Het maximaal aantal kanalen dat tot nu toe gepresenteerd werd voor een Phased-Array multigolflengtelaser is 18. Meestal is het aantal kanalen echter beperkt tot 8 à 10. Bij het opvoeren van het aantal kanalen moet er immers rekening gehouden worden met een toenemende kans op fabricagefouten.

2.3.2 Kanaalspatiëring

De kleinste kanaalspatiëring tot nu toe gerapporteerd is 75 GHz. De nauwkeurigheid op de kanaalspatiëring is meestal heel goed en wordt bepaald door de spatiëring tussen de longitudinale modes. Dit betekent meteen ook dat wanneer de caviteitslengte verkort wordt om de modulatiebandbreedte te verhogen, de nauwkeurigheid op de kanaalspatiëring afneemt.

Het filter is volledig gerealiseerd in passief materiaal zodat geen drift of degradatie van de kanaalspatiëring verwacht wordt.

2.3.3 Nauwkeurigheid op de absolute golflengte

Om de centrale golflengte van de laser met een redelijke nauwkeurigheid vast te leggen is een heel strikte controle van alle procesparameters nodig. Een afwijking van de effectieve

brekingsindex met minder dan 0.1 % kan al leiden tot een afwijking van 1 nm in de centrale golflengte van de laser.

Om alle kanalen tegelijk in golflengte te verschuiven kan de temperatuur van de laser veranderd worden. Typisch wordt een afstembaarheid van 0.11 nm/K opgemeten.

2.3.4 Drempelstroom en uitgangsvermogen

Opdat multigolflengtelasers praktisch bruikbaar zouden zijn, moet hun vermogenconsumptie vergelijkbaar zijn met die van hun discrete tegenhangers. Bovendien neemt de betrouwbaarheid en de levensduur van lasers over het algemeen toe naarmate de drempelstroom afneemt.

Zowel de drempelstroom als de externe differentiële efficiëntie worden vooral bepaald door het verlies binnen de caviteit. Wanneer een monolithisch integratieschema wordt gebruikt speelt vooral het propagatieverlies van de passieve golfgeleiders daarbij een belangrijke rol. Bij hybride geïntegreerde PIC's kunnen de passieve golfgeleiders volledig onafhankelijk van de versterkers worden geoptimaliseerd maar kan het verlies aan de overgang tussen beide chips belangrijk worden.

De laagste drempelstroom die tot nu toe gerapporteerd werd is 18 mA voor een laser met kwantumputten als actieve laag. Het uitgangsvermogen van deze component was ongeveer 1.0 mW bij een stroom van 100 mA (vezelgekoppeld). De beste hybride lasers die wij gerealiseerd hebben (bulk actieve laag), hadden een drempelstroom van minder dan 35 mA en een uitgangsvermogen van 3.5 mW bij 100 mA (niet vezelgekoppeld, zie hoofdstuk 5).

2.3.5 Onderdrukking van versterkte spontane emissieruis en zijmodes

De onderdrukking van de zijmodes (SMSR - side mode suppression ratio) is zowel bepaald door de onderdrukking van de longitudinale modes binnen dezelfde doorlaatband van de demultiplexer als door de onderdrukking van modes in naburige doorlaatbanden (onderdrukking van "multi-passbandlasing").

Om lasermodes in naburige doorlaatbanden te onderdrukken zijn verschillende methodes voorgesteld zoals het vergroten van de periode van de demultiplexer, het gebruik van bulk actieve lagen en het "chirpen" van de transfer door de Phased-Array. Deze laatste methode is de meest efficiënte en zorgt ervoor dat de periodiciteit van de Phased-Array demultiplexer gebroken wordt waardoor de transfer door de naburige doorlaatbanden onderdrukt wordt.

Door de grote caviteitslengte vallen verschillende longitudinale modes binnen één doorlaatband van de multiplexer. Daarom zou kunnen verwacht worden dat het moeilijk is laserwerking in slechts één mode te verkrijgen. Gelukkig zorgt een niet-lineair interactie-effect tussen de longitudinale modes onderling ervoor dat de mode met het hoogste vermogen bevoordeeld wordt ten opzichte van de andere modes wat, als de bandbreedte van het filter voldoende klein is, kan zorgen voor een stabiele laserwerking in één enkele mode. Dit effect is in meer detail besproken in hoofdstuk 3.

Als geen uitgangsversterker wordt gebruikt, is de onderdrukking van de ASE-ruis heel hoog (beter dan 60 dB). Met een uitgangsversterker is de onderdrukking minder goed maar nog altijd voldoende voor commerciële toepassingen.

2.3.6 Modulatiebandbreedte

De lange caviteit van Phased-Array lasers begrenst de bandbreedte voor directe modulatie. Toch is al een experiment gerapporteerd waarbij een 16-kanaalslaser succesvol gemoduleerd werd met 16 verschillende 622 Mbit/s datasignalen, zij het bij een beperkte extinctieverhouding. Ook experimenten waarbij een laser extern gemoduleerd werd met een 2.5 Gbit/s signaal zijn gerapporteerd.

Als slechts één kanaal tegelijk wordt aangestuurd is het mogelijk om een modulator te integreren op dezelfde chip.

2.3.7 Lijnbreedte

Voor de in hoofdstuk 6 gerapporteerde permanent geïntegreerde hybride PAL hebben we een lijnbreedte van minder dan 1 MHz opgemeten. Andere auteurs hebben waarden tussen 1 MHz en 21 MHz gerapporteerd.

2.3.8 Controle, betrouwbaarheid en levensduur

Daar de golflengtespatiëring vast is, moet slechts één kanaal worden gecontroleerd om alle kanalen op de gewenste frequentie af te stemmen. Verder is de multiplexer volledig gerealiseerd in passief materiaal wat de kans op degradatie of een golflengteverschuiving verkleint.

Vermits de drempelstroom in de buurt kan liggen van die voor discrete lasers, verwachtten we dat dit type laser een redelijke levensduur zal hebben. Op dit vlak is echter nog geen systematisch onderzoek gerapporteerd.

De kleinste tot nu toe gerealiseerde Phased-Array laser had een oppervlakte van 2 x 3 mm^2. Een oppervlakte van 5 x 5 mm^2 is echter meer gebruikelijk. Dit is relatief groot en kan de kans op fabricagefouten sterk vergroten.

2.4 Besluiten

De belangrijkste voordelen van de Phased-Array laser zijn de nauwkeurige kanaalspatiëring, de eenvoudige karakteriserings- en verpakkingsprocedure, de beperkte nood aan controle-elektronica en de zeer goede SMSR. Het uitgangsvermogen daarentegen is nog te laag en het grote chipoppervlakte verhoogt de kans op fabricagefouten. De fabricage zelf is echter eenvoudig vermits geen tralies nodig zijn en één vezel-chipkoppeling kan gebruikt worden voor meerdere golflengtekanalen tegelijk.

Het belangrijkste nadeel is de modulatiebandbreedte. Tot nu toe is die beperkt tot 622 Mbit/s voor directe modulatie. Als een alternatief kan gedacht worden aan externe modulatie. Alhoewel daarvoor de signalen terug gedemultiplexeerd moeten worden, kan zelfs in

dat geval het gebruik van een multigolflengtelaser belangrijke voordelen opleveren wat betreft het aantal benodigde componenten en het aantal kritische vezel-chipkoppelingen.

3 Integratietechnologie

De Phased-Array laser bestaat uit een actief gedeelte (de versterkers) en een passief gedeelte (de Phased-Array). De versterkers moeten voldoende winst leveren ter compensatie van de caviteitsverliezen en de lasergolflengte wordt bepaald door de bandgapgolflengte van de actieve laag in dit gebied. Het passieve gedeelte van de component daarentegen is niet gepompt en om te vermijden dat alle in het actieve gedeelte gegenereerde licht geabsorbeerd wordt, moet de bandgapgolflengte van de filmlagen in dit gebied veel lager zijn dan de lasergolflengte. Dit betekent dus dat twee verschillende golfgeleidertypes moeten geïntegreerd worden binnen één component. In het kader van deze thesis werden zowel een monolithische als een hybride integratietechnologie bestudeerd. De ontwikkeling van de monolithische integratietechnologie op zich was geen onderdeel van dit werk. Omdat we echter meegewerkt hebben aan de ontwikkeling van de optische versterkers en de golfgeleiders die deel uitmaakten van dit integratieschema en de resultaten daarvan gerapporteerd zijn in hoofdstuk 4, wordt het hier kort beschreven (paragraaf 3.1).

De ontwikkeling van het hybride integratieschema was een volwaardig onderdeel van dit werk en is in detail beschreven in de hoofdstukken 5 & 6. In paragraaf 3.2 wordt het hybride integratieschema kort ingeleid.

3.1 Selectieve groei als een monolithische integratietechnologie

Bij de courant gebruikte monolithische integratieschema's worden eerst de lagen voor één type component gegroeid over het volledige chipoppervlak. Vervolgens worden deze weggeëtst in de gebieden waar ander componenten dienen te komen en vindt een hergroei plaats. Wanneer een selectief groeiproces gebruikt wordt is dit echter niet langer nodig. In dat geval worden de gebieden waar de versterkers moeten komen omringd met SiO_2 maskers. Daardoor neemt de groeisnelheid lokaal toe en verschuift de emissiegolflengte van de kwantumputlagen naar een hogere waarde. Dit laat toe om in één enkele groeistap componenten met een verschillende functie te realiseren. Gebaseerd op deze technologie werd een volledig monolithisch integratieschema ontwikkeld. Zowel in het passieve als in het actieve gebied werd daarbij een golfgeleider van het ridge-type gebruikt. Het voordeel van het ontwikkelde integratieschema is de eenvoud ervan. Het groeien van lagen met goede kwaliteit lijkt momenteel het belangrijkste probleem te zijn.

Volgens ons is het belangrijkste voordeel van de selectieve epitaxiaalgroei als een monolithische integratietechnologie in vergelijking met meer courant gebruikte technieken zoals buttkoppeling of lokale verwijdering van de actieve laag het feit dat verschillende types actieve componenten (detectoren, modulatoren, versterkers) elk met een verschillende bandgap-

golflengte, kunnen geïntegreerd worden op één chip, zonder de processing verder te compliceren.

3.2 Hybride integratie

In het door ons ontwikkelde hybride integratieschema wordt een InP versterkerrij gekoppeld met een InP passieve golfgeleiderchip. Om reflecties aan de overgang tussen beide chips te vermijden worden de golfgeleiders afgebogen ten opzichte van de normaal met het facet. De koppeling wordt uitgevoerd op een optische tafel en geoptimaliseerd door het maximaliseren van het uitgangsvermogen. Oorspronkelijk werden beide chips slechts tijdelijk gekoppeld. Later werd ook een permanente integratietechniek ontwikkeld waarbij een UV-uithardende epoxy werd gebruikt om de twee chips te verbinden.

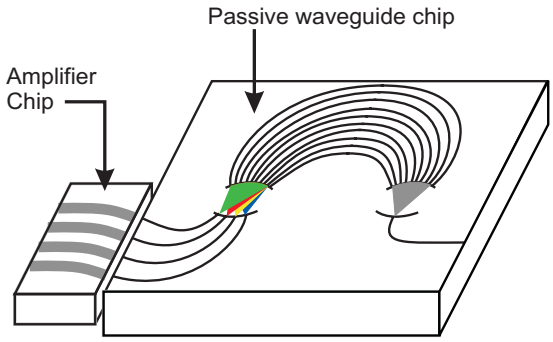

Fig. 1-1 Hybride gekoppelde multigolflengtelaser

4 Doel van dit werk en structuur van de thesis

Bij de aanvang van dit project was er al door enkele groepen een Phased-Array multigolflengtelaser gerapporteerd. De karakteristieken van deze lasers waren echter nog niet bijzonder goed. Ze hadden hoge drempelstromen, lage uitgangsvermogens en een lage modulatiebandbreedte. Op dat moment was het dan ook nog niet duidelijk of dit type laser bruikbaar zou zijn voor toepassing in praktische WDM-systemen. Daarom werd als doel voor dit werk het ontwerpen en praktisch realiseren van multigolflengtelasers met verbeterde karakteristieken vooropgesteld. Het was daarbij eveneens de intentie om de theoretische kennis over dit type lasers te bevorderen en de theoretische limieten, bijvoorbeeld wat betreft de modulatiebandbreedte, te onderzoeken. In parallel daarmee, was het de bedoeling nieuwe methodes voor het ontwerpen van complexe fotonische IC's, zoals de Phased-Array laser, te onderzoeken.

Hoofdstuk 2 van dit werk is gewijd aan de gebruikte computerondersteunde ontwerphulpmiddelen. Het eerste deel van dit hoofdstuk is vooral gewijd aan de diverse analysemethodes die gebruikt werden, terwijl in het tweede deel dieper wordt ingegaan op de synthese van PIC's en enkele problemen die daarbij optreden. Ook het werkingsprincipe en het ontwerp van Phased-Array demultiplexers wordt kort aangeraakt.

In hoofdstuk 3 worden de statische en dynamische karakteristieken van lange-caviteitslasers bestudeerd. De resultaten van deze analyse werden gebruikt voor het optimaliseren van het ontwerp van de Phased-Array demultiplexer en vergeleken met experimentele resultaten in hoofdstuk 5 & 6. Aan het eind van hoofdstuk 3 worden enkele belangrijke ontwerpregels samengevat.

In hoofdstuk 4 word het ontwerp en de karakterisatie van de subcomponenten voor zowel de monolithisch geïntegreerde als de hybride geïntegreerde multigolflengtelaser besproken. Daarbij komen respectievelijk de versterkers, de passieve golfgeleiders en de koppeling tussen beide aan bod.

In hoofdstuk 5 wordt de niet-permanente hybride koppelingstechniek die we ontwikkelden voor het karakteriseren van complexe PIC's gedetailleerd besproken. Na een uitgebreide inleiding waarbij een overzicht van meer klassieke hybride integratietechnologieën wordt gegeven, worden de experimentele resultaten voor zowel een standaard Phased-Array multigolflengtelaser als voor een multigolflengtelaser met winstvergrendelde uitgangsversterker uitgebreid behandeld. Ook een nieuw type afstembare laser wordt kort besproken.

In hoofdstuk 6 wordt de hybride integratietechnologie waarbij twee chips permanent verbonden worden met UV-uithardende epoxy behandeld en worden de resultaten van een eerste volledig verpakte hybride Phased-Array multigolflengtelaser gepresenteerd.

Hoofdstuk 2

Computerondersteunde ontwerphulpmiddelen voor geïntegreerde optische circuits

1 Ontwerp van geïntegreerde fotonische circuits

Het ontwerp van een gecompliceerde fotonische IC (PIC: photonic integrated circuit) bestaat typisch uit een aantal deeltaken. Startend van een functionele beschrijving zal de ontwerper een blokdiagram voor de PIC opstellen en vervolgens, gebaseerd op zijn intuïtie en ervaring, een materiaalsysteem selecteren en voor ieder blok een meer specifieke component kiezen. Daarna moeten voor alle parameters van de componenten waarden worden gekozen. Soms kan dit gebeuren door gebruik te maken van simpele ontwerpregels, afgeleid uit vroegere experimenten of uit theoretische overwegingen. Vaak echter zullen ook numerieke ontwerphulpmiddelen nodig zijn.

Als alle componenten van de PIC gekwantificeerd zijn, kan een analyse van de volledige component worden uitgevoerd. Als de specificaties die aan het begin van het ontwerpproces werden vooropgesteld gehaald worden, kan een masker worden gegenereerd en kan de fabricage starten. Vaak is dit echter niet onmiddellijk het geval en moet één of meerdere stappen teruggekeerd worden in de ontwerpcyclus.

Bij dit alles zijn krachtige computerondersteunde hulpmiddelen onmisbaar geworden. Zo'n tools worden al lang gebruikt voor het analyseren van circuits op het subcomponentniveau. Naarmate de complexiteit van de PIC toeneemt, wordt het echter alsmaar belangrijker dat ook volledige circuits kunnen worden geanalyseerd. Dit kan immers zowel helpen bij het reduceren van het aantal ontwerpcyclussen als bij het beter begrijpen van experimentele resultaten. Alhoewel de onderliggende algoritmes daarvoor al in de jaren '80 ontwikkeld werden, zijn slechts sinds enkele jaren betrekkelijk gebruiksvriendelijke CAD-tools commercieel beschikbaar. In het volgende deel van dit hoofdstuk wordt een overzicht gegeven van de CAD-tools die we gebruikt hebben in het kader van dit werk. Vermits voor de Phased-Array laser zowel actieve als passieve componenten nodig waren, vormt dit echter meteen ook een min of meer compleet overzicht van de op dit moment meest gebruikte ontwerphulpmiddelen. In deel 3 van dit hoofdstuk wordt dieper ingegaan op de synthese van optische circuits en in deel 4 wordt het werkingsprincipe en het ontwerp van Phased-Array demultiplexers behandeld.

2 Ontwerphulpmiddelen voor de ontwikkeling van fotonische IC's

2.1 Optische modebepalers

Alhoewel optische modebepalers in de eerste plaats ontworpen worden voor het zoeken van de eigenmodes van een longitudinaal invariante golfgeleiderstructuur, hebben ze een veel ruimer toepassingsgebied. Zo kunnen ze ook gebruikt worden voor het bepalen van het verre veld van een golfgeleider, voor het berekenen van het verlies aan discontinuïteiten of in gebogen golfgeleiders of voor het berekenen van de transmissie door stuksgewijze continue golfgeleiders.

De eenvoudigste modebepalers kunnen gebruikt worden voor het zoeken van de eigenmodes van een eendimensionale meerlagengolfgeleider. In de context van dit werk werden twee zo'n modebepalers gebruikt, *REMUS* en *CEMUS*, respectievelijk voor het zoeken van modes in golfgeleiders met reële en imaginaire brekingsindex.

Tot enkele jaren geleden waren modebepalers voor tweedimensionale golfgeleiderstructuren te traag voor praktische toepassingen en werden ze enkel gebruikt ter verificatie van resultaten verkregen met benaderde methodes. Door het beschikbaar komen van krachtiger computers en verbeterde algoritmes is dat niet langer het geval. In het kader van dit werk is een commerciële tweedimensionale modebepaler gebruikt die gebaseerd is op de filmmode-aanpassingsmethode. Deze methode kan worden gezien als een uitbreiding van de effectieve index methode en is vooral bruikbaar voor golfgeleiders die bestaan uit een reeks rechthoekige gebieden met constante brekingsindex. Voor dergelijke golfgeleiders wordt de filmmode-aanpassingsmethode beschouwd als een van de meest nauwkeurige die op dit moment beschikbaar zijn.

In de volgende paragrafen worden de belangrijkste toepassingen van modebepalers kort besproken.

2.1.1 Berekening van de propagatieconstante

De meest evidente maar ook de meest relevante toepassing van modebepalers is het berekenen van de propagatieconstanten van de geleide en de stralende modes van een golfgeleider. Dit laat ons bijvoorbeeld toe het aantal geleide modes van een golfgeleider te bepalen. Verder geeft het imaginaire gedeelte van de propagatieconstante informatie over het verlies of de winst van de golfgeleidermode en in golfgeleiders met bundelexpansiestructuren geeft het verschil tussen de propagatieconstanten van de eerste twee even modes een idee van de minimumlengte voor adiabatische werking. Ook de lengte van interferometrische componenten zoals een directionele koppelaar of een multimode interferometer is bepaald door het verschil tussen twee propagatieconstanten.

2.1.2 Berekening van de ruimtelijke verdeling van het optisch veld

Soms kan ook de ruimtelijke verdeling van het optisch veld informatie geven over de werking van de component. Zo kan de sterkte van het veld ter hoogte van de overgang golfgeleider - lucht een idee geven over de te verwachten verstrooiingsverliezen. In lekkende golfgeleiders (bochten, golfgeleiders met een hoge-indexsubstraat) biedt de kennis van veldverdeling inzicht in de stralingsverliezen.

2.1.3 Koppelingsefficiëntie aan een golfgeleiderjunctie

In een optische IC komen overgangen tussen golfgeleiders met een verschillende doorsnede vaak voor. Typische voorbeelden zijn de overgang tussen begraven en dijkgolfgeleiders, de koppeling tussen een smalle monomodale golfgeleider en een bredere golfgeleider aan de ingang van een MMI-koppelaar of de overgang tussen een geïntegreerde golfgeleider en een optische vezel. Om verlies en reflecties aan deze overgangen te minimaliseren, moet de koppelingsefficiëntie tussen de verschillende modes van de golfgeleiders berekend worden. Dit kan op een rigoureuze manier door het toepassen van een mode-expansiemethode. Zo'n aanpak vereist echter de berekening van een hele reeks eigenmodes voor beide golfgeleiders. Daarom wordt vaak de overlapintegraal van de laagste orde eigenmodes gebruikt als een maat voor het transitieverlies. Dit geeft echter geen informatie over de gereflecteerde velden en bovendien wordt het transitieverlies op die manier vaak onderschat omdat geen rekening gehouden wordt met de Fresnelverliezen. In het kader van dit werk hebben we daarom twee alternatieve formules onderzocht die deze problemen deels omzeilen, zonder de berekening te compliceren. Uit berekeningsvoorbeelden blijkt dat deze meestal heel goede resultaten opleveren.

2.1.4 Reflectie aan een schuin facet

Voor het realiseren van de hybride PAL zijn versterkers met heel lage facetreflectiviteit nodig. Om dat mogelijk te maken worden de golfgeleiders aan het facet afgebogen t.o.v. de normaal op het facet. Om de reflectie aan zo'n facet te berekenen werd een methode toegepast die origineel door Marcuse werd voorgesteld en hier uitgebreid is naar tweedimensionale golfgeleiderstructuren. Enkele berekeningsvoorbeelden tonen aan dat, bij een vaste hoek, vooral de breedte van het verre veld bepalend is voor de grootte van de residuele reflectie.

2.1.5 Verreveldberekeningen

Modebepalers kunnen ook gebruikt worden voor het berekenen van het verreveld van de golfgeleiders. Een veel toegepaste techniek is het ontbinden van de golfgeleidermode in vlakke golven. Vervolgens wordt de transmissie en de reflectie van elke vlakke golf aan de overgang golfgeleider - lucht berekend en worden ze verder gepropageerd door het uniforme medium. Gebruik maken van een mode-expansietechniek is het mogelijk het verre veld

iets rigoureuzer te berekenen vermits zo'n aanpak ook rekening houdt met modeconversie aan de interface.

2.1.6 Berekening van bochtverliezen

Modebepalers kunnen ook gebruikt worden voor het bepalen van de stralingsverliezen van een gebogen golfgeleider. Eén van de daarbij meest toegepaste technieken is de conforme transformatietechniek, die de gebogen golfgeleider omzet in een equivalente rechte golfgeleider met een getransformeerd indexprofiel. Het is dan eenvoudig om de propagatieconstante van deze golfgeleider te berekenen met een standaard modebepaler. Uit een reeks berekeningen is een empirische formule afgeleid voor het berekenen van de bochtverliezen voor $2\,\mu m$ brede golfgeleiders met een gegeven lateraal indexcontrast

2.1.7 Opsluitingsfactor

Uit de kennis van de ruimtelijke verdeling van het optisch veld kan de opsluitingsfactor Γ_i voor ieder gebied Ω_i van de golfgeleider berekend worden. De opsluitingsfactor is een belangrijke parameter voor laserdiodes vermits de kennis ervan toelaat de modale winst te berekenen. Meer in het algemeen, kan de winst of het verlies van een golfgeleider worden berekend als een gewogen som van de winst- of absorptiecoëfficiënten voor ieder gebied, waarbij de opsluitingsfactor als gewichtsfactor gebruikt wordt.

2.1.8 Propagatie door stuksgewijze constante golfgeleiders

Modebepalers kunnen ook gebruikt worden om de transmissie van een optisch veld door een stuksgewijze continue golfgeleiderstructuur te berekenen. Daarbij wordt het veld ontbonden in de lokale eigenmodes van de golfgeleider die vervolgens elk afzonderlijk worden gepropageerd. Aan elke overgang wordt het in paragraaf 2.1.3 besproken formalisme gebruikt om de transmissie- en reflectiecoëfficiënten voor elke mode te berekenen. Deze methode is vooral voordelig bij het modelleren van de transmissie van een optisch veld door golfgeleiderstructuren die bestaan uit een beperkt aantal rechte of gebogen golfgeleiders zoals MMI-koppelaars. Voor het modeleren van continu variërende golfgeleiders zoals bundelexpansiestructuren zijn BPM-algoritmes over het algemeen een betere keuze. In dat geval kunnen mode-expansiepropagatiealgoritmes gebruikt worden ter verificatie van andere algoritmes.

2.2 Bundelpropagatiemethodes (BPM)

Om de transmissie door gecompliceerde golfgeleiderstructuren te berekenen wordt vaak een bundelpropagatiemethode (BPM - beam propagation method) gebruikt. Typisch aan deze methodes is dat het veld in kleine stapjes door de golfgeleiderstructuur gepropageerd wordt. Een benadering die eigen is aan alle BPM-algoritmes is de keuze van de propagatie-as. Afhankelijk van het gebruikte algoritme moet de propagatie binnen een zekere hoek met deze

as blijven. Om de berekeningstijd te verkorten kunnen nog verschillende andere benaderingen worden toegepast zoals een semi-vectoriele of scalaire benadering, een paraxiale benadering of een reductie van de driedimensionale structuur naar een equivalente tweedimensionale vorm.

2.3 Modellering van actieve componenten

Naast de tools die we zelf hebben ontworpen en die beschreven zijn in hoofdstuk 3, hebben we ook twee commerciële CAD-pakketten gebruikt voor het simuleren van de werking van de multigolflengtelaser: *CLADISS* en *OPALS*. Beide programma's zijn gebaseerd op heel nauwkeurige algoritmes voor het modelleren van lasercaviteiten. Ze zijn vooral gebruikt ter verificatie van resultaten bekomen met benaderde algoritmes.

3 Synthese van complexe PIC's

De ontwerphulpmiddelen die nu beschikbaar zijn focussen vooral op de analyse van optische IC's. Ze kunnen helpen bij het beter begrijpen van experimentele resultaten en bij het reduceren van het aantal experimentele stappen. De situatie is echter nog ver van ideaal. Weinig van de commercieel verkrijgbare programma's zijn specifiek ontwikkeld voor de synthese van een complex optisch circuit naar een gegeven specificatie. Bovendien zijn voor het ontwerp van gecompliceerde circuits zoals de multigolflengtelaser, waarbij de structuur van één deel van de PIC een sterke invloed heeft op andere delen van de PIC en waarbij een sterke koppeling optreedt met elektrische en thermische problemen, nog geen geschikte CAD-tools beschikbaar.

Ruwweg gesproken zijn er twee problemen te onderscheiden en hun oplossing is op het eerste zicht onverenigbaar. Langs de ene kant zijn de nu gebruikte methodes vaak onnauwkeurig en dat op verschillende niveaus van het ontwerp. De componentstructuur kan onnauwkeurig gedefinieerd zijn of overgesimplificeerd. Vaak is ook het gebruikte model gesimplificeerd of kan de numerieke implementatie aanleiding geven tot fouten. In de meeste gevallen wordt bovendien de koppeling met andere problemen - thermische of elektrische - verwaarloosd. De oplossing voor dit probleem lijkt voor de hand liggend: het gebruik van meer rigoureuze algoritmes, betere definitie van de toepassingsgebieden en sensitiviteitsstudies voor parameters waarvan de waarde niet exact gekend is. Dit brengt ons echter meteen bij het tweede probleem, de berekeningstijd. Naarmate meer rigoureuze berekeningsmethodes worden toegepast neemt die enorm toe. Dit wordt vooral een probleem wanneer een grote parameterruimte moet worden onderzocht of als de koppeling met andere problemen in rekening wordt gebracht. Het lijkt op dit moment niet denkbaar dat binnen afzienbare tijd rigoureuze elektromagnetische oplossers beschikbaar zullen worden die op een redelijke termijn complexe PICs kunnen analyseren.

Volgens ons is een mogelijke uitweg uit deze impasse de evolutie naar kennisgedreven hulpmiddelen, waarbij de nadruk niet langer ligt op de veldberekeningen op zich maar

veeleer op het manipuleren en verwerken van vooraf bekomen resultaten. De basis van zo'n pakket wordt dan gevormd door een database ("knowledge base"), waarin de vooraf bekomen gegevens zijn opgeslagen en een tool ("inference engine") die de gegevens uit de database kan verwerken. Die database kan daarbij gegevens in verschillende vormen bevatten zoals goed ontworpen golfgeleiderelementen, ontwerpregels, tabellen met data voor een geparameteriseerde golfgeleider … Natuurlijk zullen ook een krachtige gebruikersinterface en een interface tussen de programma's die de veldberekeningen doorvoeren en de database nodig zijn.

Deze aanpak werd geïllustreerd aan de hand van het ontwerp van een monolithisch geïntegreerde Phased-Array laser, gebaseerd op een selectieve groeitechniek. Doordat hierbij de lagenpakketten in het actieve en het passieve gebied identiek zijn (op een reductie van de diktes met een factor 1.5 na), is de werking van de versterkers en de passieve golfgeleiders sterk gecorreleerd en is het onmogelijk beide types golfgeleiders apart te optimaliseren.

4 Phased-Array demultiplexers: werkingsprincipe en ontwerp

4.1 Werkingsprincipe

Een Phased-Array demultiplexer is opgebouwd uit twee sterkoppelaars die via een dispersieve golfgeleiderrij met elkaar verbonden zijn. Licht uit een ingangsgolfgeleider wordt via de sterkoppelaar in de golfgeleiderrij gekoppeld. De rij is zo ontworpen dat het optisch weglengteverschil tussen twee opeenvolgende armen gelijk is aan een geheel aantal keren de centrale golflengte. Dat heeft als gevolg dat de velddistributie van de ingangsapertuur gereproduceerd wordt aan de uitgangsapertuur en dat voor deze golflengte het licht wordt gefocusseerd in het centrum van het beeldvlak. Als de golflengte van het invallend licht echter afwijkt van de centrale golflengte, zal het golffront aan de uitgangsapertuur, tengevolge van de lineaire faseverschuiving in de golfgeleiderrij, gekanteld zijn en de focus in het beeldvlak verschuift, weg van het centrum. Als nu op geschikte plaatsen in het beeldvlak golfgeleiders aangebracht worden, kan het licht gescheiden worden in de gewenste golflengtekanalen. Merk op dat de werking van de Phased-Array reciprook is: als we de propagatierichting omkeren en uit de verschillende golfgeleiders licht laten invallen met de correcte golflengte, zullen alle kanalen in één golfgeleider gemultiplexeerd worden. Het is in deze opstelling dat de Phased-Array gebruikt wordt in de PAL.

4.2 Ontwerp van een Phased-Array multiplexer voor een multigolflengtelaser

Bij het ontwerp van Phased-Arrays die gebruikt worden als passieve demultiplexer, worden meestal de overspraak met naburige kanalen en het totale verlies van de component als belangrijkste criteria gehanteerd bij het ontwerp. Wanneer de Phased-Array echter ontworpen wordt voor gebruik in een multigolflengtelaser, zijn de periode (*FSR* - free spectral range) en

de bandbreedte meer relevante parameters. Om laserwerking in verschillede doorlaatbanden van de Phased-Array te voorkomen moet de *FSR* immers voldoende groot gekozen worden en om stabiele laserwerking in één enkele longitudinale mode te verkrijgen moet de filterbandbreedte zo klein mogelijk zijn. Zowel het vergroten van de *FSR* als het verkleinen van de filterbandbreedte zorgen er echter voor dat de caviteitslengte toeneemt, waardoor de longitudinale modes dichter bij elkaar komen te liggen. Het is dan ook duidelijk dat er een afweging zal moeten gemaakt worden tussen het minimaliseren van de filterbandbreedte en het minimaliseren van de caviteitslengte, om de werking van de laser te optimaliseren. Daarom werd de geometrie van de Phased-Array in meer detail bestudeerd en werd een optimaal ontwerp bepaald, gebaseerd op een in de literatuur gerapporteerde formule voor de optimale verhouding tussen filterbandbreedte en longitudinale modespatiëring.

Hoofdstuk 3

Theoretische analyse van Phased-Array multigolflengtelasers

1 Inleiding

In dit hoofdstuk wordt de werking van een langecaviteitslasers met een golflengteselectief filter binnen de caviteit theoretisch onderzocht. Daarbij wordt geen rekening gehouden met details die specifiek zijn voor het gebruikte integratieschema of voor het type demultiplexer.

Fig. 3-1 toont een principeschets van de onderzochte laser: een rij met N versterkers (de kanaalversterkers of de signaalversterkers) is gekoppeld met N ingangspoorten van een multiplexer. De uitgangspoort van de multiplexer kan verbonden zijn met een gewone passieve golfgeleider of met een andere versterker (de uitgangsversterker). De lasercaviteit wordt gevormd door de spiegels aan de uiteinden van de component. Meestal zijn dit de gekliefde facetten van de chip, al dan niet gecoat. Vermits alle versterkers tegelijk worden gefabriceerd, veronderstellen we dat ze allemaal gekarakteriseerd worden door dezelfde materiaalparameters en dezelfde geometrische parameters. Alleen de lengte van de versterkers wordt gevarieerd. Deze veronderstelling vereenvoudigd de notatie aanzienlijk maar doet geen afbreuk aan de algemeenheid van de analyse

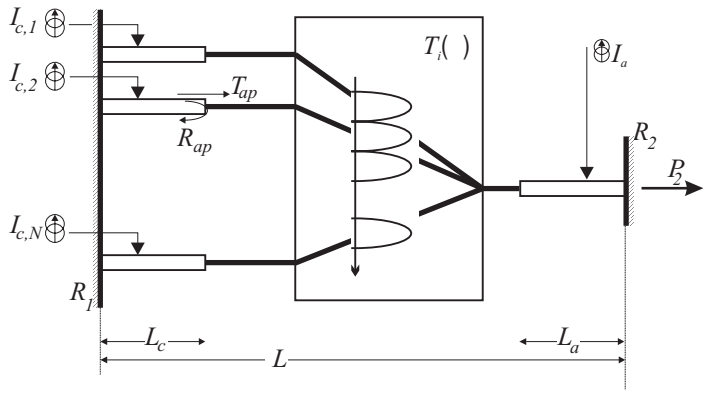

Fig. 3-1 Schematische afbeelding van de multigolflengtelaser zoals die wordt besproken in dit hoofdstuk.

Daar de onderdrukking van de overspraak tussen de verschillende poorten van de multiplexer over het algemeen veel beter is dan 20 dB, kunnen de kanalen van een multigolflengtelaser zonder uitgangsversterker voor de meeste toepassingen onafhankelijk van elkaar worden beschouwd. Daarom wordt in deel twee van dit hoofdstuk uitgebreid aandacht besteed aan de werking van een laser die bestaat uit een versterker en een lange passieve caviteit met een zeker verlies. In deel drie van dit hoofdstuk wordt dan de volledige laser zoals voorgesteld in Fig. 3-1 besproken, waarbij vooral aandacht wordt besteed aan de

overspraak die ontstaat in de gemeenschappelijke uitgangsversterker. In het laatste deel van dit hoofdstuk worden enkele ontwerpregels voor multigolflengtelasers samengevat.

2 Eénkanaalslangecaviteitslasers zonder gemeenschappelijke uitgangsversterker

Vermits, zoals hierboven uitgelegd, de koppeling tussen de verschillende kanalen van een multigolflengtelaser zonder uitgangsversterker meestal verwaarloosbaar is, wordt in dit hoofdstuk de werking van een éénkanaalslangecaviteitslaser onderzocht. In een eerste paragraaf worden de tempovergelijkingen voor deze laser afgeleid. In de volgende paragrafen worden dan respectievelijk de statische en de dynamische karakteristieken afgeleid.

2.1 Tempovergelijkingen voor een éénkanaalslangecaviteitslaser

Bij transmissie door de lasercaviteit wordt het licht versterkt door gestimuleerde emissie. Als de totale versterking bij een doorgang door de caviteit gelijk wordt aan de daarbij optredende verliezen, zal laserwerking optreden. Uit deze vaststelling kunnen de waarde van de drempelwinst en de laserfrequentie worden afgeleid. Ze worden respectievelijk gegeven door:

$$\begin{aligned}\Gamma g_{th} &= \alpha_s + \frac{1}{2L_a}\ln\left(\frac{1}{R_1R_2}\right) + \frac{1}{L_a}\ln\left(\frac{1}{f}\right) \\ &= \alpha_s + \alpha_m + \alpha_p\end{aligned} \tag{3-1}$$

en

$$\nu_{th} = \frac{mc}{2\left(L_a n_a + L_p n_p\right)} = \frac{mc}{2Ln_e} \tag{3-2}$$

Hierbij is f het verlies dat optreed in de passieve caviteit. Zoals gewoonlijk kan α_m worden beschouwd als het gedistribueerde spiegelverlies. Analoog kunnen we α_p beschouwen als het gedistribueerde verlies door de passieve caviteit.

Het is mogelijk om zowel voor de fotondichtheid als voor de ladingsdragersdichtheid een geschikte tempovergelijking op te stellen. Met $S^{\#}$ het totaal aantal fotonen in het actieve gedeelte van de caviteit vinden we:

$$\begin{aligned}S^{\#}(t) &= f^2 R_1R_2 \exp\left[2\left(\Gamma g - \alpha_s\right)L_a\right]S^{\#}\left(t-\tau_L\right) + KR_{sp}^{'} \\ &\approx \left[1 + 2\left(\Gamma g - \alpha_s - \alpha_m - \alpha_p\right)L_a\right]S^{\#}\left(t-\tau_L\right) + KR_{sp}^{'}\end{aligned} \tag{3-3}$$

en :

$$R_{sp}^{'} = 2\frac{\left(L_a\right)^2}{L}\Gamma g n_{sp} \tag{3-4}$$

Hierbij is n_{sp} de inversiefactor. Deze uitdrukking voor de spontane emissie werd oorspronkelijk afgeleid door Henry en slaat op het aantal fotonen dat in een enkele longitudinale mode wordt gekoppeld. De spontane emissiefactor *K* wordt gegeven door:

$$K = \left[\frac{\left(\sqrt{R_1} + f\sqrt{R_2}\right)\left(1 - f\sqrt{R_1 R_2}\right)}{f\sqrt{R_1 R_2}\,\ln\left(1/R_1 R_2 f^2\right)} \right]^2 \tag{3-5}$$

Als het verlies in de passieve caviteit laag is, is K ongeveer gelijk aan één en kan de spontane emissiefactor worden verwaarloosd. Als het verlies in de caviteit echter toeneemt kan deze factor belangrijk worden (>20).

Als de variaties gedurende de tijd τ_L die nodig is voor het volledig doorkruisen van de caviteit, klein zijn, kan de term $S^{\#}(t-\tau_L)$ in vergelijking (3-3) vervangen worden door een gepaste differentiaalterm en wordt de standaardtempovergelijking voor korte-caviteitslasers teruggevonden. In het hier beschouwde geval is dit echter niet het geval en moet uitdrukking (3-3) gebruikt worden.

Naast de tempovergelijking voor $S^{\#}$, kan ook een vergelijking voor de fase worden opgesteld. We vinden:

$$\phi(t+\tau_L) - \phi(t) = \alpha L_a \frac{\partial g}{\partial N}(N - N_{th}) \tag{3-6}$$

Deze uitdrukking geeft de verandering van de fase door een verandering van de ladingsdragersdichtheid weer. In vergelijking met een standaardlaser zonder externe caviteit is deze verandering voor een langecaviteitslaser kleiner met een factor L_a/L. Dit is een gevolg van het feit dat een modulatie van de ladingsdragersdichtheid enkel invloed heeft op de brekingsindex van het actieve gedeelte van de caviteit en het passieve gedeelte ongemoeid laat.

Als laatste kunnen we ook een tempovergelijking opstellen voor de ladingsdragersdichtheid. Deze wordt gegeven door:

$$\frac{dN}{dt} = \frac{I}{eV_a} - R(N) - \mathrm{v}_g g S \tag{3-7}$$

met S de gemiddelde fotondichtheid in het actieve gedeelte van de caviteit en:

$$R(N) = AN + BN^2 + CN^3 \tag{3-8}$$

met A, B en C respectievelijk the monomoleculaire, de bimoleculaire en de Auger-recombinatiecoëfficiënt.

2.2 Drempelstroom en uitgangsvermogen

De drempelstroom wordt eenvoudig afgeleid uit de uitdrukking voor de ladingsdragersdichtheid (3-7) en gegeven door:

$$I_{th} = eV_a R(N_{th}) \tag{3-9}$$

N_{th} wordt daarbij bepaald uit de kennis van de drempelwinst $g_{th}(N_{th})$.

Voor de externe differentiële efficiëntie vinden we:

$$\begin{aligned}
\frac{\Delta P_1}{\Delta I} &= \frac{h\nu}{e}\eta_{ext,1} = \eta_i \frac{h\nu}{e}\frac{\alpha_p + \alpha_m}{\alpha_s + \alpha_p + \alpha_m}\frac{(1-R_1)f\sqrt{R_2}}{\left(1-f\sqrt{R_2R_1}\right)\left(f\sqrt{R_2}+\sqrt{R_1}\right)} \\
\frac{\Delta P_2}{\Delta I} &= \frac{h\nu}{e}\eta_{ext,2} = \eta_i \frac{h\nu}{e}\frac{\alpha_p + \alpha_m}{\alpha_s + \alpha_p + \alpha_m}\frac{(1-R_2)f\sqrt{R_1}}{\left(1-f\sqrt{R_2R_1}\right)\left(f\sqrt{R_2}+\sqrt{R_1}\right)}
\end{aligned} \tag{3-10}$$

Hierbij is η_i de interne differentiële efficiëntie.

Gebruikmakend van bovenstaande uitdrukkingen is het mogelijk om het uitgangsvermogen van de laser als functie van de stroom te bepalen. We hebben resultaten die op deze manier werden verkregen vergeleken met resultaten van een rigoureus lasermodel (*CLADISS)*. Er blijkt slechts een minieme afwijking te zijn die iets toeneemt bij stijgende caviteitsverliezen. Dit is te wijten aan het feit dat we verondersteld hebben dat de ladingsdragersdichtheid constant is over het actieve gedeelte van de caviteit.

We hebben dit model o.a. gebruikt om de ideale lengte van de versterker van een lange-caviteitslaser te bepalen, als functie van het verlies in de passieve caviteit.

2.3 Onderdrukking van naburige lasermodes

De fotontempovergelijking kan eenvoudig worden uitgebreid naar het geval waar meerdere longitudinale modes belangrijk zijn. Uitgaande van deze uitdrukkingen kan dan een voorwaarde worden opgesteld voor het minimale verschil in modale winst voor twee modes opdat de verhouding tussen het vermogen in beide modes voldoende hoog zou zijn. Deze uitdrukking kan gebruikt worden in gevallen waar de afstand tussen beide modes groot genoeg is zodat niet-lineaire effecten geen rol spelen. Dit is bijvoorbeeld het geval voor modes in een verschillende doorlaatband van de Phased-Array.

Door de grote lengte van de caviteit is de afstand tussen longitudinale modes binnen één doorlaatband van de Phased-Array echter zo klein (2 tot 8 GHz) dat niet-lineaire effecten een belangrijke rol gaan spelen. Het blijkt dat door een intermodulatie van de longitudinale modes een faserooster ontstaat waaraan verstrooiing optreedt die als gevolg heeft dat zowel modes met een hogere intensiteit als modes met een lagere frequentie bevoordeeld worden. Wanneer dit effect gecombineerd wordt met een voldoende nauw filter, kan een heel stabiele, monomodale laserwerking worden verkregen. Uit een nauwkeurig stabiliteitonderzoek kan worden afgeleid dat er in de buurt van het centrum van de doorlaatband een stabiliteitsgebied is voor de laserende mode. Zolang de actieve mode binnen dit gebied blijft, treden geen modehops op. Wanneer de actieve mode echter uit dit gebied schuift (bvb. door een temperatuurverandering), zal een modehop optreden en zal de laserwerking verschuiven naar een nabijgelegen longitudinale mode.

2.4 Lijnbreedte

Zoals gewoonlijk is ook de lijnbreedte van een laser met een passieve caviteit omgekeerd evenredig met het uitgangsvermogen, maar in vergelijking met de formule voor een standaard laser bevat de hier afgeleide uitdrukking een extra term $(L_a/L)^2$. Dit betekent dat deze lasers extreem smalle lijnbreedtes kunnen hebben.

2.5 Dynamische eigenschappen

Uitgaande van de in paragraaf 2.1 afgeleide tempovergelijkingen kan de kleinsignaalrespons van een laser met een passieve caviteit worden afgeleid:

$$\frac{\Delta P_2}{\Delta I} = \eta_{ext,2} \frac{1}{\left[\frac{1}{\omega_r^2 \tau_L}\left(1-\exp\left(-j\omega\tau_L\right)+\gamma\right)\left(j\omega+\frac{1}{\tau_e}+\mathrm{v}_g\frac{\partial g}{\partial N}\langle S\rangle\right)+1\right]} \qquad (3\text{-}11)$$

De factor $(1-\exp(-j\omega\tau_L))$ volgt uit het optreden van de term $S^{\#}(t-\tau_L)$ in de tempovergelijking voor de fotonen (3-3) en is verantwoordelijk voor een quasi-periodische respons. Voor lage frequenties kan deze factor benaderd worden door ($j\omega\tau_L$) en wordt de klassieke kleinsignaalrespons voor kortecaviteitslasers teruggevonden.

De resonantiefrequentie ω_r^2 die in deze uitdrukking voorkomt bevat een extra term L_a/L wat als gevolg heeft dat de bandbreedte van dit type laser afneemt met toenemende caviteitslengte. Om (3-11) te verifiëren werden resultaten berekend met deze formule vergeleken met resultaten van een rigoureus laser model (*CLADISS*). Alhoewel de vereenvoudigde formule (3-11) de demping bij lage frequenties iets lijkt te overschatten, is over het algemeen de gelijkenis vrij goed. Zo wordt de invloed van een veranderende caviteitslengte en de ligging van de resonantiepieken correct voorspeld.

3 Multigolflengtelasers met uitgangsversterker

3.1 Meerkanaals-tempovergelijkingen

De tempovergelijkingen die afgeleid werden in paragraaf 2.1 kunnen worden uitgebreid zodat de volledige laser als afgebeeld in Fig. 3-1 wordt beschreven. Dit resulteert in een niet-lineair stelsel van $2N+1$ vergelijkingen met evenveel onbekenden, dat numeriek kan worden opgelost. Om de resultaten te verifiëren werd het uitgangsvermogen van een laser gevormd door twee versterkers aan de uiteinden van een verlieshebbende passieve caviteit vergeleken met het uitgangsvermogen van een laser gevormd door één enkele versterker met de dubbele lengte en een passieve caviteit. Zowel *CLADISS* als de door ons afgeleide tempovergelijkingen voorspellen een hoger uitgangsvermogen voor het eerste type laser, zelfs indien rekening gehouden wordt met een redelijk extra verlies te wijten aan de tweede actief-passiefovergang.

3.2 Signaalverstoring en overspraak door de uitgangsversterker

Wanneer meerdere kanalen tegelijk worden aangestuurd, zal een verandering in het vermogen in één van de kanalen onmiddellijk een invloed hebben op de ladingsdragersdichtheid in de gemeenschappelijke uitgangsversterker. Vermits daardoor de winst van de versterker beïnvloed wordt heeft dit ook gevolgen voor het vermogen in de andere kanalen en geeft dit aanleiding tot signaalverstoring en overspraak.

Met behulp van de in de vorige paragraaf afgeleide tempovergelijkingen werden de gevolgen hiervan onderzocht bij statische laserwerking. Het blijkt dat het voordeel van het gebruik van de uitgangsversterker sterk afneemt bij een toenemend aantal kanalen. Verder is het zo dat de verandering van de ladingsdragersdichtheid in de gemeenschappelijke versterker bepaald wordt door de effectieve leeftijd van de ladingsdragers die, afhankelijk van de ladingsdragersdichtheid en het vermogen, kan variëren tussen 200 ps en enkele nanoseconden. Daardoor zal dit effect ook de dynamische eigenschappen van de laser beïnvloeden.

3.3 Elektronische compensatie

Om overspraak in de gemeenschappelijke versterker te vermijden moet de ladingsdragersdichtheid constant gehouden worden. Verschillende auteurs hebben voorgesteld om dit te doen door aan de stroom een component evenredig met het uitgangsvermogen toe te voegen. Zowel feedback- als feedforwardschema's werden daarbij voorgesteld. Beide vereisen echter een heel nauwkeurige afstelling van de bijhorende elektronica en zijn niet zo eenvoudig praktisch te realiseren.

3.4 Winstvergrendeling

Als een alternatief voor de elektronische compensatieschema's van de vorige paragraaf, stellen we hier een andere aanpak voor om de winst van de uitgangsversterker te vergrendelen. Deze methode vereist geen bijkomende elektronische uitrusting en bemoeilijkt de processing niet. Er is alleen een kleine aanpassing van de geometrie nodig. Zoals getoond in Fig. 3-2a wordt één van de ingangsversterkers vervangen door een passieve golfgeleider. Als de uitgangsversterker aangeschakeld wordt, zal de laserwerking in de caviteit gevormd door deze versterker en de passieve golfgeleider ervoor zorgen dat de winst van de uitgangsversterker vergrendeld blijft. Als nu andere kanalen worden aangeschakeld zal het vermogen in het winstvergrendelingskanaal dalen maar er zal geen overspraak meer optreden tussen de kanalen onderling.

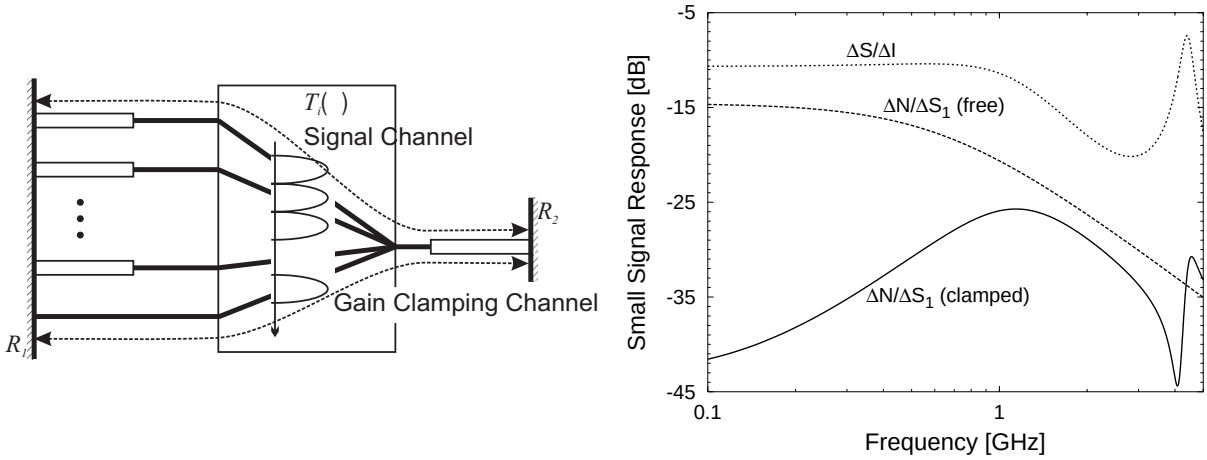

Fig. 3-2 a) Principeschets van de multigolflengtelaser met winstvergrendelde uitgangsversterker. b) Modulatie van de ladingsdragersdichtheid ΔN in een laser met en zonder winstvergrendeling onder invloed van een externe modulatie ΔS_1. Ter vergelijking is ook de kleinsignaalrespons ΔS_0 door een stroommodulatie ΔI weergegeven.

De tempovergelijkingen van paragraaf 3.1 werden gebruikt om de werking van een winstvergrendelde multigolflengtelaser te onderzoeken. Verder is het dynamisch gedrag van zo'n laser bestudeerd. Daarvoor werd de modulatie van de ladingsdragersdichtheid ΔN onder invloed van een extern geïnjecteerd signaal bestudeerd. De resultaten zijn getoond in Fig. 3-2b. Daaruit blijkt dat voor frequenties waar de kleinsignaalrespons belangrijk is (< 2 GHz), de vergrendelde versterker beduidend minder beïnvloed wordt door het externe signaal dan de niet-vergrendelde versterker.

4 Conclusie en ontwerpregels

Om dit hoofdstuk af te sluiten vatten we hier enkele ontwerpregels voor multigolflengtelasers samen. Het "ideale ontwerp" is echter sterk afhankelijk van de precieze toepassing waarvoor de laser zal gebruikt worden en die moet bij het ontwerpen dan ook altijd in het achterhoofd gehouden worden.

Uitgangsversterker

Als slechts één kanaal tegelijk gebruikt wordt, bijvoorbeeld als de laser als reservebron wordt gebruikt, kan een gemeenschappelijke versterker nuttig zijn om een hoger uitgangsvermogen te verkrijgen of om modehopping te voorkomen. Als echter meerdere kanalen tegelijk worden aangestuurd is het voordeel van een gemeenschappelijke versterker minder duidelijk. Door het geschikt kiezen van de stromen is het nog altijd mogelijk om een hoger uitgangsvermogen per kanaal te verkrijgen voor een gegeven stroom. Als de kanalen worden gemoduleerd treedt echter overspraak op door winstonderdrukking in de uitgangsversterker. Dit kan worden voorkomen door het vergrendelen van de winst van deze versterker zoals voorgesteld in paragraaf 3.4 of door het gebruik van het in paragraaf 3.3 beschreven

elektronische compensatieschema. Over het algemeen denken we echter dat het in zulke gevallen beter is geen uitgangsversterker te gebruiken.

Caviteitslengte

Om de modulatiebandbreedte van de laser te vergroten is het belangrijk de lengte van de caviteit zo kort mogelijk te houden. Er moet daarbij echter rekening gehouden worden met het feit dat de nauwkeurigheid van de kanaalspatiëring bepaald wordt door de longitudinale modespatiëring. Bij het ontwerp van de Phased-Array laser is het vooral belangrijk dat de lengte van de toegangsgolfgeleiders zo kort mogelijk wordt gehouden. Dit laat toe om de bandbreedte van het filter gevoelig te versmallen zonder de totale caviteitslengte op te voeren, wat de stabiliteit van de laser erg ten goede komt.

Multi-passband lasing

De beste methode om te voorkomen dat de laser in meerdere doorlaatbanden gaat opereren is het chirpen van de Phased-Array. Als dit niet mogelijk is moet de *FSR* van de demultiplexer zo groot mogelijk worden gekozen. Verder is het voordelig om de lengte van de versterkers te vergroten.

Reflecties

Om de laserwerking niet te verstoren moeten reflecties binnen de caviteit zoveel mogelijk worden vermeden. Op basis van experimentele resultaten denken we dat ook externe reflecties de laserwerking kunnen beïnvloeden. Alhoewel hun effect niet systematisch werd onderzocht, denken we dat het nuttig is om een isolator te gebruiken.

Hoofdstuk 4

Ontwerp, fabricage en karakterisatie van de subcomponenten voor een Phased-Array laser

Zoals uitgelegd in hoofdstuk 1, worden in het monolithische integratieschema versterkers van het ridge-type gebruikt, om de overgang met de passieve golfgeleiders te vereenvoudigen. Ook de versterkers die door Optospeed werden gefabriceerd en gebruikt werden voor de hybride integratie, waren van dit type. Daarom worden in het eerste deel van dit hoofdstuk de voor- en nadelen van dit type versterker besproken. In paragraaf 1.1 wordt de algemene theoretische achtergrond geschetst, terwijl in de paragrafen 1.2 en 1.3 respectievelijk de versterkers die ontworpen werden voor de monolithische en de hybride integratie worden besproken. Het tweede deel van dit hoofdstuk is gewijd aan het ontwerp en de karakterisatie van de passieve golfgeleiders die werden gebruikt in de context van dit werk. Opnieuw worden de golfgeleiders die gebruikt zijn in het monolithische en in het hybride integratieschema in een aparte paragraaf besproken. De laatste twee delen van dit hoofdstuk zijn gewijd aan de verliezen die optreden bij de overgang tussen de actieve en de passieve golfgeleiders.

1 Versterkers en lasers van het ridge-type

1.1 Theoretische beschrijving

Het belangrijkste voordeel van ridge-type lasers en versterkers is de eenvoudige fabricageprocedure. Er is immers slechts één groeistap nodig. In de praktijk blijkt de precieze etsdiepte echter een heel kritische parameter te zijn. Doordat de injectie van de ladingsdragers zorgt voor een verlaging van de brekingsindex in het centrum van de golfgeleider is het noodzakelijk om voor een zeker minimum ingebouwd lateraal indexcontrast te zorgen. Verder zorgt het lagere laterale indexcontrast voor een hogere drempelstroom en, waar bij begraven golfgeleiderstructuren de actieve laag omringd is door transparante lagen, strekt de mode bij ridge-type versterkers zich uit in een sterk absorberende laag.

Om het exacte stroomverloop en de verdeling van de ladingsdragers te bepalen moet teruggegrepen worden naar numerieke modellen. Om toch enig inzicht te verwerven in de werking van dit type lasers wordt vaak een ééndimensionale benadering gemaakt, met behulp van de effectieve index methode. Meestal wordt ook de invloed van het optisch vermogen op de ladingsdragersverdeling verwaarloosd zodat de analyse alleen maar strikt geldig is beneden de drempelstroom.

Wij hebben een methode gebruikt waarbij uit de diffusievergelijking voor de ladingsdragers in de actieve laag de verdeling van de ladingsdragers $N(y)$ over de actieve laag wordt berekend. Uitgaande van deze verdeling kan dan het effectieve complexe brekingsindexprofiel worden bepaald als de som van het ingebouwde brekingsindexprofiel en de perturbatie veroorzaakt door de ladingsdragersinjectie. De modale winst kan dan eenvoudig worden berekend van het imaginaire deel van de propagatieconstante van de golfgeleidermode. Deze procedure is samengevat in Fig. 4-1 die schematisch het ingebouwde brekingsindexcontrast, de ladingsdragersdichtheid en het effectieve brekingsindexprofiel toont. In de laatste figuur is ook het effectieve brekingsindexcontrast $\Delta n'_{eff}$ aangeduid.

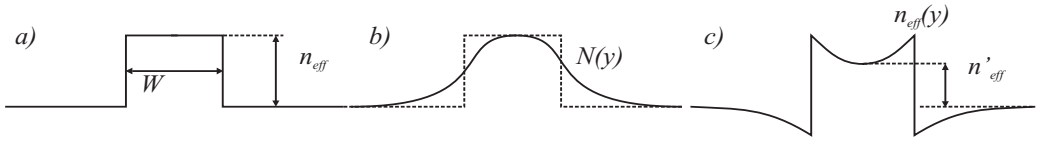

Fig. 4-1 Schematisch overzicht van a) het ingebouwde brekingsindexcontrast, b) de geïnjecteerde ladingsdragersdichtheid en c) het geperturbeerde brekingsindexprofiel.

1.2 Ridge-type lasers voor het selectieve-groei-gebaseerde monolithische integratieschema

Vaak wordt de dikte van de filmlagen die de actieve laag omringen zo gekozen dat de opsluiting van het elektrisch veld in de actieve laag gemaximaliseerd wordt. In het monolithische integratieschema dat wij onderzocht hebben vormen deze lagen echter ook de geleidende laag voor de golfgeleiders in het passieve gedeelte van de component (op een reductie van de dikte met een factor 1.5 na, ten gevolge van de selectieve groei). Om het caviteitsverlies zoveel mogelijk te beperken is het daarom voordelig de hoge-indexfilmlagen zo dik mogelijk te maken. Het effect hiervan op de werking van de lasers is zowel experimenteel als theoretisch bestudeerd.

1.2.1 Experimentele resultaten

Vertrekkend van een lagenstructuur met een filmlaag die in totaal bijna 900 nm dik was, werden lasers met verschillende breedte en verschillende etsdiepte gefabriceerd. De actieve laag werd gevormd door 5 InGaAs kwantumputlagen. Het bleek dat de lasers die 100 nm diep in de actieve laag waren geëtst (Δn_{eff} =0.024), beduidend beter werkten dan de lasers met andere etsdieptes. De beste lasers hadden een drempelstroom van 19 mA en een externe differentiële efficiëntie van 34 % per zijde ($W = 3\,\mu m$). De lasers met een lager brekingsindexcontrast vertoonden helemaal geen laserwerking (Δn_{eff} =0.009) of alleen voor de grotere breedtes (Δn_{eff} =0.015). Dit kan verklaard worden door de in de vorige paragraaf besproken indexreductie ten gevolge van de ladingsdragersinjectie.

Voor enkele van de gefabriceerde lasers werd het winstspectrum bepaald uit het spontane-emissiespectrum met behulp van de Hakki-Paoli methode. Uit de resultaten bleek dat de beste lasers heel lage interne verliezen hadden. Ook de maximumwinst als functie van de stroomdichtheid en de piekgolflengte werden bepaald.

1.2.2 Berekening van de modale winst

Met het theoretisch model van paragraaf 1.1 hebben we de drempelstroom en de transparantiestroom van een $3\,\mu m$ brede laser theoretisch berekend. Door deze waarden te fitten met de experimentele resultaten van de vorige paragraaf, vonden we waarden voor de differentiële winst ($a = 4.63\times10^{-16}$ cm^{-2}) en de transparantieladingsdragersdichtheid ($N_0 = 1.2\times10^{-18}$ cm^{-3}) van de kwantumputlagen die vergelijkbaar zijn met in de literatuur gerapporteerde waarden en die ons toelieten de drempelstroom voor de $5\,\mu m$ brede lasers correct te voorspellen. We hebben ook de invloed van de etsdiepte op de modale winst onderzocht.

1.2.3 Het gebruik van een etsstoplaag

Omdat de precieze etsdiepte erg kritisch is, zou het handig zijn als de bovenkant van de geleidende laag als een selectieve etsstoplaag kan worden gebruikt, terwijl het ideale indexcontrast (Δn_{eff} =0.024) behouden blijft. Het blijkt dat dit mogelijk is door de totale dikte van de geleidende laag iets te verkleinen, tot zo'n 650 nm. Dit zal leiden tot een iets hoger absorptieverlies, vermits de opsluiting in de gedoteerde mantellagen toeneemt maar daar ook de opsluiting in de kwantumputten toeneemt, vermoeden we dat dit niet zal leiden tot een gevoelige verandering van de laserperformantie.

1.3 Optische versterkers voor de hybride integratie

Voor de realisatie van de hybride Phased-Array laser (hoofdstuk 5 & 6) zijn optische versterkers met één hoogreflectief facet en één niet-reflecterend facet nodig. Deze RSOA's (reflective semiconductor optical amplifiers) werden ontworpen in samenwerking met en gefabriceerd door Optospeed SA (paragraaf 1.3.1). Voor de verdere ontwikkeling van het hybride integratieproces hebben we zelf vergelijkbare versterkerrijen en laserrijen gerealiseerd. Het ontwerp en de karakterisatie van deze componenten zijn besproken in paragraaf 1.3.2.

1.3.1 Ontwerp en karakterisatie van de RSOA-rijen gefabriceerd door Optospeed SA

Voor de versterkers die ontwikkeld werden in samenwerking met Optospeed SA werd een lagenstructuur bestaande uit een 100 nm dikke bulk actieve laag en een 70 nm dikke Q1.27 filmlaag met InP mantellagen gebruikt. De Q1.27 laag werd als selectieve etsstoplaag aangewend. Eén zijde van de chip is HR-gecoat, langs de andere zijde maakt de golfgeleider een hoek van 10 graden met de normaal op het facet en is de chip AR-gecoat. Voor de bocht is een adiabatisch ontwerp gekozen zodat geen offsets nodig zijn en de golfgeleider is verbreed

van $2\,\mu m$ aan het HR-gecoate facet tot $3\,\mu m$ aan het facet dat de overgang moet vormen met de passieve chip. Dit vergemakkelijkt de koppeling enigszins en zorgt ook voor een verdere reductie van de residuele reflectie aan dit facet. De lengte van de versterkers is $400\,\mu m$. De versterkers werden uitgebreid gekarakteriseerd (LI-curven, transparantiestroom als functie van de golflengte, ASE-spectrum). Ook de kleinsignaalrespons werd opgemeten. Uit de 3 dB-bandbreedte kon de effectieve leeftijd van de ladingsdragers worden bepaald als functie van de instelstroom. Door deze te fitten aan theoretische resultaten werden realistische waarden voor de monomoleculaire, de bimoleculaire en de Auger-recombinatiecoëfficiënten gevonden.

1.3.2 Ontwerp en karakterisatie van de in Gent gefabriceerde RSOA-rijen

Voor het ontwikkelen van de techniek voor het permanent aan elkaar verbinden van twee InP-chips (hoofdstuk 6), waren veel componenten nodig. Daarom is een masker ontworpen dat kon gebruikt worden voor de fabricage van RSOA-rijen en laserrijen. Het ontwerp van de RSOA-rijen was gelijkaardig aan het in de vorige paragraaf beschreven ontwerp van de RSOA-rijen gefabriceerd door Optospeed SA. Alleen werd in dit geval de breedte van de golfgeleiders gevarieerd tussen 2.0 en $4.0\,\mu m$.

Omdat de eerste versterkers niet zo goed waren werd het winstspectrum en het interne verlies van een $600\,\mu m$ lange laser opgemeten met de Hakki-Paoli methode. Het interne verlies bleek groot te zijn (~ 25 cm^{-1}), terwijl de differentiële winst relatief laag was. Voor deze versterkers werd een lagenpakket met een p-gedoteerde InP-mantellaag van slechts $1\,\mu m$ gebruikt. Omdat uit simulaties blijkt dat in zo'n geval het TiAu-contact de werking van de laser kan beïnvloeden werd een nieuwe lagenstructuur gegroeid met een dikkere InP-mantellaag.

De breedste lasers ($50\,\mu m$) met deze lagenstructuur hadden een drempelstroomdichtheid $J_{th} = 1365\,A/cm^2$ en $J_{th} = 1090\,A/cm^2$ voor respectievelijk $400\,\mu m$ en $600\,\mu m$ lange lasers (gepulste meting). De drempelstroomdichtheid voor de smallere lasers was echter veel hoger en nam, zoals verwacht, sterk toe met afnemende golfgeleiderbreedte. Bovendien was de externe differentiële efficiëntie laag. De precieze oorzaak hiervan is nog niet helmaal duidelijk.

2 Ontwerp en karakterisatie van passieve golfgeleiders

Zowel in het kader van het hybride integratieschema als in de context van het monolithische integratieschema werden passieve golfgeleiders onderzocht. De golfgeleiders die werden ontwikkeld voor het monolithische integratieschema hadden gedoteerde mantellagen. Het effect hiervan werd zowel theoretisch als experimenteel bestudeerd. Het type golfgeleider dat gebruikt werd in het hybride integratieschema is al uitgebreid beschreven in de litera-

tuur en in hoofdstuk twee werden al enkele theoretische resultaten besproken. Daarom wordt hier alleen het resultaat van een typische verliesmeting gegeven.

Alle verliezen die hier gerapporteerd worden zijn verkregen met de Fabry-Pérot meetmethode. Deze methode levert betrouwbare resultaten voor verliezen gelegen tussen 0.5 dB en 4 dB. De reproduceerbaarheid voor onafhankelijke metingen ligt in de buurt van 0.1 dB. Bij verschillende gelegenheden werden ook resultaten vergeleken van golfgeleiders die zowel door ons als door de Technische Universiteit Delft werden gekarakteriseerd. Daarvoor werd ongeveer een zelfde reproduceerbaarheid verkregen. De grootste onzekerheid verbonden met de methode is de precieze waarde van de reflectiecoëfficiënten. Ook voor multimodale golfgeleiders is de onzekerheid groter.

2.1 Passieve golfgeleiders voor de monolithisch geïntegreerde Phased-Array laser

In het monolithische integratieschema is het lagenpakket in het passieve gebied identiek aan het lagenpakket in het actieve gebied, op een reductie van de laagdiktes met een factor 1.5 na. Daarom werden passieve golfgeleiders gefabriceerd met dezelfde structuur als de in paragraaf 1.2 van dit hoofdstuk besproken lasers. Alleen de dikte van de lagen werd aangepast.

Er werden golfgeleiders met twee verschillende etsdieptes gefabriceerd en met breedtes die varieerden tussen 1.2 en 4 μm. Tegen de verwachtingen in, blijkt het verlies voor de minst diep geëtste golfgeleiders ongeveer constant te zijn als functie van de breedte (~ 1.5 dB/cm). Uit simulaties blijkt dat dit een gevolg zou kunnen zijn van een sterkere opsluiting van het licht in de sterk absorberende p-gedoteerde mantellaag bij een stijgende golfgeleiderbreedte. Dit kan het effect van het dalende verstrooiingsverlies compenseren.

Verder werd de minimumbochtstraal berekend als functie van de etsdiepte en de dikte van de filmlaag en vergeleken met experimentele resultaten. Ook de absorptie in de p-gedoteerde mantellaag werd berekend als functie van de dikte filmlaag.

2.2 Karakterisatie van de passieve golfgeleiders voor de hybride geïntegreerde PIC's

De passieve golfgeleiders die werden gebruikt voor de hybride integratie werden gefabriceerd in een lagenstructuur bestaande uit een 600 nm dikke Q1.3 laag ($n = 3.395$) met een 300 nm dikke InP mantellaag. Voor de definitie van de golfgeleiders werd een droog etsproces gebruikt (typische etsdiepte 50 à 100 nm in de Q1.3 laag). De breedte van de golfgeleiders was meestal 2 μm en de minimum bochtstraal 500 μm. De door ons opgemeten verliezen voor deze golfgeleiders lagen meestal tussen 1.0 dB/cm en 2.0 dB/cm. De golfgeleiders die gebruikt werden voor de realisatie van de winstvergrendelde Phased-Array laser hadden echter nog lagere verliezen (0.6 dB/cm).

3 Hybride koppeling

Bij de hybride koppeling worden de in paragraaf 1.3 besproken versterkers gekoppeld met de passieve golfgeleiders van de vorige paragraaf. Om de efficiëntie van deze koppeling te schatten en de invloed van alignatiefouten te onderzoeken hebben we de transmissie tussen beide golfgeleiders gesimuleerd met *Fimmprop3D,* een commercieel pakket gebaseerd op een driedimensionaal mode-expansiepropagatiealgoritme.

Beide golfgeleiders zijn verbreed tot $3\,\mu m$ aan het facet en zijn AR-gecoat. Zonder luchtspleet tussen beide golfgeleiders is de koppelingsefficiëntie heel hoog (~ 96 %). Wanneer de afstand tussen beide golfgeleiders toeneemt, neemt de koppelingsefficiëntie echter bijzonder vlug af. Voor een luchtspleet van $1\,\mu m$ is het transitieverlies al 2.5 dB, voor $d_{gap} = 2\,\mu m$ neemt het verlies toe tot 4.5 dB. Wanneer tussen beide golfgeleiders een medium met een hogere brekingsindex (bvb. een epoxy met typisch $n = 1.5$) wordt gebracht, stijgt de koppelingsefficiëntie wat. Deze stijging is belangrijker naarmate de afstand tussen beide chips toeneemt.

Ook de invloed van een transversale of een laterale alignatiefout werd bestudeerd. Als er geen luchtspleet is tussen beide chips, is de invloed van een transversale alignatiefout veel groter dan die van een laterale alignatiefout. Wanneer de luchtspleet tussen beide chips echter toeneemt worden de rollen omgedraaid. Dit is een gevolg van het feit dat het verreveld veel breder is in verticale richting dan in horizontale richting. Voor $d_{gap} = 2\,\mu m$ verwachten we dat het effect van beide soorten alignatiefout ongeveer gelijk is. Dit kon ook experimenteel worden geverifieerd (zie hoofdstuk 5).

Ter vergelijking hebben we ook het transitieverlies tussen twee laagcontrastgolfgeleiders met een typische begraven golfgeleiderstructuur berekend als functie van de longitudinale afstand tussen beide golfgeleiders. Waar voor de door ons gebruikte hoogcontrastgolfgeleiders de maximale afstand voor een transitieverlies van 1 dB kleiner is dan $0.4\,\mu m$, is bij de laagcontrastgolfgeleiders het transitieverlies zelfs voor $d_{gap} = 20\,\mu m$ kleiner dan 0.5 dB.

Voor het verhogen van de koppelingsefficiëntie en het verhogen van de tolerantie voor alignatiefouten kunnen natuurlijk bundelexpansiestructuren worden geïntegreerd in zowel de passieve als de actieve golfgeleiders. Dit verhoogt echter de complexiteit van de processing gevoelig. Als een tussenoplossing kunnen golfgeleiders worden gebruikt met een kleinere verreveldbreedte. Het is daarbij vooral belangrijk het verreveld in verticale richting te vernauwen, vermits dit tot drie keer zo breed kan zijn als het verreveld in horizontale richting. Dit is mogelijk door het verlagen van de brekingsindex van de filmlagen. Als de brekingsindex echter teveel wordt verlaagd kan het contrast met het substraat zo laag worden dat het, onafhankelijk van de etsdiepte, niet meer mogelijk is om golfgeleiders met de gewenste minimumbochtstraal te realiseren. Een alternatief is het gebruik van lagenstructuren waarvan de brekingsindex geleidelijk toeneemt naar het centrum.

4 Overgang tussen de actieve en de passieve golfgeleiders in het monolithische integratieschema

In het monolithische integratieschema dat besproken werd in hoofdstuk 1, worden de versterkers gedefinieerd door een nat etsproces. De passieve golfgeleiders daarentegen (o.a. de Phased-Array demultiplexer), worden droog geëtst. Tijdens het etsen van het ene type golfgeleiders wordt het ander type afgeschermd met een passend masker. De overgang tussen de droog geëtste en de nat geëtste golfgeleiders vindt plaats in het planair gegroeide gebied. In de praktijk blijkt het onmogelijk om beide maskers die gebruikt worden voor het afschermen van de golfgeleiders perfect te aligneren. Daardoor overlappen beide maskers wat en zal er een klein gebied zijn waar geen golfgeleiders gedefinieerd worden, ofwel is er daarentegen een spleet tussen beide maskers en zullen de golfgeleiders in dit gebied dieper geëtst worden. Uit simulaties blijkt dat de eerste optie minder extra verliezen oplevert voor maskeralignatiefouten kleiner dan $2\,\mu m$. Daarom laten we beide maskers met opzet enigszins overlappen. Bovendien verlaagt het transitieverlies gevoelig wanneer de golfgeleiders plaatselijk verbreed worden van $2\,\mu m$ tot $3\,\mu m$, wat te verklaren is door de gevoelig kleinere verreveldbreedte in het laatste geval.

Hoofdstuk 5

Ontwikkeling van hybride gekoppelde Phased-Array multigolflengtelasers

1 Inleiding

Het almaar toenemende succes van golflengtegemultiplexeerde optische telecommunicatienetwerken zorgt voor een toenemende vraag naar complexe fotonische IC's. Er is lang geloofd dat alleen monolithisch geïntegreerde circuits gebaseerd op een InP/InGaAsP materiaalsysteem commercieel interessant zouden zijn voor dergelijke toepassingen. Dit materiaalsysteem laat immers toe om verschillende optische functies zoals winst, absorptie of brekingsindexveranderingen te realiseren, binnen heel beperkte afmetingen. Bovendien zijn zo'n componenten geschikt voor massaproductie en dus potentieel goedkoop. Jammer genoeg vereisen deze circuits een heel complexe epitaxiaalgroeiprocedure en een ingewikkelde processing, waardoor het moeilijk is om betrouwbare componenten te fabriceren en een goede uniformiteit te verkrijgen. Bovendien biedt een monolithische integratietechnologie meestal geen oplossing voor het koppelen van een optische vezel met de chip, alhoewel net dit voor een groot stuk de prijs van de component kan bepalen.

Als een alternatief voor de monolithisch geïntegreerde PIC's (photonic integrated circuit), hebben verschillende bedrijven een hybride integratietechnologie ontwikkeld. Vertrekkend van goed gekende technieken zoals V-groefetsen, de fabricage van passieve golfgeleiders in silica op silicium en laserdiodes met geïntegreerde bundelexpansiestructuren, konden complexe hybride geïntegreerde componenten in slechts enkele jaren tijd commercieel beschikbaar gemaakt worden. Momenteel ziet het er dan ook naar uit dat voor de komende paar jaar alleen dit type componenten aan de grote vraag naar optische circuits zal kunnen voldoen.

Bij de ontwikkeling van de PAL in het kader van dit werk is een analoge evolutie opgemerkt. Oorspronkelijk was het de bedoeling de component volledig monolithisch te fabriceren maar dat bleek al gauw moeilijker dan verwacht. Daarom ontwikkelden we een alternatieve, hybride integratietechnologie, gebaseerd op het koppelen van een InP golfgeleiderchip en een InP optische versterkerrij. Om reflecties aan de koppeling tussen beide chips te vermijden, worden de golfgeleiders plaatselijk afgebogen ten opzichte van de normaal met het facet. Onze aanpak verschilt aanzienlijk van de courante hybride integratietechnologieën aangezien enkel InP-chips gebruikt worden. Bovendien werken we alleen met standaardcomponenten, waarvoor geen speciale processing nodig is of die commercieel beschikbaar zijn. Er werd een actieve alignatietechniek gebruikt, waarbij het uitgangsvermogen van de component gemaximaliseerd werd. Gezien het beperkt aantal componenten dat gerealiseerd werd en het feit dat ze enkel bedoeld waren voor het verkrijgen van experimentele informatie,

leken de extra processing die vereist is om een volledig passieve alignatie toe te laten en het daarbij optredende extra verlies hier immers niet verantwoord.

In het volgende deel van dit hoofdstuk wordt een overzicht gegeven van de hybride integratietechnologieën die nu courant worden gebruikt. Daarna wordt onze eigen aanpak meer gedetailleerd besproken en worden experimentele resultaten van een hybride gekoppelde PAL gepresenteerd. In de laatste twee delen van dit hoofdstuk worden resultaten gegeven van respectievelijk een multigolflengtelaser met een winstvergrendelde uitgangsversterker en een afstembare laser met een ringresonator binnen de caviteit.

2 Overzicht van courant gebruikte hybride integratietechnologieën

De nu meest courant gebruikte hybride integratietechnologieën gebruiken silicium als substraat. De thermische geleidbaarheid van silicium is minder goed dan die van diamant maar veel beter dan die van alumina en aluminiumnitride die ook courant gebruikt worden als substraat. Bovendien is silicium veel gemakkelijker te verwerken dan keramische substraten of diamantsubstraten. Een bijkomend voordeel is dat silicium, door zijn gebruik in de halfgeleiderindustrie, heel eenvoudig te verkrijgen is en goed gekarakteriseerd is.

Voor commerciële toepassingen wordt meestal gebruik gemaakt van passieve alignatietechnieken. Dit vereist een complexere processing maar de daarmee gepaard gaande meerkost wordt, voor grote volumes, ruim gecompenseerd door de reductie van de assemblagekosten. Om passieve alignatie mogelijk te maken worden meestal verschillende technieken gecombineerd. De belangrijkste zijn het etsen van V-groeven in het siliciumsubstraat wat een nauwkeurige positionering van de optische vezel toelaat, flip-chipmontage voor de alignatie van de optisch actieve componenten en laserdiodes met geïntegreerde bundelexpansiestructuren die de koppelingstoleranties gevoelig vergroten. Een bijkomend voordeel van het gebruik van laserdiodes met geïntegreerde bundelexpansiestructuren is dat geen microlenzen meer nodig zijn in het optisch pad. Dat maakt het mogelijk om de hele component in te kapselen in silicone of een soortgelijk product en maakt de weg vrij naar niet-hermetische verpakkingstechnieken.

De belangrijkste problemen die nog optreden bij de realisatie van hybride PIC's zijn de elektrische interconnectie en de grote nauwkeurigheid die vereist is bij de processing. Er is immers een gelijke tolerantie vereist als bij de fabricage van elektronische IC's ($< 1\,\mu m$) terwijl de afmetingen van de onderdelen veel groter ($> 50\,\mu m$) zijn. Dit bemoeilijkt de lithografie aanzienlijk.

Enkele voorbeelden tonen aan dat hybride integratie wel degelijk almaar belangrijker wordt. Componenten gebaseerd op een silicium "optical bench" vormen de basis van nu courant verkrijgbare goedkope transmitter- en receivermodules en ook de completere hybride PLC-platformen, die passieve golfgeleiders in silica gebruiken voor het routeren van de signalen, staan op de rand van een commerciële doorbraak.

3 Onze aanpak

Deze sectie beschrijft hoe we de hybride koppeling in de praktijk uitvoeren. In Fig. 5-1 is een schematische voorstelling van de gebruikte opstelling getoond. Gebruik makend van precisietranslatietafels wordt een versterkerrij gekoppeld met een passieve chip. Door een microscoop kan de spleet tussen beide chips gecontroleerd worden. De koppeling wordt geoptimaliseerd door het uitgangsvermogen, dat gemeten wordt met een optische vermogenmeter, te maximaliseren. Om de koppeling in longitudinale richting te optimaliseren worden beide chips in contact gebracht met elkaar. Daarbij wordt automatisch ook de alignatie rond de verticale rotatie-as geoptimaliseerd. Het meest tijdrovende onderdeel van de procedure is de alignatie rond de horizontale rotatie-assen.

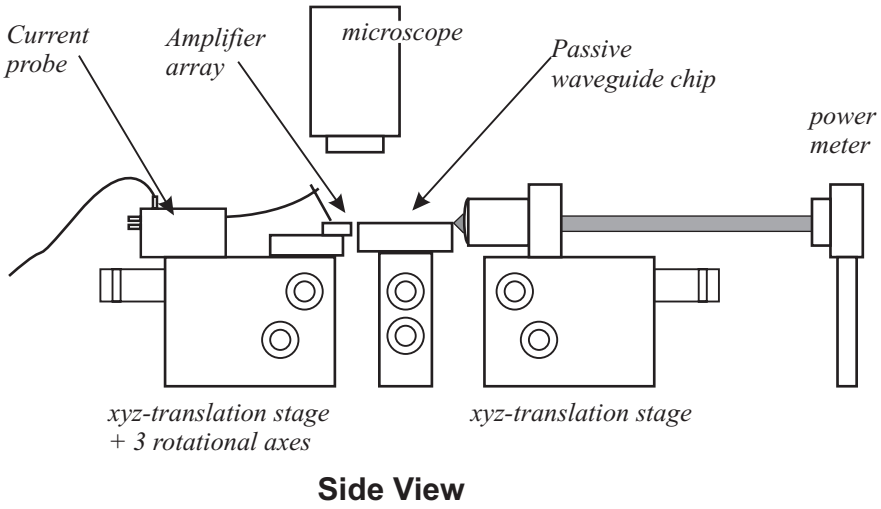

Fig. 5-1 Opstelling gebruikt voor het hybride koppelen van twee InP-chips.

Het is moeilijk te schatten hoeveel tijd nodig is voor de volledige koppelingsprocedure. Als vertrokken wordt van een enigszins gealigneerde opstelling, is voor het koppelen van één kanaal typisch 10 tot 30 minuten nodig. Als meerdere kanalen moeten gekoppeld worden neemt de benodigde tijd echter snel toe, soms tot meerdere uren.

Vermits de chips in fysisch contact zijn, is het heel belangrijk dat het facet van beide chips compleet vlak is. Kleine stofdeeltjes kunnen al een succesvolle koppeling belemmeren. Belangrijker nog is de kwaliteit van de klief zelf. Zo moeten facetonzuiverheden ter hoogte van de kliefkrassen absoluut worden vermeden.

Voor de meeste toepassingen is het noodzakelijk om reflecties aan de overgang tussen beide chips zoveel mogelijk te reduceren. Rekening houdend met een propagatieverlies van 2 dB voor de passieve chip, een verlies van 5 dB aan het facet en een verlies van 4 dB aan de overgang tussen beide chips, is de maximale terugkoppeling naar de versterker minstens 17 dB lager dan het oorspronkelijke signaal. Voor een goede werking van de component is het dus belangrijk dat de residuele reflectie aan de overgang tussen beide chips veel kleiner is dan deze waarde. Dit zou kunnen gerealiseerd worden met een heel goede AR-coating. Het realiseren van zo'n coatings vereist echter een extreem nauwkeurige controle van de laagdikte

en de waarde van de brekingsindex, wat niet overeenkomt met ons doel om de processing zo eenvoudig mogelijk te houden. Bovendien reduceert een AR-coating de reflectie maar over een beperkt golflengtegebied. Daarom is gekozen voor een alternatieve optie waarbij langs één kant van de chip de golfgeleiders worden afgebogen ten opzichte van de normaal met het facet. Dit garandeert dat het grootste gedeelte van het gereflecteerde licht niet in de golfgeleider terechtkomt maar in het substraat wordt afgestraald.

Zoals al aangehaald, worden geen verticale bundelexpansiestructuren gebruikt. Daardoor is de tolerantie voor alignatiefouten extreem klein wat maakt dat, zolang beide chips niet permanent verbonden zijn, zelfs een minieme thermische expansie van één van beide chips de koppelefficiëntie kan beïnvloeden. Dit kan bijvoorbeeld het geval zijn wanneer de stroom verandert. In de praktijk blijkt dat de niet-permanente hybride koppeling stabiel genoeg is om een aantal experimenten uit te voeren bij een constante stroom. Wanneer de stroom echter over een ruimer bereik (> 10 mA) gewijzigd wordt, blijkt het transitieverlies soms te variëren. Bovendien is het vaak moeilijk om onderscheid te maken tussen effecten te wijten aan de veranderende koppelingsefficiëntie en effecten inherent aan de component zelf.

4 Realisatie van een hybride gekoppelde Phased-Array laser

4.1 Demonstratie van de haalbaarheid van de aanpak

Om de haalbaarheid van de hierboven voorgestelde aanpak aan te tonen, werden versterkerrijen met vier optische versterkers gefabriceerd. Deze hadden een begraven golfgeleiderstructuur en waren, aan het facet dat gekoppeld wordt met de passieve chip, 5 graden afgebogen ten opzichte van de normaal met het facet. Ook een corresponderende passieve chip met een Phased-Array demultiplexer werd gefabriceerd. Door beide chips te koppelen kon een eerste PAL worden gerealiseerd. De drempelstroom van deze component was 90 mA en het maximale uitgangsvermogen 0.42 mW (bij 180 mA). Het was mogelijk om laserwerking in alle vier de kanalen te verkrijgen, zonder de alignatie van de chips te wijzigen. Door thermische overspraak kon echter slechts één kanaal tegelijk worden aangestuurd. Op de oscillatiespectra die voor verschillende kanalen werden opgemeten, zijn de longitudinale modes van de laser zelf niet zichtbaar door de beperkte resolutie van de spectrumanalyser. De spectra vertonen echter wel een relatief grote rimpel te wijten aan de nog te hoge residuele reflectie aan de overgang tussen beide chips. Daarom werd er bij het ontwerp van de nieuwere componenten voor gekozen om de hoek die de golfgeleider maakt met de normaal op het facet te vergroten tot 10 graden.

4.2 Hybride gekoppelde Phased-Array laser

Omdat een hoek van 5 graden niet voldoende was om alle reflecties te voorkomen (zie vorige paragraaf), werden nieuwe versterkerrijen ontworpen waarbij de golfgeleiders 10 graden afgebogen waren. Deze versterkers werden gefabriceerd door het Zwitserse Optospeed SA en hebben een bulk InGaAsP actieve laag. Het ontwerp en de karakterisatie van deze ver-

sterkers werd al besproken in hoofdstuk 4. Oorspronkelijk werden ze gemonteerd op een aluminasubstraat. Later werd het aluminasubstraat vervangen door een siliciumsubstraat, wat de warmteafvoer ten goede komt. Om de koppeling met een andere chip mogelijk te maken zijn de versterkerrijen zo gemonteerd dat hun rand 50 tot 100 μm over de rand van het substraat komt, zoals te zien is in de schematische voorstelling van Fig. 5-1.

De passieve golfgeleiderchips met de Phased-Array multiplexers werden gefabriceerd aan de Technische Universiteit Delft, vertrekkend van in Gent gegroeide epitaxiaallagen. Twee types multiplexer werden ontworpen, één met een 200 GHz kanaalspatiëring en één met een 400 GHz kanaalspatiëring. De golfgeleiderstructuur is al besproken in hoofdstuk 4. Met deze chips werden verschillende hybride Phased-Array lasers gerealiseerd.

4.2.1 Transitieverlies en tolerantie voor alignatiefouten.

Door het vergelijken van de versterkte spontane emissie geëmitteerd door een versterker op zich en door een versterker gekoppeld met een passieve golfgeleider die over de hele lengte van de chip onder een hoek van 10 graden is geplaatst, konden we bepalen dat het transitieverlies tussen beide chips 4 à 5 dB is. Voor Fabry-Pérotlasers gevormd door een versterker en een rechte golfgeleider, was de minimum drempelstroom 28 mA. De externe differentiele efficiëntie voor zo'n laser was tussen 8 % en 12 %. Rekening houdend met het hierboven geschatte cijfer voor het transitieverlies en een verlies van 1 dB voor de passieve chip, komt dit overeen met de waarden die in hoofdstuk 3 theoretisch werden voorspeld.

Ook de tolerantie voor alignatiefouten werd onderzocht. De invloed van een alignatiefout in laterale en transversale richting werd opgemeten, als functie van de afstand tussen beide chips. Ook de invloed van het vergroten van de afstand tussen beide chips op het maximaal getransmitteerde vermogen werd bepaald en blijkt goede overeenkomst te vertonen met het theoretische resultaat uit hoofdstuk 4. Uit de verschillende metingen kunnen we afleiden dat de minimale afstand tussen twee chips die hybride gekoppeld zijn tussen 1 en 2 μm ligt.

4.2.2 Drempelstroom en uitgangsvermogen van een hybride PAL

De hybride Phased-Array lasers werden uitgebreid gekarakteriseerd. Voor een hybride PAL gerealiseerd met een op een aluminasubstraat gemonteerde versterkerrij en gekarakteriseerd bij kamertemperatuur, vonden we een drempelstroom variërend tussen 44 mA en 48 mA. Het uitgangsvermogen per kanaal was ongeveer 1 mW (bij 100 mA). Verschillende van de LI-curven vertoonden één of meerdere discontinuïteiten. Meestal waren die relatief klein maar voor sommige kanalen zijn sprongen van 0.8 mW opgemerkt. Oorspronkelijk dachten we dat dit een gevolg was van een variatie van de koppelingsefficiëntie te wijten aan het opvoeren van de instelstroom. Bij het karakteriseren van de permanent verbonden hybride PAL (hoofdstuk 6) werden echter ook dergelijke discontinuïteiten opgemeten, zij het in mindere mate. In dat geval konden we de discontinuïteiten in de vermogenkarakteristiek relateren met discontinuïteiten in de golflengte (modehops).

Ook voor een Phased-Array laser die gevormd werd door het koppelen van een versterkerrij gemonteerd op een siliciumsubstraat met een passieve demultiplexer en gekoeld werd tot 17°C, zijn LI-curven opgemeten. Door de betere thermische geleidbaarheid van het substraat was het uitgangsvermogen daarbij veel hoger (3.5 mW bij 100 mA) en de drempelstroom daalde tot 38 mA. Wanneer vier kanalen simultaan werden aangestuurd was het maximaal uitgangsvermogen 6.2 mW (instelstroom per kanaal: 100 mA). De hier opgemeten waarden voor de drempelstroom en het uitgangsvermogen zijn, voor zover wij weten, de beste die tot nu toe voor een Phased-Array laser met een bulk actieve laag werden gerapporteerd. Het uitgangsvermogen bij 100 mA is bovendien vergelijkbaar met dat voor de beste, op kwantumputlagen gebaseerde lasers die tot nu in de literatuur werden voorgesteld.

4.2.3 Optisch spectrum

In Fig. 5-2a zijn oscillatiespectra getoond voor vier afzonderlijk aangestuurde kanalen van de hybride PAL ($I = 80$ mA). Door het filterend effect van de Phased-Array wordt de ASE-ruis van de versterkers onderdrukt met meer dan 60 dB ten opzichte van de centrale pieken. Links van het spectrum zijn kleinere pieken zichtbaar die veroorzaakt worden door de transmissie van de ASE door de lagere doorlaatband van de Phased-Array. Fig. 5-2b toont het oscillatiespectrum van dezelfde component waarbij nu 4 kanalen tegelijk werden aangestuurd. Anders dan in Fig. 5-2 zijn nu extra pieken zichtbaar in de buurt van de centrale laserlijnen. Deze worden veroorzaakt door een "four-wave-mixing"-effect in de passieve uitgangsgolfgeleider. Dit effect wordt in meer detail besproken in hoofdstuk 6.

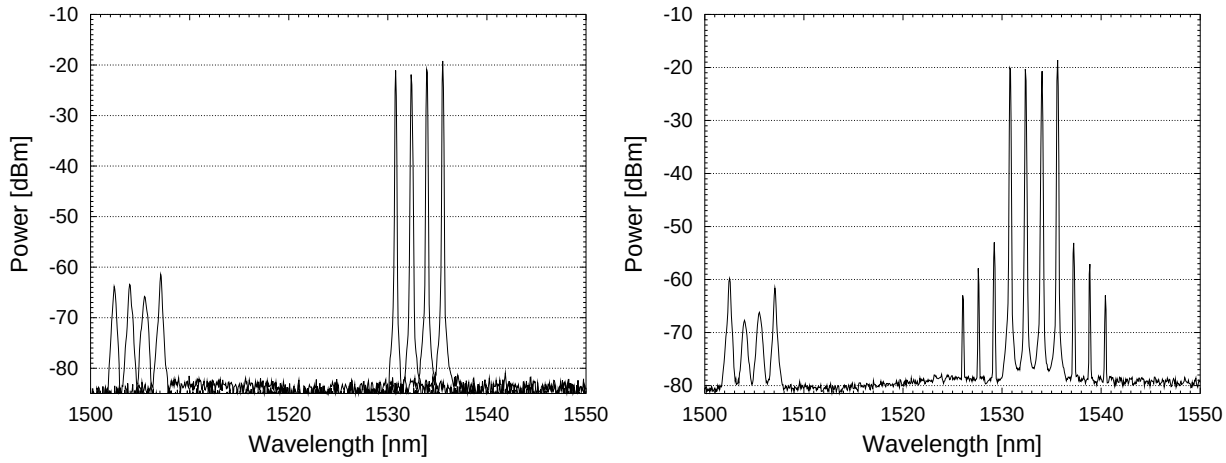

Fig. 5-2 a) Oscillatiespectra van vier afzonderlijk aangestuurde kanalen van de hybride PAL. b) Oscillatiespectrum van vier simultaan aangestuurde kanalen van de hybride PAL

4.2.4 Longitudinale modestabiliteit

Omdat de resolutie van een standaard spectrumanalyser te beperkt is, werd een Fabry-Pérot interferometer gebruikt om het longitudinale modespectrum te onderzoeken.

Uit deze experimenten konden we afleiden dat de laser met de 200 GHz kanaalspatiëring over het algemeen in één enkele longitudinale mode opereerde. Bij sommige kanalen trad

echter een modehop op bij bepaalde instelstromen. Het optreden van deze modehops werd in meer detail bestudeerd. Zoals verwacht van de theoretische resultaten in hoofdstuk 3 is de lasermode verschoven naar een lagere frequentie ten opzichte van het centrum van de doorlaatband van de Phased-Array. Voor alle kanalen veranderde de laserfrequentie, afgezien van modehops, met 115 MHz/mA. Vermits de frequentie daalt bij toenemende instelstroom, veronderstellen we dat dit een gevolg is van een stijging van de temperatuur.

In tegenstelling tot de Phased-Array laser met de 200 GHz kanaalspatiëring, opereert de laser met de 400 GHz kanaalspatiëring in vele gevallen in meerdere longitudinale modes tegelijk. Hoogstwaarschijnlijk is dit te wijten aan de hogere bandbreedte van het filter.

4.2.5 Dynamische metingen

De kleinsignaalrespons van de laser werd bepaald met een hoogfrequentprobe met ingebouwde serieweerstand. De opgemeten bandbreedte varieerde van 500 MHz net boven de drempelstroom tot 1100 MHz bij een instelstroom van 90 mA. Uitgaande van deze metingen verwachtten we dat deze component bruikbaar zou zijn voor modulatie met datasignalen bij een frequentie van 622 Mbit/s. Daarom werden oogdiagramma's opgemeten van een laser die gemoduleerd werd met een 300 Mbit/s en een 600 Mbit/s pseudorandom datasignaal. Deze bleken echter volledig gesloten te zijn. Ook de respons voor een bloksignaal bleek een vreemd gedrag te vertonen. Een mogelijke verklaring zou kunnen zijn dat het laagste niveau te dicht in de buurt van de drempelstroom lag. In dit gebied heeft de laser enige tijd nodig om te beslissen in welke longitudinale mode hij zal opereren en dit heeft potentieel een nadelig effect voor het modulatiegedrag. Dit effect is verder onderzocht in hoofdstuk 6 voor de permanent geïntegreerde PAL.

5 Realisatie van een hybride gekoppelde Phased-Array laser met winstvergrendelde uitgangsversterker

In hoofdstuk 3 werd voorgesteld om de winst van de gemeenschappelijke versterker van een Phased-Array laser te vergrendelen door één van de signaalversterkers te vervangen door een passieve golfgeleider. Daardoor is het mogelijk om overspraak tussen de kanalen veroorzaakt door variaties van de ladingsdragersdichtheid in de gemeenschappelijke versterker te vermijden. Om dit principe experimenteel te verifiëren werd een nieuwe passieve chip ontworpen met een extra passieve golfgeleider langs de ingangszijde van de multiplexer en een uitgangsgolfgeleider die kan gekoppeld worden met een versterker. Met deze chip was het mogelijk simultane laserwerking in vier signaalkanalen en het winstvergrendelingska-

naal te verkrijgen[1]. In het beste geval was de drempelstroom voor het winstvergrendelingskanaal 40 mA, terwijl de drempelstroom voor de signaalkanalen varieerde van 14 mA tot 16 mA, wat nauwelijks hoger is dan de opgemeten transparantiestroom voor deze versterkers (zie hoofdstuk 4). De onderdrukking van de ASE-ruis was beter dan 35 mA en de laser werkte stabiel in één enkele doorlaatband van de multiplexer.

Om het principe van de winstvergrendeling te verifiëren, veranderden we de instelstroom van één van de versterkers terwijl alle andere stromen constant gehouden werden. Het vermogen in elk kanaal afzonderlijk werd bepaald met een optische spectrumanalyser. In enkele gevallen kon de winstvergrendeling overtuigend worden aangetoond. Verschillende metingen leverden echter ook minder eenduidige resultaten op. We vermoeden dat de belangrijkste redenen hiervoor de thermische overspraak tussen de verschillende kanalen en het veranderend transitieverlies bij een veranderende stroom zijn. Dit zou moeten te verhelpen zijn door het permanent verbinden van beide chips.

6 Realisatie van een hybride gekoppelde afstembare laser

Om aan te tonen dat de hybride koppeling ook andere toepassingsgebieden heeft dan de in de vorige paragrafen gedemonstreerde Phased-Array lasers werd een compleet nieuw type afstembare laser ontworpen, opgebouwd uit een optische versterker, een passief ringresonatorfilter en een afstembare reflectieve Mach-Zehnder interferometer. Deze laatste werd gevormd door twee versterkers en een passieve 3-dB koppelaar en heeft een weinig golflengteselectieve transferfunctie. Door deze echter te laten overlappen met één van de scherpe pieken van de ringresonator zal de laser deze golflengte selecteren. Door het verschuiven van de centrale golflengte van de Mach-Zehnder interferometer kan een andere piek van de ringresonator worden geselecteerd.

Deze laser werd gerealiseerd met de in dit hoofdstuk besproken hybride koppelingstechniek. De drempelstroom was 44 mA wanneer beide versterkers van de reflectieve MZI aangestuurd werden met een stroom van 35 mA. Laserwerking in 12 verschillende kanalen van de laser werd verkregen.

---

[1] Dit was zelfs mogelijk wanneer gebruik werd gemaakt van een op een aluminasubstraat gemonteerde versterkerrij die een heel slechte warmteafvoer heeft. Gekoppeld met een standaard Phased-Array konden in dat geval slechts drie kanalen tegelijk worden aangestuurd, wat het voordeel van de gemeenschappelijke uitgangsversterker aantoont.

Hoofdstuk 6

Ontwikkeling van een hybride integratietechnologie voor Phased-Array multigolflengtelasers

1 Inleiding

De in hoofdstuk 5 gepresenteerde experimentele resultaten tonen aan dat de hybride koppeling wel degelijk bruikbaar is voor het realiseren van complexe fotonische IC's. Zolang beide chips echter niet definitief verbonden zijn, is het niet mogelijk om de PIC (photonic integrated circuit) te transporteren of te gebruiken in een compleet optisch netwerk. Bovendien hebben we gezien dat de koppelefficiëntie soms wijzigt bij metingen die veel tijd vergen of als de stroom verandert. Daarom is onderzocht of het mogelijk is om beide chips permanent te koppelen, door gebruik te maken van een geschikte lijm. De aanpak die we daarbij gevolgd hebben, is voorgesteld in het tweede deel van dit hoofdstuk. In deel 3 bespreken we de koppeling van de PIC met een optische vezel en de elektrische interconnectie. De volledige procedure is samengevat in deel 4 en in deel 5 van dit hoofdstuk worden experimentele resultaten gepresenteerd.

2 Permanent verbinden van twee hybride gekoppelde chips

Fig. 6-1a en Fig. 6-1b vatten de procedure samen die gebruikt werd voor het integreren van beide chips. Net als voorheen wordt de chip met de optische versterkers op een siliciumsubstraat gemonteerd. Dit substraat wordt vervolgens op een metalen drager geplaatst die vooraan een U-vormige uitsparing heeft. De golfgeleiderchip wordt ondersteund door een vacuümnaald die precies in de U-vormige uitsparing past. In eerste instantie worden beide chips gealigneerd volgens de in het vorige hoofdstuk besproken procedure. Vervolgens wordt de spleet tussen beide chips terug wat vergroot en wordt een UV-uithardende epoxy aangebracht (Fig. 6-1b, "epoxy 1"). Capillaire krachten zorgen voor een gelijkmatige verdeling over de facetten van beide chips. Na het heraligneren van beide chips en het optimaliseren van het uitgangsvermogen wordt de epoxy uitgehard. In een laatste stap wordt een tweede type epoxy aangebracht aan de uiteinden van de passieve chip om de PIC te stabiliseren (Fig. 6-1b, "epoxy 2").

De epoxy die aangebracht wordt tussen beide chips ("epoxy 1") moet zorgen voor een heel rigide en thermisch stabiele verbinding. Bovendien moet deze epoxy optisch transparant zijn en een lage krimp bij uitharding vertonen. De epoxy die gebruikt wordt om de PIC te stabiliseren daarentegen ("epoxy 2"), moet de verplaatsingen tussen de InP passieve chip en

de metaaldrager ten gevolge van een verschillende thermische expansie kunnen opvangen. Deze epoxy moet dus een hoge elasticiteit hebben.

In de volgende paragrafen worden enkele aspecten van de hierboven beschreven procedure nader belicht.

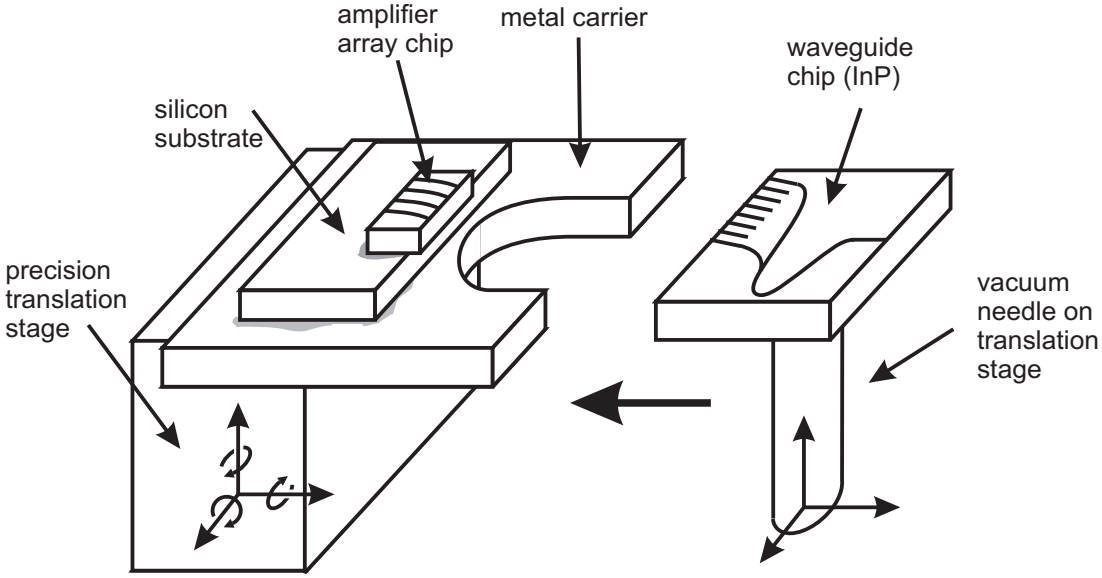

Fig. 6-1a Deze figuur toont hoe de chip met de versterkers gemonteerd is op het siliciumsubstraat en de metaaldrager. De golfgeleiderchip wordt ondersteund door een vacuümnaald die tussen de benen van de U-vormige uitsparing in de metaaldrager past.

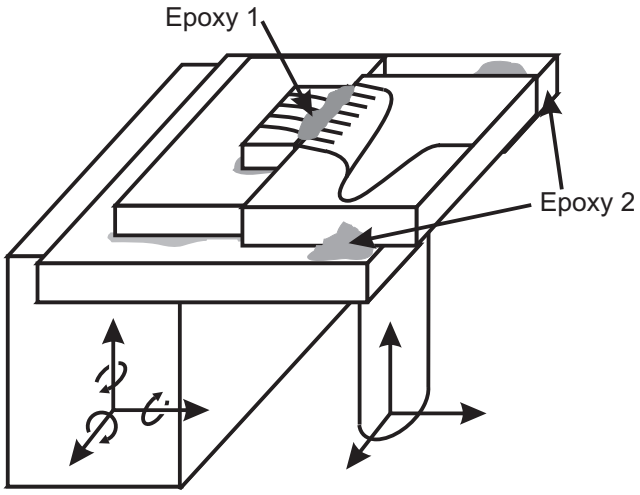

Fig. 6-1b Aanbrengen van "epoxy 1" en "epoxy 2".

2.1 Aanbrengen van de epoxy tussen beide chips

De epoxy tussen beide chips wordt aangebracht met behulp van een optische vezel die in een precisietranslatietafel geklemd is. Als de viscositeit van deze epoxy voldoende laag is, verdeelt de epoxy zichzelf gelijkmatig over de facetten door capillaire krachten. Aan de andere kant mag de viscositeit ook niet te laag zijn, om te vermijden dat de epoxy van de facetten

lekt. De viscositeit van de epoxy die wij gebruikten (450 cps) lijkt ideaal te zijn voor deze procedure.

2.2 Adhesie

Uit experimenten met testchips konden we afleiden dat de verbinding die gevormd wordt door de epoxy tussen twee chips heel sterk is. De facetoppervlakte van de versterkerchip die gebruikt wordt voor de hybride PAL is echter relatief klein, wat de totale sterkte van de verbinding beperkt.

2.3 Indexaanpassingeffect

Wanneer lijm tussen beide chips wordt aangebracht, gebeurt het vaak dat de koppelefficiëntie gevoelig verbetert. Deze verbetering is een gevolg van het feit dat de breedte van het verre veld van de golfgeleiders omgekeerd evenredig is met de brekingsindex van het medium tussen beide chips. Dit effect werd al voorspeld in hoofdstuk 4 aan de hand van theoretische berekeningen.

2.4 Afstand tussen beide chips

De experimenten die werden uitgevoerd met testchips waren meestal succesvol. Wanneer we echter de versterkers voor de hybride PAL probeerden te verbinden met een passieve chip, bleek het vaak dat de epoxy tussen beide facetten, zelfs na heel lange belichtingstijden, totaal niet uitgehard was. We vermoeden dat dit te wijten is aan het feit dat in het laatste geval de spleet tussen beide chips extreem smal kan zijn, wat het UV-licht verhinderd om tot bij de epoxy te raken. Daarom hebben we geprobeerd om de spleet met opzet wat te verbreden door kleine groeven te maken in het facet van de passieve chip door laserablatie. De afzetting die door dit proces gevormd wordt aan de rand van de groeven zorgt ervoor dat de minimale afstand tussen beide chips iets groter wordt. Deze aanpak bleek inderdaad het succes van de integratieprocedure gevoelig te vergroten en werd ook gebruikt bij de realisatie van de volledige module die verder in dit hoofdstuk is voorgesteld. Het nadeel is natuurlijk dat de koppelefficiëntie wat verlaagt.

2.5 Belichtingstijd en -intensiteit

Eén van de belangrijkste parameters van het uithardingproces is de hoeveelheid UV-licht die het chipoppervlak bereikt. Voor het uitharden werd een UV-bron met een flexibele lichtgeleider gebruikt. Om een goede uniformiteit te verkrijgen wordt deze geleider meestal zo dicht mogelijk tegen het oppervlak geplaatst (3 à 5 cm). Omdat de chips bij bestraling gevoelig kunnen opwarmen - wat kan leiden tot een verandering van de koppelefficiëntie - wordt het uithardingproces gestart bij lage energieën en uitgevoerd in korte tijdsintervallen (~ 90 s). Naarmate het uithardingproces vordert wordt de intensiteit van de straling geleidelijk opgevoerd.

3 Vezel-chipkoppeling en elektrische interconnectie

Om de optische en elektrische toegang tot de module te vereenvoudigen moet de hybride geïntegreerde module verder worden verpakt. Daarvoor hebben we de KAP10-lasermodule van Radians-Innova gebruikt, die zowel een thermo-elektrische temperatuurcontroller bevat als een translatietafeltje met de optische vezel en een microlens. Voor een eenvoudige montage in de module moet de PIC op een geschikte adapterplaat worden geplaatst.

Om een elektrische toegang tot de PIC mogelijk te maken, zijn de versterkers verbonden met goudcontacten op het siliciumsubstraat. Deze goudcontacten zijn op hun beurt verbonden met semi-rigide coaxiaalkabeltjes die afgesloten zijn met een SMA-connector, bevestigd aan de buitenkant van de module.

4 Samenvatting van de verpakkingsprocedure

Fig. 6-2 toont een foto van de verpakte module. Rechts op de foto is het siliciumsubstraat met het interconnectiepatroon te zien, waarop de optische versterkerrij is gemonteerd. In het centrum van de figuur is de passieve chip met de Phased-Array demultiplexer zichtbaar. Ook de koppelingslens en de semi-rigide coaxiaalkabeltjes zijn zichtbaar op deze foto.

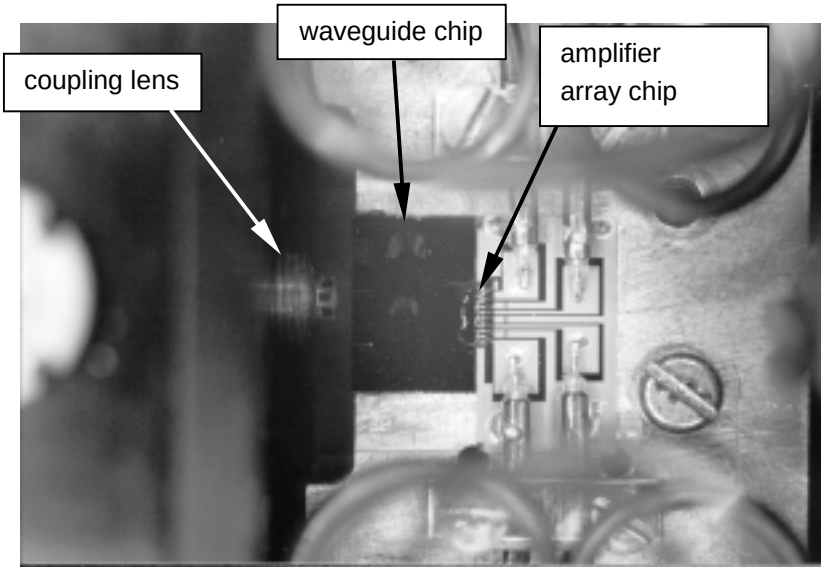

Fig. 6-2 Foto van de verpakte hybride geïntegreerde Phased-Array laser

5 Experimentele resultaten

5.1 Inleiding

In de volgende paragrafen worden de experimenteel opgemeten karakteristieken van de module getoond in Fig. 6-2, voorgesteld. Voor deze module werden dezelfde chips gebruikt als voor de niet-permanent gekoppelde PAL die in het vorige hoofdstuk werd besproken. Zoals al uitgelegd in paragraaf 2.4, werden, om het uithardingproces te bevorderen, door laserablatie kleine groeven gemaakt in het facet van de passieve golfgeleiderchip. De afzet-

ting aan de rand van deze groeven zorgt ervoor dat de spleet tussen beide chips wat vergroot wat de bereikbaarheid van de epoxy tussen de facetten voor het UV-licht ten goede komt. Door de toename van de afstand tussen beide chips neemt echter ook de koppelingsefficiëntie af, wat hier resulteerde in een stijging van de drempelstroom van 40 mA tot meer dan 80 mA. Na aanbrengen van de epoxy tussen beide chips verbeterde de koppelingsefficientie terug enigszins en daalde de drempelstroom naar 52 mA voor het beste kanaal.

Oorspronkelijk kon slechts voor drie kanalen laserwerking worden verkregen. Tijdens het karakteriseren werd één van deze kanalen beschadigd. In een poging om het te herstellen werd extra lijm aangebracht op het chipoppervlak, ter hoogte van de overgang tussen beide chips. Dit resulteerde niet in het herstel van dit kanaal maar het uitgangsvermogen van beide andere kanalen bleek wel verhoogd te zijn en ook kon nu laserwerking in nog drie extra kanalen worden verkregen. Deze verbetering is waarschijnlijk te wijten aan een verbeterde afvoer van de geproduceerde warmte naar de omgeving. In de volgende paragrafen zal waar nodig vermeld worden of de getoonde karakteristieken werden opgemeten voor of na het aanbrengen van deze epoxy.

5.2 Statische karakteristieken

Fig. 6-3a toont LI-curven die werden opgemeten na het aanbrengen van de extra epoxy. Voor de beste kanalen is de drempelstroom ongeveer 52 mA en het maximale uitgangsvermogen 0.8 mW (bij 100 mA). Net boven de drempel is de externe differentiële efficiëntie 2.5 %. Uitgaande van de theoretische waarden uit hoofdstuk 3, kunnen we daaruit afleiden dat het totale verlies in het passieve gedeelte van de laser (transitieverlies + propagatieverlies) ongeveer 13 dB is, of 7 dB hoger dan in het geval voor de niet-permanent gekoppelde PAL.

Na montage in de KAP10-lasermodule werd een verlies van 5.25 dB opgemeten voor de koppeling van de PIC naar de optische vezel. Het opgemeten vermogen voldoet aan de specificaties die vooropgesteld werden voor de APEX-testbed (zie hoofdstuk 1). Voor toepassing in reële optische netwerken is deze waarde echter te laag. Hieraan kan enigszins verholpen worden door het verbeteren van de koppelingsefficiëntie met de optische vezel. Het is echter belangrijker om het transitieverlies tussen beide hybride geïntegreerde chips te verkleinen. Daardoor moet het mogelijk worden om een uitgangsvermogen dat vergelijkbaar is met dat voor de niet-permanent gekoppelde PAL te verkrijgen (> 3 mW). Door het verlengen van de versterkers kan dan het uitgangsvermogen verder worden opgevoerd.

Fig. 6-3b toont een oscillatiespectrum dat werd opgemeten terwijl drie kanalen (2, 3 & 4) tegelijk werden aangestuurd. In vergelijking met de niet-permanent gekoppelde laser, werkt deze laser in een lagere doorlaatband van de Phased-Array demultiplexer. Dit is te wijten aan de hogere drempelstroom en de daarmee gepaard gaande verschuiving van de winstcurve. Deze module vertoont een stabiele laserwerking in één enkele doorlaatband van de multiplexer en de onderdrukking van de versterkte spontane emissie is beter dan 55 dB (bij een resolutie van 0.1 nm). De onderdrukking van de transmissie in de nabijgelegen door-

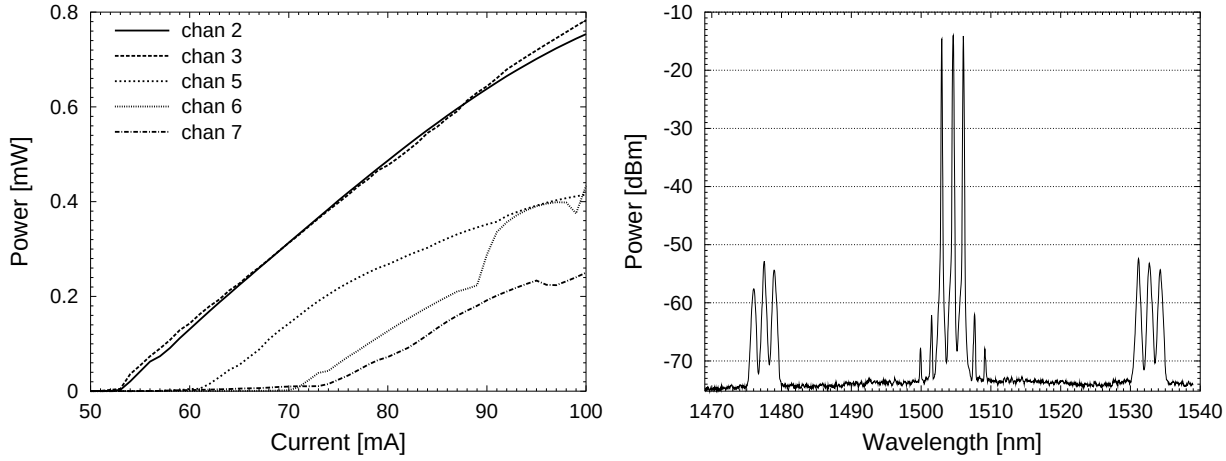

Fig. 6-3 a) LI-curven van hybride geïntegreerde Phased-Array laser. b) Oscillatiespectrum opgemeten terwijl drie kanalen tegelijk werden aangestuurd.

laatbanden van de demultiplexer is iets minder goed dan voor de niet-permanent gekoppelde laser maar nog altijd beter dan 35 dB.

Voor deze module werd ook het "four-wave mixing" effect in de passieve uitgangsgolfgeleider in meer detail bestudeerd. Dit effect is verantwoordelijk voor de kleine piekjes die zichtbaar zijn in het oscillatiespectrum, vlak naast de centrale laserpieken. Uit de verhouding tussen het vermogen in de hoofdpieken en de secondaire pieken konden we een waarde voor de tweede orde niet-lineaire brekingsindexcoëfficiënt afleiden. Om het optreden van deze secondaire pieken te vermijden moet de lengte van de passieve uitgangsgolfgeleider zo kort mogelijk gehouden worden.

Met behulp van een golflengtemeter werd onderzocht of de laser bij een verandering van de stroom in een zelfde longitudinale mode blijft opereren of als er modehops optreden. Het blijkt dat voor de kanalen[1] met het hoogste uitgangsvermogen een heel stabiele werking wordt verkregen. Alleen net boven de drempelstroom treden enkele modehops op. Bij hogere stromen zijn noch in de golflengtekarakteristiek, nog in de vermogenkarakteristiek discontinuïteiten zichtbaar. De andere kanalen daarentegen vertonen zowel in de vermogenkarakteristiek als in de golflengtekarakteristiek verschillende discontinuïteiten. Het blijkt dat deze te wijten zijn aan het verspringen van de lasermode naar een nabijgelegen longitudinale mode.

Om de afstembaarheid van de module te onderzoeken hebben we de golflengtekarakteristiek en de vermogenkarakteristiek ook opgemeten als functie van een veranderende temperatuur. Daarbij werd de thermo-elektrische controller van de KAP10-lasermodule gebruikt. De golflengte verandert ongeveer met 0.113 nm/K wat een typische waarde is voor dit soort

[1] Kanaal 2 voor het aanbrengen van de extra lijm en kanalen 2 en 3 na het aanbrengen van de extra lijm.

componenten. Ook hier was het zo dat de curven voor de kanalen met het hoogste uitgangsvermogen beduidend minder discontinuïteiten vertoonden dan deze voor de kanalen met een lager uitgangsvermogen. De in de vermogenkarakteristiek optredende discontinuïteiten kunnen terug worden toegewezen aan modehops. Vreemd genoeg bleek het uitgangvermogen een maximum te vertonen bij een temperatuur van 24°C. Waarschijnlijk is dit te wijten aan thermische spanningen die optreden bij een veranderende temperatuur. Het maximum bij 24°C zou kunnen verklaard worden door het feit dat de module geassembleerd werd bij deze temperatuur. Tijdens de temperatuursscan werd ook de spanning over de versterker opgemeten. In deze karakteristiek werden analoge discontinuïteiten opgemeten als in de vermogen- en de golflengtekarakteristiek. Uit deze grafieken kan bovendien worden afgeleid dat de laser niet altijd opereert in de longitudinale mode met de laagste drempelstroom. Dit is te wijten aan het in hoofdstuk 3 besproken intermodulatie-effect dat ervoor zorgt dat er in de buurt van het maximum van de doorlaatband van de passieve filter een stabiliteitzone is voor de laserwerking. Zolang de longitudinale mode binnen deze zone blijft treden geen modehops op.

Ook de lijnbreedte van de Phased-Array laser is opgemeten. Daarbij werden waarden beneden 1 MHz opgemeten. Door vergelijking met de theoretische formule die werd afgeleid in hoofdstuk 3, vonden we een waarde $\alpha \sim 3.6$ voor de lijnverbredingsfactor van Henry. Deze waarde is vrij laag maar niet onrealistisch gezien het hoge injectieniveau en het feit dat de laser werkt langs de lagegolflengtezijde van de winstcurve.

5.3 Dynamische karakteristieken

In eerste instantie werd de kleinsignaalrespons van de laser opgemeten met een hoogfrequentprobe (met ingebouwde 45 Ohm serieweerstand), voor verschillende instelstromen. De resultaten vertonen een goede gelijkenis met de in hoofdstuk 3 voorgestelde theoretische resultaten. De 3-dB bandbreedte stijgt min of meer evenredig met de stroom van 800 MHz net boven de drempelstroom tot 1600 MHz bij een stroom van 120 mA. Dit is waarschijnlijk de hoogste waarde die tot op heden werd gerapporteerd voor dit type laser.

De kleinsignaalrespons werd ook opgemeten via de semi-rigide coaxiaalkabeltjes. De resultaten van dit experiment waren echter beduidend minder goed. Dit was deels te wijten aan het feit dat het uitgangsvermogen van het hiervoor gebruikte kanaal lager was, maar we vermoeden dat ook parasitaire effecten in het elektrische circuit optreden.

Naast de kleinsignaalrespons werden ook oogdiagramma's opgemeten voor een laser die gemoduleerd werd met een pseudorandom datasignaal. Bij lage frequenties (300 MHz) werden zelfs voor heel hoge extinctieverhoudingen (14 dB) volledig open oogdiagramma's opgemeten. Bij hogere frequenties werd bij deze extinctieverhouding een belangrijke turn-on-jitter waargenomen. Wanneer de extinctieverhouding verlaagd wordt verdwijnt deze echter en bij een extinctieverhouding van 7 dB konden volledig open oogdiagramma's worden opgemeten bij een frequentie van 1.22 GHz. Ook andere auteurs hebben opgemerkt dat

het moeilijk is om een hoge extinctieverhouding te verkrijgen voor dit type laser. Dit is waarschijnlijk te wijten aan het feit dat net boven de drempelstroom de laser een zekere tijd nodig heeft om de meest voordelige longitudinale mode te kiezen.

6 Besluit

Gebruik makend van de hybride integratietechnologie werden heel performante Phased-Array lasers gedemonstreerd. De in hoofdstuk 5 besproken lasers hadden de laagste drempelstromen en het hoogste uitgangsvermogen dat tot op heden werd gerapporteerd voor dit type laser, met bulk actieve lagen. De permanent gekoppelde lasers (hoofdstuk 6) hebben een iets hogere drempelstroom maar de beste kanalen werken in één enkele longitudinale mode. Bovendien werd een bandbreedte opgemeten van 1600 MHz, wat voor zover we weten de hoogste waarde is die tot op heden werd gerapporteerd voor dit type laser. De lijnbreedte was kleiner dan 1 MHz en er werden volledig open oogdiagramma's opgemeten bij een frequentie van 1.24 Gbit/s en een extinctieverhouding van 7 dB.

Deze resultaten tonen aan dat de door ons ontwikkelde hybride integratietechnologie wel degelijk bruikbaar is voor het realiseren van geavanceerde PIC's. Het grootste probleem blijft tot nu toe de kleine tolerantie voor alignatiefouten. Vooral de tolerantie in de longitudinale richting is daarbij heel kritisch en enkel wanneer de chips extreem dicht bij elkaar worden gebracht, kan het transitieverlies voldoende klein worden gehouden. Dit kan echter bemoeilijkt worden door facetruwheden en verhindert bovendien de uitharding van de epoxy tussen beide facetten bij het permanent verbinden van de chips. De meest evidente oplossing lijkt het incorporeren van bundelexpansiestructuren in zowel de actieve als de passieve golfgeleiders. Dit kan de fabricage van de componenten echter terug bemoeilijken. Als een tussenoplossing kan gedacht worden aan het gebruik van golfgeleiders met een smaller verreveld.

De lasermodule die gebruikt werd voor het verpakken van de component biedt een heel flexibele oplossing om een snelle karakterisatie mogelijk te maken. Enkele aspecten, zoals de elektrische interconnectie en de thermische eigenschappen moeten echter nog verder onderzocht worden. Misschien zou het in die context nuttig zijn om de versterkers op het substraat vast te maken met een flip-chiptechnologie. Dit zou niet alleen een preciezere alignatie mogelijk maken maar ook voor een betere warmteafvoer en een betere elektrische interconnectie zorgen. Om de kans op een succesvolle integratie te verhogen zou het misschien ook beter zijn om kleinere versterkerrijen, bijvoorbeeld met slechts vier versterkers, te gebruiken.

Over het algemeen denken we echter dat een hybride integratietechnologie zoals die in de context van dit werk werd ontwikkeld heel nuttig kan zijn. Op onderzoeksniveau is het belangrijk te kunnen beschikken over een technologie die toelaat om snel ideeën voor nieuwe componenten praktisch uit te testen, zonder beroep te moeten doen op de gecompliceerde processing die nodig is bij het gebruik van een monolithische integratietechnologie. Voor

zo'n toepassingen is het belangrijk dat de componenten zo eenvoudig mogelijk gehouden worden en lijken actieve alignatietechnieken het meest voor de hand liggend.

Om uit te maken of een hybride integratietechnologie die enkel gebruik maakt van InP-chips ook bruikbaar zal zijn voor commerciële toepassingen zou een complete kostenanalyse moeten gemaakt worden, rekening houdend met alle mogelijke technologieën. Gezien het succes van de "silicon-bench" hybride integratietechnologieën (zie inleiding hoofdstuk 5), lijkt het ons echter niet onmogelijk dat ook het soort van hybride integratietechnologie dat hier werd onderzocht succesvoller zal zijn dan monolithische integratietechnologieën.

SUMMARY

CHAPTER 1

GENERAL INTRODUCTION

Chapter 1

General introduction

In modern optical telecommunication systems, the technique of wavelength division multiplexing (WDM) is widely adopted now. By employing multiple wavelength channels for transferring the information, the capacity of existing optical fibre networks may be extended considerably. Until now, wavelength division multiplexing (WDM) has been mainly used to enhance the capacity of point-to-point connections (Fig. 1-1a). More recently, one also started to set up more complex networks in which the wavelength is used to route the information through the network (Fig. 1-1b).

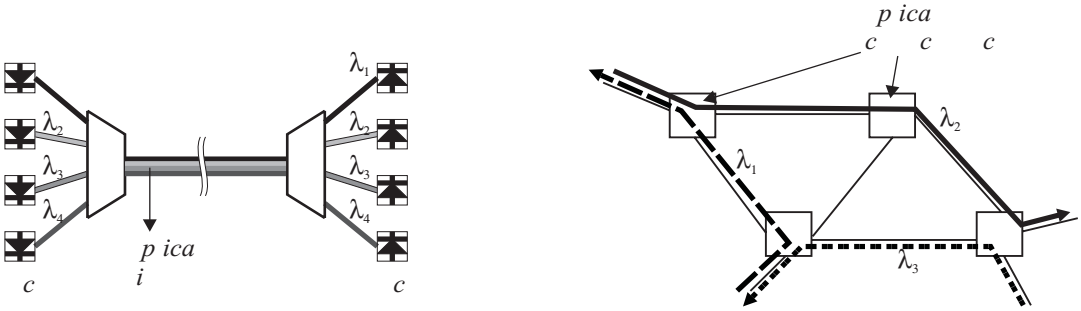

Fig. 1-1 a) WDM in point-to-point links. b) Optical routed WDM networks

An important part of these networks are the laser sources. Three different types may be distinguished:

- *Discrete lasers with fixed wavelength*: this is the option that is currently used. Highly performant devices are available. However, if the number of wavelength channels increases, the management overhead may become complex.
- *Tunable lasers*: can be used as backup laser to replace a complete set of discrete backup lasers.
- *Multiwavelength lasers:* single devices that are able to provide multiple wavelength channels at once, all of them separately modulated. One device may replace a complete array of discrete lasers, thereby reducing the packaging cost and the management overhead considerably.

The goal of this work was to design and realise a multiwavelength laser by integrating a multiplexer and an amplifier array within one optical cavity, and to characterise and optimise the fabricated devices. This chapter is intended to provide a general introduction to the topic of multiwavelength laser sources and shortly reviews the integration technology we used. In paragraph 1.1, the operating principle of multiwavelength lasers is introduced. Next, we explain why we chose to use a Phased-Array as the demultiplexer for realising the device (paragraph 1.2) and we discuss the desired specifications (paragraph 1.3).

Section 2 of this chapter provides a review of the operating characteristics of current state-of-the-art multiwavelength lasers. Both short-cavity and long-cavity multiwavelength lasers are considered and their respective advantages and disadvantages are discussed.

To integrate the multiplexer with the amplifier array, both a monolithic and a hybrid integration technology were used. The development of the monolithic integration technology itself was no part of this work. However, we worked on the design and the characterisation of amplifiers and passive waveguides that were part of this integration scheme and the results are reported in chapter 4. To understand these, the monolithic integration scheme is introduced in paragraph 3.1. The development of the hybrid integration technology on the other hand formed an integral part of this work. The principle is shortly discussed in paragraph 3.2 of this chapter. In chapters 5 & 6, the hybrid integration technology as it was used for realising the Phased-Array multiwavelength laser is described in detail.

1 Multiwavelength lasers: device principle and general design considerations

1.1 Device principle

As explained above, multiwavelength lasers promise to be attractive sources for wavelength division multiplexed (WDM) networks. Since all wavelength channels are coupled together into one output waveguide, they can share one optical pigtail and one optical isolator, thereby resulting in a very compact device size and providing a much-simplified optical packaging. Moreover, as will be explained further in this chapter, they may considerably decrease the management overhead. Multiwavelength sources may be employed as wavelength selectable lasers at reconfigurable add-drop nodes or as standby transmitter sources for reliability assurance. Most of them can also be used as true multiwavelength sources,

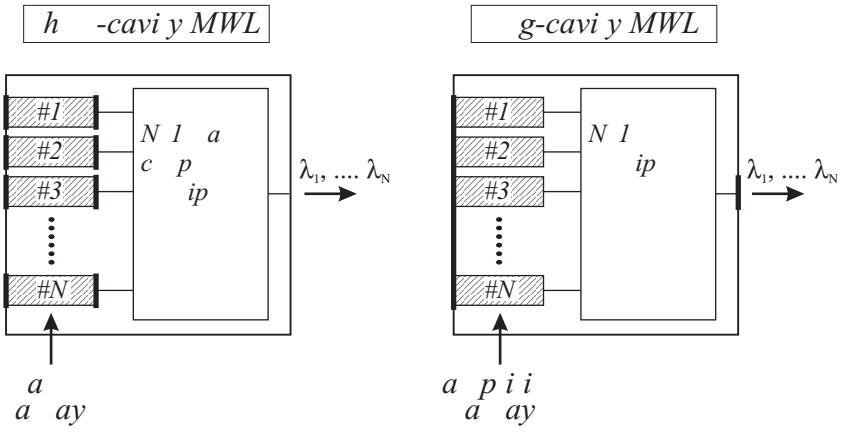

Fig. 1-2 Two approaches to realise an MWL: (a) an array of separate short-cavity lasers coupled together using a passive star coupler and (b) an MWL realised by combining an amplifier and a demultiplexer within one cavity. The bold vertical lines in both figures denote the dimensions of the laser cavity.

simultaneously operating at multiple frequencies, each of them separately modulated.

Two general approaches exist to realise a multiwavelength laser (MWL): coupling an array of separate lasers into one output waveguide using a passive coupler (Fig. 1-2a) or integrating an amplifier array with a passive wavelength selective multiplexer into one cavity (Fig. 1-2b).

For the first approach (short-cavity MWL), an array of DFB-lasers is typically combined with a passive star coupler. DFB-lasers have a short cavity and thus allow for high bit rate operation. Moreover, they reliably oscillate in a single longitudinal mode. However, it is difficult to obtain the required channel spacing accuracy and the star coupler has a high intrinsic loss.

The second approach is the one that was followed in the context of this work (long-cavity MWL). An amplifier array is integrated with a passive demultiplexer within one optical cavity formed by the cleaved facets of the chip. When one of the amplifiers is turned on, its spontaneous emission is filtered by the multiplexer and the amplifier receives a wavelength selective feedback. If the amplifier gain is high enough to compensate for the cavity losses, the device will start lasing at the frequency selected by the multiplexer. If a different amplifier is turned on, it will start lasing at a different frequency (the transfer of the multiplexer is different for each access waveguide). The channel spacing is determined by the multiplexer and is typically very accurate. However, the modulation speed of this type of laser is limited by the long cavity.

1.2 Use of a Phased-Array as the demultiplexer

Several types of integrated optical demultiplexers have been demonstrated in literature. The most important ones are grating demultiplexers [15][16], Phased-Array demultiplexers [17][18][19] and multileg Mach-Zehnder interferometer demultiplexers [20][21]. Grating demultiplexers use an etched diffraction grating as the dispersive element and they can provide an accurate channel spacing. However, the etching of the diffraction grating is rather difficult and their losses are relatively high [22]. Phased-Array demultiplexers and multileg MZI demultiplexers on the other hand, are based on a standard planar waveguide technology and do not require additional processing steps. Phased-Array demultiplexers employ an array of waveguides with increasing optical path length as the dispersive element. The array is connected with the input and output waveguides by two free space star couplers (see chapter 2, section 4). A Phased-Array demultiplexer can provide a very accurate channel spacing, high crosstalk suppression and low insertion losses. Further, they do not require complicated processing steps and they are rather tolerant to fabrication errors. Realised in a low contrast waveguide technology (silicon on silica / silica on glass), Phased-Array demultiplexers are commercially available now, from several manufacturers.

The third type of demultiplexer, the multileg Mach-Zehnder interferometer demultiplexer, may be regarded as a generalised Mach-Zehnder interferometer. Two multimode interferometer couplers are connected to each other using a limited number of arms (4 to 10) with

varying length. Although they neither require difficult processing steps, their performance is rather sensitive to phase errors in the connecting waveguides. Further, in our opinion, they will not be able to suppress multi-passband lasing, even in a chirped design [23], due to their small free spectral range.

In literature, multiwavelength lasers employing grating demultiplexers as well as Phased-Array demultiplexers have been demonstrated. However, the latter showed clearly the best performance (see section 2 of the current chapter for more details). Moreover, in the context of the European ACTS projects *BLISS* and *APEX*, we could rely on the expertise of one of the partners[1] in manufacturing high quality passive InP Phased-Array demultiplexers. For these reasons, we decided to use this type of demultiplexer for the development of our multi-wavelength laser. A typical device layout is shown in Fig. 1-3.

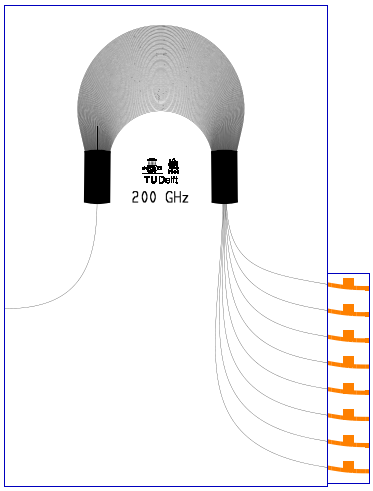

Fig. 1-3 Phased-Array multiwavelength laser

1.3 Desired specifications

In the context of two European ACTS-projects (BLISS & APEX), some generic specifications for multiwavelength lasers were defined. The most relevant ones are summarised in Table 1-1.

Specification	Required value
# of channels	4
channel spacing	400 GHz
channel frequency / wavelength	193.5 THz, 193.9 THz, 194.3 THz, 194.7 THz (1549.32 nm, 1552.52 nm, 1555.75 nm, 1558.97 nm)
minimum output power	- 10 dBm
(optical) crosstalk performance	- 20 dB
direct modulation speed	622 Mbit/s

[1] Delft University of Technology.

Table 1-1 Specifications for multiwavelength laser module

To allow for the transport of the laser and its use in the testbed, it has to be packaged in a fibre-connected module. This module should also facilitate an easy electronic access to the four laser channels.

The specifications for lasers to be used in real world optical communication systems are a lot more stringent than those described in Table 1-1. In actual networks, the absolute operating frequencies are determined by the ITU-grid[1], which defines a set of wavelengths spaced by 50 GHz. Either this 50 GHz channel spacing or a multiple of it (100 GHz, 200 GHz, 400 GHz) may be used[2]. Most recent systems even employ a 25 GHz channel spacing. The required absolute frequency accuracy is typically 10% of the employed channel spacing.

The required output power depends on the application and may vary between 0 dBm (1 mW) and 20 dBm (100 mW). It must be noted that this high output power is often required for single wavelength lasers that are combined externally using a high loss passive combiner. For multiwavelength lasers, the latter is no longer necessary and the specifications for the output power may be relaxed somewhat.

The crosstalk suppression is defined as the ratio of the power in the operation channels to the maximum power emitted in between the channels. A minimum value of 30 dB is generally accepted.

A data rate of 622 Mbit/s appears to be the absolute minimum for sources to be used in modern wavelength division multiplexed optical communication networks. However, for transmission networks higher data rates are often used now (2.5 Gbit/s and 10 Gbit/s).

1.4 Terminology

In literature, many different names are utilised for denoting the Phased-Array demultiplexer. The most important ones are:

- Phased-Array (PA)
- Phasar
- Arrayed waveguide grating (AWG)
- Waveguide grating router (WGR)

In this work, the term Phased-Array demultiplexer will be used. Also for the laser, different names are employed. The most important terms are:

- Multiwavelength laser (MWL) - Multifrequency laser (MFL): this is a general term denoting a device that operates at multiple wavelength channels, coupled together into one output waveguide, as described in section 1.1. Sometimes it is also used more specifically for a Phased-Array multiwavelength laser.

---

[1] ITU: international telecommunications union

[2] $\Delta\nu = 100$ GHz is equivalent to $\Delta\lambda = 0.8$ nm at 1550 nm

- Phased-Array multiwavelength laser (PAL): an MWL formed by integrating a Phased-Array and an amplifier array
- Waveguide grating router multifrequency laser: cf. supra
- Shared angular dispersive element laser (SADE-laser): more general term also including MWLs using other multiplexers than the Phased-Array.

We mostly utilise the first two terms (MWL and PAL).

2 State of the art of multiwavelength lasers

This section provides a review of current state-of-the-art multiwavelength lasers. In paragraphs 2.1 and 2.2 multiwavelength lasers of respectively the first type (short-cavity laser array with passive combiner - Fig. 1-2a) and the second type (amplifier array with multiplexer - Fig. 1-2b) are discussed. In paragraph 2.3 the operating characteristics of Phased-Array multiwavelength lasers are outlined in more detail.

2.1 Short-cavity multiwavelength lasers

As explained in the introduction (paragraph 1.1), these lasers are realised by integrating a laser array and a passive combiner. Both DFB- and DBR-laser arrays can be used. DFB-lasers show an excellent side-mode suppression and a high reliability. They typically show an operating wavelength drift of ~0.1 nm over their lifetime so external frequency control may be necessary. DBR-laser arrays on the other hand, provide a more flexible wavelength allocation due to their tunability.

In most cases, a star coupler or a cascade of Y-junctions, both showing an intrinsic 1/N splitting loss, is used for the combiner. In a few cases, a Phased-Array demultiplexer was used, which becomes interesting for a high number of wavelengths. To compensate for the splitting losses, an SOA may be integrated on the same chip. High-speed modulation may be obtained by integrating a modulator with each laser. Fig. 1-4 and the comment below provide an summary of a few of the most important realisations.

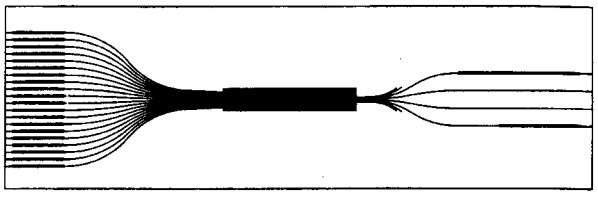

(a)

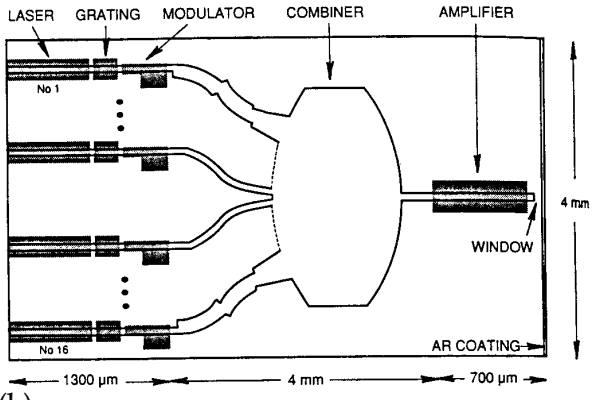

(b)

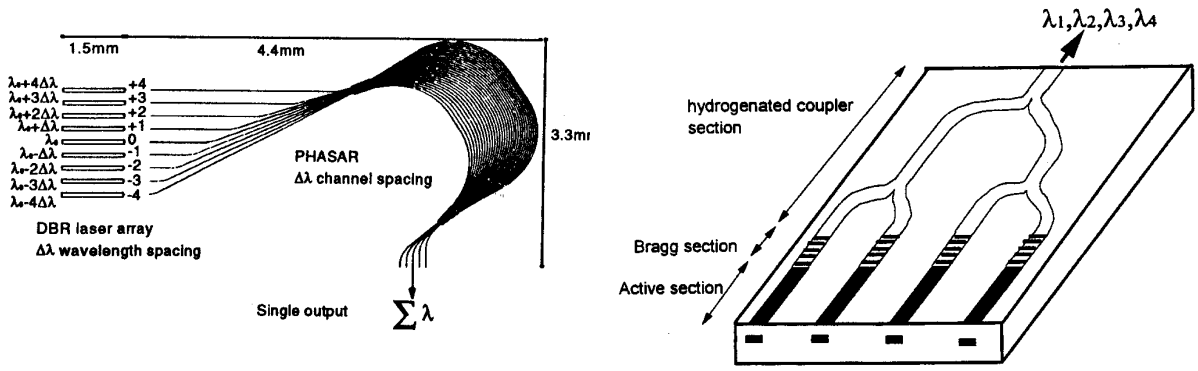

Fig. 1-4 Summary of multiwavelength lasers realised by integration of an array of short-cavity lasers and a combiner.

Fig. 1-4a: DFB-laser array with star coupler [24](Bellcore)

- 8 wavelength channels (spacing 2 nm and 200 GHz).
- 2 identical lasers per wavelength were used to provide redundancy and enhance the device yield.
- array yield for a wavelength accuracy of ±0.2 nm and ±0.1 nm was 80% and 40% respectively
- power per laser coupled in SMF was -13.5 and 0.5 dBm without and with on-chip amplification respectively, under simultaneous operation
- size: 4.3 x 1.6 mm^2
- SMSR > 30 dB
- 9 GHz 3-dB bandwidth / 2.5 Gbit/s error free transmission through 120 km SMF demonstrated.
- integration scheme: evanescent field coupling
- used in *MONET* and *ONTC* system testbeds (see refs. in [24]), intensively tested.

Fig. 1-4b: DBR-laser array with star coupler and integrated modulators [25](Lucent)

- 16 channels @ 0.6 nm (±0.1 nm)
- power: -8 dBm in SMF
- size: 4.0 x 6.0 mm^2
- modulator extinction: 10 dB (2.5V) / modulator 3dB bandwidth: 2.5 GHz
- common amplifier used

Fig. 1-4c: DBR-laser array with demultiplexer [26](OPTO+)

- 10 channels @ 1.6 nm (±0.2 nm)
- I_{th}: 12-18 mA
- -15 dBm into SMF
- SMSR > 30dB
- size: 3.3 x 5.9 mm^2
- passband of Phased-Array flattened (3dB-width = 1.2nm)

- DBR-laser tunable over 9 nm

Fig. 1-4d: DBR-laser array with cascade of Y-junctions [27](OPTO+)

- 4 channels @ 4 nm (±0.2 nm)
- wavelength switching time < 4 ns
- I_{th}: 20-28 mA
- SMSR > 30 dB
- 0.6 - 0.9 mW @ 100 mA (free space)
- size: 1.0 x 3.0 mm^2

Advantages of short-cavity multiwavelength lasers:

- Both DFB- and DBR-lasers allow for high-speed modulation.
- The integration of a separate modulator with each channel is possible. For single DFB-lasers this is a well known and highly successful technology
- Due to its tunability, a DBR-laser array shows higher flexibility.
- Equipment savings: only one temperature control unit, one isolator and one pigtail necessary.

Disadvantages of short-cavity multiwavelength lasers:

- Fine grid grating required
- Intrinsic 1/N loss when using star coupler (when the number of wavelengths reaches a certain minimum value, it may be advantageous to use a multiplexer instead - see Fig. 1-4c).
- The required channel spacing accuracy is difficult to obtain. For DFB-laser arrays, the integration enables to move the complete wavelength comb simultaneously but removes at the same time the ability to independently temperature tune the individual laser elements. To improve the device yield, special measures, such as the use of redundant devices, can be undertaken (cf. Fig. 1-4a). For DBR-laser arrays, the channel accuracy is determined by the FP-mode spacing if no phase section is used.
- The wavelength selective filter is realised in active material: this results in a frequency shift due to amplifier heating or gain change. A typical wavelength drift of 0.1 nm is observed over the lifetime of a DFB-laser. In narrow channel spacing systems, this results in the need for external wavelength stabilisation.
- For DBR-lasers, the light is collected at the grating side, which means that a compromise between side-mode suppression and output power has to be made.
- DBR-lasers require supplementary control.

2.2 Long-cavity multiwavelength lasers

2.2.1 Reflective configuration

First demonstrations of laser arrays with a passive intra-cavity wavelength selective filter (cf. Fig. 1-2b) used a demultiplexer in a reflective configuration. The Multichannel Grating Cavity Laser (MGC) [24] (Fig. 1-5a) is simply an extension of a standard external grating cavity laser. Stable, simultaneous operation at multiple wavelengths could be obtained and the issue of crosstalk in the common amplifier was mentioned for the first time. A solution in the form of a feedback scheme was proposed and demonstrated [29]. However, the MGC-laser is based on bulk components, which requires a very stable setup. To overcome this, Kirby proposed a more compact version, based on the monolithic integration of an amplifier array and an etched diffraction grating [30].

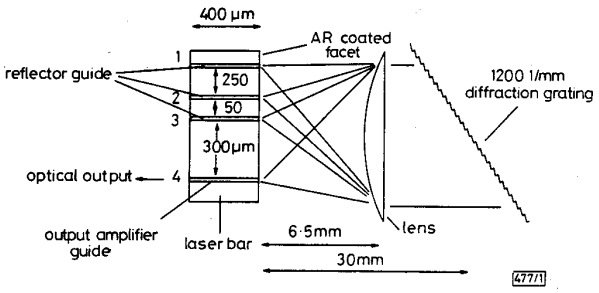

(a) MGC-laser (1990)

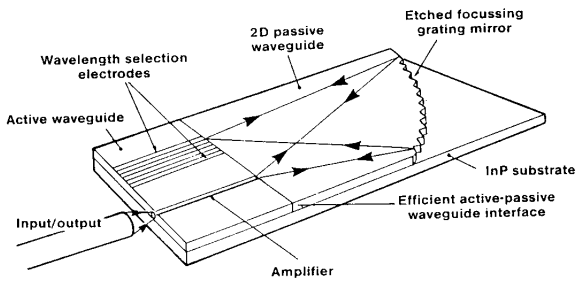

14 x 3 mm^2

(b) MAGIC-laser (1992)

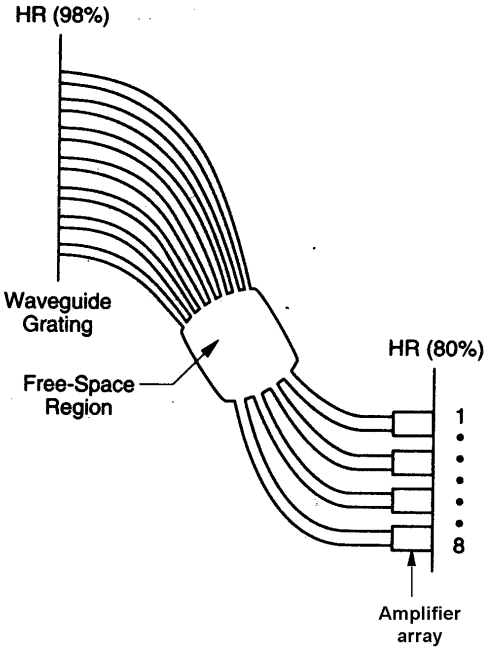

(c) PAL in reflective configuration ('94)

Fig. 1-5 multiplexer used in a reflective configuration

Such a Multiple Array Grating Integrated Cavity laser (MAGIC - Fig. 1-5b) was realised in 1992 at Bellcore [31][32][33]. A device with 9 wavelength channels spaced by 2 nm with an accuracy of ±0.02 nm was demonstrated. This channel spacing accuracy is better by an order of magnitude compared to that of the short cavity laser arrays described in the previous paragraph. However, the other operating characteristics were not as good: threshold currents were 300 mA (channel amplifier + common amplifier - pulsed operation), the maximum output power was 1 mW and the use of broad amplifier stripes (7 µm) resulted in a poor SMSR (10 dB). The suppression of the ASE-noise was between 20 and 25 dB and simultaneous operation of 4 channels was reported.

In 1993, the first device employing a Phased-Array demultiplexer was demonstrated [34]. A Phased-Array was cleaved symmetrically through the grating arms and integrated with amplifiers (Fig. 1-5c), thus obtaining a laser with a cavity length of 7 mm (threshold current: 37 mA, maximum output power: 0.7 mW, SMSR: 25 dB, ASE noise suppression: 35 dB). However this device was not suitable for multiwavelength operation: by turning on two amplifiers *i* and *j* together, one gets lasing not only at the peak filter wavelengths λ_i and λ_j from the individual amplifiers, but also at the peak filter wavelength from both amplifiers together λ_{ij}. A transmissive configuration as described in the following paragraph solves this problem.

2.2.2 Transmissive configuration

Since 1994, different groups demonstrated a multiwavelength laser using a Phased-Array in a transmissive configuration. A typical layout for such a device was shown in Fig. 1-3. Table 1-2 gives a summary of the most important operating characteristics of several published devices. In Fig. 1-6, the integration technology employed for realising each of these MWLs is demonstrated.

	Lu1 [37]	**Lu2 [36]**	**Lu3 [43]**	**Ph1 [38]**	**BC1 [39]**	**D1 [57]**	**G1 [3]**	**G2 [3]**
N	9	10	8	9	8	8	4	4
$\Delta\nu / \Delta\lambda$	145 GHz	100 GHz	203 GHz	400 GHz	200 GHz	400 GHz	200 GHz	400 GHz
accuracy	2 GHz	-	3 GHz	-	9.6GHz	-	-	-
λ_0	1555 nm	1600 nm*	1545 nm	1545 nm	1550	1545	1530	1540
Ith	18-22 mA	<18 mA	30 mA	+100 mA	65-70 mA	78-108 mA	35 mA	54 mA
ASE suppr.	50 dB	> 50 dB	50 dB	30 dB	40 dB	55 dB	60 dB	35 dB
SMSR	***	***	54 dB**	20 dB	40 dB	55 dB	40 dB	35 dB
P_{out}	.4-1.2 mW	0.58 mW	.6-1.5 mW	.1-.4 mW	0.65mW	-	3.5 mW	-
I	100 mA	100 mA	190mA	200 mA	90 mA		100 mA	
FC/FS****	FC	FC	FC	FC	FS		FS	
# arms	68	70	80	50	-	-	-	-
MUX 3dB	-	-	26 GHz	1.7 nm		-	60 GHz	120 GHz
$L / \delta\nu$ *****	3.8 GHz	3.6 GHz	3.15 GHz	6 mm	7.5 GHz	-	10 mm	-
Common amplifier	no	no	yes	no	yes	no	No	Yes
Size [mm²]	5.5x4.5	4.7x5.9	-	3.5x2.5	3x2	4x4	5x5	5x5
SOA length	950 µm	900 µm	2x950 µm	500 µm	400-600 µm	1000 µm	400 µm	400 µm
Linewidth	-	-	1 MHz	21 MHz	-	-	< 1 MHz	-

* High wavelength intended for use as L-band source

** The Phased-Array is chirped, so the only visible side modes are these caused by wave mixing in the common amplifier under simultaneous operation.

*** The Phased-Array is chirped and an extremely short passive output waveguide is used: even under simultaneous operation the side modes are suppressed by more than 55 dB

**** FS: Free Space - FC: Fibre coupled

***** $\delta\nu$ denotes the cavity mode spacing, L the cavity length. These are related as $\delta\nu = c/(2Ln_g)$

Table 1-2 Device characteristics of published Phased-Array MWLs

Lu1, Lu2 & Lu3 (Lucent Technologies [37])

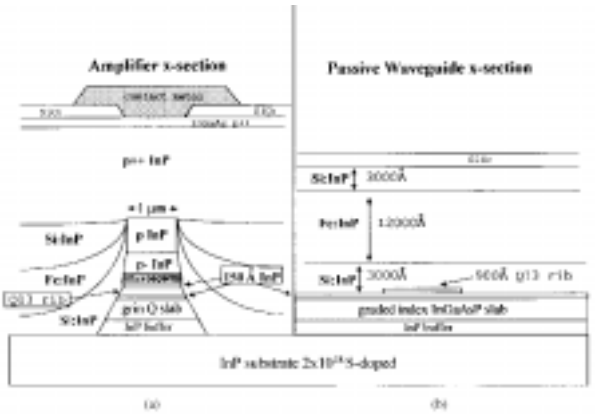

- Integration technology: active-layer removal (evanescent field coupling)
- Active layer: quantum wells
- Intensive device optimisation: (1994: I_{th}=100mA, P_{out}=1.2mW, free space [35] - 1999 : I_{th}=18mA, P_{out}=1.0mW, fibre coupled [37])
- Used in several system testbeds (direct and external modulation)

Ph1 (Philips [38]-1996)

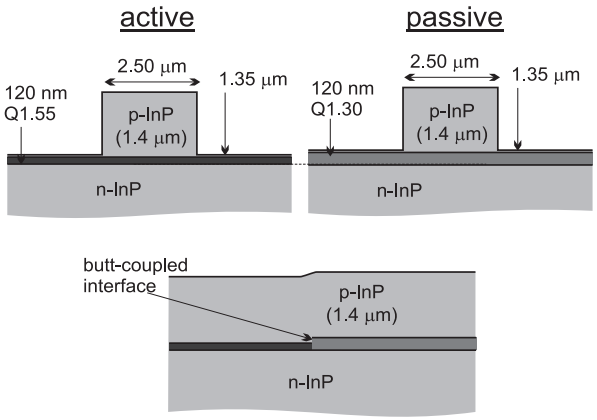

- Integration technology: butt coupling
- active layer: bulk
- No common amplifier
- Size: 3.5 x 2.5 mm^2

BC1 (Bellcore [39] - 1997)

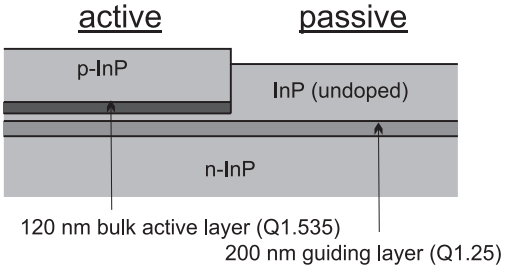

- Integration technology: active-layer removal
- Active layer: bulk
- Common amplifier used
- Size: 2 x 3 mm^2

G1 & G2 (This work [3][4]-1999)

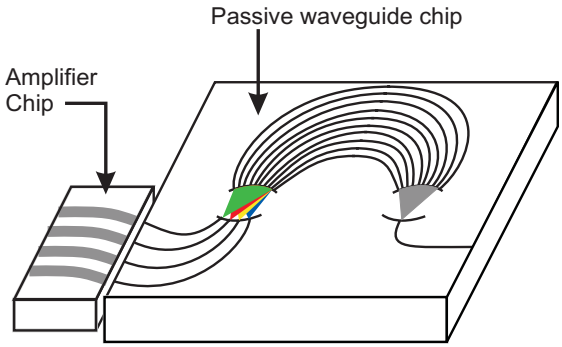

- Integration technology: hybrid integration (permanent and non-permanent)
- Active layer: bulk
- With / without gain clamping
- Size 5 x 5 mm²

Fig. 1-6 Integration technologies employed to realise a Phased-Array multiwavelength laser

2.3 Operating characteristics of Phased-Array multiwavelength lasers

2.3.1 Number of channels

The maximum number of channels for a PAL that was demonstrated is 18 [40]. In fact, this was a 24 channel device. However, 1 channel was defective and 5 had to be eliminated due to multipassband lasing (the multiplexer was not chirped). Simultaneous operation on all 18 channels was possible. A channel number between 8 and 10 however is more frequently used. Since the device yield decreases exponentially with the number of channels ($y_{dev} \sim (y_{chan}^{N} + \text{cte})$ with y_{chan} the yield per channel), this appears to be a good compromise between yield optimisation and device integration. The use of redundant amplifiers as demonstrated for DFB-laser arrays [24], is not possible for Phased-Array lasers.

Very recently, a 40 (5 x 8) channel device with only 14 (5+8+1) amplifiers was demonstrated [49] that can be used as a rapidly and digitally tunable laser (100 GHz channel spacing). The output power into fibre was -10 dBm (Fig. 1-7).

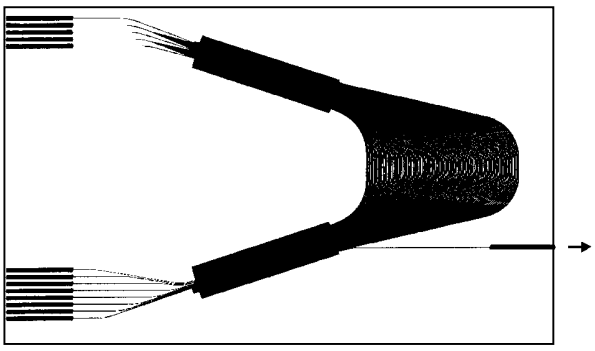

Fig. 1-7 40-wavelength rapidly digitally tunable laser

2.3.2 Channel spacing and channel spacing accuracy

The *channel spacing* is determined by the passive demultiplexer and is, when correctly designed, very accurate. The minimum channel spacing demonstrated is 75 GHz [47]. De-

signing a InP-Phased-Array with smaller channel spacing (50 GHz) is more difficult and requires stringent control of the process parameters since phase errors can lead to a severe degradation of the crosstalk level.

The *channel spacing accuracy* is typically very good and determined by the FP-mode spacing. This reveals immediately a trade-off on the device length: decreasing the device length improves the single mode stability and the modulation bandwidth, but at the same time the FP-mode spacing is increased and thus the channel accuracy decreased (e.g. compare Table 1-2 - Lu1 and BC1).

The multiplexer is fully realised in passive material so neither degradation nor shift of the channel spacing accuracy has to be expected during the device lifetime.

2.3.3 Absolute wavelength accuracy

To obtain a good absolute wavelength accuracy, a stringent process control and characterisation is necessary. A deviation of the effective refractive index of less than 0.1% already results in a 1 nm deviation of the central wavelength of the device. However, such accuracy is shown obtainable from chip to chip and wafer to wafer [41].

The temperature may be used to tune the whole wavelength comb. A typical tuning range of 0.11 nm/K is obtained. The wavelength is expected to be independent of drive conditions since the multiplexer is passive. If a common output amplifier is used, multiple output waveguides may be provided. In that case, the central wavelength is determined by selecting the correct amplifier.

2.3.4 Threshold current and output power

For multiwavelength lasers to be useful, their power consumption per channel must be similar to that of their discrete counterparts. Moreover, the lower the threshold current of a laser, the better its performance in the long term.

The threshold current and the external quantum efficiency are predominantly determined by the cavity loss. The most important cavity losses are the multiplexer loss, which in turn is determined by the passive waveguide loss, and the active-passive transition loss. Therefore, an integration scheme minimising both of these is required. In [38] (Fig. 1-6b), the same p-doped cladding layer is used for both the amplifiers and the passive waveguides, resulting in an estimated waveguide loss of 20 dB/cm and equally high threshold currents (100 to 120 mA). However, intensive optimisation of the monolithic integration process led to devices (quantum well active layer) with a threshold current as low as 18 mA per channel and an output power between 0.8 and 1.2 mW at 100 mA (coupled to SMF) [34].

In chapters 5 & 6, we demonstrate a hybrid integration scheme that allows to optimise both the active and the passive part separately. In that way, very low waveguide losses may be obtained (0.6 dB/cm, see chapter 4). The active-passive transition loss on the other hand, is

higher[1] for hybridly coupled PICs compared to the monolithic ones. In the context of this work, we realised devices (bulk active layer) with rather low threshold current (< 35 mA), and probably the highest output power for a PAL reported until now: 3.5 mW for single channel operation and a total power of 6.2 mW when 4 channels are operated simultaneously (free-space)(see chapter 5). For the permanently packaged hybrid PAL, the best figures until now are a threshold current of 52 mA and an output power of 1.5 mW at 100 mA (chapter 6).

2.3.5 Side mode suppression ratio - ASE noise suppression - Longitudinal mode stability

The side mode suppression ratio is determined by both the suppression of the neighbouring longitudinal modes in the same passband as by the suppression of modes in another passband of the Phased-Array.

To obtain a good suppression of the modes in neighbouring passbands and prevent Multi Passband Lasing (MPL) several approaches are possible:

- *Increasing the FSR* [40], which increases the size of the Phased-Array.
- Following [39], *bulk active material* prevents MPL due to a reduced gain bandwidth compared to quantum well active material. However, although we used 400 μm long bulk RSOAs for the hybrid PAL, we noticed MPL in some cases.
- *Chirping of the Phased-Array:* by chirping the Phased-Array, neighbouring passband transmissivity may be suppressed by 5 to 10 dB thereby cancelling MPL completely. Chirping the Phased-Array has only consequences at the level of the mask design and does not alter the device fabrication. Further, it allows changing the linewidth enhancement parameter α deliberately by moving the quantum well gain peak with respect to the central wavelength as is often done for DFB-lasers. A reduced linewidth enhancement parameter means a narrower linewidth and a reduced direct-modulation chirp.

Obtaining single longitudinal mode stability and avoiding mode hopping is more difficult: for a typical 200 GHz Phased-Array laser (3-dB bandwidth = 60 GHz, cavity length 10 mm) approximately 15 longitudinal modes fit within the passband. Fortunately, these modes are spaced closely enough in frequency so that their beatings experience gain compression due to carrier depletion. Together with an appropriate cavity filter, this wave mixing effect can provide stable single longitudinal mode operation and effectively prevent rapid mode-hopping. To increase the stability, it is necessary to decrease the filter bandwidth and the cavity length as much as possible and to avoid intra cavity reflections. This effect is described in more detail in chapter 3 (theoretically) and chapter 6 (experimentally).

The suppression of the ASE-noise is very high. Values better than 60 dB have been measured for devices without common amplifier (e.g. Fig. 5-19a). When multiple channels are

[1] estimated value between 3 and 5 dB

operated together, wave mixing in the passive output waveguide of the Phased-Array gives rise to additional mixing products in the output spectrum (e.g. Fig. 5-19b). If the mixing product of two channels overlaps with a third channel, this effect may be responsible for some power fluctuation. By reducing the length of the output waveguide, this may be solved [35]. When a common amplifier is used, the ASE-noise suppression is reduced but is still good (e.g. Fig. 5-28).

2.3.6 Modulation capabilities

The long cavity limits the direct modulation speed of the PAL. However, direct modulation of a 16-channel device up to 622 Mbit/s (all channels modulated simultaneously) was demonstrated [44]. In [45], a 16-wavelength transmitter, built by interleaving two 8-wavelength PALs, was externally modulated at 2.5 Gbit/s. A power penalty of less than 0.4 dB was measured for all channels after transmission through 627 km of conventional fibre (Fig. 1-8a). When the PAL is used as a wavelength selectable source and no simultaneous operation of multiple channels is required, a modulator may be integrated on the same chip by attaching it to the output star coupler of the WGR, one period away from the shared amplifier connection (Fig. 1-8b). In [47], an amplifier identical to the signal amplifiers was used as the modulator, which does not increase the fabrication complexity but also limits the modulation speed to 250 MHz. Using selective area growth, it should be possible to integrate the PAL with a high-speed electro-absorption amplifier without increasing the number of processing steps (see also paragraph 3.1).

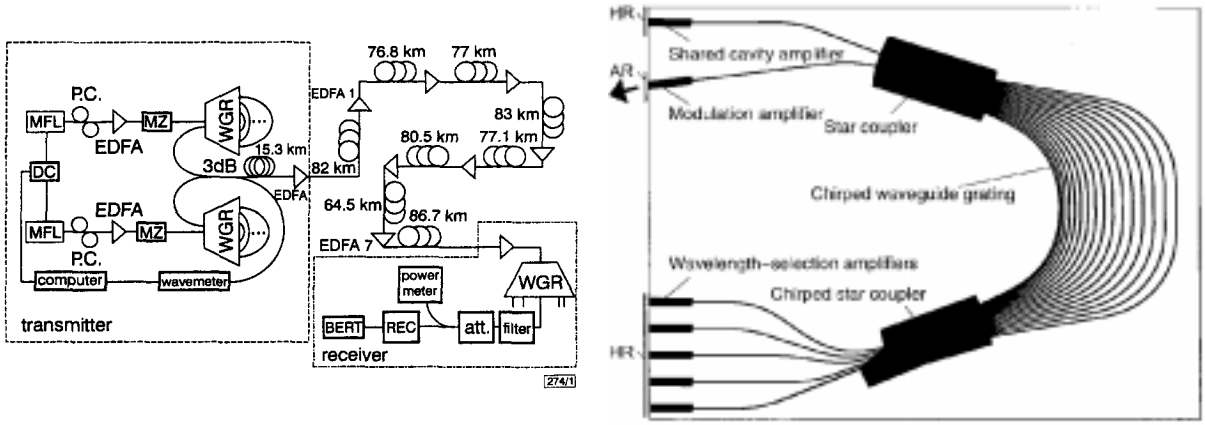

Fig. 1-8 a) Experimental setup used in [45]. b) PAL integrated with modulation amplifier [47]

We measured the small signal response for the permanently bonded hybrid PAL of chapter 6 (Fig 6-15b). A 3-dB frequency of 1600 MHz for a bias current of 120 mA was found. We also measured eye-diagrams of the hybrid PAL modulated with a 300 GHz, 622 GHz and 2.5 GHz pseudo-random signal channel (Fig. 6-17)

In [48], a PAL is used as an eight-wavelength fast packet switching transmitter: a 2.5-Gb/s stream is directed to 8 different locations by sequentially turning on different channels of the

laser. The switching time was less than 2.8 ns and limited by the electrical inductance of the packaging. If the amplifier is driven below threshold in the off state, the switching time increases to 10 ns.

2.3.7 Laser Linewidth

We measured an oscillation linewidth below 1 MHz for the permanently packaged hybrid PAL (Fig 6-14). Other authors reported values of 1 MHz [43] and 21 MHz [38].

2.3.8 Control and reliability

Since the wavelength spacing is fixed, control of only one wavelength channel is necessary to tune the whole wavelength comb to the desired value. As already mentioned, the filter is realised completely in passive material so no degradation or shift has to be expected.

When a common amplifier is used, it may be necessary to use a feed-forward scheme when multiple channels are operated together, to avoid crosstalk from carrier density changes [46]. Another approach is to clamp the gain of the common amplifier as was proposed for the first time in the context of this work ([3], chapter 5) and which requires no additional control. However, it is better to use no common amplifier at all for multiple channel operation.

As described in 2.3.4, the threshold current of these devices can be comparable to that of their discrete counterparts, indicating that they possibly may turn out to be reliable devices. However, stringent reliability testing has not yet been published.

A minimum device size of 2 x 3 mm^2 has been reported, however a size of 5 x 5 mm^2 is more common. This is rather large and may be a problem for large-scale fabrication.

2.4 Conclusions

The most important advantages of Phased-Array multiwavelength lasers appears to be the accurate channel spacing, their simple characterisation and packaging procedure and the reduced management overhead. Moreover, the whole wavelength comb may be tuned to the desired grid at once by changing the operating temperature and the filter is realised completely in passive material so no wavelength drift due to ageing is to be expected. Further, the side mode suppression ratio is much better than required for current state of the art WDM-networks. The output power, on the other hand, is generally considered still too low. The large chip size and the high number of amplifiers will enhance the probability for fabrication errors considerably and to obtain an acceptable yield, the total number of channels will have to be limited. The fabrication itself however is simple since no fine grid gratings are required and only one fibre-chip coupling unit is required for multiple wavelength channels.

The most important drawback is the modulation speed, which is limited due to the long cavity length. Direct modulation at 622 Mbit/s has been demonstrated, but higher data rates are becoming increasingly more common in today's optical networks. As an alternative, one

may consider external modulation. If the laser is used as a wavelength selectable source and only one channel is operated at a time, this is a very straightforward option. The modulator may even be integrated on the same chip as shown in Fig. 1-8b. If multiple channels of the multiwavelength laser are operated simultaneously, they first have to be demultiplexed again as shown in Fig. 1-9a. This may seem pointless at first sight. However, in our opinion this is not completely true. If the number of channels is high enough, the total number of devices is still reduced considerably compared to the case where discrete lasers are used (Fig. 1-9b). More importantly, the number of critical pigtails (those between InP-based components and optical fibre) and the number of isolators are both reduced from N, the number of channels, to 1.

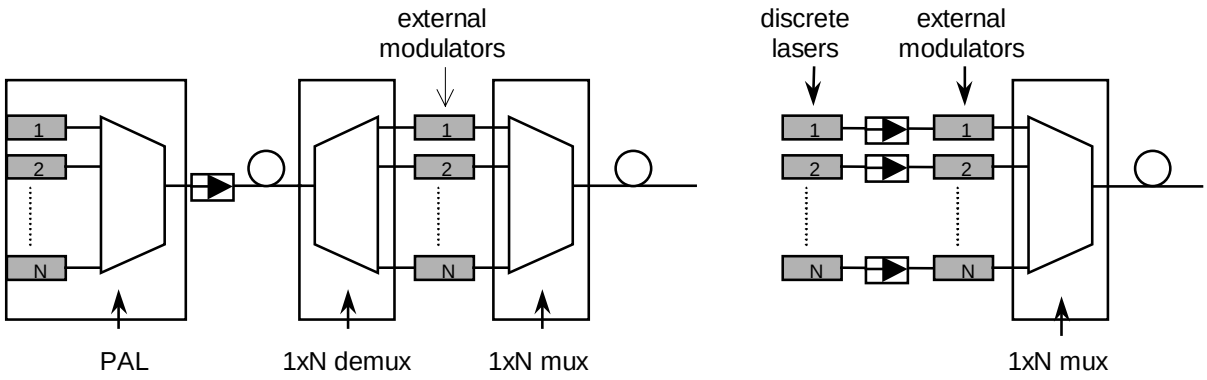

Fig. 1-9 a) External modulation of PAL under simultaneous multi-channel operation. b) External modulation of a series of discrete lasers

3 Integration technology

The Phased-Array multiwavelength laser consists of an "active part" (the amplifiers) and a "passive part" (the multiplexer). The active part is pumped and has to provide gain. The operating wavelength of the laser will be equal to the bandgap wavelength of the active layer in this section. The passive part on the other hand, is left unpumped. To avoid complete absorption of the light generated in the active part, the bandgap wavelength of the material in the passive section must be considerably lower than the operating wavelength. This means that two different waveguide types have to be integrated in one device. In the context of this thesis, both a monolithic and a hybrid integration technology were investigated. The development of the monolithic integration technology itself was no part of this work. However, we worked on the design and the characterisation of amplifiers and passive waveguides that were part of this integration scheme and the results are reported in chapter 4. To understand these, the monolithic integration scheme is shortly discussed in the next paragraph (partly taken from [58]). In paragraph 3.2, the hybrid integration scheme is introduced.

3.1 Selective area growth as a monolithic integration technology

Several monolithic integration schemes have been demonstrated in literature. Typical examples are butt-joint coupling, active layer removal (evanescent field coupling), selective area growth and quantum well intermixing. The first two are the most commonly used (e.g. see Fig. 1-6 and [50]). They both involve growing epitaxial layers suitable for a first type of device over the whole substrate. Subsequently, these layers are etched away where other devices are needed and different ones are grown in the openings. We chose for another approach, based on the selective area epitaxial growth[1]. This technique allows for variation of the bandgap of quantum well material in the same plane within a single growth step, so it is not necessary to etch layers away in certain regions of the device.

The concept of the selective area epitaxial growth technique [51]-[56] is shown in Fig. 1-10. The regions of the substrate surrounding the place where the active material has to be grown are masked using SiO_2. Source material arriving from the gas phase will grow epitaxially in the regions where the mask is open. Where source material lands on the SiO_2, it will not readily nucleate. If the growth conditions are well chosen, species deposited on the mask will re-enter the gas phase and diffuse, due to the local concentration coefficient, to find an unmasked region. Quantum wells grown in between two SiO_2 stripes will be thicker and richer in Indium compared to those grown in the planar region and from both these effects their bandgap is shifted towards lower energy values.

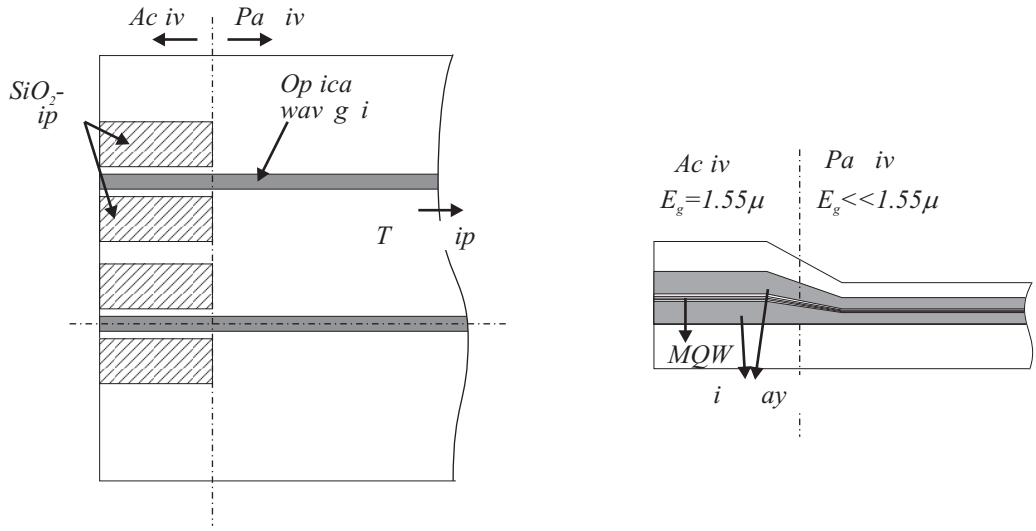

Fig. 1-10 Principle of selective area growth

Using the selective area epitaxial growth technique, a complete active-passive integration scheme was developed. From the beginning of the project, it was decided to use a ridge-type waveguide cross-section for the passive waveguides. Therefore, although buried waveguide types are generally considered more suitable for active devices (see also chapter 4), we chose

[1] The term selective area epitaxial growth is sometimes also used to refer to a different monolithic integration approach, based on molecular beam epitaxy (MBE) [57].

to employ also a ridge-type waveguide cross-section for the amplifiers. This facilitates an easy and reflection-free integration scheme. In a first step, the SiO_2 masks are deposited next to the region where the amplifier layer stack has to be grown. This is followed by the selective epitaxial growth of a multi-quantum well layer stack (InGaAs QWs with Q1.25 barrier material, sandwiched between Q1.1 film layers) and a 300 nm InP cladding layer. After removal of the oxide stripes, a thick p-doped InP cladding layer and the InGaAs contacting layer are grown[1]. In a next step, the InGaAs contact layer is selectively etched away in the passive region. Subsequently, the amplifier ridges are defined using a wet etching process. The upper film layer of the active layer stack is thereby used as a selective etch stop layer. During this process, the region for the passive waveguides is shielded using a photo resist layer. Then, the passive waveguides for the demultiplexer are defined using a reactive ion etching process, while the active region is covered. The transition between the wet-etched waveguides and the dry-etched waveguides takes place in the planarly grown region. In chapter 4, the losses and residual reflection occurring at this transition are modelled. In a final step, the amplifier contacts are defined, using polyimide as an isolation layer. The resulting waveguide cross-sections are discussed in chapter 4

The apparent advantage of this integration scheme is its simplicity. Only two epitaxial growth steps and a limited number of processing steps are required. Further, the continuity of the guiding layer promises to provide a low-loss and reflection free transition region. For the moment, the major problem appears to be obtaining high quality selectively grown active layers. The substrate preparation in particular seems to be very critical.

In our opinion, the main advantage of the selective area growth technique as a monolithic integration technology over classical integration technologies such as active layer removal or butt joint coupling, is that multiple types of active components such as amplifiers, detectors and modulators - each requiring a different bandgap energy - may be integrated on a single chip without further complicating the integration scheme. One only has to vary the width of the gap in between the SiO_2 masks where these elements have to be grown, as shown in Fig. 1-11. To illustrate this further we refer to Fig. 1-9b, taken from [47]. In that case, the Phased-Array laser was integrated with a modulator. However, for not complicating the processing, which was based on active layer removal, this modulator had an identical cross-section as the gain sections, thereby limiting the modulation speed to approximately 250 MHz. Using a selective area growth based integration scheme, it would be possible to replace the modulating amplifier by a high performant modulator, without complicating the integration process.

---

[1] The whole layer stack is not grown in one step, because this would result in non-flatness of the selectively grown material that is beyond tolerance.

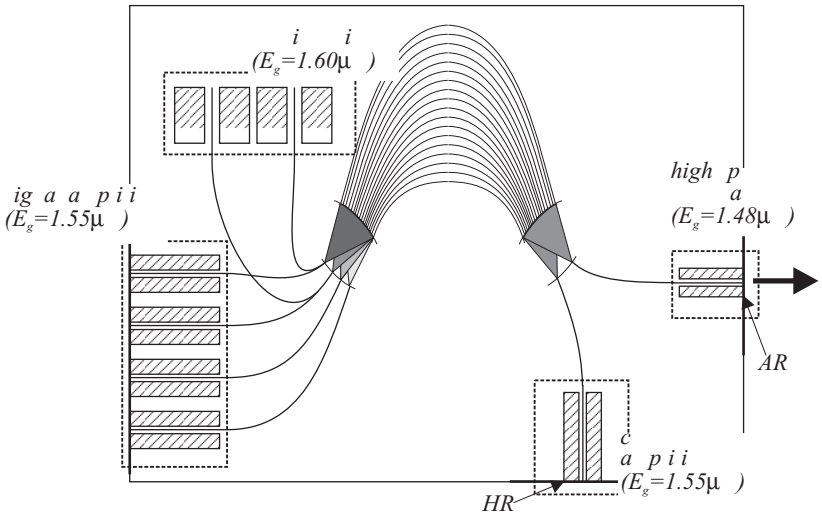

Fig. 1-11 Hypothetical design for a multiwavelength laser incorporating a common amplifier, monitor diodes and a high-speed modulator, each requiring an active layer with a different bandgap wavelength. This laser could be realised using a selective area growth based monolithic integration scheme by varying the width of the gap in between the SiO_2-masks.

3.2 Hybrid integration for device prototyping

In the hybrid integration scheme, an InP amplifier array is butt-coupled with an InP passive waveguide chip. To avoid reflections at the interface between both chips, the waveguides are slanted towards the facet (see Fig. 1-6). The coupling is carried out on an optical bench by visual inspection and by optimising the output power of the laser (active alignment). Originally, the chips were only temporarily coupled. This gives a large flexibility and allows for interchanging the passive chips. However, sometimes it is difficult to keep the coupling efficiency between both chips constant over a longer time interval. Moreover, it is not possible to use such devices in system tests. Therefore, we developed also a technique to bond both chips permanently together, using a UV-curing epoxy. In that way, we could demonstrate a complete, fibre-connected multiwavelength laser.

The development of the hybrid integration technology was an integral part of this work and is described in detail in chapters 5 & 6. In these chapters, we use the term “hybridly coupled PIC” for denoting a PIC that was realised by non-permanently coupling two chips on an optical bench (chapter 5). The term “hybridly integrated PIC” denotes a PIC realised by permanently bonding two chips together (chapter 6). In the other chapters of this work, this term is used for both permanently and non-permanently coupled chips.

4 Goal of this work, structure of the thesis and main achievements

When this work was initiated, some groups already had demonstrated a Phased-Array multiwavelength laser. However, these devices suffered from high threshold current values, had a low output power and a low modulation bandwidth. At that moment, it was not yet obvi-

ous if such lasers could be useful for use in practical WDM-systems. Therefore, the goal of this work was to design and develop multiwavelength lasers with improved operating characteristics. We thereby wanted to enhance the theoretical knowledge of the device operation and to investigate the theoretical limits of this type of laser. In parallel, we wanted to investigate and develop new methods for designing complicated PICs such as the multiwavelength laser.

In chapter 2, we discuss the design procedure for photonic integrated circuits as it is commonly employed today and as it was carried out in the context of this work. The first part of this chapter provides a review of the analysis methods and CAD-tools that were used for designing the multiwavelength laser presented here. Several analytical formulas and simplified design rules are derived and verified. In the remainder of the chapter, we discuss methods for the synthesis of complex photonic ICs, point out some weaknesses of today's approaches and propose an alternative, knowledge driven approach. The latter is illustrated using the Phased-Array multiwavelength laser as an example. In the last section of this chapter, we shortly introduce the basic operating principle of Phased-Array demultiplexers and demonstrate how their design may be optimised for use in a long-cavity laser.

In chapter 3, both the static and dynamic operating characteristics of long-cavity multiwavelength lasers are theoretically investigated using a black-box description, thereby hiding implementation specific properties such as the type of multiplexer or the active-passive integration scheme. The results of this analysis are used to optimise the Phased-Array laser design and compared to experimental results in chapters 5 and 6. Some general design rules for multiwavelength lasers are summarised at the end of this chapter.

In chapter 4, the design and the characterisation of the subcomponents for the Phased-Array laser (amplifiers, passive waveguides and active-passive transition) are discussed, both for the hybridly and for the monolithically integrated device. In the first section of this chapter, we analyse the operation principle of ridge-type lasers and subsequently use the results from this analysis to optimise the design of the amplifiers for the monolithically integrated PAL. In addition, the design and the characterisation of the reflective SOA-arrays, which were used to develop the hybridly integrated PICs, is discussed and some material parameters, which were used for the theoretical analysis of chapter three, were obtained. The largest part of the second section of chapter 4 is devoted to the design and characterisation of the passive waveguides for the monolithically integrated PAL. Further, we also present some loss measurements for waveguides that were used for realising the hybridly integrated PAL. Finally, in a third section of this chapter, the coupling loss and the misalignment tolerances for two hybridly coupled PICs are modelled.

In chapter 5, the (non-permanently) hybrid coupling scheme we developed is discussed in detail and we present experimental results for hybrid Phased-Array lasers that were realised. The first sections of this chapter present a review of more classic, silicon bench based, hybrid integration techniques and their increasing importance for practical applications is demon-

strated. In the following sections, we discuss our own hybrid integration technology. The tolerances for misalignment errors are investigated and the operating characteristics of the hybridly coupled Phased-Array lasers are presented. We successively describe the static characteristics (threshold current, output power, oscillation spectrum, single longitudinal mode stability) and the dynamic characteristics (small-signal response and large signal response). Also the experimental verification of the gain-clamping principle for multiwavelength lasers that was proposed for the first time in the context of this work, is described in this chapter. Finally, we present a hybrid tunable laser incorporating an intra-cavity ring resonator filter and a tunable Mach-Zehnder interferometer.

In chapter 6, the development of the hybrid integration technology based on the permanent bonding of two InP chips is described in detail and the realisation of the first completely packaged hybrid multiwavelength laser is discussed. The operating characteristics of this laser module are investigated and compared with theoretical results. The final section of this chapter summarises the most important results and presents some ideas for future work.

5 Publications in the context of this work

[1] D. Van Thourhout, A. Vanhove, J. De Merlier, T. Van Caenegem, I. Moerman, P. Van Daele, R. Baets X.J.M. Leijtens, M.K. Smit, "Packaged hybridly integrated phased-array multiwavelength laser", Electronics Letters (accepted)

[2] D. Van Thourhout, G. Sarlet, G. Morthier, R. Baets, "Comparison of multiwavelength and widely tunable laser diodes", Optical & Quantum electronics (submitted)

[3] D. Van Thourhout, J. De Merlier, T. Van Caenegem, L. Vanwassenhove, I. Moerman, P. Van Daele, C. G. P. Herben, X. J. M. Leijtens, J. W. M. van Uffelen, M. K. Smit, R. Baets, “Elimination of crosstalk in the common output amplifier of a multiwavelength source by gain clamping”, OFC' 99 San Diego, ThV2, 1999

[4] D. Van Thourhout, J. De Merlier, T. Van Caenegem, K. Vandeputte, C. G. P. Herben, X. J. M. Leijtens, J. W. M. van Uffelen, M. K. Smit, I. Moerman, P. Van Daele, R. Baets, “Demonstration of multiwavelength laser with a gain-clamped output amplifier”, Leos'98, Orlando, ThV2, 1998

[5] D. Van Thourhout, A. Van Hove, T. Van Caenegem, K. Vandeputte, P. Vandaele, I. Moerman, X. Leijtens, M.K.Smit, R.Baets, “Phased-Array multiwavelength laser using hybridly integrated PICs”, ECTC 2000, Las Vegas.

[6] D. Van Thourhout, T. Van Caenegem, R. Baets, "Optimising a multiwavelength laser design using an expert system based approach", IPR ‘98, Victoria, Canada

[7] D. Van Thourhout, T. Van Caenegem, L. Vanwassenhove, I. Moerman, P. Van Daele, R. Baets, "Realisation of multiwavelength Phased-Array laser by hybrid coupling of active and passive waveguide chips", Cleo Europe' 98, Glasgow, CWB2, Sep. 1998

[8] R. Baets and D. Van Thourhout, "Computer aided design for integrated optical circuits: task flow and tools", LEOS'97, San Fransisco, Dec. 1997

[9] B. Vanderhaegen, D. Van Thourhout, G. Sarlet, I. Moerman, L. Vanwassenhove, P. Van Daele, R. Baets, X. J. M. Leijtens, J. W. M. van Uffelen, M. K. Smit, "Loss measurements on InGaAsP ring resonator filters", ECIO'99, Torino, Italy, Apr. 1999.

[10] D. Van Thourhout, International laserworkshop 1997, Pitlochry, UK, Sep. 1997

[11] D. Van Thourhout, J. De Merlier, T. Van Caenegem, L. Vanwassenhove, C.G.P. Herben, X.J.M. Leijtens, J.W.M. van Uffelen, M.K. Smit, I.Moerman, P. Van Daele, R. Baets, 'Demonstration of phased-array laser with a gain-clamped output amplifier', 1998 IEEE/LEOS Benelux Chapter, Gent, pp. 249, Nov. 1998

[12] T. Van Caenegem, D. Van Thourhout, I. Moerman, P. Van Daele, R. Baets, P. Demeester, M. K. Smit, "Active-Passive integration by MOVPE Selective Area growth for multiwavelength lasers", 1997 IEEE/LEOS Benelux Chapter, Twente, 1997

[13] M. Zhao, D. Van Thourhout, G. Morthier, R. Baets, "Optimisation of SOA based transmitters for spectral slicing", 1999 IEEE/LEOS Benelux Chapter, Mons, Nov. 1999.

[14] D. Van Thourhout, J. De Merlier, T. Van Caenegem, L. Vanwassenhove, C.G.P. Herben, X.J.M. Leijtens, J.W.M. van Uffelen, M.K. Smit, I.Moerman, P. Van Daele, R. Baets, 'Demonstration of phased-array laser with a gain-clamped output amplifier', IEEE LEOS Benelux Workshop on integrated Optics, Brugge, 1998

6 References

[15] J. B. D. Soole, A. Sherer, H. P. Leblanc, N.C Andreadakis, R. Bhat, M. A. Koza, “Monolithic InP-based grating spectrometer for wavelength division multiplexed systems at 1.5 micron”, El. Lett., Vol. 27, 132-137, 1991

[16] C. Cremer, G. Ebbinghaus, G. Heise, R. Muller-Nawrath, M. Schienle, L. Stoll, “Grating spectrograph in InGaAsP/InP for dense wavelength division multiplexing”, Appl. Phys. Lett., Vol. 59, 627-629, 1991

[17] M. K. Smit, C. van Dam, “Phasar-based WDM-devices: principles, design and applications”, IEEE J. Sel. Topics Quant. Electron., Vol. 2, 236-250, 1996

[18] A. Himeno, K. Kato, T. Miya, “Silica-based planar lightwave circuits”, IEEE J. Sel. Topics Quant. Electron., Vol. 4, 913-924, 1998

[19] C. Dragone, “An N X N optical multiplexer using a planar arrangement of two star couplers”, IEEE PTL, Vol. 3, 812-815, 1991

[20] M. R. Amersfoot, “Phased-Array wavelength demultiplexers and their integration with photodetectors”, PhD. Thesis, Delft University of Technology, The Netherlands, 1994

[21] M. R. Paiam, R. I. MacDonald, “Design of phased-array wavelength division multiplexers using multimode interference couplers”, Applied Optics, Vol. 36, 5097-5108, 1997

[22] E. Pennings, G. Khoe, M. K. Smit, T. Staring, "Integrated-optic versus microoptic devices for fiber-optic telecommunication: a comparison", IEEE J. Sel. Topics Quant. Electron., Vol. 2, 151-164, 1996

[23] C. G. P. Herben, C. G. M. Vreeburg, X. J. M. Leijtens, H. Blok, F. H. Groen, I. Moerman, J. W. Pedersen, and M. K. Smit, "Chirping of a MMI-PHASAR Demultiplexer for application in Multiwavelength Lasers", IEEE PTL, Vol. 9, pp 1116-1118, 1997

[24] C. Zah, M. R. Amersfoort, B. N. Pathak, F. J. Favire, P. S. D. Lin, N. C. Andreakis, A. W. Rajhel, R. Bhat, C. Caneau, M. A. Koza, J. Gamelin, "Multiwavelength DFB laser arrays with integrated combiner and optical amplifier for WDM optical networks", IEEE JSTQE, Vol. 3, 584-597, 1997

[25] M. G. Young, U. Koren, B. I. Miller, M. A. Newkirk, M. Chien, M. Zirngibl, C. Dragone, B. Tell, H. M. Presby, G. Raybon, "A 16 x 1 Wavelength Division Multiplexer with integrated distributed bragg reflector lasers and electroabsorption modulators", IEEE PTL, Vol.. 8, pp 908-910, 1993

[26] S. Menezo, A. Talneau, F. Delorme, S. Grosmaire, F. Gaborit, S. Slempkes, "10-Wavelength 200-GHz channel spacing emitter integrating DBR lasers with a Phasar on InP for WDM applications", IEEE PTL, Vol.. 11, pp 785-787, 1999

[27] A. Talneau, M. Allovon, N. Bouadma, S. Slempkes, A. Ougazzaden, H. Nakajima, "Agile and fast switching monolithically integrated four wavelength selectable source at 1.55 um", IEEE PTL, Vol. 11, pp 12-14, 1999

[28] I. H. White, "A Multichannel Grating Cavity Laser for wavelength division multiplexing applications", IEEE JLT, Vol.. 9, pp 893-899, 1991

[29] K. O. Nyairo, I. H. White, C. J. Armistead, P.A. Kirkby, "Multiple channel signal generation using multichannel grating cavity laser with crosstalkcompensation", El. Lett., Vol.. 28, pp261-263, 1992

[30] P. A. Kirkby, "Multichannel Wavelength-switched transmitters and receivers-new component concepts for broad-band networks and distributed switching systems", IEEE JLT, Vol.. 8, 202-211, 1990

[31] J. B. D.Soole, K. R. Poguntke, A. Sherer, H. P. Leblanc, C. Chang-Hasnain, C. Caneau, R. Bhat, M. A. Koza, "Multistripe array grating integrated cavity (magic) laser: a new semiconductor laser for WDM applications", El. Lett., Vol.. 28, 1805-1807, 1992

[32] J. B. D. Soole, K. R. Poguntke, A. Sherer, H. P. Leblanc, C. Chang-Hasnain, C. Caneau, J. R. Hayes, R. Bhat, M. A. Koza, "Wavelength-selectable laser emission from a multistripe array grating integrated cavity laser", Appl. Phys. Lett., Vol.. 61, 2750-2752, 1992

[33] K. R. Poguntke, J. B. D. Soole, A. Sherer, H. P. Leblanc, C. Caneau, R. Bhat, M. A. Koza, "Simultaneous multiple wavelength operation of a multistripe array grating integrated cavity laser", Appl. Phys. Lett., Vol.. 62, pp 2024-2026, 1993

[34] M. Zirngibl, C. H. Joyner, L. W. Stulz, U. Koren, M.-D. Chien, M.G. Young, B. I. Miller, "Digitally tunable laser based on the integration of a waveguide grating multiplexer and an optical amplifier", IEEE PTL, Vol. 6, 516-518, 1994

[35] M. Zirngibl and C.H. Joyner, "High performance, 12 frequency optical multichannel controller", El. Lett, Vol. 30, 700-701, 1994

[36] C. R. Doerr, C. H. Joyner, L. W. Stulz, "Multifrequency laser with reduced intracavity wave mixing", IEEE PTL, Vol. 11, 635-637, 1999

[37] C. H. Joyner, C. R. Doerr, L. W. Stulz, J. C. Centanni, M. Zirngibl, "Low-Threshold Nine-Channel Waveguide grating router-based continuous wave transmitter", IEEE JLT, Vol. 17, 647-651, 1999

[38] A. A. M. Staring, L. H. Spiekman, J. J. Binsma, E. J. Jansen, T. van Dongen, P. J. A. Thijs, M. K. Smit, and B. H. Verbeek , "A compact nine-channel multiwavelength laser", IEEE PTL, Vol.. 8, pp. 1139-1141, 1996

[39] M. R. Amerfoort, J. B. D. Soole, C. Caneau, H. P. Leblanc, A. Rajhel, C. Youtsey, I. Adesida, "Compact arrayed waveguide grating multi-frequency laser using bulk active material", Ell. Let., Vol.. 33, pp 2124-2126, 1997

[40] M. Zirngibl, C. H. Joyner, C. R. Doerr, L. W. Stulz, H. M. Presby, "An 18-Channel Multifrequency Laser", IEEE PTL, Vol. 8, pp 870-872, 1996

[41] C. R. Doerr, M. Zirngibl, C. H. Joyner, L. W. Stulz, "Chirped waveguide grating router multifrequency laser with absolute wavelength control", IEEE PTL, Vol. 8, 1606-1608, 1996

[42] C. R. Doerr, M. Zirngibl, C. H. Joyner, "Single longitudinal-mode stability via wave mixing in long-cavity semiconductor lasers", IEEE PTL, Vol. 7, pp 962-964, 1995

[43] C. R. Doerr, C. H. Joyner, L. W. Stulz, J. C. Centanni, "Wavelength selectable laser with inherent wavelength and single-mode stability", IEEE PTL, Vol. 9, 1430-1432, 1997

[44] R. Monnard, C. R. Doerr, M. Zirngibl, C. H. Joyner, L. W. Stulz, "Direct modulation of a multifrequency laser up to 16 x 622 Mbit/s", IEEE PTL, Vol. 9, 815-817, 1997

[45] R. Monnard, A. K. Srivastava, C. R. Doerr, M. Zirngibl, C. H. Joyner, L. W. Stulz, Y. Sun, J. W. Sulhoff, J. L. Zyskind, C. Wolf, "16-channel 50 GHz channel spacing long-haul transmitter for DWDM systems", El. Lett, Vol. 34, 765-767, 1998

[46] C. R. Doerr et al. , "Elimination of signal distortion and crosstalk from carrier density changes in the shared semiconductor amplifier of multifrequency signal sources", IEEE PTL, Vol. 7, pp. 1131-1133, 1995

[47] R. Monnard, C. R. Doerr, M. Zirngibl, C. H. Joyner, L. W. Stulz, "Demonstration of an eight-wavelenght fast packet switching transmitter of 2.5 Gbit/s stream", IEEE PTL, Vol. 10, 430-432, 1998

[48] R. Monnard, C. R. Doerr, M. Zirngibl, C. H. Joyner, L. W. Stulz, "Demonstration of an eight-wavelenght fast packet switching transmitter of 2.5 Gbit/s stream", IEEE PTL, Vol. 10, 430-432, 19 98

[49] C. R. Doerr, C. H. Joyner, L. W. Stulz, "40-wavelength rapidly digitally tunable laser", IEEE PTL, Vol. 11, 1348-1350, 1999

[50] E. J. Murphy, "Integrated optical circuits and components", Marcel Dekker Inc., New York, 1999

[51] T. Van Caenegem, I. Moerman, P. Demeester, "Selective area growth on planar masked InP substrates by metal organic vapour phase epitaxy (MOVPE)", Prog. Crystal Growth and Charact., Vol. 35, 263-288, 1997

[52] O. Kayser, "Selective growth of InP/GaInAs in LP-MOVPE and MOMBE/CBE", J. Crystal Growth, Vol. 107, 989, 1991

[53] M. Aoki, M. Suzuki, T. Taniwatari, H. Sano, T. Kawano, "New photonic device integration by selective-area MOVPE and its application to optical modulator / laser integration", Microwave and Optical Technology Letters, Vol. 7, No. 3, 1994

[54] T. Takeuchi, T. Sasaki, M. Hayashi, K. Hamamoto et al , "A Transceiver PIC for Bi-directional Optical Communication Fabricated by Bandgap Energy Controlled Selective MOVPE", IEEE PTL, Vol. 8, March 1996

[55] C. H. Joyner, M. Zirngibl, J. P. Meester, "A multifrequency waveguide grating laser by selective area epitaxy", IEEE PTL, Vol. 6, 1277-1279, Nov 94

[56] C. H. Joyner, S. Chandrasekhar, J. W. Sulhoff, A. G. Dentai, "Extremelylarge band gap shifts for MQW structures by selective epitaxy on SiO2 masked substrates", IEEE PTL, Vol. 4, 1006-1009, 1992

[57] P. J. Harmsma, C. A. Verschuren, M. R. Leys, H. Vonk, Y.S. Oei, "Phased-Array multi-wavelength lasers fabricated using selective area chemical beam epitaxy", 1999 IEEE/LEOS Symposium Benelux Chapter Symposium, Mons, Belgium.

[58] D. Van Thourhout, T. Van Caenegem, I. Moerman, R. Baets, X. J. M. Leijtens, M. K. Smit, "Report on Phased-Array laser fabrication and performance", ACTS - BLISS Deliverable D025, 1998

CHAPTER 2

COMPUTER AIDED DESIGN TOOLS FOR INTEGRATED PHOTONIC CIRCUITS

Chapter 2

Computer aided design tools for integrated photonic circuits

This chapter is intended to provide a review of computer aided design tools for integrated photonic circuits as they are used today. In section 1, the general design procedure for photonic integrated circuits (PIC) that is commonly applied today is discussed. In section 2, a review of the CAD-tools, which were used in the context of this work for the analysis of optical integrated components, is given[1]. In paragraph 2.1, (mode solvers) and 2.2 (BPM-algorithms) two types of CAD-tools for passive devices are discussed, while in paragraph 2.3 two different tools for active devices are shortly introduced. Paragraph 2.4 provides a short summary of the material parameters we used for the simulations.

In section 3 of this chapter, we point out some of the weaknesses of today's available CAD-tools and propose an alternative, knowledge driven approach, where the emphasis is no longer on field calculation as such but rather on combining and manipulating previously obtained data. This idea is illustrated, using the design of a Phased-Array laser as an example.

Finally, in the last section of this chapter, the basic operation of Phased-Array demultiplexers is explained and we outline a procedure for designing multiplexers that are to be used in multi-wavelength lasers.

1 Design of photonic integrated circuits: task flow

The design of a complicated photonic integrated circuit (PIC) typically consists of a series of interrelated subtasks, as illustrated in Fig. 2-1. Starting from a functional description for the device, the designer will define a block diagram for the PIC[2] to be realised. Subsequently, based on his experience and intuition, he must define the type of component to be used for each block and choose a material system. Of course, the waveguide fabrication technology to be used will influence the choice of the components. For example, when designing a 50/50 splitter for a low index contrast waveguide fabrication technology such as silica-on-silicon or polymer waveguides, a Y-junction is an obvious choice. However, for high index contrast waveguides, a multimode interference coupler (MMI) would be the better choice. On the other hand, the type of components to be used may also determine the choice of the material system. If one, for example, decides to use a ring resonator for one of the sub-components, a

---

[1] Since our work covered a broad range of both active and passive devices, this will at the same time be a more or less complete review of today's available CAD-tools.

[2] PIC: a planar circuit integrating passive and/or active optical waveguide based components. Both monolithic and hybrid integration technologies are considered here.

very short bend radius is required so that only high index contrast waveguide fabrication technologies are suitable[1] in that case.

Once the material system is chosen and the subcomponents are defined, the designer has to put down numbers for all the parameters of the components. Sometimes this can be done using simple design rules obtained from previous experimental results or analytical formulas derived from theory. Often however, he will have to turn to numerical simulation tools.

Having quantified the components of the PIC, an overall analysis can be performed. If the specifications defined at the beginning of the design cycle are met, a mask can be generated and the fabrication can be started. Often, however, this is not immediately the case and one has to go backwards in the design cycle, adapting the quantitative definition of the subcomponents, the definition of the subcomponents themselves or even the functional specification for the PIC.

Following the device fabrication and characterisation, the obtained performance is compared with the original functional description. Depending on the outcome, one may accept the results as satisfactory or decide to start a new design procedure.

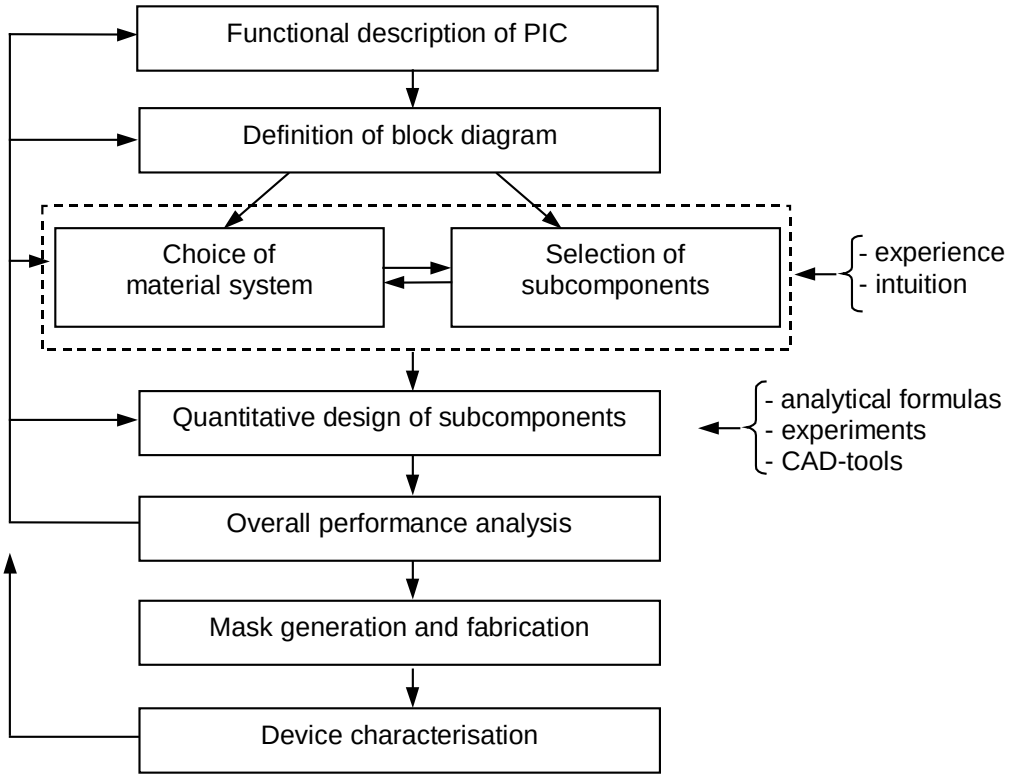

Fig. 2-1 Task flow of design procedure for PICs

In this development process, powerful design tools have become indispensable. For years now, they have been used for the quantitative design of devices at the "subcomponent" level:

[1] In practice, the available technologies typically depend on the environment where the designer works. This can pose limits to the definition of the block diagram or even to the functional specification of the PIC.

more or less simple components such as tapers, Y-junctions and facets. However, with the increasing complexity of PICs, also tools capable of analysing complete circuits become increasingly important, since they can reduce the number of iterations in the design procedure outlined above and may help to understand experimental results.

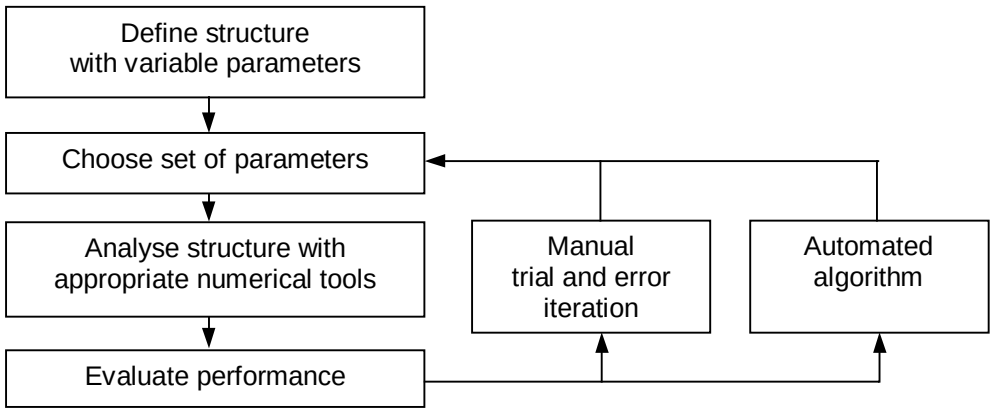

Fig. 2-2 Operating principle of a typical CAD-tool

The operating principle of most CAD-tools is similar and sketched in Fig. 2-2. Before analysing a component, its structure and parameters have to be defined symbolically, either graphically or textually. Next, one iterates through the parameter space, until the performance of the component meets the specifications. Using the currently available tools, this process is largely done by trial and error. Most CAD-tools provide the possibility to scan one or more variables but real optimisation procedures are almost never implemented. In literature there are some scattered examples of automated optimisation, based on optimal control theory [5][6], genetic algorithms [2] [4] or simulated annealing [3]. These statistical optimisation methods are particularly interesting in cases where the parameter space has many dimensions, because they provide a reasonable chance of finding a good design within a reasonable time.

A practical CAD-tool should at least incorporate the following properties:

- User friendly structure / layout definition
- Providing accurate results within a reasonable time
- Hiding underlying models and numerical algorithms for inexperienced users, however also providing accurate documentation and leaving enough flexibility for experienced users.
- Providing sensible suggestions for numerical parameters controlling the underlying algorithm (e.g. the propagation step or the reference index in BPM-packages) or controlling the numerical implementation (e.g. grid size for packages based on finite differences or finite elements).
- There is always a trade-off between calculation time and numerical accuracy. A user-friendly CAD-tool should provide means for easily determining the minimal numerical effort required (as determined by the grid-size, the calculation window, the number of slab modes…) to obtain a given accuracy level.
- Flexible output and input.

Although the underlying algorithms were mainly developed during the eighties, only since a few years reasonably user-friendly CAD-tools have become commercially available. Two main groups may be distinguished. The first one focuses on passive devices (although they may incorporate active elements such as heaters or electrodes). The most important underlying numerical routines are the beam propagation method, mode solvers and the coupled mode theory. Most packages only use one of these algorithms. However, some also combine them through an S-matrix approach [29][7]. The second group of CAD-tools focuses on active devices such as amplifiers and lasers. Often, they are limited to the design of a single laser cavity and do not allow for the design of complex cavity structures [31][32]. Some however are more flexible and allow for the simulation of such complex components as the Phased-Array multi-wavelength laser [46].

2 Design tools for the Analysis of Photonic integrated circuits

2.1 Optical mode solvers

Although optical modes solvers are primarily developed for finding the eigenmodes of longitudinal invariant waveguide structures, their application reaches much further. Some typical examples are shown in Fig. 2-3.

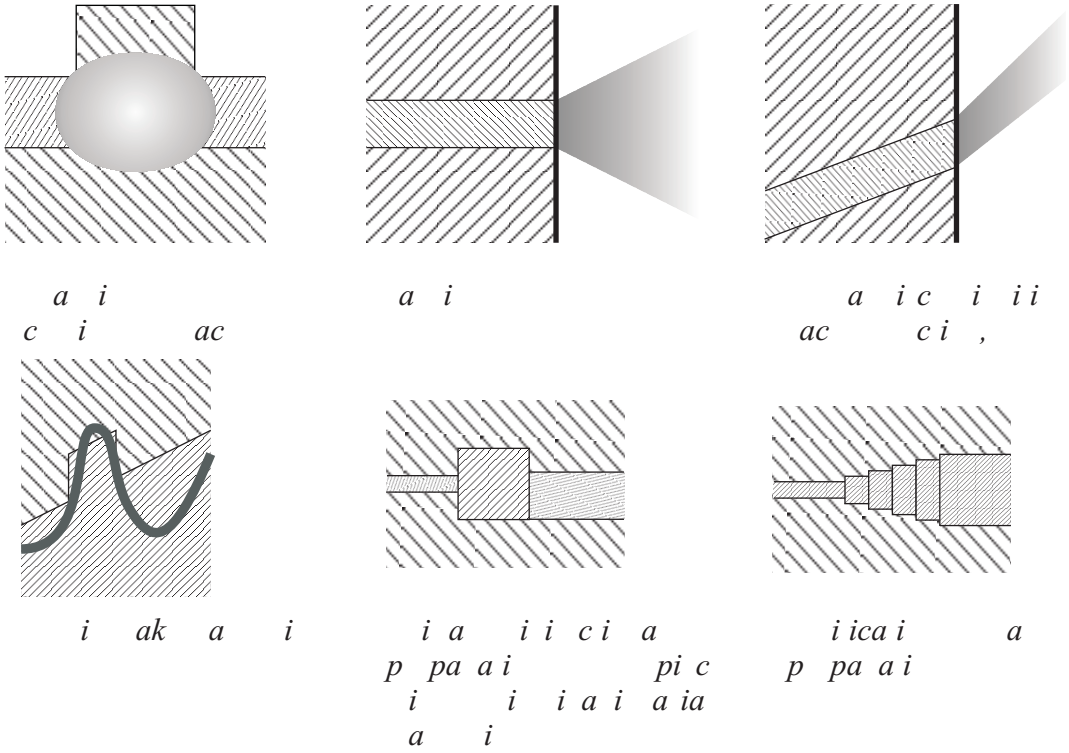

Fig. 2-3 Some typical applications of mode solvers

The simplest mode solvers are the so-called slab solvers, which calculate the modes of waveguides structure invariant in two directions. In the context of this work, two such solvers were used, *REMUS* [16] and *CEMUS* [17], both based on a scattering matrix approach

[9][10]. The first was developed for lossless waveguide structures, the second one can be used for layers having imaginary refractive indices. We extended *CEMUS* so that it also can be used for calculating radiation losses in leaky waveguides such as bends. For a long time, the 1D mode solvers have been the workhorse of the optical design engineer, mainly due to the success of the effective index method, which allows for easily reducing the 2D-crosssection of a real-world device to an equivalent 1D one and gives fairly accurate results (e.g. see [40]).

Until a few years ago, the rigorous 2D mode solvers were considered too slow for practical applications and only used for verification of the results obtained from approximate methods. Now, with the advent of much more powerful desktop computers and more sophisticated algorithms, also more rigorous, 2D mode solvers that can be used to analyse an optical component within a reasonable time period are available. Chiang [8] and later Vassallo [1] both have given a review of the algorithms that were developed during the last years. Following Vassallo, mode solvers can be classified into two groups, whether the unknown corresponds to the field within a two-dimensional domain (the global methods) or along a special line in the cross-section (the resonance methods).

Global methods include finite-element methods (FE), finite-difference methods (FD), global moment methods and integral methods. Generally, no specific analytic work is done and they usually lead to high rank systems, hence high requirements in memory and CPU-time.

The resonance methods on the other hand include the modal transverse resonance method or the mode matching method [11], the method of lines (MOL) [13] and the spectral index method [14]. From a comparative study, including all relevant algorithms, Vassallo concludes that the best results at the lowest computing cost are obtained by the resonance methods, using either a semi- or a full-vectorial algorithm. If a simple implementation is important, the MOL and FD methods are advantageous, the latter especially if the mode solver is part of a FD-BPM simulation. Again following Vassallo, it appears to be useless to implement a full-vectorial FE or FD method, unless one really needs the minor field components.

In the context of this work, we used a commercial 2D mode solver (*Fimmwave* [15]) based on a resonance method (film mode matching) [11][12]. The film mode matching method is one of the oldest numerical techniques used for the calculation of modal fields in dielectric waveguides and it is particularly useful for waveguides with a cross-section consisting of rectangular areas with constant refractive index. In fact, it can be regarded as an extension of the above-mentioned effective index method. For calculating the mode field, the waveguide cross-section is divided in horizontal slices. In each slice, the field is written as a superposition of the slab modes of that particular slice. At the interface between the slices, the tangential components of the field vectors have to be matched. From this matching procedure, an indirect eigenvalue problem for the propagation constant is formulated, which can be readily solved. The solver we used is able to handle waveguides with complex refractive index.

The film mode matching method can be employed for full-vectorial, semi-vectorial or scalar calculations. If only a limited number of modes are of interest, e.g. the lowest order guided modes, less numerical effort is required compared to FD- and FE-approaches. Moreover it is probably one of the most accurate methods available for waveguides that can be modelled by a number of rectangular waveguides and several authors have used values obtained in this way as a reference for comparing other methods.

In the following paragraphs, the most important applications of mode solvers are shortly introduced and some calculation examples, relevant for the remainder of this work, are provided.

2.1.1 Calculation of propagation constant

The most relevant information to be obtained from solving the eigenmode equations describing the optical problem are often the propagation constants (or the effective indices[1]) of the guided and radiating eigenmodes:

- From the propagation constants, we can determine the number of guided modes and whether a guide is monomodal or not.
- The imaginary part of the propagation constant of a waveguide with gain or loss gives information about the change of amplitude of a propagating mode.
- In tapered waveguides, the difference between the propagation constant of the first two even modes can give an idea of the minimal length for lossless operation [18].
- The optimal length of interferometric devices, such as MMI-couplers or directional couplers, is proportional to their coupling length. The coupling length of a directional coupler is given by $L_c = 1/(\beta_+ - \beta_-)$ with β_+ and β_- the propagation constants of the supermodes of the coupled waveguide. For an MMI-coupler the coupling length is given by $L_c = 1/(\beta_0 - \beta_1)$ with β_0 and β_1 the first two guided modes of the multimodal waveguide. In this context, it is interesting to note Fig. 2-6. This figure gives a comparison between propagation constants of a multimodal waveguide calculated using the effective index method, a semi-vectorial mode solver and a full-vectorial one. Although the difference between the effective indices calculated using the three methods is very small (< 0.02 %), the difference between the coupling length $L_c = 1/(\beta_0 - \beta_1)$ calculated from these results (Fig. 2-6b) can become larger than 5%.

As an example, we calculated the propagation constants of the waveguide depicted in Fig. 2-4. This type of waveguide was described already by several authors (e.g. see [35]) and was used for the passive part of the hybridly coupled PICs described in chapters 5 & 6. Fig. 2-5

---

[1] The relation between the propagation constant β and the effective index n_{eff} of a waveguide mode is given by $\beta = 2\pi\nu n_{eff}/c = 2\pi n_{eff}/\lambda_0$, with λ_0 the vacuum wavelength.

shows the propagation constants for the guided modes of this waveguide, as function of the waveguide width (Fig. 2-5a) for a fixed etching depth (100 nm into the quaternary layer) and as function of the etch depth (Fig. 2-5b) for a fixed width ($W = 2\mu m$). The horizontal line in the left picture denotes the effective index of the first guided TE slab mode in the region besides the ridge ($n = 3.258$). Below this index, the quasi TE modes of the 2D waveguide are no longer guided. The cut-off index for quasi-TM modes is lower ($n = 3.228$), however these modes become very broad for effective index values below the TE cut-off, making that the calculation of their propagation constant is influenced by the width of the calculation window (for this particular calculation, we used $W_b = 10\mu m$).

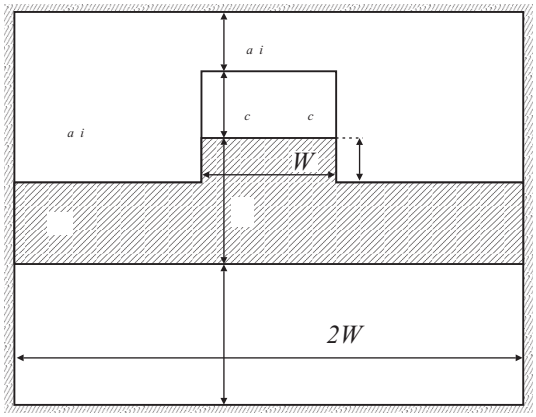

- $d_{sub} = 2\,\mu m$, $n_{sub} = 3.17$
- $d_f = 0.6\,\mu m$, $n_f = 3.395$
- $d_{cl} = 0.3\,\mu m$, $n_{clad} = 3.17$
- $d_{air} = 0.2\,\mu m$, $n_{air} = 1.0$
- t: the etching depth with respect to the top of the guiding layer[1]
- W: ridge width
- $2W_b$ width of calculation window
- The window can be surrounded with ideal electric or magnetic walls. Here, we used electric walls.

Fig. 2-4 Cross-section and calculation window of the waveguide used in this chapter for illustrating the properties of mode solvers.

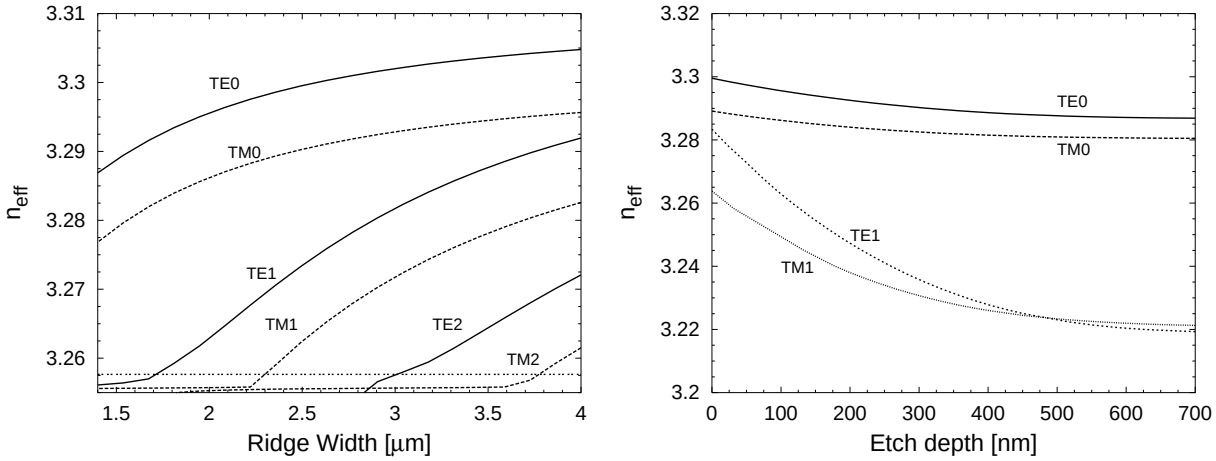

Fig. 2-5 Effective indices of the guided modes of a waveguide with the cross-section depicted in Fig. 2-4, as function of the ridge width W (etch depth 100 nm) (left) and as function of the etch depth ($W = 2\,\mu m$), calculated using a full-vectorial method.

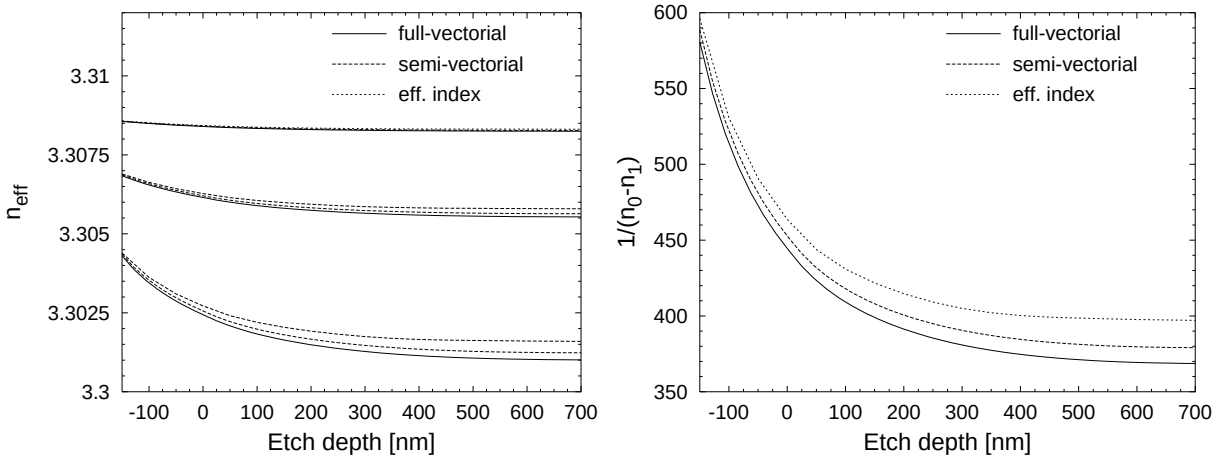

Fig. 2-6 a) Effective indices of the first three guided modes of a multimodal waveguide with the cross-section depicted in Fig. 2-4 ($W = 10\,\mu m$) versus the etch depth, calculated using a full-vectorial, a semi-vectorial and the effective index method. b) The coupling length $L_c = 1/(n_0 - n_1)$ calculated from the results shown in the left figure.

For investigating the convergence properties of the 2D mode solver, we calculated the effective index of the waveguide shown in Fig. 2-4 with etch depth $t = 100$ nm and width $W = 2\,\mu m$, for a varying number of transversal slab modes and varying dimensions of the calculation window. For comparing the results, it is useful to introduce a normalised propagation constant b defined by

$$b = \frac{n_{eff}^2 - n_{clad}^2}{n_{co}^2 - n_{clad}^2} \tag{2-1}$$

where n_{clad} and n_{co} are relevant refractive indices such that b varies between 0 and 1. We used $n_{clad} = 3.17$ and $n_{co} = 3.395$. The advantage of using the normalised propagation constant is that, while the first digits of the effective index n_{eff} are in most cases not relevant, all digits of the normalised propagation constant are significant. Vassallo [1] emphasises that so far, no method can claim to give b-values with more than 4 accurate digits (for some methods, even the fourth digit is sometimes not reliable). In Table 2-1, results for calculations where we varied the dimensions of the calculation window are summarised. For obtaining these, we used 200 slab modes. If we consider the value obtained for the largest box ($W_b = 4\,\mu m$, $d_{cl} = 2\,\mu m$) as the reference value (b_{exact}), we see that, except for the smallest box dimensions (#5 and #9), the b-values are identical up to at least 4 digits (and in most cases up to 5 digits). Also for the smallest substrate dimensions (#5, $d_{cl} = 1\,\mu m$), the b-value is accurate up to 2.10^{-4}. Only in the case for $W_b = 1\,\mu m$ the calculation window seems really to small to give accurate results. In Fig. 2-7b and Fig. 2-7c the difference between the calculated

[1] This convention is used throughout this work.

value for b and b_{exact} as function of respectively the cladding layer thickness and the width W_b is given.

In Fig. 2-7a the difference $(b - b_{exact})$ is given as function of the number of slab modes, for the cases indicated in bold in Table 2-1. From this figure it is obvious that using 30 slab modes is enough to obtain b-values accurate up to 2.10^{-4}, which is already better than most other types of mode solvers can obtain. Using 50 modes should give values accurate up to four digits. We expected the convergence speed to increase with decreasing cladding layer thickness. However, this is not really apparent from this picture.

	#	$d_{cl}[\mu m]$	$W_b[\mu m]$	n_{eff}	b
d_{cl} varied	**1**	**2**	**4**	**3.295569**	**0.549631**
	2	1.75	4	3.295569	0.549630
	3	**1.5**	**4**	**3.295568**	**0.549627**
	4	1.25	4	3.295564	0.549609
	5	**1**	**4**	**3.295538**	**0.549493**
W_b varied	6	1.75	4	3.295569	0.549630
	7	1.75	3	3.295569	0.549631
	8	**1.75**	**2**	**3.295571**	**0.549641**
	9	1.75	1	3.295701	0.550220

Table 2-1 Results from 2D mode solver convergence test. The value in the upper right corner is used for b_{exact}

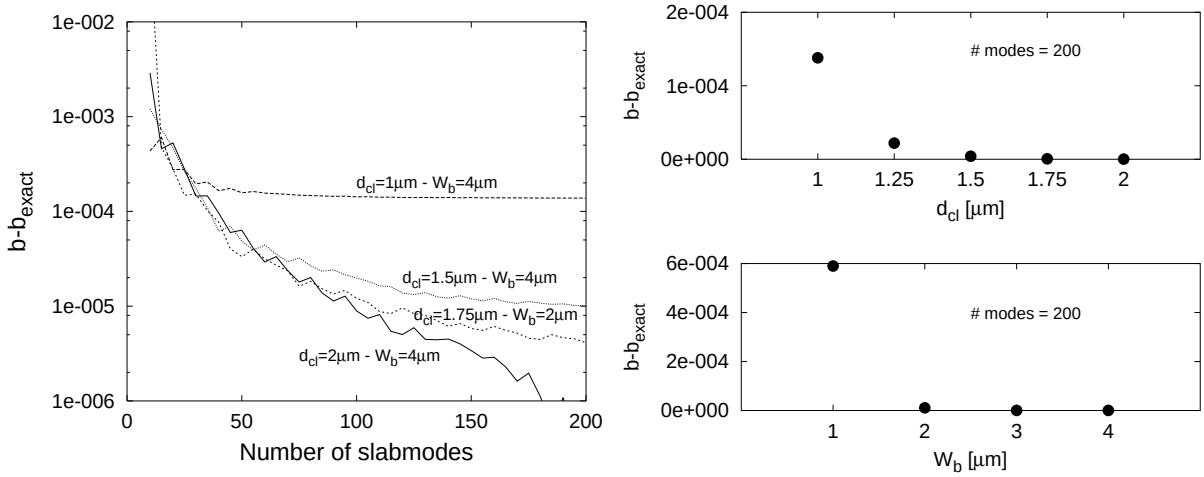

Fig. 2-7 Results from 2D mode solver convergence test

2.1.2 Calculation of the spatial distribution of the optical field

Sometimes, also the spatial distribution of the optical field in the waveguide can give relevant information about its operation in an integrated PIC. For example, the strength of the optical field at a waveguide-air interface can give an idea about the scattering loss to be ex-

pected. In leaky waveguides such as bends [35] or GaAs laser diodes [17][1], the spatial field distribution provides physical insight in radiation losses. At waveguide junctions, overlap integrals of the field distributions determine the transmission and reflection coefficients (see paragraph 2.1.3) and also the confinement factor (see paragraph 2.1.7) and the far field (see paragraph 2.1.5) are calculated from the near field distribution.

In most cases, only the transversal electric or magnetic field components are needed (for respectively quasi-TE and quasi-TM modes). Only in a limited number of cases, such as for polarisation converters, also the minor field components are important. As an illustration, Fig. 2-8 shows the field-components of the zeroth order quasi TE mode for the waveguide depicted in Fig. 2-4 with etch depth $t = 0.1\,\mu m$ and ridge width $W = 2\,\mu m$. These field profiles were calculated using 200 slab modes for every slice. Note the large discontinuity in E_x-field at the vertical interface (due to the boundary conditions). The E_y-field is negligible, except at the corner where the field diverges as was already noted in [42].

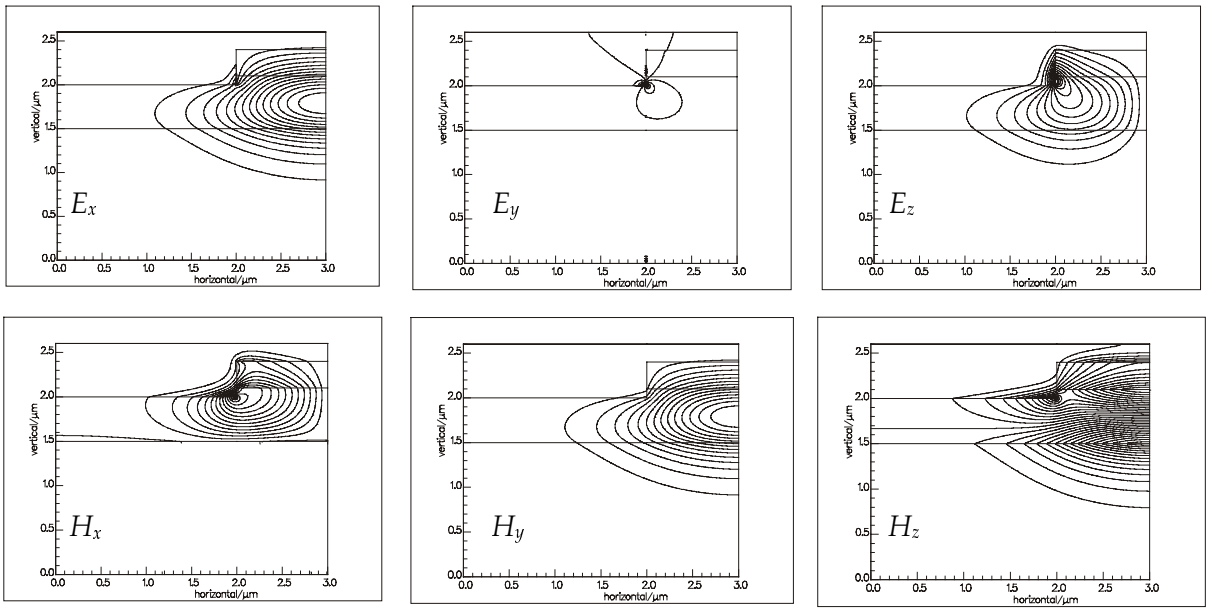

Fig. 2-8 Field components for the waveguide depicted in Fig. 2-4, with $W = 2\,\mu m$ and $t = 0.1\,\mu m$

2.1.3 Coupling efficiency at a waveguide junction

In a photonic IC, transitions between waveguides with dissimilar cross-sections occur frequently. Examples are the transition between a buried and a ridge waveguide at an active/passive interface, the coupling between a small, monomodal waveguide and a broader one at the entrance of an MMI-coupler or the transition from a semiconductor waveguide to an optical fibre. To optimise these junctions, one needs to be able to calculate the transmis-

[1] The refractive index of the GaAs substrate is higher than or equal to that of the layers which are used for fabricating the waveguide itself.

sion efficiency between the modes of both waveguides. In many cases one also wants to know the reflected power, since the latter may, for example, alter the operation conditions of active devices. Here we first explain a well-known rigorous approach to model a waveguide junction, based on an eigenmode expansion, and subsequently two approximate methods, for which only the lowest order guided modes have to be determined and which were investigated in the context of this work.

Rigorous approach

Consider a vertical junction between two optical waveguides. Due to the difference between both waveguides, part of the field will be reflected and part will be transmitted. Both the reflected and transmitted field may be represented by a superposition of all the guided modes and a set of radiation modes. The latter may be discretised by introducing electric or magnetic walls alongside the structure. The expansion coefficients obtained from this procedure determine the amount of power carried by each mode. They can be determined by expressing the continuity relations for the electric and magnetic field at the interface. If we restrict ourselves to the 1D-case, these are given by:

$$\begin{aligned} \sum_i \tau_i^1 \psi_i^1 + \sum_i \rho_i^1 \psi_i^1 &= \sum_i \tau_i^2 \psi_i^2 \\ r^1 \sum_i \beta_i^1 \tau_i^1 \psi_i^1 - r^1 \sum_i \beta_i^1 \rho_i^1 \psi_i^1 &= r^2 \sum_i \beta_i^2 \tau_i^2 \psi_i^2 \end{aligned} \tag{2-2}$$

ψ_i being the transversal field component of the *i*-th mode, τ_i^1 and ρ_i^1 the amplitudes of respectively the incident and reflected fields in the first section and τ_i^2 the amplitudes of the transmitted field components. The coefficients *r* are given by $r = 1$ for TE-polarised modes and $r = n^{-2}(x)$ for TM-polarised modes.

If we define

$$c_{ij}^{\alpha\beta} = \int r^{\alpha} \psi_i^{\alpha} \psi_j^{\beta} dx \tag{2-3}$$

and use the orthogonality relation

$$c_{ij}^{\alpha\alpha} = \delta_{ij} \tag{2-4}$$

equations (2-2) may be transformed to a set of 2*N* linear equations:

$$\begin{aligned} \tau_j^2 - \sum_i c_{ji}^{21} \rho_i^1 &= \sum_i c_{ji}^{21} \tau_i^1 \qquad j = 0,1,\ldots N-1 \\ \beta_j^2 \tau_j^2 + \sum_i \beta_i^1 \rho_i^1 c_{ij}^{12} &= \sum_i \beta_i^1 \tau_i^1 c_{ij}^{12} \qquad j = 0,1,\ldots N-1 \end{aligned} \tag{2-5}$$

Since there are also 2*N* unknowns (the amplitude coefficients τ_i^1 of the incident field are supposed to be known), these equations may be readily solved using standard matrix manipulation routines. This formalism may easily be extended to the calculation of the facet reflectivity of a waveguide by replacing the second waveguide by a homogenous half space [17].

The modes in this half space are again obtained by introducing electric walls alongside the structure.

Although the procedure outlined above is straightforward, the problem is that (2-2) is only strictly valid for N, the number of modes, going to infinity. In practice, of course, one has to limit N to a finite value. However, to obtain a convergent solution the required value for N may become very large, especially if the method is extended to 2D-waveguides.

Approximate solutions

Because the rigorous calculation can be quite lengthy, one often simply uses the overlap integrals $c_{0j}^{\alpha\beta}$ to approximate the transmission from the zeroth order mode of the first waveguide to the eigenmodes of the second waveguide. However, such an approach gives no information about the reflected field and in cases where the index contrast between both waveguides is large, the deviation with the results obtained from the rigorous calculation may become important. Therefore, we investigated two alternative options, which give a better approximation but require no more numerical effort than calculating the overlap integral.

The first approximation is based on the set of equations (2-5). If we suppose that the coupling to higher order modes is negligible and solve these equations for N=1, the following values are obtained for the reflection and transmission coefficients of the fundamental mode:

$$\begin{aligned} \rho^1 &= \frac{\beta^1 c^{12} - \beta^2 c^{21}}{\beta^1 c^{12} + \beta^2 c^{21}} \tau^1 \\ \tau^2 &= \frac{2\beta^1 c^{12} c^{21}}{\beta^1 c^{12} + \beta^2 c^{21}} \tau^1 \end{aligned} \qquad \text{(2-6)}$$

(To simplify the notation, the subscripts denoting the mode number are left away). For TE-modes we have $c^{12} = c^{21}$, yielding:

$$\begin{aligned} \rho^1 &= \frac{\beta^1 - \beta^2}{\beta^1 + \beta^2} \tau^1 \\ \tau^2 &= \frac{2\beta^1}{\beta^1 + \beta^2} c^{12} \tau^1 \end{aligned} \qquad \text{(2-7)}$$

For uniform media, these equations reduce to the well-known Fresnel coefficients. The power carried by an optical mode in the longitudinal direction is proportional to the product of its propagation coefficient with the square of the amplitude coefficient ($P_{i,z} \sim \beta_i |\tau_i|^2$), so the reflection and transmission coefficients are respectively given by:

$$R = \left(\frac{\beta^1 - \beta^2}{\beta^1 + \beta^2} \right)^2$$
$$T = \frac{4\beta^1\beta^2}{\left(\beta^1 + \beta^2\right)^2} \left(c^{12}\right)^2 \tag{2-8}$$

The second approximation was first proposed by D. Gallagher [19] and is based on an adapted overlap integral calculation (we restrict ourselves further to the TE-case):

$$\chi_{ij}^{12} = \int t_{fr}(x) \psi_i^1 \psi_j^2 dx$$
$$\chi_{ij}^{11} = \int r_{fr}(x) \psi_i^1 \psi_j^1 dx \tag{2-9}$$

The first equation is used for calculating the transmitted power, the second one for the reflected power. For the *x*-dependent coefficients $t_{fr}(x)$ and $r_{fr}(x)$ two alternative expressions were employed, respectively called the normal and the oblique Fresnel approximation:

- *Normal Fresnel*:

$$t_{fr} = \frac{2n^1(x)}{n^1(x) + n^2(x)}$$
$$r_{fr} = \frac{n^1(x) - n^2(x)}{n^1(x) + n^2(x)} \tag{2-10}$$

with $n^\alpha(x)$ the local refractive index of the waveguides.

- *Oblique Fresnel:*

$$t_{fr} = \frac{2\beta^1}{\beta^1 + \beta^{2'}(x)}$$
$$r_{fr} = \frac{\beta^1 - \beta^{2'}(x)}{\beta^1 + \beta^{2'}(x)} \tag{2-11}$$

$\beta^{2'}(x)$ is an alternative *x*-dependent propagation coefficient (see Fig. 2-9), calculated based on the requirement that the transversal component of the *k*-vector is constant in each layer:

$$\left(\beta^{2'}(x)\right)^2 = \left(k_0 n^2(x)\right)^2 - \left(k_0 n^x(x)\right)^2$$

with (2-12)

$$\left(k_0 n^x(x)\right)^2 = \left(k_0 n^1(x)\right)^2 - \left(\beta^1\right)^2$$

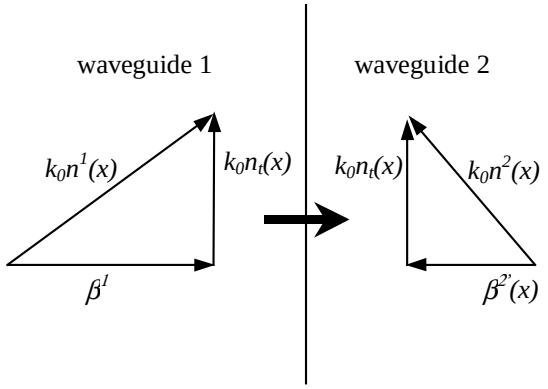

Fig. 2-9 Determination of $\beta^{2'}(x)$ for the oblique Fresnel formula

Using the alternative overlap integrals (2-9), the reflected and transmitted power is respectively calculated as $R=\left(\chi_{ij}^{11}\right)^2$ and $T=\frac{\beta^2}{\beta^1}\left(\chi_{ij}^{12}\right)^2$.

To verify the validity of these formulas, we compared them to results obtained from rigorous calculations, for some typical waveguide structures depicted in Fig. 2-10.

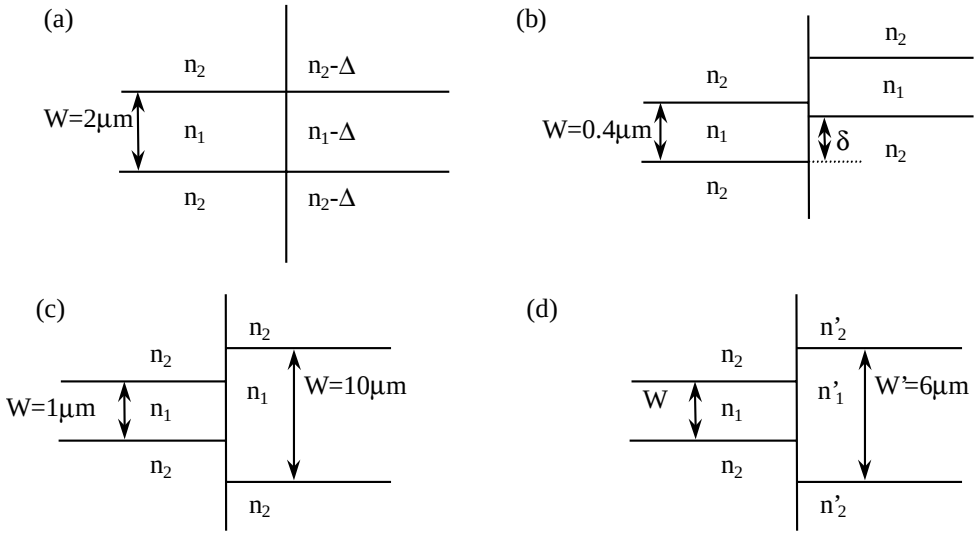

Fig. 2-10 Waveguide junctions for the diverse examples described in this paragraph.

The waveguide junction used for the first example is shown in Fig. 2-10a. The refractive indices were given by $n_1=3.3$ and $n_2=3.2$. Δ was varied from zero to 2.75 and the wavelength was set at $\lambda=1.55\,\mu m$. The results are shown in Fig. 2-11. As one may see, the simple overlap integral gives no good approximation for the transmitted power. However, the approximate results obtained from equations (2-8) and (2-9) are very close to the rigorous solution for which a minimum of 80 eigenmodes per section were used. Fig. 2-11b shows results from an analogous calculation with the refractive index of the cladding layers set at $n_2=1$.

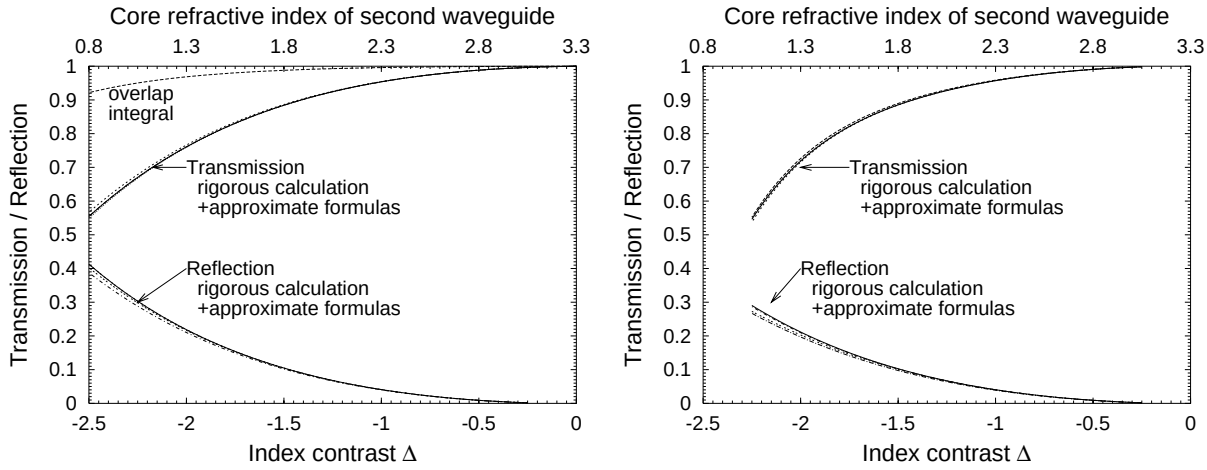

Fig. 2-11 Results for the example of Fig. 2-10a.

The second example is taken from [20] and shown in Fig. 2-10b. In this case, the transmission between two identical waveguides with a lateral offset was calculated. The refractive indices were given by $n_1 = 3.2071$ and $n_2 = 1$. The wavelength was 1.31 μm. Due to the high index contrast between the semiconductor waveguide and the air cladding, it is obvious that the reflection at the junction will be important for large offsets. However, since both waveguides have the same propagation coefficient, the reflection coefficient cannot be calculated using the first alternative formula (2-8), which simply reduces to the classical overlap integral in this case. Fig. 2-12 shows a comparison between the rigorous calculation, the overlap integration and the adapted overlap calculation using the normal Fresnel coefficients given by (2-10). The results obtained for the exact calculation agree well with those presented in [20]. For large offsets, the return loss saturates to a constant value corresponding to the case of an abrupt waveguide termination. From the difference between the exact curve for the return loss, and the adapted overlap calculation, it is obvious that the latter will not be useful for calculating facet reflectivity of a waveguide with an acceptable accuracy.

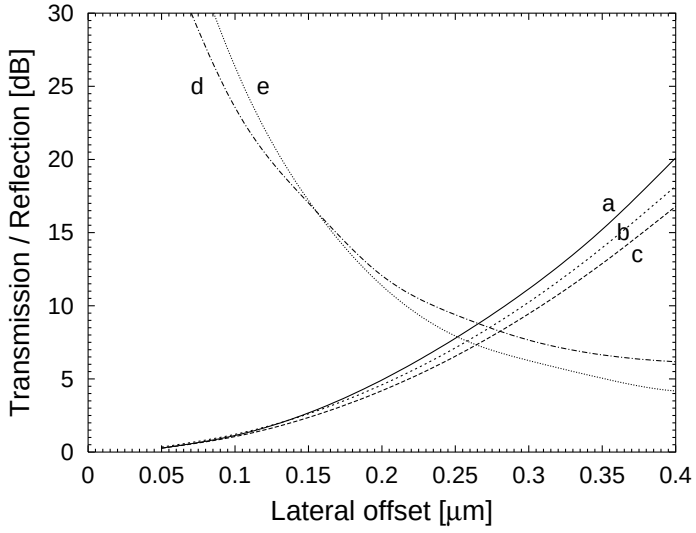

Fig. 2-12 Coupling loss and return loss for the example of Fig. 2-10b: rigorous calculation (a+e), results from the "normal Fresnel" calculation (b+d) and the overlap calculation (c)

The third example is a junction between a monomodal and a multimodal waveguide, which is typical for an MMI-coupler (Fig. 2-10c). The refractive indices were set at $n_1 = 3.25$ and $n_2 = 3.2$, the wavelength at $1.55\,\mu m$. The results are shown in Fig. 2-13. As expected, the coupling to the asymmetric modes is negligible. For the other modes, the difference between the approximate and the rigorous results is very small. Also the standard overlap integral gives a good approximation.

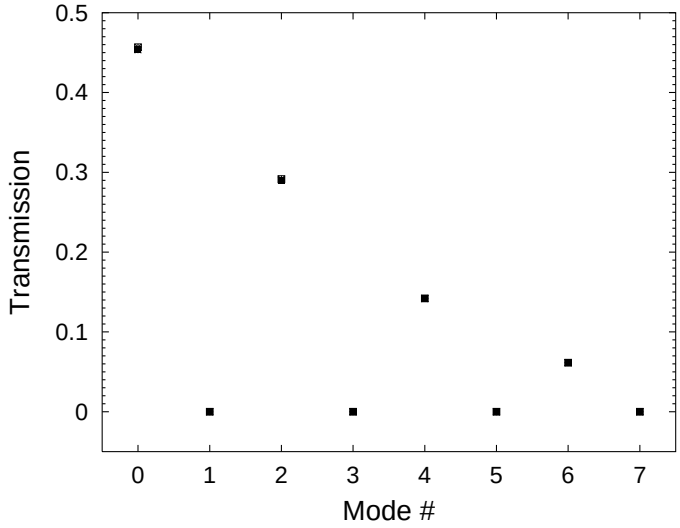

Fig. 2-13 Transmission between monomodal and multimodal waveguide, calculated using the rigorous method and the approximated formulas. The difference between those methods is not visible.

The last example (Fig. 2-10d) models the coupling between a laser diode and an optical fibre. The core and cladding refractive indices of the first waveguide were $n_1 = 3.23$ and $n_2 = 3.2071$. The width was varied from $W = 0.05\,\mu m$ to $W = 0.40\,\mu m$. The width of the second waveguide was $6\,\mu m$ and its refractive indices were $n'_1 = 1.4619$ and $n'_2 = 1.4572$ respectively. The wavelength was $1.31\,\mu m$. The results are shown in Fig. 2-14. As expected, there is a clear optimum in the curve for the transmission (around $W = 0.19\,\mu m$). The overlap integral without the correction for the Fresnel losses overestimates the transmission considerably. The reflected power is rather independent of the width of the laser diode. Note that the other approximated formulas again give a very good estimation for the transmission coefficient.

From these examples, it is obvious that the approximate formulas for calculating the transmission and reflection at an optical waveguide junction give good results in most practical cases. The calculations shown here were performed for the TE case but we obtained analogous results for the TM case. Based on these results, the adapted overlap integrals (2-9) were extended to the 2-dimensional case and incorporated in Fimmprop3D [15], a commercial CAD-package that calculates the transmission through piecewise constant waveguides.

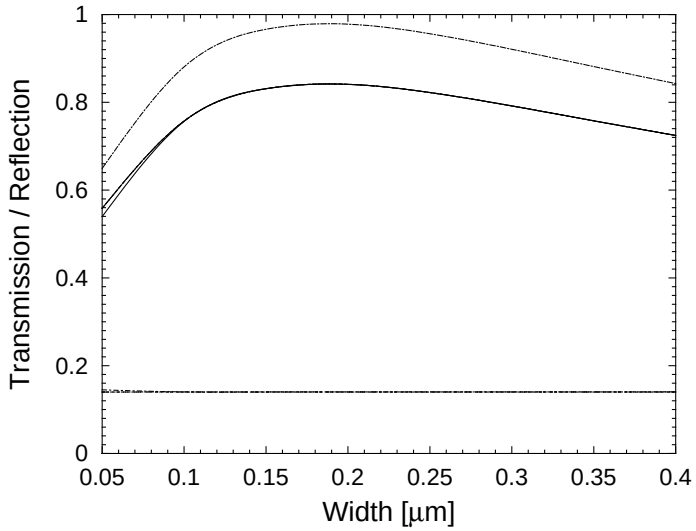

Fig. 2-14 Coupling between laser diode and optical fibre (Fig. 2-10d)

2.1.4 Reflection from tilted end mirror

To realise the hybrid Phased-Array laser (chapters 5 & 6), amplifiers with very low facet reflectivity ($R < 10^{-4}$) are needed. To obtain such values using only an AR-coating, very tight control of the layer thickness and refractive index is required. Moreover, an AR-coating reduces the reflectivity only over a limited wavelength range. An alternative approach is to use a slanted-facet structure: angling the facet prevents reflected light from coupling back in the waveguide, providing an inherently broadband reduction in facet reflectivity.

To calculate the residual reflection from a tilted waveguide facet, we used an approach original proposed by Marcuse [21] for three-layer slab waveguides and illustrated in Fig. 2-15. For a perfectly reflecting mirror, the problem of finding the reflection coefficient of a guided mode that turns back on itself (wave A to C) is equivalent to the problem of computing the tilt loss for a waveguide with angle 2θ (wave A to C'). In that case, the loss is caused by a misalignment of the phase fronts. This effect may be accounted for by multiplying the incident field by a phase factor $\exp(-j2\theta\beta x)$, with β the propagation constant of the guided mode and x the transversal co-ordinate along the facet, and overlapping the resulting field with the field of the outgoing waveguide. Therefore, the power in wave C is proportional to:

$$\int \exp(-j2\theta\beta x)\left|\psi(x)\right|^2 dx \qquad (2\text{-}13)$$

For a mirror with finite reflectivity, the tilt loss must be multiplied by the Fresnel reflection loss, to obtain the real residual reflection. We extended this approach to 2D waveguides, using field profiles calculated by Fimmwave.

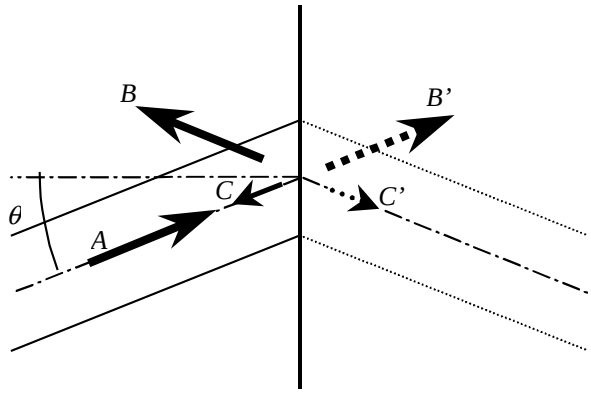

Fig. 2-15 Calculation of residual reflection of waveguide with tilted end facet.

Using this approach, we calculated the reflection coefficient as function of the angle θ with respect to the facet, for a buried waveguide as shown in the inset of Fig. 2-16a & b. In the left picture the core refractive index n_2 was varied from 3.25 to 3.37, in the right picture we varied the width of the waveguide from 2.0 μm to 4.5 μm. The reflection coefficient increases with increasing core refractive index and with decreasing waveguide width. In both cases, this originates from an increasing far field angle.

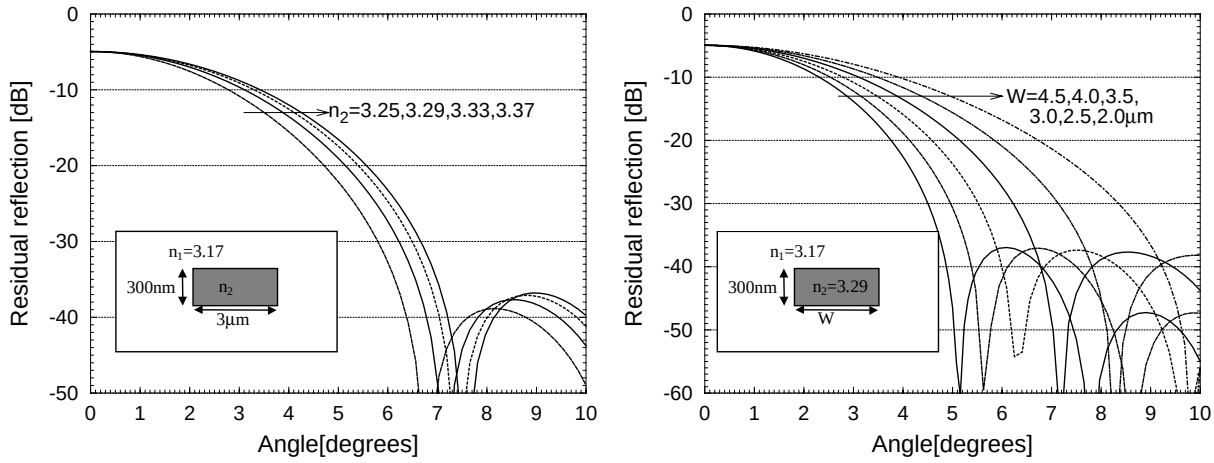

Fig. 2-16 Calculated reflection coefficient for the buried waveguide shown in the inset. In the left picture, the core refractive index was varied, for the right picture, we varied the waveguide width.

2.1.5 Far field calculations

Mode solvers may also be used to calculate the far field of a waveguide. A commonly used approach is to expand the field at the interface into its plane-wave spectrum. Subsequently, the transmission and reflection of each plane wave at the interface is calculated, using the Fresnel coefficients. The propagation of the plane waves is trivial, since they are eigenmodes of the homogeneous space. When calculating the far field in this way, one supposes that the mode conversion at the facet is negligible. Using the mode expansion algorithm of paragraph 2.1.3, the far field can be calculated more rigorously. The latter was implemented for

slab waveguides by Haes [17]. *Fimmwave* uses the plane-wave expansion for calculating the far field of a waveguide, taking into account the mixing of the field components.

Knowledge of the far field properties may be very important for a number of practical applications such as optical recording or laser to fibre coupling. In the context of this work, far field calculations were used to estimate the transition loss between two hybridly coupled waveguides (see chapter 4).

2.1.6 Calculation of bend loss

Calculating the radiation losses of a curved optical waveguide is another important application of mode solvers. One of the most well known techniques developed for this purpose is the conformal transformation method as described in [22]. In a first step, the effective index method is employed to reduce the three dimensional problem to a two dimensional one. Subsequently, the curved waveguide is transformed into an equivalent straight one with a transformed index profile (Fig. 2-17, a → b). By using a staircase approximation (Fig. 2-17, b → c), this problem may be readily solved using a slab solver capable of handling leaky waveguides. We extended *CEMUS* so that it can calculate the radiation loss and mode profiles of curved optical waveguides with varying bend radius or index contrast. As an illustration, Fig. 2-18 shows the radiation loss versus bend radius for a $2\,\mu m$ wide slab waveguide. The wavelength was $1.55\,\mu m$, the refractive index of the cladding layers n_2 = 3.17, and the core refractive index n_1 was varied from 3.19 to 3.28.

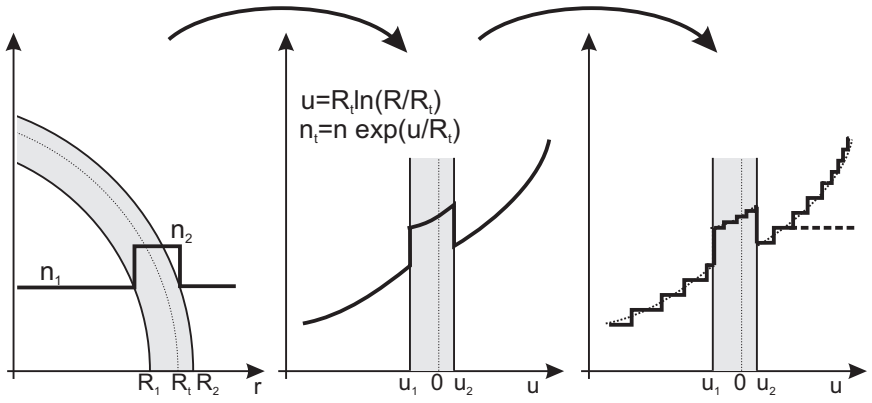

Fig. 2-17 Conformal transformation and staircase approximation for curved optical waveguides. The dashed line in the rightmost picture indicates a further approximation that can be made for calculating the optical mode profile using a real optical mode solver (see below).

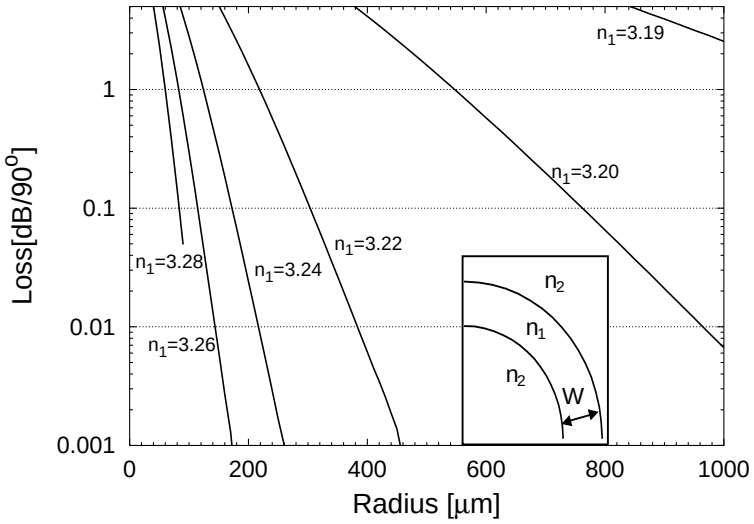

Fig. 2-18 Loss of curved slab waveguide as function of bend radius ($W = 2\,\mu m$, n_2 =3.17, $\lambda = 1.55\,\mu m$, TM polarisation)

In Fig. 2-19a a contour plot of the radiation loss versus the refractive index contrast $(1-n_2^2/n_1^2)$ and the normalised radius of curvature $k_0 R n_1$ is shown. In addition, the index contrast for some typical waveguide structures is indicated. A and B are for the waveguide of Fig. 2-4 with the etching depth respectively equal to $t = 0\,\mu m$ and $t = 0.1\,\mu m$. For these waveguides, the effective index of the central slab is given by $n_1 = 3.312$. C is for a buried waveguide with core refractive index 3.395 (Q1.3) surrounded with InP ($n = 3.17$). This waveguide has a central slab effective index $n_1 = 3.245$.

Note that the small region marked by the contour lines is the region which is interesting for integrated optics: in the upper right corner the loss goes to zero but the radius becomes very large while in the opposite corner, the radius goes to zero but the loss goes to infinity

The straightness of the contour lines may be used to obtain a useful interpolation. They can be approximated linearly by:

$$\log\left(1-\frac{n_2^2}{n_1^2}\right) = -A\log(k_0 R n_1) + B(\alpha) \tag{2-14}$$

or

$$k_0 R n_1 \left(1-\frac{n_2^2}{n_1^2}\right)^{\gamma} = C(\alpha) \tag{2-15}$$

Since all contour lines are approximately parallel, γ is constant. The dependence of $C(\alpha)$ on α is shown in Fig. 2-19b. For loss values typically employed in today's PICs (< 0.1 dB/90°), this curve too can be approximated by a straight line:

$$C(\alpha) = C_1 - C_2 \log\left(\frac{\alpha}{1dB/90^o}\right) \tag{2-16}$$

This approach was first proposed by Pennings [23] for whispering gallery modes[1]. He obtained the following values for the constants in equations (2-15) and (2-16): γ =1.54, C_1=13.7 and C_2 =3.72. From the contour lines in Fig. 2-18 for 2 μm wide waveguides we obtained the values: γ =1.73, C_1=7.14 and C_2 =2.58[2]. These values were calculated for TM polarisation (implying quasi TE polarised 2D modes in the effective index approximation).

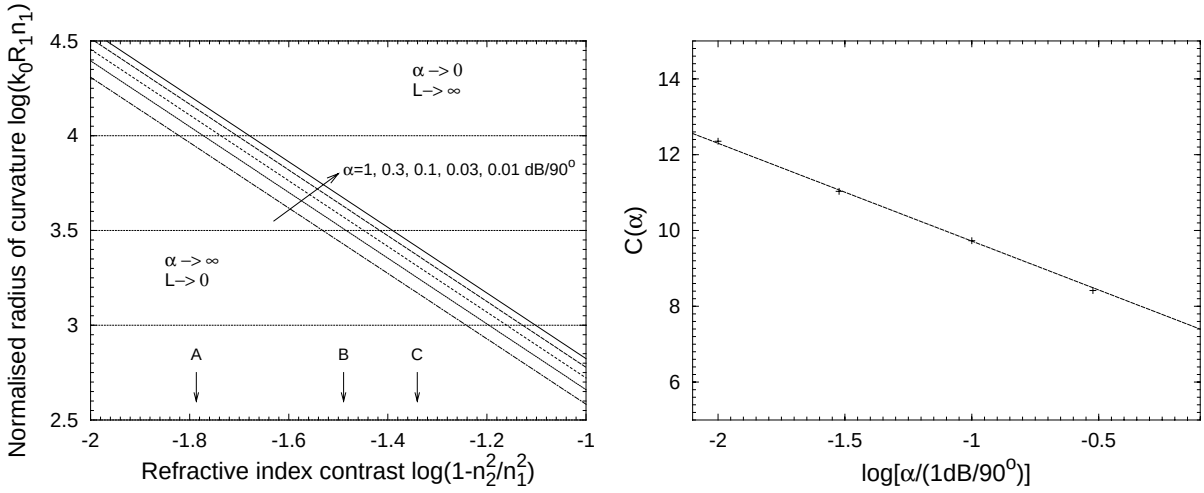

Fig. 2-19 a) Contour plot of the radiation losses versus the refractive index contrast and the normalised radius of curvature for a 2 μm wide waveguide. b) The constant $C(\alpha)$ from eq. (2-15) as obtained from the results in Fig. 2-18. The straight line is fitted using a least-square procedure.

The optical field in a curved waveguide is narrower than the field in an equivalent straight waveguide and its centre is shifted towards the outer edge [23]. This effect will cause an additional loss at the junction between the straight and the curved waveguides, next to the radiation losses. To reduce this transition loss as much as possible, one typically applies an offset between the centres of the curved and the straight waveguides and often the width of the latter is adapted. For easily calculating the optimal offset and waveguide width, the staircase approximation may be cut off in such a way that the transformed index profile does not exceed the effective index of the waveguide, as indicated by the dashed line in Fig. 2-17c. The eigenmodes of this waveguide may be calculated using a real slab mode solver and resemble very well the actual waveguide modes of the curved waveguide as shown in Fig. 2-19b.

---

[1] In waveguides with sufficiently small bending radius, the field strength at the inner edge vanishes and the mode is fully guided by the outer edge. Such a mode is called a Whispering Gallery Mode.

[2] One has to be careful when employing this values. While the values obtained by Pennings in [23] are wavelength independent, our values are only valid for λ =1.55 μm .

A completely normalised approach to calculate the optimal offset and the radiation losses for whispering gallery modes is given in [24].

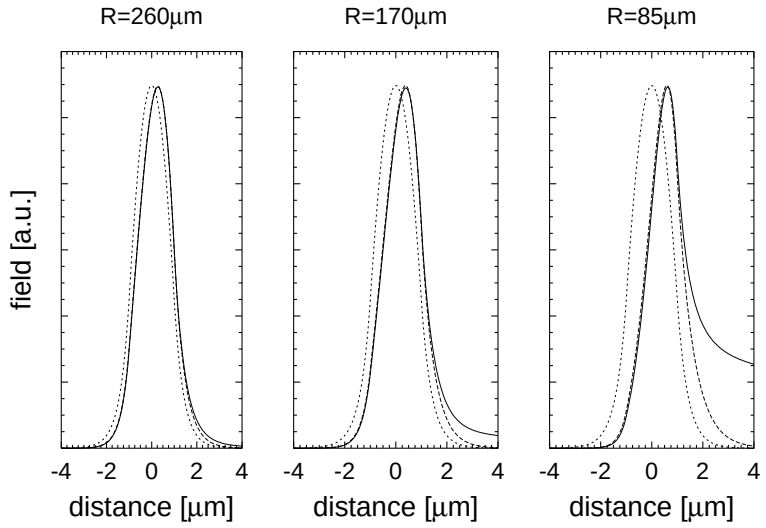

Fig. 2-20 Fundamental mode of a curved waveguide, calculated from the exact refractive index profile using a complex mode solver and from the approximated index profile using a real mode solver ($W = 2\,\mu m$, n_1=3.24, n_2=3.17, $\lambda = 1.55\,\mu m$). For reference, also the mode profile of the equivalent straight waveguide is given, clearly indicating the increasing offset between the centre of the eigenmodes of the curved and the straight waveguides, for decreasing bend radius.

2.1.7 Confinement factor

From the spatial distribution of the optical mode, also the confinement factor Γ_i for each region Ω_i of the waveguide may be obtained[1]. The confinement factor is an important parameter for laser diodes, since the modal gain is well approximated by a weighted sum of the individual gain or absorption levels of each region, with weighting factor the confinement of the power flux or the electric field intensity in each layer:

$$g_{\mathrm{mod}} = \frac{1}{n_{eff}} \sum_i n_i \Gamma_i g_{mat,i} \qquad (2\text{-}17)$$

In this formula, the sum is taken over all regions of the cross-section with a constant refractive index. n_i and $g_{mat,i}$ are respectively the real part of the refractive index and the gain (or absorption) of the *i*-th region. More in general, this formalism can be used to calculate the loss or gain for a large range of waveguides with a complex refractive index profile. Only, in some cases where power leaks to higher index substrate or cladding layers, as is often the case for GaAs laser diodes, this approach cannot be used.

[1] For the exact definition and aspects concerning TM-polarised modes see [17] [25]

2.1.8 Propagation through piecewise constant waveguides

Mode solvers can also be used to investigate the propagation of an optical field through longitudinal piecewise constant waveguide structures. For that purpose the field is decomposed into the local modes of the waveguide, which are subsequently propagated ($\psi_i(\mathbf{r}_t, L) = \exp(-j\beta_i L)\psi_i(\mathbf{r}_t, 0)$). At each waveguide junction, the formalism described in paragraph 2.1.3 may be used to calculate the transmission and reflection coefficients. The mode expansion propagation method has a clear advantage over BPM-algorithms when calculating the transmission through waveguide structures consisting of a limited number of straight or curved waveguides such as MMIs. For continuously varying structures such as tapers, the refractive index profile has to be discretised into a concatenation of longitudinally invariant sections. In these cases, BPM-algorithms may be more appropriate. However, it was shown that the eigenmode expansion propagation algorithms can be used for verification of other propagation algorithms [17][27]. An additional advantage of the eigenmode expansion propagation technique is that it can easily be extended to take into account bi-directional propagation.

In the context of this work, we employed mode expansion propagation algorithms using either 1D modes (*BEP* [26]) or 2D modes (*Fimmprop* [15]). *BEP* uses 1D modes calculated using *REMUS* (see paragraph 2.1). *Fimmprop* on the other hand, uses 2D modes calculated by *Fimmwave*. In the 2D case, it is difficult to obtain a reasonably complete set of eigenmodes. For that reason, the "adapted overlap integrals" of section 2.1.3 are often used (equation (2-9)).

2.2 Beam Propagation Methods (BPM)

To simulate the transmission through complicated waveguides structures, often the beam propagation method (BPM) is employed. Common to all BPM-algorithms is that the propagation through the PIC is calculated step-by-step, starting from a known field. Originally, FFT-algorithms were used for this purpose. Most commercially available BPM-packages now employ a finite-difference-based approach. However, BPM-algorithms can also rely on Green's functions, the method of lines, finite elements or Lanczos reduction. For a review, see [28].

The main simplification made in all BPM-solvers is the choice of a propagation axis. The propagation must remain within a certain angle from this axis. The maximum allowable angle depends on the particular algorithm employed. This also implies that reflections at waveguide junctions are not taken into account.

To reduce the calculation time, a number of other approximations may be made:

- Very often, the effective index method is used to reduce the full 3D problem to an equivalent 2D one.
- The full-vectorial problem may be reduced to a semi-vectorial problem by disregarding the coupling terms in the Helmholtz equation but still taking into account the electrical

field discontinuities at dielectric interfaces, which depend on the polarisation of the propagating field.

- For weakly guiding structures, the semi-vectorial problem may further be simplified to a scalar one by also ignoring the field discontinuities at interfaces.
- The propagation is described by a differential operator. The exact form of this operator determines whether the wave equation will be reduced to a paraxial or wide-angle approximation.
- The calculation domain has to be limited by using suitable boundary conditions. If "hard boundaries", such as metallic walls, are used, power radiated out of the waveguide will be reflected by the walls and re-enters the calculation domain. To avoid this, absorbing or transparent boundary conditions have to be employed.

In the context of this work, we used BPM_CAD, a commercial CAD-package from Optiwave Corporation [29][30]. It allows for modelling of both 2D and 3D structures. It includes different propagation algorithms (paraxial or wide-angle) and uses fully transparent boundary conditions.

2.3 Modelling of active devices

Next to the tools we developed by our own and which are described in chapter 3, we used also 2 commercial CAD tools for simulating the operating characteristics of the multi-wavelength laser: *CLADISS*, which was developed at INTEC [32] and is commercially available from *Photon Design* [15] and *OPALS*, commercially available from Virtual Photonics [46].

CLADISS can be used to model laser cavities consisting of multiple active and passive sections. It uses a transfer-matrix model and was originally intended for the simulation of DFB-

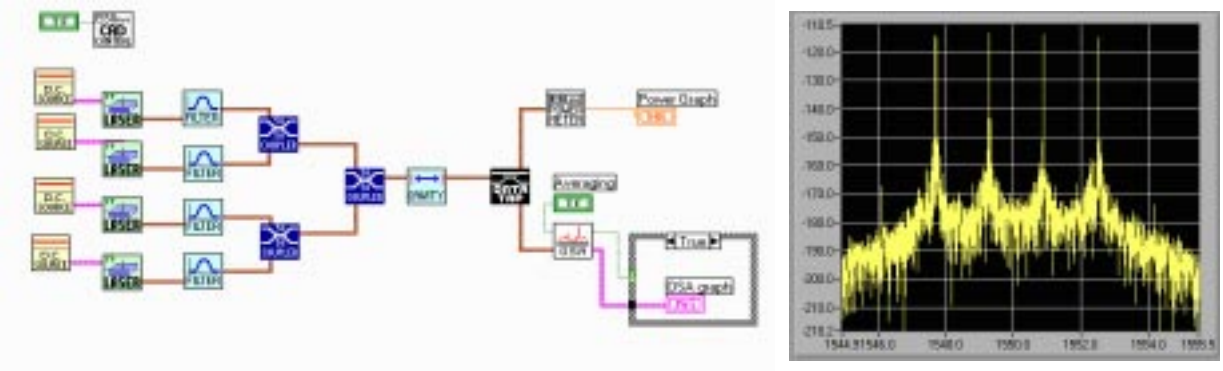

Fig. 2-21 Example of simulation of 4-channel multi-wavelength laser using *OPALS*.

and DBR-lasers. However, it may also be used for modelling long cavity lasers built of an amplifier and a passive section. We used *CLADISS* as a reference for our own static laser model and to simulate the small signal response of the Phased-Array laser (chapter 3).

OPALS allows for simulating more complex PICs. Using *LABVIEW* as a graphical interface, it combines very accurate models for amplifiers and lasers (based on the transmission line laser model [33]) with simple passive elements such as filters and combiners. We used it to study the longitudinal mode stability of the Phased-Array laser because the model takes into

account the modal intermodulation effect [34], which is responsible for an improved suppression of non-lasing longitudinal modes in long-cavity lasers (chapter 3). Fig. 2-21 shows how a 4-channel multi-wavelength laser is simulated using *OPALS*.

As already mentioned, the models employed by these packages are very accurate. However, consequently, it takes a considerable amount of time to simulate a laser structure. For that purpose, we developed simpler, analytic models (see chapter three), which were verified using *CLADISS* and *OPALS.*

2.4 Material parameters

Refractive index and group index of InGaAsP alloys:

The refractive index of the $In_{1-x}Ga_xAs_yP_{1-y}$ alloys was calculated from data on GaInP and GaInAs, using an interpolation method as described in [43]. Fig. 2-22 shows the refractive index and the group refractive index as function of the optical wavelength for some alloys, which were often used in the context of this work. For shortness, the alloys (lattice matched to InP) are denoted as Qλ_g, with λ_g the bandgap wavelength.

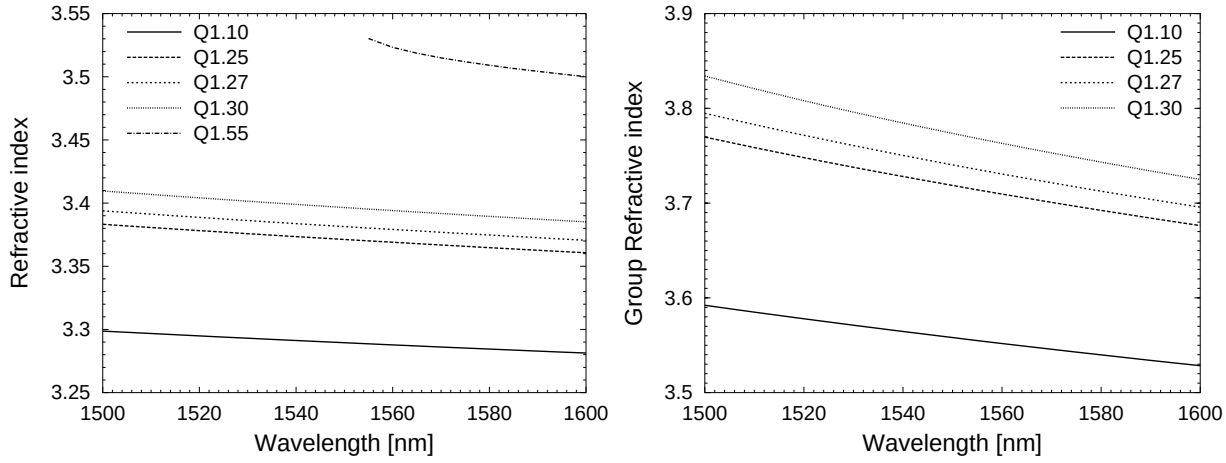

Fig. 2-22 Refractive index (left) and group index (right) of some InGaAsP alloys that were used in the context of this work.

Absorption in doped layers

Intervalence-band absorption due to electron transitions from the split-off band to holes in the heavy-hole band is the dominant loss mechanism below bandgap for p-doped InP and InGaAsP-alloys [38]. The carrier induced absorption coefficient is proportional to the carrier density and rather independent of the material composition. It can be well approximated by:

$$\alpha_{IVB}[cm^{-1}] = 4.25\times10^{-16}\exp\left(\frac{-4.533}{\lambda}\right)P \qquad (2\text{-}18)$$

with λ the wavelength (in μm) and P the hole density (in cm^{-3}).

3 Towards a knowledge driven tool for the synthesis of PICs ?

3.1 Synthesis of complicated PICs

The now available design tools mainly focus on the analysis of photonic integrated circuits and their subcomponents. They may help to understand experimental results and may reduce the number of experimental iteration steps. However, the situation is still far from ideal. As already mentioned in the introduction, almost no tools are specifically developed for synthesis towards a given specification[1]. For the design of complicated PICs such as a multi-wavelength laser, where the structure of one part of the PIC has a strong influence on the other parts of the design, no suitable CAD-tools are available yet. Therefore, one is often forced to choose some parameter values by gambling rather than by precise design. Even worse is the situation where the designer believes that his design is precise by believing that the methods he has used are more accurate than they actually are. In those cases there is only one way out and that is trial and error in the fabrication loop, which is obviously costly and time-consuming. Roughly speaking two problems can be discerned with today's CAD-tools and their solutions are rather incompatible:

The first problem relates to accuracy, at various levels in the design:

- The device structure can be oversimplified: neglect of interface roughness, walls are straightened, thin layers are neglected, …
- The device structure can be inaccurately defined: unknown refractive index or gain, etching errors, unknown laser parameters, …
- The model is simplified: reduction of 3D problem to 2D problem, reduction of vectorial problem to paraxial problem, scalar approximation, neglect of carrier diffusion in ridge type amplifiers, …
- The numerical implementation gives rise to errors: finite grid size, finite calculation window, boundaries …
- The coupling to other problems is neglected: if active devices are involved, the optical field modelling needs to be combined with electrical and thermal modelling, which all can be mutually coupled.

For illustrating this, we can refer back to the design of the MMI already described in paragraph 2.1.1. Methods using the effective index method to reduce the 3D problem to an equivalent 2D problem (2D *BPM* and *BEP*) predict an optimal length that may differ by 5% of the length predicted by full 3D methods (3D *BPM* and *Fimmprop3D*). So one might conclude that 3D methods are indispensable for the accurate design of such devices. However, in practice the uncertainties introduced by process variations (such as waveguide width and refractive index), may be much more important than the inaccuracies introduced by the ef-

[1] Probably the only exceptions are some CAD-tools that were specifically developed for the design of Phased-Array demultiplexers and allow to perform the design-task starting from given specifications for the device.

fective index approximation. Moreover, this particular component was developed for use in the passive part of a laser cavity. The exact operating wavelength of this laser, which influences also the operation of the MMI, will not only depend on the laser parameters itself but also on the total loss of the passive part of the cavity, including the MMI.

The solution to the accuracy problem seems obvious: development and use of more rigorous modelling algorithms, better definition of applicability ranges[1] and sensitivity studies to parameter uncertainties.

The second problem relates to the calculation time. As CAD-methods move to 3D and vectorial problems, the calculation time may increase considerably. This may not seem dramatic if it comes to analysing single structures as the MMI-coupler described above. However, if one wants to include also the complete Phased-Array and the amplifier into an optimisation process or a sensitivity analysis, calculation time becomes an important issue. More in general, problems rise when one wants to analyse a large parameter space (even if an S-matrix approach can be used for calculating the overall response) or when the optical field modelling needs to be combined with the electrical and thermal modelling. Today it is not conceivable that rigorous electromagnetic solvers will become so time efficient that complex system calculation or extensive optimisation will become practical[2].

In our opinion, a possible way out of this deadlock situation is to move towards a knowledge driven tool, in which the emphasis is no longer on field calculation as such but rather on combining and manipulating previously obtained data. The basis of such a tool would be formed by a database (the "knowledge base") and a tool, which can handle the data (the "inference engine"). Of course, also a practical user interface would be required.

The "*knowledge base*" must contain, for a given PIC-technology, validated information for a range of basic waveguide elements. The information can be available in different forms:

- It may be restricted to a library of well designed waveguide elements such as straight and curved waveguides, tapers, couplers …
- It may be a table, containing data for a parameterised waveguide. For example, this table may list properties as the propagation constant, the confinement factor and the minimum bend radius as function of parameters as the layer thickness, the width and the etching depth for a certain type of waveguide.
- It can also be a set of formulas and design rules, describing the behaviour of a component over the allowed parameter range. A typical example is the formula for the bend loss derived in paragraph 2.1.6.

---

[1] This is in particular important for novice users or users that are not completely familiar with the theoretical algorithms behind the tool.

[2] And it is very likely that by the time solvers, which can handle today's PICs, are available, the order of complexity of the PICs we want to analyse by then, will have increased also, leaving us with the same sort of difficulties as encountered now.

- In an advanced system, the database could also contain knowledge of human experts.

The information in the knowledge base may have been validated by experimental results or by rigorous calculation.

The other important part in such a tool, the "*inference engine*", should allow for analysing a design by intelligent combination and manipulation of the previously obtained data stored in the knowledge base. In that case, the global optimisation of a PIC (or a sensitivity analysis) is performed by a data flow oriented circuit simulation, rather than by a field manipulation as such. Of course, the role of field calculation methods will remain important. The user should be able to still use these methods (mode solvers, BPMs, etc.) and should be able to store the results into the knowledge base. This also means that the tool should have well defined and easy to use interfaces to field calculation methods. The data format at these interfaces - for 2D or 3D structure definition, for fields and for material parameters - should become standardised so that the system can communicate with any numerical tool complying with that standard.

Next to the knowledge base and the inference engine, a practical useful expert system will of course also require a (symbolic) circuit definition tool and an interface to a mask layout generator.

3.2 Example

To illustrate these ideas, we used the design of the Phased-Array multi-wavelength laser as an example. The device is to be realised using a monolithic integration scheme based on selective area epitaxial growth as described in chapter 1. Therefore, the layer structure of the active and passive waveguides is identical, except for a reduction of the thickness by a factor 1.5 in the passive region. Further, different from the case described in chapter 1, we assume that all waveguides (active & passive) are etched in a single step. This makes that their is a very strong correlation between the waveguide cross-section used for the Phased-Array and that used for the amplifiers and that it is impossible to optimise them separately.

The device can be optimised towards different goals such as maximum external differential efficiency to fibre, minimum threshold current or maximum modulation bandwidth. Thereby several primary design parameters have to be defined: material composition, layer thickness, number of quantum wells, waveguide width, device length, etch depth, … These in turn determine other parameters such as the confinement factor in the quantum well layers or the absorbing cladding layers, the amount of scattering loss, the minimum bend radius and the number of transversal modes. Some of the primary design parameters can be separately optimised for each part of the PIC (e.g. the amplifier length or the waveguide width), others are constant over the wafer or are interdependent (e.g. the etching depth and the thickness of the layers).

We built a table containing data such as the propagation constants, confinement factors for each region and the integrated field strengths at the waveguide-air interface, for a parameterised waveguide with the layer structure depicted in Table 2-2.

	n	$d_{act}[\mu m]$	$d_{pas}[\mu m]$
Planarly grown cladding layer (InP)	3.17	1.0	1.0
Selectively grown cladding layer (InP)	3.17	0.45	0.3
Q1.1	3.29	$d_{f,a}$	$d_{f,p}$
Q1.25 with QW	3.39	0.180	0.120
Q1.1	3.29	$d_{f,a}$	$d_{f,p}$
Bottom cladding	3.17	∞	∞

Table 2-2 Layer structure used for simulating monolithically integrated PAL using knowledge driven approach. The thickness of the Q1.1 layers is varied such that $d_{f,a}=1.5d_{f,p}$. The etching depth is again denoted with respect to the top of the film layer. Due to the difference in the thickness of the respective InP top cladding layers, the etching depth in the active region (t_a) will be 150 nm smaller than that in the passive region (t_p).

In a first step, we calculated the loss α_p in the passive part of the device, which we assume to be proportional to the length of the passive waveguides, yielding:

$$\alpha_p = L_p(\alpha_{scat}+\alpha_{abs}) \tag{2-19}$$

α_{scat} is the scattering loss of the waveguides, α_{abs} the absorption loss in the p-doped top cladding layer. The minimum bend radius is thereby chosen in such a way that the radiation loss in the curved waveguides is negligible ($\alpha_{rad}<10^{-2}db/90^0$). We further suppose that the total length L_p is linear dependent on the minimum bend radius:

$$L_p = A_1 + A_2 R_{\min} \tag{2-20}$$

With A_1 and A_2 suitable chosen constants. The scattering loss is given by ([45]):

$$\alpha_{scat} = C\frac{E_s^2\Delta n}{P} \tag{2-21}$$

E_s being the integrated field strength at the waveguide boundary[1], Δn the refractive index contrast and C an empirical constant, depending on the etch process used for defining the

[1] E_s was calculated using an effective index approximation. It has been shown that this is a very crude approximation [45]. However, since it is used only for illustrating the knowledge driven approach, this is not relevant here.

waveguides. We determined *C* by fitting experimental data to (2-21). The absorption loss is calculated using eq. (2-17) from paragraph 2.1.7, yielding:

$$\alpha_{abs} = \sum_i \Gamma_i \alpha_i \tag{2-22}$$

with the sum taken over all absorbing sections.

The relevant parameters for the active region are the confinement factor for the active layer, which is stored in the database, and the material gain as function of the current density. The latter was determined by fitting the function

$$g/g_0 = \ln(J/J_0)+1 \tag{2-23}$$

to experimentally obtained data. From the knowledge of the loss in the passive part of the device, the mirror losses and the internal loss of the amplifier, the required threshold gain and the external differential efficiency are easily calculated.

As an example, we tried to minimise the bias current required for obtaining a certain output power, by choosing the etch depth and the thickness of the Q1.1 film layers adequately (see Table 2-2). For simplicity, we consider the waveguide width to be constant in both the active and the passive region ($W = 2\,\mu m$). Fig. 2-23a shows the scattering loss of the passive

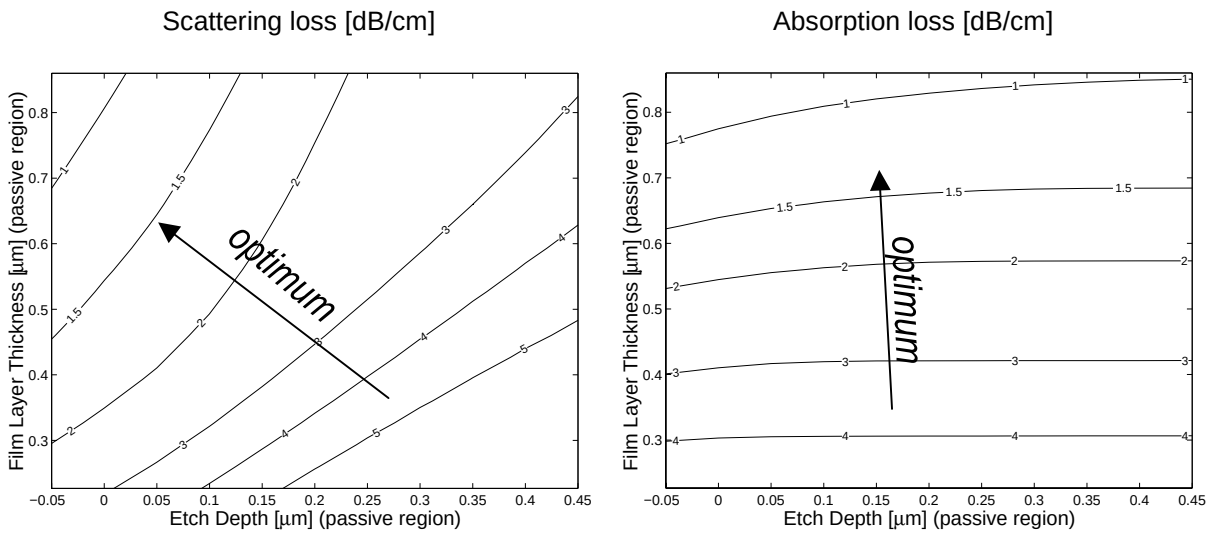

Fig. 2-23 Scattering and absorption loss of the passive waveguide, as function of the etch depth and the total film layer thickness ($2d_{f,p} + 120nm$).

waveguides, calculated using (2-21). As expected, the scattering loss increases with increasing etch depth and decreasing film layer thickness. Fig. 2-23b shows the absorption loss, which is rather independent on the etch depth but decreases strongly with increasing film layer thickness. In Fig. 2-24a, the minimum bend radius is depicted, calculated using eq. (2-15) of paragraph 2.1.6.

From the results shown in Fig. 2-23 and Fig. 2-24a, and using eq. (2-19) and (2-20), the total loss of the passive part can be calculated. The result, for $A_1 = 0$ and $A_2 = 8$, is shown in Fig.

2-24b. The optimum can be found in the upper right corner. This stems partly from our choice for A_1 and A_2, which favours devices with a short bend radius. In the following section of this chapter, we will see that for actual devices, A_1 may become rather large. This will shift the optimum more in the direction of the upper left corner.

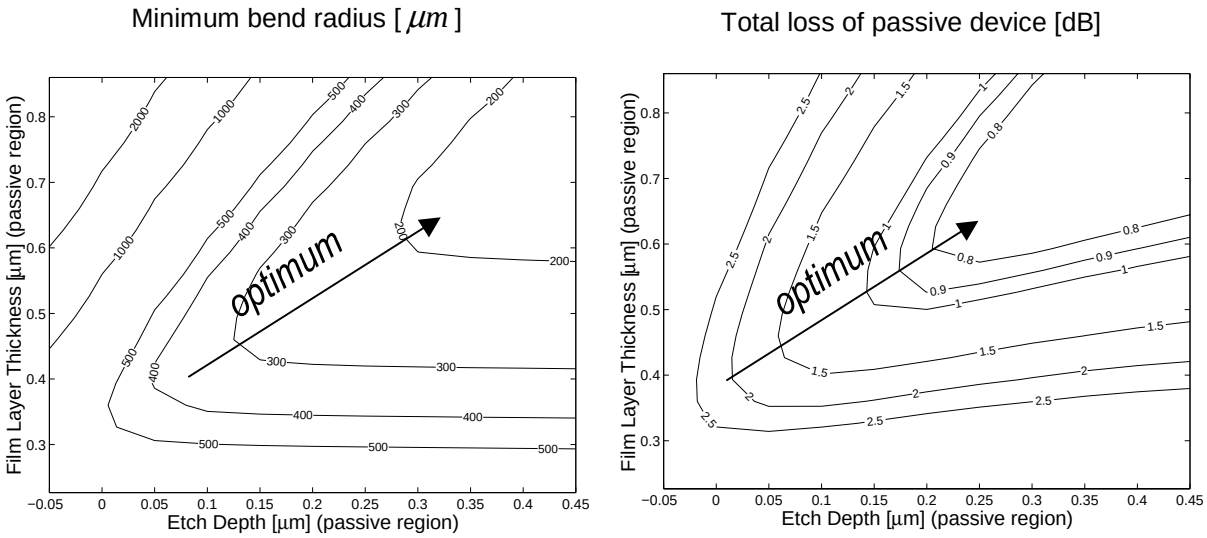

Fig. 2-24 a) Minimum bend radius. b) Total loss of passive device

In Fig. 2-25a, the confinement factor in the active layer is shown. By combining the results from Fig. 2-24b and Fig. 2-25a, we calculated the bias current required for obtaining an output power of 0.5 mW into an optical fibre. The result, for a 600 μm long amplifier containing 4 QWs, is shown in Fig. 2-25b. As could be expected from the fact that the optimal cross-

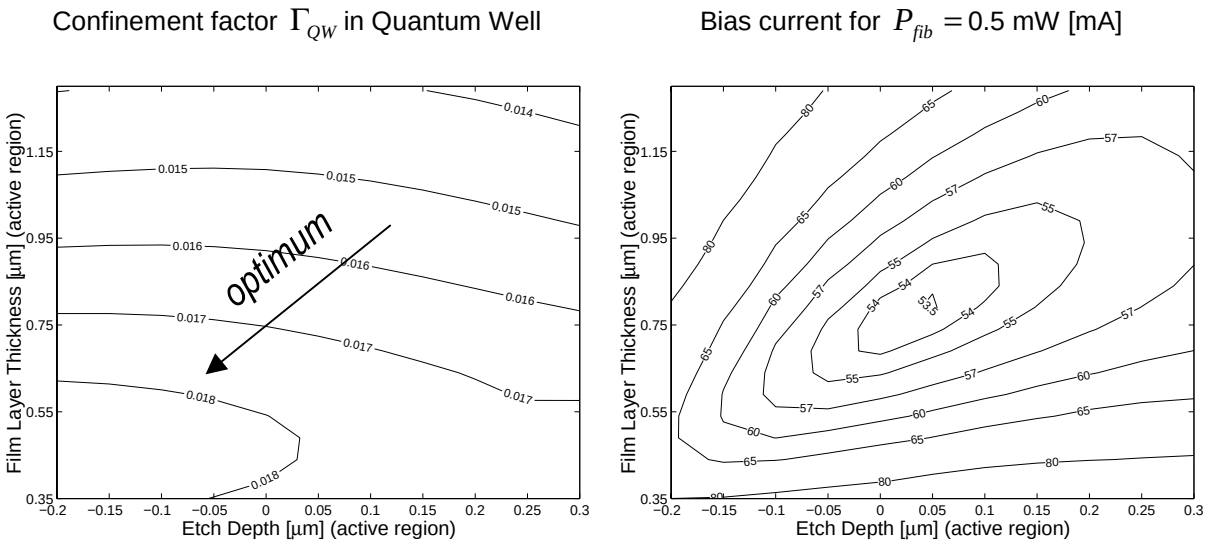

Fig. 2-25 a) Confinement factor in the active layer. b) Bias current for obtaining a power of 0.5 mW into an optical fibre, with a 600 μm long amplifier containing 4 QWs.

section for the amplifiers and the passive waveguides can be found into two opposite corners of the parameter space, the global optimum is located in the centre of this graph. By repeating this procedure for varying amplifier length and varying number of quantum wells (Fig.

2-26), a minimum bias current of 53 mA, for a device with a 500 μm long amplifier containing 5 QWs is obtained. The optimal etching depth and film layer thickness are respectively given by 200 nm (50 nm) and 540 nm (800 nm) in the passive (active) region.

The example outlined above shows how we built a simple database containing data in different forms: a table of properties for a parameterised waveguide and a set of design rules such as the formula for calculating the loss or the gain of a waveguide using the confinement factor (2-17) or the formula for the bend loss (2-15). The system contained also some information obtained from earlier experiments such as suitable doping profiles and the empirical constant *C,* determining the scattering loss of a waveguide. Some of the design rules were verified experimentally or by more rigorous calculations. Using this "knowledge base", we could optimise the design of multi-wavelength laser. In addition, it is very easy to obtain an idea about the sensitivity of the optimum with respect to the different parameters. The main difference with more classical approaches is that in this case all field calculations were performed before starting the actual optimisation process. Moreover, for carrying out a sensitivity analysis or when changing some parameters such as the constants defining the relation between the minimum bend radius and the total cavity length (eq. (2-20)), no additional field calculations are required.

Therefore, we believe that the knowledge driven approach proposed in this section may be a

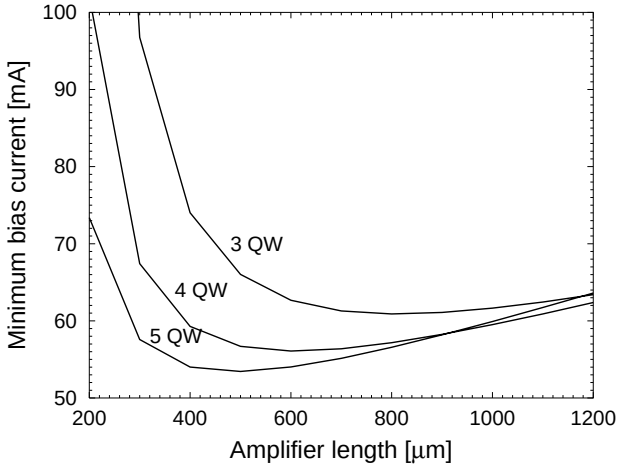

Fig. 2-26 Bias current for an output power of 0.5 mW into an optical fibre versus the amplifier length, 3, 4 and 5 quantum well layers.

solution for the restrictions of the currently available CAD-tools with respect to calculation time and accuracy.

4 Phased-Array Demultiplexers: basic operation and design

4.1 Basic operation

Fig. 2-27 shows a schematic layout of the Phased-Array demultiplexer (for a real mask layout, e.g. see chapter 5). The most important part is the dispersive waveguide array in the

centre. This array can contain up to 400 waveguides [38], although values between 40 and 200 are more common, and is designed in such a way that the length difference between two successive waveguides is constant. The array is connected with the transmitter and receiver waveguides at the input and output of the device through two star couplers. When light enters the first star coupler, it is diffracted towards the entrance of the waveguide array. At the transition with the array, the light is coupled into the individual array waveguides where it will propagate further towards the second star coupler. If the constant length difference between the waveguides is a multiple of the wavelength of the light, the phase front at the end of the waveguide array will be identical to that at the entrance of the array and the light will be focussed on the central receiver waveguide. If the wavelength differs from this "central wavelength", the phase front at the entrance of the second star coupler will still have the same form but due to the linear length increase of the array waveguides, it will be tilted towards a receiver waveguide further away from the centre on which the light will focus. The transfer through the Phased-Array is periodic. If the phase shift equals 2π, the light will again focus on the central receiver.

Alternatively, one can use a transmitter guide further away from the centre. It is easy to see that in that case, light with the central wavelength (light that is guided from the central transmitter to the central receiver) will be focussed on a receiver guide equally far away from the centre but to the opposite side. More in general, Fig. 2-28 shows the routing properties of an NxN Phased-Array demultiplexer (in this case $N = 5$) for which the period (the free spectral range) equals N times the channel spacing $\Delta\lambda_{ch} = \lambda_i - \lambda_{i-1}$. A drawback of this configuration is that the insertion loss of the peripheral input and output ports is 2-3 dB higher than that for the central ports[1]. Fig. 2-29 depicts the transfer through a typical Phased-Array demultiplexer.

Note that the operation of the Phased-Array is reciproque: if light with wavelength λ_{ij} is guided from the *j*-th transmitter guide to the *i*-th receiver guide, light with that wavelength will also be guided from the *i*-th receiver to the *j*-th transmitter.

[1] This issue was solved by the development of the so-called uniform-loss and cyclic-frequency Phased-Arrays [38][39].

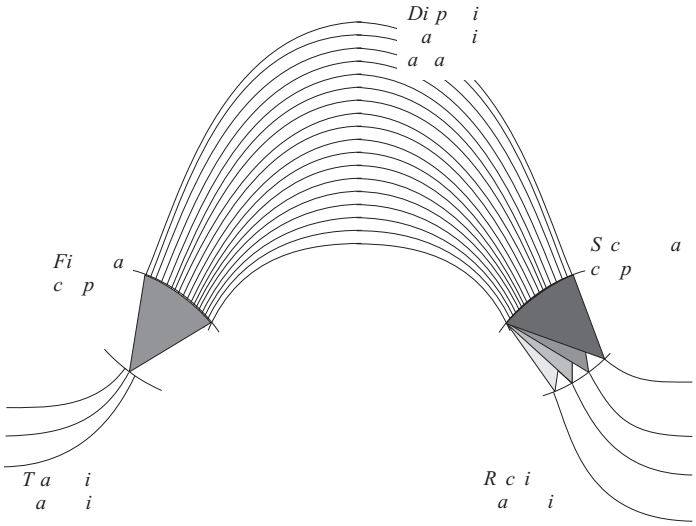

Fig. 2-27 Schematic layout of Phased-Array demultiplexer

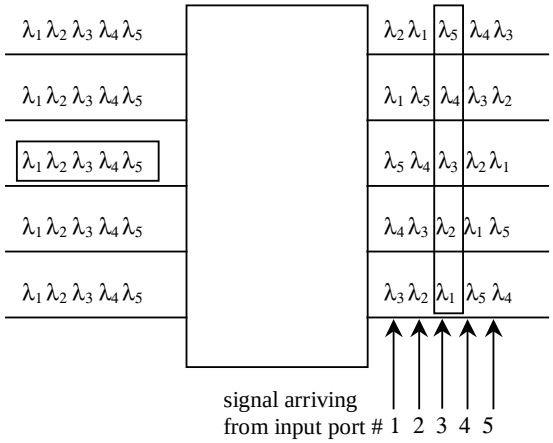

Fig. 2-28 Routing properties of a Phased-Array demultiplexer

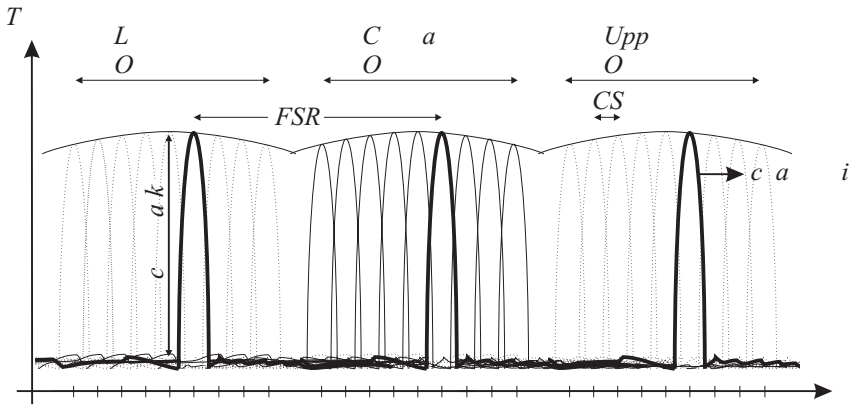

Fig. 2-29 Wavelength transfer through a Phased-Array demultiplexer. The bold line represents the transfer from the central transmitter waveguide to the receiver waveguide located immediately next to the central receiver waveguide. The other curves represent the transmission to other receiver guides.

Fig. 2-30 shows the star coupler in more detail. The array waveguides are located on an arc (the grating line) with radius f (the focal distance) and centre located on the image plane. The focal line of this array is an arc with radius $f/2$ (the Rowland circle [40]). The transmitter (receiver) waveguides are located along this line.

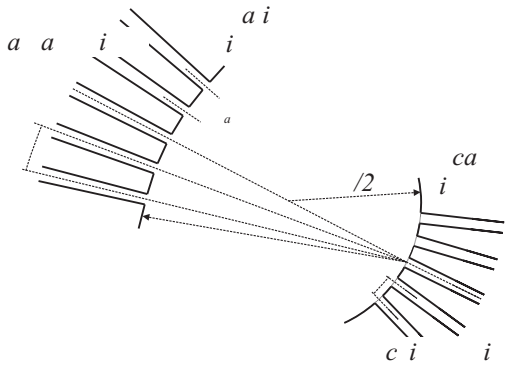

Fig. 2-30 Geometry of the star coupler of a Phased-Array demultiplexer

Below the most important relations describing the operation of a Phased-Array are summarised. Most of the symbols are explained in Fig. 2-30. For a more detailed review, see [35][37].

As explained before, the length of the array arms increases linearly. The constant arm length difference is given by

$$\Delta L = m\frac{\lambda_c}{n_{eff}} = m\frac{c}{n_{eff}\nu_c} \tag{2-24}$$

m is the order of the multiplexer and n_{eff} is the effective index of the array waveguides. The dispersion D, which is defined as the lateral displacement ds along the focal line as function of the frequency change $d\nu$, is given by:

$$D = \frac{ds}{d\nu} = \frac{n_g}{n_{FPR}}\frac{\Delta L}{\nu_c}\frac{1}{\Delta\alpha} = \frac{n_g}{n_{FPR}}\frac{\Delta L}{\nu_c}\frac{f}{d_a} \tag{2-25}$$

n_g is the group index of the zeroth order mode of the array waveguides and n_{FPR} is the effective index of the slab region (the star coupler). $\Delta\alpha$ is the angle between two successive array waveguides and is given by $\Delta\alpha = d_a / f$ with d_a the distance between the centres of the array waveguides and f the focal length.

As already noted, the response of the Phased-Array is periodic. The period or free spectral range (*FSR*) is given by:

$$\Delta\nu_{FSR} = \frac{c}{n_g\Delta L} = \frac{\nu_c}{m}, \tag{2-26}$$

or, in the wavelength domain

$$\Delta\lambda_{FSR} = \frac{\lambda_c^2}{n_g \Delta L} = \frac{\lambda_c}{m'}$$

with $m' = (n_g / n_{eff})m$. (m' may be interpreted as the beam order, see [35]).

If the far field of the transmitter is wider than the array aperture, power will be lost at the transition between the first star coupler and the array waveguides. Moreover, due to the truncation of the field, additional crosstalk will occur in the in the wavelength transfer function. Therefore, it is important to use enough array waveguides so that all the power emitted by the transmitter guide is captured by the array.

Using a Gaussian beam approximation, the far field intensity of the transmitter waveguides is given by:

$$I(\theta) = I_0 \exp\left(-2\theta^2/\theta_0^2\right) \tag{2-27}$$

The width θ_0 of the far field is given by:

$$\theta_0 = \frac{\lambda}{n_{FPR}} \frac{1}{w_e \sqrt{2\pi}} \tag{2-28}$$

with w_e the effective mode width of the transmitter waveguide, which is defined as the width of a uniform distribution having the same maximum intensity and the same power content as the zeroth order eigenmode of the waveguide. For the ridge waveguide of Fig. 2-4 (600 nm Q1.3 film layer, etched 100 nm into the quaternary material, $W = 2\mu m$), the effective mode width is given by $w_e = 1.47\mu m$ ($\lambda = 1.55\mu m$), resulting in a far field width $\theta_0 = 7.3^o$.

To avoid crosstalk and excess loss due to a limited array aperture, the latter has to be chosen wide enough. $\theta_a > 2\theta_0$ appears to be a save margin in most cases (θ_a is the array aperture half angle). The number of array waveguides is then given by

$$N_a = \mathrm{int}\left(2 f \theta_a / d_a\right) \tag{2-29}$$

For a more rigorous estimation of the minimum array aperture required to obtain a given crosstalk and loss level, we refer again to [35][37].

Again using a Gaussian approximation for the modal fields, the *L*-dB bandwidth $\Delta\nu_L$ for the transmission through the demultiplexer can be estimated to be:

$$\Delta\nu_L = 0.77 \frac{w_e}{D} \sqrt{L} = 0.77 \frac{w_e}{d_r} \Delta\nu_{ch} \sqrt{L} \tag{2-30}$$

$\Delta\nu_{ch}$ being the channel spacing of the demultiplexer.

4.2 Design of a Phased-Array demultiplexer for a multi-wavelength laser

When designing a Phased-Array, which is to be used as a passive demultiplexer, one typically wants to optimise the channel crosstalk and the total insertion loss of the device. Other

parameters as the free spectral range, the dispersion and the cavity length follow then automatically. In [35][36][37], such a design strategy is described.

However, if the multiplexer has to be used for the realisation of a multi-wavelength laser, the *FSR* and the filter bandwidth become more relevant parameters. As will be shown theoretically in chapter 3 and experimentally in chapters 5 and 6, the free spectral range has to be large enough to suppress multi-passband lasing. Further, to obtain single longitudinal mode operation, the filter bandwidth must be smaller than a certain minimum value, depending on the laser characteristics and the total cavity length (see chapter 3). Therefore, another design strategy, which is outlined below, should be followed in this case.

Starting from a given waveguide structure and a given central wavelength, the minimum *FSR* and maximum bandwidth $\Delta\nu_L$ are chosen, taking the before mentioned considerations in mind. From the *FSR*, the arm length difference ΔL is determined, using (2-26). From $\Delta\nu_L$ the dispersion D is obtained using (2-30). Using these results, equation (2-25) can be used to calculate $\Delta\alpha = d_a / f$. To minimise the total propagation losses, d_a should be minimised[1]. This in turn determines the focal length f.

The channel spacing $\Delta\nu_{ch}$ is determined by the spacing between the receiver waveguides and the dispersion: $\Delta\nu_{ch} = d_r / D$. The minimum receiver spacing is determined by the maximum allowable crosstalk level. However, for a demultiplexer intended for use in a multi-wavelength laser, the crosstalk level is not so important so it will be possible to obtain a rather narrow channel spacing.

Note that increasing the free spectral range results in an increase of the focal length. Since the far field width θ_0 of the transmitter waveguide is constant, increasing the focal length results in a proportional increase of the required number of array waveguides (2-29). Also decreasing the filter bandwidth results in an increase of the focal length. In the design strategy outlined above, we started from the idea that for obtaining stable single longitudinal mode operation it is favourable to minimise the filter bandwidth of the Phased-Array. However, since it turns out that this may considerably increase the length of the laser cavity and consequently decrease the distance between the longitudinal modes, it is obvious that their will be a trade-off between minimising the filter bandwidth and minimising the cavity length.

---

[1] d_a is the distance between the centres of the array waveguides at the aperture and it is given by the sum of the waveguide width and the minimum gap between two waveguides. The latter is defined by the finite resolution of the lithographic process.

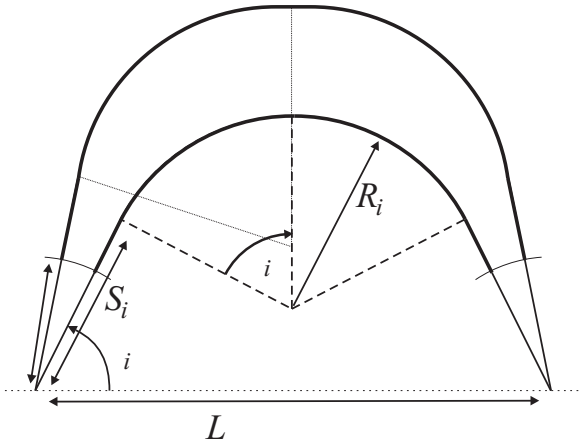

Fig. 2-31 Layout of Phased-Array demultiplexer

To investigate this in more detail, it is necessary to look in more in detail at the layout of the Phased-Array. Fig. 2-31 shows the geometry of the Phased-Array as it was designed in the context of this work. Each guide of the array consists of a straight waveguide and a curved waveguide and is fully determined by the angle α_i and the bend radius R_i. S_i is equal to the sum of the focal length and the length of the straight piece of the array arm. If the bandwidth and the free spectral range are chosen, the other parameters of the design (ΔL, $\Delta\alpha$, f) may be determined as described above. For determining the actual layout of the multiplexer however, also the distance between the focal points (L), the angle α_0 (with $\alpha_i = \alpha_0 + i\Delta\alpha$) and the length l_0 (with $l_i = l_0 + i\Delta L$) have to be chosen, taking the following boundary conditions into account:

$$\begin{aligned} R_i &> R_{\min} \\ S_i &> f \end{aligned} \tag{2-31}$$

For a standard design, this is typically done in such a way that the total chip surface occupied by the Phased-Array is minimised. However, for application in a multi-wavelength laser, it is important that the total cavity length, which is mainly determined by the cavity length through the demultiplexer ($l_{N/2} = l_0 + N/2\Delta L$), is minimised. This is done in the following way. From the boundary conditions (2-31), two conditions[1] involving the distance between the focal points are obtained:

$$\begin{aligned} f_1(l_i, \alpha_i, f) &> L \qquad 1 < i < N \\ f_2(l_i, \alpha_i, R_{\min}) &< L \qquad 1 < i < N \end{aligned} \tag{2-32}$$

As a result, l_0 and α_0 have to be chosen in such a way that:

[1] Actually, there is a third boundary condition saying that the height of successive guides should increase by an amount at least equal to two times the waveguide width [37]. This boundary condition was checked afterwards for the designs described here but put no additional restrictions to the geometry.

$$f_1(l_i, \alpha_i, f) > f_2(l_i, \alpha_i, R_{\min}) \qquad 1 < i < N \tag{2-33}$$

L is chosen as $\max_i(f_2)$.

For a given angle α_0, the minimum length l_0 that makes (2-32) true is easily obtained. Fig. 2-32 shows the length $l_{N/2} = l_0 + N/2\Delta L$, which was obtained in this way, as function of the angle α_0, for a Phased-Array with $FSR = 38.4$ nm, $\nu_{1dB} =$ 32 GHz and $R_{\min} = 500\,\mu m$. For the waveguides, a core and cladding refractive index of respectively $n_1 = 3.3075$ and $n_2 = 3.2537$ was supposed, and they were $2\,\mu m$ wide. The minimum cavity length (4.72 mm) is obtained for $\alpha_0 = 66^0$.

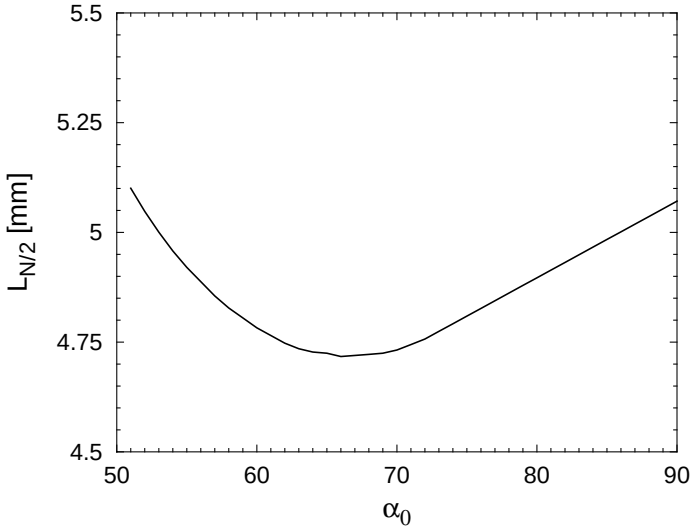

Fig. 2-32 Minimum length $l_{N/2} = l_0 + N/2\Delta L$ as function of the angle α_0

This procedure can be repeated for several values of the spectral bandwidth $\Delta\nu_L$. This is shown in Fig. 2-33 for a Phased-Array with the same parameters as used for obtaining Fig. 2-32. As expected, the cavity length $l_{N/2}$ increases strongly with decreasing $\Delta\nu_{1dB}$. As explained above, it is important to minimise both $\Delta\nu_{1dB}$ and $l_{N/2}$ for obtaining stable single longitudinal mode operation. In [44], it was shown that the optimal design is obtained by minimising:

$$\Delta\nu_{1dB} L_{cav}^3 \tag{2-34}$$

with $L_{cav} = l_{N/2} + L_{res}$ the total cavity length. L_{res} is equal to the sum of the lengths of the access waveguides, the amplifiers and $l_{N/2}$. In Fig. 2-33b, $\Delta\nu_{1dB} L_{cav}^3$ is shown for various values of L_{res} (for clarity, $\Delta\nu_{1dB} L_{cav}^3$ was multiplied with a factor dependent on L_{res}). This figure shows that the optimal filter bandwidth decreases with an increasing value for L_{res} and reveals that it is very important to minimise the lengths of the access waveguides as

much as possible. For $L_{res} = 2\,\text{mm}$, a total cavity length of only 4.76 mm may be obtained. For $L_{res} = 4$ mm, however, the cavity length increases to 8 mm, for the optimal bandwidth of 40 GHz.

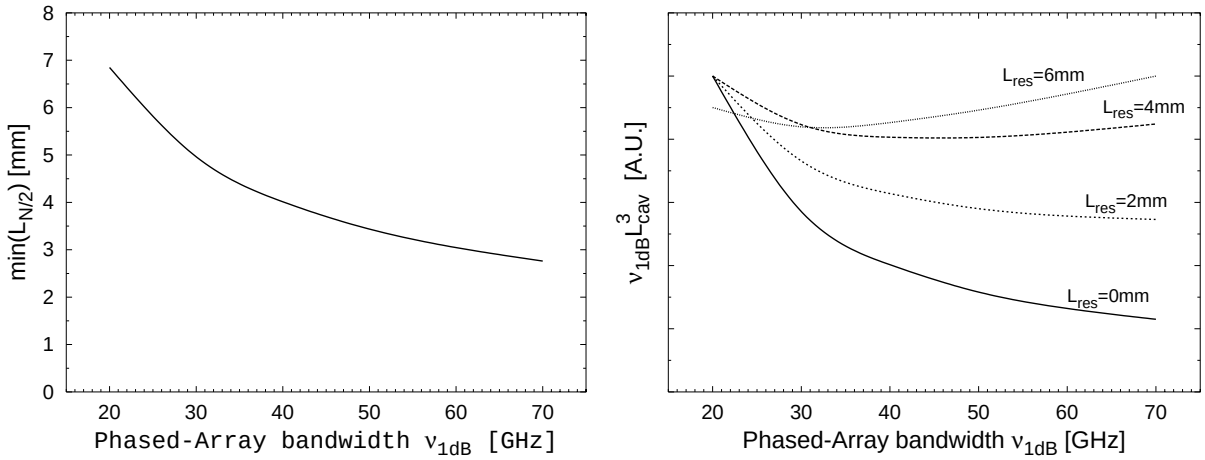

Fig. 2-33 Minimum cavity length (left) and $\Delta\nu_{1dB}L_{cav}^3$ (right) as function of the spectral bandwidth $\Delta\nu_{1dB}$.

The optimal bandwidth is strongly dependent on the weight one designates to L_{cav} in minimising $\Delta\nu_{1dB}L_{cav}^i$. The results in Fig. 2-33 were obtained using a power $i = 3$ for L_{cav}, which was obtained in [44]. In Fig. 2-34, $\Delta\nu_{1dB}L_{cav}^i$ is shown for $L_{res} = 2\,\text{mm}$ and i varied from 1.5 to 3.

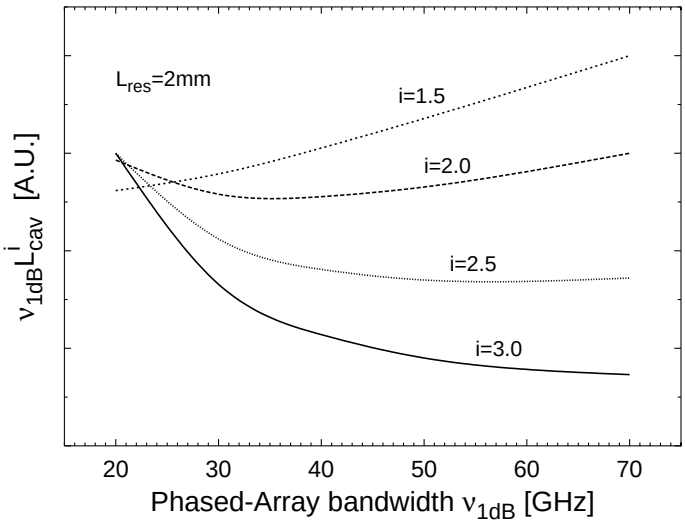

Fig. 2-34 $\Delta\nu_{1dB}L_{cav}^i$ versus the spectral bandwidth with *i* varied.

For obtaining Fig. 2-35a, we calculated the minimum cavity length $l_{N/2}$ through the Phased-Array as function of the optical bandwidth, for a varying minimum band radius $R_{\min}$. Although, as expected, $l_{N/2}$ is reduced for decreasing $R_{\min}$, the decrease is less than expected.

This stems from the fact that the cavity length $l_{N/2}$ is mainly determined by the sum $2f + N/2\Delta L$, which is independent of $R_{\min}$. For $\Delta\nu_{1dB} = 70$ GHz, we find $2f + N/2\Delta L \sim 1.6$ mm, for $\Delta\nu_{1dB} = 20$ GHz, this sum increases to 5.5 mm (the number of required waveguides thereby increases from 84 to 294). Fig. 2-35b again shows $\Delta\nu_{1dB} L_{cav}^3$, for a varying $R_{\min}$.

For the calculations in this paragraph, we took into account a rather large value for the free spectral range ($FSR = 38.4$ nm). Such a large value may be required for preventing multi-passband lasing. However, by chirping the transmission through the Phased-Array (see chapter 3), MPL is completely annihilated and it is possible to use a smaller *FSR*, which will also reduce the total cavity length. This will shift the optimum value for the bandwidth to smaller values.

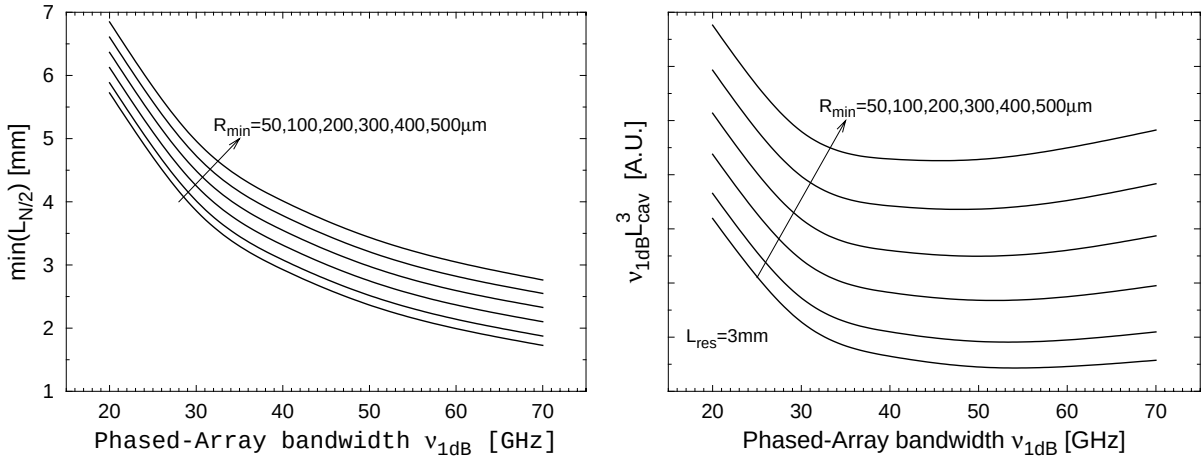

Fig. 2-35 Length (left) through Phased-Array and $\Delta\nu_{1dB} L_{cav}^3$ (right), as function of the spectral bandwidth $\Delta\nu_{1dB}$ with the minimum bend radius varied from 50 μm to 500 μm.

5 Summary

This chapter gave a review of the methods we used for designing the multi-wavelength laser. In section 1, the task flow for designing a complex photonic IC was outlined. It follows that powerful CAD-tools are indispensable in this process. We discussed the general operating principle of such a tool and defined some minimum requirements for a user-friendly CAD-package.

The CAD-tools we used in the context of this work were summarised in section 2. The largest part of this section was devoted to mode solvers and their applications. However, also BPM solvers and some laser modelling packages were shortly introduced. Thereby several design rules and analytic formulas were derived, which can be used for simplifying the design of complex PICs.

In section 3, some of the weaknesses of classical CAD-tools are discussed. We show that for analysing today's PICs more accurate tools are required having better defined applicability ranges and allowing to carry out sensitivity studies to parameter uncertainties. However,

this increases the calculation time considerably and it is not conceivable that such tools will be capable of analysing complex devices such as a Phased-Array multi-wavelength laser. As a way out, we proposed an alternative approach, which starts from a knowledge base containing stored data for a broad range of waveguide types, possibly in several different forms. By combining this knowledge base with a suitable inference engine, the optimisation process or the sensitivity analysis is carried out by manipulating previously obtained data rather than by field calculation as such. This approach was illustrated with the design of a multi-wavelength source as an example.

In the last section of this chapter, the operating principle of the Phased-Array demultiplexer was discussed. We introduced the most important relations describing the behaviour of this device and we demonstrated how the geometrical design of the Phased-Array demultiplexer might be optimised for use in a multi-wavelength laser.

6 References

[1] C. Vassallo, "1993-1995 optical mode solvers", Opt. Quantum El., Vol. 29, S95-114, 1997

[2] V. Magnin, I. Cayrefour, Q. J. Harari, D. Decoster, "Optimization of optical switches using BPM and genetic algorithms", ECOC '99, 1999

[3] D. Emi, M. Spuhler, J. Frohlich, "A generalized evolutionary optimization procedure applied to waveguide mode treatment in non-periodic optical structures", ECIO '97, EThC1, Stockholm, Sweden, 1997

[4] R. Moosburger, C. Kostrzewa, G. Fischbeck, K. Petermann, "Shaping the digital optical switch using evolution strategies and BPM", IEEE PTL, Vol. 11, 1484-1486, 1997

[5] D. K. Pant, R. D. Coalson, M. I. Hernandez, J. Campos-Martinez, "Optimal control theory for optical waveguide design: application to Y-branch structures", Applied Optics, Vol. 38, 3917-3923, 1999

[6] D. K. Pant, R. D. Coalson, M. I. Hernandez, J. Campos-Martinez, "Optimal control theory for the design of optical waveguides", IEEE JLT, Vol. 16, 292-300, 1998

[7] X. J. M. Leijtens, L. H. Spiekman, C. van Dam, L. C. N. de Vreede, M. K. Smit, J. L. Tauritz, "CAD-tool for integrated optics", ECIO'95, Delft, 463-466, 1995

[8] K. S. Chiang, "Review of numerical and approximate methods for the modal analysis of general optical dielectric waveguides", Opt. Quantum El., Vol. 26, S113-134, 1994

[9] K. H. Schlereth, M. Tacke, "The complex propagation constant of multilayer waveguides: an algorithm for a personal computer", IEEE JQE, Vol. 26, 627-630, 1990

[10] R. E. Smith, S. N. Houde-Walter, G. W. Forbes, "Mode determination for planar waveguides using the four-sheeted dispersion relation", IEEE JQE, Vol. 28, 1520-1526, 1992

[11] A. S. Sudbo, "Film mode matching: a versatile method for mode field calculations in dielectric waveguides", J. Europ. Opt. Soc. A, Pure Appl. Opt. 2, Vol. , 211, 1993

[12] A. S. Sudbo, "Numerically stable formulation of the transverse resonance method for mode-field calculations in dielectric waveguides", IEEE PTL, Vol. 5, 342, 1993

[13] U. Rogge, R. Pregla, "Method of lines for the analysis of dielectric waveguides", IEEE JLT, Vol. 11, 2015-2020, 1993

[14] C. J. Smartt, T. M. Benson, G. M. Berry, S. V. Burke, P. Kendall, P. Robson, "Exact polarised rib waveguide analysis", El. Lett., Vol. 30, 1127-1128, 1994

[15] Fimmwave / Fimmprop3D / Cladiss, http://www.photond.com

[16] J. Willems, "Modellering en ontwerp van geïntegreerde optische filters en lasers met een in golflengte breed afstembereik", PhD thesis, University of Gent, 1995

[17] J. Haes, "Study of beam properties of laser diodes and design of integrated beam expansion structures", Ph.D. thesis, University of Gent, 1996.

[18] J. D. Love, W. M. Henry, W. J. Stewart, R. J. Black, S. Lacroix, F. Gonthier, "Tapered single-mode fibres and devices", IEE Proc. J, Vol. 138, 343-364, 1991

[19] D. Gallagher, personal communication

[20] G. Kweon, I. Park, "Splicing losses between dissimilar optical waveguides", IEEE JLT, Vol. 3, 690-703, 1999

[21] D. Marcuse, "Reflection loss of laser mode from tilted end mirror", IEEE JLT, Vol. 7, 336-339, 1989

[22] M. Heiblum, J. H. Harris, "Analysis of curved optical waveguides by conformal transformation", IEEE JQE, Vol. 11, 75-83, 1972

[23] E. C. M. Pennings, "Bends in optical ridge waveguides", Ph.D. thesis, Delft University of Technology, Delft, The Netherlands, 1990

[24] M. K. Smit, E. C. M. Pennings, H. Blok, "A Normalised approach to the design of low-loss optical waveguide bends", IEEE JLT, Vol. 11, 1737-1742, 1993

[25] J. Haes, B. Demeulenaere, T. D. Visser, D. Lenstra, H. Blok, R. Baets, "Difference between TE and TM modal gain in amplifying waveguides: analysis and assessment of two perturbation approaches", Opt. Quantum Elec., Vol. 29, 263-273, 1997

[26] J. Willems, J. Haes, R. Baets, "The bidirectional mode expansion method for two dimensional waveguides: the TM-case", Opt. Quantum Electronics, Vol. 27, 995-1007, 1995

[27] J. Haes, R. Baets, C. M. Weinert, M. Gravert, H. P. Nolting, M. A. Andrade, A. Leite, H. Bisseneur, J. B. Davies, R. D. Ettinger, J. Ctyroky, E. Ducloux, F. Ratovelomanana, N. Vodjdani, S. Helfert, R. Pregla, F. H. G. M. Wijnands, H. J. W. M. Hoekstra, G. J. M. Krijnen, "A comparison between different propagative schemes for the simulation of tapered step index slab waveguides", IEEE JLT, Vol. 14, 1557-1569, 1996

[28] H. J. W. M. Hoekstra, "On beam propagation methods for modelling in integrated optics", Opt. Quantum El., Vol. 29, 157-171, 1997

[29] V. P. Tzolov, D. Feng, S. Tanev, Z. J. Jakubczyk, "Modelling tools for integrated and fiber optical devices", Integrated Optics Devices III, Photonics West '99, Jan. 23-29, 1999, San Jose, CA

[30] Optiwave Corporation, http://www.optiwave.com

[31] PICS3D, CrossLight Software Inc., http://www.crosslight.ca

[32] P. Vankwikelberge, G. Morthier, R. Baets, "Cladiss - A longitudinal Multi-Mode Model for the analysis of the static, dynamic and stochastic behaviour of diode lasers with distributed feedback", JQE, Vol. 21, pp 1985-1963, 1985

[33] A. J. Lowery, "New time domain model for active mode-locking based on the transmission line laser model", IEE Proc. J, Vol. 136, 264-272, 1989

[34] L. V. T. Nguyen, M. J. L. Cahill, A. J. Lowery, D. Novak, P. C. R. Gurney, D. D. Sampson, "Effects of carrier-induced modal intermodulation on dynamic spectral characteristics of multimode Fabry-Pérot lasers", Opt. Quantum Elec., Vol. 28, pp 1067-1080, 1996

[35] C. van Dam, "InP-based polarisation independent wavelength demultiplexers", PhD. Thesis, Delft University of Technology, The Netherlands, 1997

[36] M. K. Smit, "Integrated optics in silicon-based aluminium oxide", PhD. Thesis, Delft University of Technology, The Netherlands, 1991

[37] M. K. Smit, C. van Dam, "Phasar-based WDM-devices: principles design and applications", IEEE J. Sel. Topics Quant. Electron., Vol. 2, 236-250, Jun 96

[38] E. J. Murphy, "Integrated optical circuits and components - design and applications", Marcel Dekker, Inc., ISBN: 0-8247-7577-5

[39] A. Himeno, K. Kato, T. Miya, "Silica-based planar lightwave circuits", IEEE J. Sel. Topics Quant. Electron., Vol. 4, 913-924, 1998

[40] R. Marz, "Integrated optics design and modelling", Boston, Artech House, 1994

[41] C. Vassallo, "Optical waveguide concepts", Amsterdam, Elsevier, 1991

[42] A.S. Sudbo, "Why are accurate computations of mode fields in rectangular dielectric waveguides difficult", IEEE JLT, Vol. 10, 418-418, 1992

[43] K. Utaka, K. Kobayashi, Y. Suematsu, "Lasing characteristics of 1.5-1.6 um GaInAsP/InP integrated twin-guide lasers with first-order distributed bragg reflectors", IEEE JQE, Vol. 17, 651-658, 1981

[44] C. R. Doerr, "Theoretical stability analysis of single mode operation in uncontrolled mode-selection semiconductor lasers", IEEE PTL, Vol. 9, 1457-1459, 1997

[45] L. H. Spiekman, "Compact Integrated optical components for telecommunication networks", PhD. Thesis, Delft University of Technology, The Netherlands, 1996

[46] OPALS, "Virtual Photonics, Inc.", http://www.virtualphotonics.com

CHAPTER 3

THEORETICAL ANALYSIS OF PHASED-ARRAY MULTI-WAVELENGTH LASERS

Chapter 3

Theoretical analysis of Phased-Array multi-wavelength lasers

1 Introduction

In this chapter, the operating characteristics of a multi-wavelength laser, realised by integrating an amplifier array and a multiplexer in one optical cavity are theoretically investigated. A black box description is used, thereby hiding implementation specific details such as the type of multiplexer or the active-passive integration scheme.

Fig. 3-1a shows the laser source as it is described in the following sections: an array of N amplifiers - the "channel" or "signal" amplifiers - is connected to the input ports of a multiplexer. The output port of the multiplexer is connected to a passive waveguide or, as shown in Fig. 3-1, to another amplifier (the "common" or "output" amplifier). The laser cavity is formed by mirrors[1] at the outer sides of the device. Since the amplifiers are fabricated in a single step, we will assume that they all have identical material and geometrical parameters. Only the

a) complete MWL:

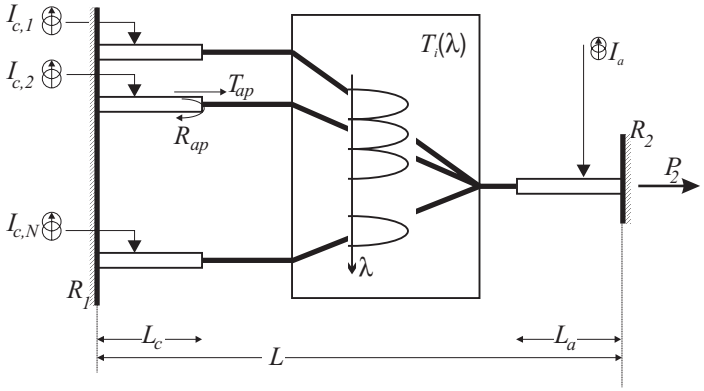

b) one channel of MWL:

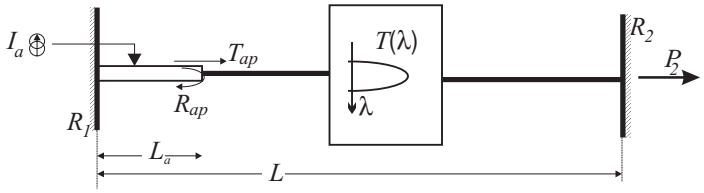

Fig. 3-1 a) Schematic layout of the multi-wavelength laser as it will be studied in this chapter. b) Limited scheme, valid when the channels may be considered to be uncoupled.

[1] Which are typically the cleaved facets of the chip

length of the amplifiers is varied. This assumption considerably simplifies the notation but has no consequences for the generality of the description. Further, we neglect the reflection at the interface between the active and passive waveguides ($R_{ap} = 0$). For a well designed monolithic integration process, this is a very good approximation. Also for the hybridly coupled devices, which incorporate slanted waveguides to reduce the facet reflection (chapters 5 & 6), this is a valid assumption.

Since the crosstalk suppression of the multiplexer is typically better than 20 dB, the channels of a multi-wavelength laser without common amplifier may be considered to be independent for most applications. Therefore, section 2 gives a detailed discussion of the operating characteristics of a single channel long-cavity laser consisting of a single amplifier and a long passive cavity, as shown in Fig. 3-1b. In paragraph 2.1 the rate-equations describing the behaviour of such a laser are derived. In paragraphs 2.2, 2.3 and 2.4, these are used to obtain the static operating characteristics of a long-cavity laser, while in paragraph 2.5, the small signal response is discussed.

In section 3, the behaviour of a single channel laser with an additional common amplifier and the influence of adding more channels are discussed. We thereby mainly pay attention to the effect of crosstalk due to carrier depletion in the common amplifier and propose a new solution to clamp the gain of this amplifier thereby cancelling this sort of gain-suppression-induced crosstalk.

The following table gives an summary of the symbols used in this chapter. For some parameters, a typical value is indicated. These are used throughout this chapter, except where otherwise noted.

Symbol	Value	Name
N		Number of signal amplifiers
L_a	400 μm	If only one amplifier is used, L_a denotes the length of this amplifier. If two amplifiers are used, L_a denotes the length of the common amplifier
L_c	400 μm	Length of the signal amplifiers
L_p	10 mm	Length of passive cavity, may differ from channel to channel due to a different length of the access waveguides to the multiplexer
L	$L_a + L_p (+ L_c)$	Total cavity length, same remark as for L_p
R_1, R_2	0.9, 0.32	Facet power reflectivity
r_1, r_2	$\sqrt{0.9}, \sqrt{0.32}$	Facet amplitude reflectivity
d	120 nm	Active layer height
w	2 μm	Active layer width
A_{eff}	wd/Γ	Effective waveguide cross-section
V_a	wdL_a	Active layer volume

Γ	0.245	Confinement factor
f		Total loss of passive cavity, including losses at the active/passive transition
α_p	$\ln(1/f)/L_a$	Distributed loss of passive cavity
α_s	2000m^{-1}	Internal loss of amplifiers
α_m	$\ln(1/(r_1 r_2))/L_a$	Distributed mirror loss
$\beta_{a/p}$	$2\pi n_{a/p}/\lambda_0$	Propagation constant in active/passive waveguides
g	m^{-1}	Material gain
$n_{a/p}$	3.229	Effective index of active/passive waveguides
$\bar{n}_{a/p}$	3.5	Effective group index of active/passive waveguides
$n_e / \bar{n}_e$		Weighted average (group) effective index ($n_e = (n_a L_a + n_p L_p)/L$)
v_g	$c/\bar{n}_e$	Group velocity
τ_L	$2L/v_g$ (0.23ns)	Roundtrip time
$\delta\nu$	$1/\tau_L$ (4.3GHz)	Longitudinal mode spacing
N (N_{th})		(threshold) carrier density
N_0	1×10^{24}m^{-3}	Transparency carrier density
$S^{\#}$		Number of photons in active part of the cavity
S	$\Gamma S^{\#}/V$	Average photon density in active part
K		Spontaneous emission enhancement factor
n_{sp}	2	Inversion factor
α	5	Linewidth enhancement factor
τ_e		Carrier Lifetime
A	0.25×10^{9}s^{-1}	Monomolecular carrier recombination coefficient
B	1×10^{-16}m^{3}s^{-1}	Bimolecular carrier recombination coefficient
C	0.3×10^{-40}m^{6}s^{-1}	Auger recombination coefficient
$\Delta\nu_{FSR}$		Free Spectral Range (FSR) of the multiplexer
$\Delta\nu_{3dB}$	75GHz	3dB-bandwidth of the multiplexer
$\Delta\nu_{CS}$	200GHz	Channel spacing

Table 3-1 Symbols and typical values

2 Single channel long long-cavity lasers without common amplifier

Since, as explained already in the introduction, the interaction between the channels of a multi-wavelength laser without common amplifier is often negligible, this section investigates the properties of a single channel long-cavity laser as shown in Fig. 3-1b. In a first step, the rate-equations describing the behaviour of such a laser are derived (paragraph 2.1). Sub-

sequently, these rate equations are solved to obtain both the static and dynamic characteristics of this type of laser.

2.1 Rate equations for single channel long cavity lasers

In the amplifier, both the forward and the backward travelling power $P_f(z)$ and $P_b(z)$ is amplified due to stimulated emission, following

$$P_f(z) = P_{f0}\exp[(\Gamma g - \alpha_s)z] \tag{3-1}$$

where we assumed the gain g and the cavity loss α_s to be constant along the cavity. In the passive cavity, the power in the forward and backward travelling wave is reduced by a factor f, accounting for both localised losses such as the active-passive transition loss and distributed losses such as scattering loss. At the facets, the power is reflected with a power reflection coefficient R_i.

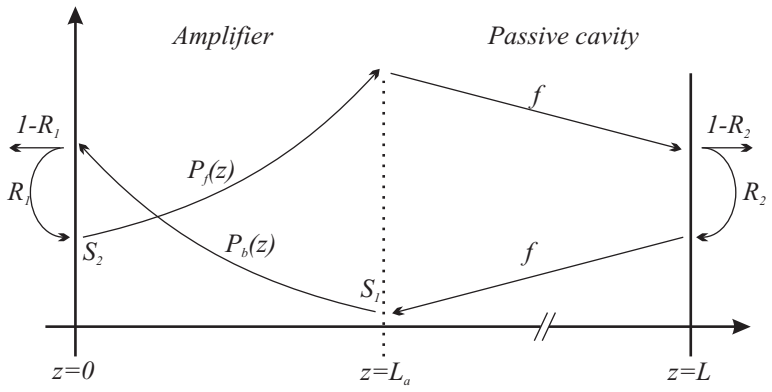

Fig. 3-2 Travelling wave model for long-cavity laser

To derive the lasing conditions, the field amplitudes instead of the optical powers should be considered. Doing so (cf. [1]), the condition for stationary laser action is easily obtained. If we define the round trip gain G_r as

$$G_r = f r_1 r_2 \exp\left(-2j\beta_a L_a - 2j\beta_p L_p + (\Gamma g - \alpha_s)L_a\right) \tag{3-2}$$

and denote the complex forward propagating field at $z = 0$ as $\mathrm{E}_{f0}(\omega)$, the threshold condition is given by:

$$\mathrm{E}_{f0}(\omega) = G_r \mathrm{E}_{f0}(\omega) \tag{3-3}$$

or

$$f r_1 r_2 \exp\left(-2j\beta_a L_a - 2j\beta_p L_p + (\Gamma g - \alpha_s)L_a\right) = 1 \tag{3-4}$$

r_1 and r_2 denote the amplitude reflection coefficients ($r_i = \sqrt{R_i}$). The absolute value of (3-4) yields the required threshold gain g_{th}, while a condition for the threshold frequency is derived from the phase of (3-1). For the threshold gain we obtain:

$$\begin{aligned}\Gamma g_{th} &= \alpha_s + \frac{1}{2L_a}\ln\left(\frac{1}{R_1 R_2}\right) + \frac{1}{L_a}\ln\left(\frac{1}{f}\right) \\ &= \alpha_s + \alpha_m + \alpha_p\end{aligned} \tag{3-5}$$

α_m is usually called the distributed mirror loss. Analogously, we may consider α_p as the distributed passive cavity loss.

From the phase of (3-4), we find:

$$\beta_a L_a + \beta_p L_p = m\pi \tag{3-6}$$

Since the propagation constants β_i are given by $\beta_i = \frac{2\pi\nu}{c} n_i$, with n_i the effective refractive index of the waveguide, this last equation yields the possible emission frequencies of the laser resonator:

$$\nu = \frac{mc}{2\left(L_a n_a + L_p n_p\right)} = \frac{mc}{2Ln_e} \tag{3-7}$$

with $L = L_a + L_p$ and n_e a weighted average of the effective refractive indices n_a and n_b. To calculate the longitudinal mode spacing, one must take into account the dispersion of the refractive index, yielding:

$$\delta\nu = \frac{c}{2\left(L_a \bar{n}_a + L_p \bar{n}_p\right)} = \frac{c}{2L\bar{n}_e} \tag{3-8}$$

with $\bar{n}_i$ the effective group index:

$$\bar{n}_i = n_i + \nu\frac{dn_i}{d\nu} \tag{3-9}$$

If we define the mean group velocity as $\mathrm{v}_g = \frac{c}{\bar{n}_e}$, the round trip time delay is given by:

$$\tau_L = \frac{2L}{\mathrm{v}_g} = \frac{1}{\delta\nu} \tag{3-10}$$

The optical gain of the amplifier is function of the injected carrier density N. Therefore, it is possible to introduce a threshold carrier density N_{th} determined by the threshold condition (3-5):

$$g\left(N_{th}\right) = g_{th}$$

The effective refractive indices n_i on the other hand, depend on the optical frequency. In the active section, the refractive index n_a depends also on the carrier density, so that the resonance frequency ν_{th} for $N = N_{th}$ may be introduced, given by:

$$\nu_{th} = \frac{mc}{2\left(L_a n_a\left(\nu_{th}, N_{th}\right) + L_p n_p\left(\nu_{th}\right)\right)} = \frac{mc}{2\left(L_a n_{a0} + L_p n_{p0}\right)} = \frac{mc}{2Ln_{e0}} \tag{3-11}$$

If the carrier density deviates slightly from its threshold value, the refractive indices in the active and the passive section may be expanded in terms of $\Delta\nu = \nu - \nu_{th}$ and $\Delta N = N - N_{th}$, yielding:

$$\begin{aligned} n_a &= n_{a0} + \frac{\partial n_a}{\partial \nu}\left(\nu - \nu_{th}\right) + \frac{\partial n_a}{\partial N}\left(N - N_{th}\right) \\ n_p &= n_{p0} + \frac{\partial n_p}{\partial \nu}\left(\nu - \nu_{th}\right) \end{aligned} \tag{3-12}$$

If these equations are inserted in (3-7) one obtains, together with (3-11)

$$\begin{aligned} \left(\nu - \nu_{th}\right) &= -\nu_{th}\frac{\partial n_a}{\partial N}\left(N - N_{th}\right)\frac{L_a}{L_a\overline{n}_{a0} + L_p\overline{n}_{p0}} \\ &= -\frac{\nu_{th}}{\overline{n}_e}\frac{\partial n_a}{\partial N}\left(N - N_{th}\right)\frac{L_a}{L} \end{aligned} \tag{3-13}$$

Eq. (3-13) also holds dynamically under modulation conditions and it forms the basis for the discussion of the FM-modulation behaviour of these lasers because it determines the relation between a carrier density variation and the induced frequency variation. Eq. (3-13) shows that for long cavity lasers the latter is smaller by a factor L_a/L compared to lasers without passive cavity.

The round trip gain G_r defined in (3-2) as

$$G_r = fr_1r_2\exp\left(-2j\beta_a L_a - 2j\beta_p L_p + \left(\Gamma g - \alpha_s\right)L_a\right) \tag{3-14}$$

may alternatively be written as

$$G_r = G_1 G_2 \tag{3-15}$$

with G_1 a frequency independent term

$$G_1 = fr_1r_2\exp\left[\left(\Gamma g - \alpha_s\right)L_a\right]\exp\left(-j\phi_G\right) \tag{3-16}$$

where

$$\phi_G = 2L_a\frac{\omega_{th}}{c}\frac{\partial n_a}{\partial N}\left(N - N_{th}\right) \tag{3-17}$$

and G_2 a frequency dependent term

$$\begin{aligned} G_2 &= \exp\left(-2j\frac{\omega_{th}}{c}L_a\left(n_{a0} + \frac{\overline{n}_a}{\omega_{th}}\left(\omega - \omega_{th}\right)\right) - 2j\frac{\omega_{th}}{c}L_p\left(n_{p0} + \frac{\overline{n}_p}{\omega_{th}}\left(\omega - \omega_{th}\right)\right)\right) \\ &= \exp\left(-j\tau_L\left(\omega - \omega_{th}\right)\right) \end{aligned} \tag{3-18}$$

The second equality holds since, by definition, $2\frac{\omega_{th}}{c}\left(L_a n_{a0} + L_p n_{p0}\right) = 2\pi m$.

Consider now the time-dependent electric field for the forward travelling wave at $z = 0$, $E_{f0}(t)$. Since this field will essentially oscillate at the threshold frequency ω_{th}, it is useful to introduce a slowly-varying complex amplitude $\hat{E}_{f0}(t)$ such that:

$$E_{f0}(t) = \hat{E}_{f0}(t)\exp(j\omega_{th}t) \tag{3-19}$$

Fourier transformation of (3-3) using (3-16) and (3-18) yields:

$$\hat{E}_{f0}(t) = G_1\hat{E}_{f0}(t-\tau_L) \tag{3-20}$$

It is convenient to introduce a normalised complex field amplitude $E(t)$, so that the absolute square of this field amplitude corresponds to the number of photons $S^{\#}(t)$ inside the active part of the laser cavity:

$$S^{\#}(t) = \left|E(t)\right|^2$$

or (3-21)

$$E(t) = \sqrt{S^{\#}(t)}\exp(j\phi(t))$$

The phase $\phi(t)$ just corresponds to the phase of the slowly varying amplitude of the forward travelling wave $\hat{E}_{f0}(t)$. Using the normalised field amplitude, (3-20) may be replaced by:

$$E(t) = G_1 E(t-\tau_L) \tag{3-22}$$

or, with (3-21):

$$\begin{aligned} S^{\#}(t) &= G_1 G_1^* S^{\#}(t) \\ &= f^2 R_1 R_2 \exp\left[2(\Gamma g - \alpha_s)L_a\right] S^{\#}(t-\tau_L) \end{aligned} \tag{3-23}$$

Since the round trip gain G_1 is close to unity, this relation may be approximated by

$$S^{\#}(t) \approx \left[1 + 2(\Gamma g - \alpha_s - \alpha_m - \alpha_p)L_a\right] S^{\#}(t-\tau_L) \tag{3-24}$$

with α_m and α_p as defined at the beginning of this paragraph.

We should also account for the spontaneous generation of photons, yielding the final rate equation:

$$\begin{aligned} S^{\#}(t) &= f^2 R_1 R_2 \exp\left[2(\Gamma g - \alpha_s)L_a\right] S^{\#}(t-\tau_L) + KR_{sp}^{'} \\ &\approx \left[1 + 2(\Gamma g - \alpha_s - \alpha_m - \alpha_p)L_a\right] S^{\#}(t-\tau_L) + KR_{sp}^{'} \end{aligned} \tag{3-25}$$

with

$$R_{sp}^{'} = 2\frac{(L_a)^2}{L}\Gamma g n_{sp} \tag{3-26}$$

where n_{sp} is the inversion factor. This expression was derived by Henry [31] and denotes the amount of spontaneous emission, which is coupled into a single longitudinal mode. K is the enhanced spontaneous emission factor and is obtained by using a travelling wave laser model [31][32]. It is given by (equation 2.93 in [1]):

$$K = \left[\frac{\left(\sqrt{R_1} + f\sqrt{R_2}\right)\left(1 - f\sqrt{R_1 R_2}\right)}{f\sqrt{R_1 R_2}\,\ln\left(1/R_1 R_2 f^2\right)} \right]^2 \tag{3-27}$$

When the loss in the passive cavity is low, K is close to one and may be neglected (e.g. for standard lasers with $R_1 = R_2 = 0.32$, $K = 1.11$). However when the loss increases, K becomes more important and values over 20 may be obtained. This is shown in Fig. 3-3. The upper trace is for a laser with one HR-coated facet, the lower trace is for a laser without coatings. For the non-permanently coupled hybrid PAL described in chapter 5, the total loss in the passive cavity (including the coupling loss) is estimated to be between 5 and 7 dB, resulting in a value for K between 2.4 and 3.9. For the permanently bonded PAL of chapter 6, the loss was much higher (~12 dB), resulting in an equally high value for the spontaneous emission enhancement factor $K = 17$.

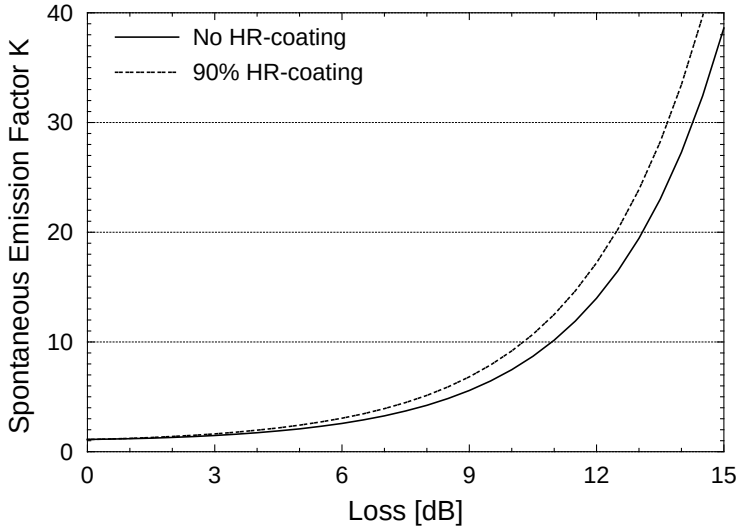

Fig. 3-3 Spontaneous emission enhancement factor K for a laser with no HR-coating ($R_1 = R_2 = 32\%$) and for a laser with HR-coating ($R_1 = 90\%$) versus the loss of the passive cavity.

If the variations during the round trip delay τ_L are small, one may use the relation $S^{\#}(t+\tau_L) - S^{\#}(t) = \tau_L \dfrac{dS^{\#}}{dt}$ to obtain:

$$\begin{aligned}\frac{dS^{\#}(t)}{dt} &= \frac{2L_a}{\tau_L}\left(\Gamma g - \alpha_s - \alpha_m - \alpha_p\right)S^{\#}(t) + KR_{sp} \\ &= \mathrm{v}_g\left(\Gamma g - \alpha_s - \alpha_m - \alpha_p\right)\frac{L_a}{L}S^{\#}(t) + KR_{sp}\end{aligned} \tag{3-28}$$

with $R_{sp} = \tau_L R_{sp}^{'} = \mathrm{v}_g\left(L_a/L\right)^2 \Gamma g n_{sp}$.

The additional term $\left(L_a/L\right)^2$ arising in this expression, compared to the expression for a laser without external cavity, may be explained as follows: as already mentioned above, R_{sp} denotes the spontaneous emission coupled into a single longitudinal mode. In the case of a laser with an external cavity, the latter are spaced much closer together than for a standard laser ($\delta\nu_{a+p}/\delta\nu_a = L_a/L$). Further, the light passes only during a fraction $\left(L_a/L\right)$ through the active part of the cavity. The latter is also the reason why the additional term $\left(L_a/L\right)$ arises in the first term of the right part of eq. (3-28).

Next to the rate-equation for the photon number, one may also set up an equation for the phase, using the relation:

$$\exp\left[j\left(\phi(t+\tau_L) - \phi(t)\right)\right] = \frac{E(t+\tau_L)E^*(t)}{\sqrt{S^{\#}(t+\tau_L)S^{\#}(t)}} \tag{3-29}$$

yielding, together with eqs. (3-16), (3-22) & (3-23):

$$\begin{aligned}\phi(t+\tau_L) - \phi(t) &= -\phi_g \\ &= -2L_a\frac{\omega_{th}}{c}\frac{\partial n_a}{\partial N}\left(N - N_{th}\right) \\ &= \alpha L_a\frac{\partial g}{\partial N}\left(N - N_{th}\right)\end{aligned} \tag{3-30}$$

for small variations during the round trip delay τ_L, this relation may be approximated by:

$$\frac{d\phi(t)}{dt} = \frac{1}{2}\alpha\mathrm{v}_g\frac{L_a}{L}\frac{\partial g}{\partial N}\left(N - N_{th}\right) \tag{3-31}$$

The latter is identical to the familiar form for short-cavity lasers, except for the term L_a/L arising from the fact that the carrier density modulation does only influence the value of the refractive index of the active part of the cavity and leaves the refractive index of the passive part unchanged.

Finally, we also need a rate equation for the carriers. If we define $N^{\#}$ as the total number of carriers and N as the carrier density, with $N^{\#} = NwdL_a$, the carrier rate equation is given by:

$$\frac{dN^{\#}}{dt} = \frac{I}{e} - R\left(N^{\#}\right) - \mathrm{v}_g \Gamma g S^{\#} \tag{3-32}$$

Alternatively, by dividing (3-32) by the volume of the active layer ($V_a = wdL_a$) and with S the average photon density in the active part of the cavity ($S = \frac{\Gamma}{wdL_A} S^{\#}$), the carrier rate equation may be written as:

$$\frac{dN}{dt} = \frac{I}{eV_a} - R(N) - \mathrm{v}_g g S \tag{3-33}$$

where

$$R(N) = AN + BN^2 + CN^3 \tag{3-34}$$

with A, B and C respectively the monomolecular, the bimolecular and the Auger-recombination coefficient.

2.2 Threshold current and output power

In this paragraph, we will derive the threshold current, the output power and the differential quantum efficiency of a long-cavity laser under static operating conditions. For that purpose, all time derivatives in the rate-equations obtained in the previous paragraph are set to zero.

From the carrier rate equation (3-33), the threshold current may be calculated by setting the photon density to zero, yielding:

$$I_{th} = eV_a R(N_{th}) \tag{3-35}$$

with the threshold carrier density N_{th} determined from the threshold gain $g_{th}(N_{th})$. Since, under laser operation, the carrier density remains clamped at its threshold level, relation (3-33) yields also:

$$\frac{\Delta S}{\Delta I} = \frac{1}{\mathrm{v}_g g_{th} eV_a} \tag{3-36}$$

S is the mean photon density in the cavity. Using a travelling wave amplifier model the incremental power emitted from both facets may be easily obtained: if S_1 and S_2 denote the photon density at the beginning of the amplifier associated respectively with the forward and the backward travelling wave as indicated in Fig. 3-2, S is given by

$$S = (S_1 + S_2)\frac{1}{L_a}\int_0^{L_a} \exp\left[(\Gamma g - \alpha_s)x\right] dx \tag{3-37}$$

The output power at the left and the right facet is respectively given by:

$$P_1 = Av_g h\nu(1-R_1)\exp[\Gamma(g-\alpha_s)L_a]S_1$$
$$P_2 = Av_g h\nu\frac{(1-R_2)}{R_2 f}S_1 \tag{3-38}$$

From (3-36)-(3-38) combined with (3-4) to eliminate the gain g_{th}, the external differential quantum efficiencies are calculated as:

$$\frac{\Delta P_1}{\Delta I} = \frac{h\nu}{e}\eta_{ext,1} = \eta_i \frac{h\nu}{e}\frac{\alpha_p+\alpha_m}{\alpha_s+\alpha_p+\alpha_m}\frac{(1-R_1)f\sqrt{R_2}}{\left(1-f\sqrt{R_2R_1}\right)\left(f\sqrt{R_2}+\sqrt{R_1}\right)}$$
$$\frac{\Delta P_2}{\Delta I} = \frac{h\nu}{e}\eta_{ext,2} = \eta_i \frac{h\nu}{e}\frac{\alpha_p+\alpha_m}{\alpha_s+\alpha_p+\alpha_m}\frac{(1-R_2)f\sqrt{R_1}}{\left(1-f\sqrt{R_2R_1}\right)\left(f\sqrt{R_2}+\sqrt{R_1}\right)} \tag{3-39}$$

or

$$\frac{\Delta P_j}{\Delta I} = \frac{h\nu}{e}\eta_{ext}\xi_j \tag{3-40}$$

with η_{ext} defined by:

$$\frac{\eta_{ext}}{\eta_i} = \frac{\alpha_p+\alpha_m}{\alpha_s+\alpha_p+\alpha_m} = \frac{\alpha_p+\alpha_m}{\Gamma g_{th}}$$

η_i is the internal differential efficiency and introduced here to account for internal leakage processes.

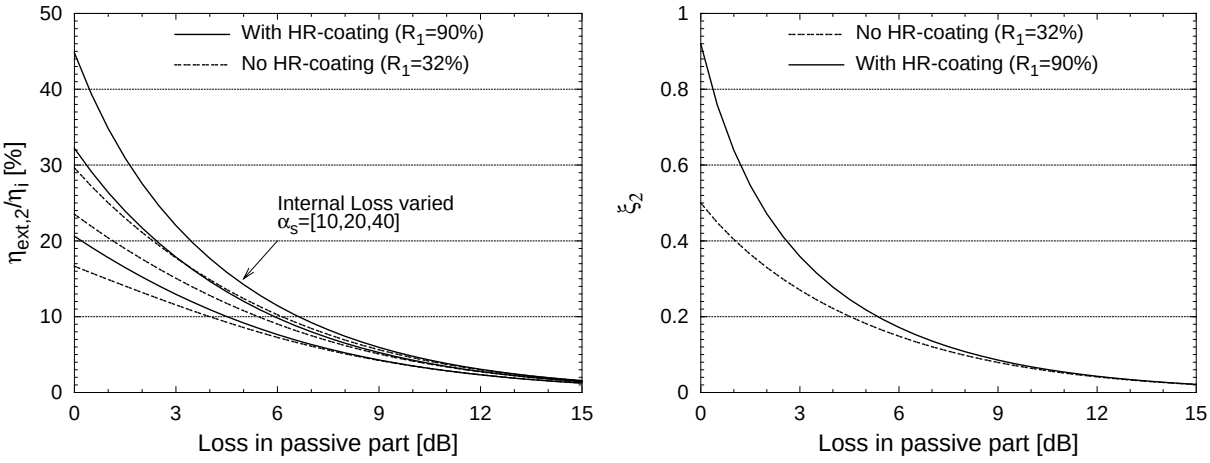

Fig. 3-4 a) Differential quantum efficiency $\eta_{ext,2}/\eta_i$ for a laser with a 400 μm long amplifier versus the loss in the passive cavity. The solid curves represent the external loss in a laser with an HR-coating applied to one facet while the broken lines are for a laser without coating. In both cases, the internal loss is varied from 10/cm to 40/cm. b) The coefficient ξ_2 defined in (3-40).

These equations may also be obtained from the standard equations for lasers without passive cavity (e.g. see eq. (2.86) in [1]) by replacing R_2 by an effective reflection coefficient

$R_{2,eff} = R_2 f^2$ and taking into account that the output power is taken after having passed the passive cavity once. Fig. 3-4 shows the external quantum efficiency $\eta_{ext,2}$ for a laser with a 400 µm long amplifier. The internal loss and the reflectivity of one facet were varied. In order to obtain the external efficiency for lasers with other amplifier lengths, the internal loss must be changed accordingly: the characteristic obtained for a laser with $L_a = 800\mu m$, $\alpha_s = 1000$ is identical to the one with $L_a = 400\mu m$, $\alpha_s = 2000$ as may be easily seen from (3-39) and the definitions of α_m and α_p. Fig. 3-4b shows the coefficient ξ_2 defined in (3-40). Both pictures reveal that an HR-coating becomes less important with increasing cavity loss.

Fig. 3-5 shows a comparison between the static laser parameters calculated using the rate equations derived here and using a rigorous laser model (CLADISS, [2]). To calculate the threshold gain we used a gain function $g(N)$, which was derived from the gain function $g(N,\lambda)$ employed in CLADISS, following:

$$\begin{aligned} g(N) &= \max_{\lambda}\left(g(N,\lambda)\right) \\ &= a_1 N^2 + a_2 N - a_3 \end{aligned} \tag{3-41}$$

with $a_1 = 7.86\times10^{-45}\text{m}^5$, $a_2 = 8.91\times10^{-21}\text{m}^2$, $a_3 = 2.61\times10^{4}\text{m}^{-1}$. This function is slightly superlinear. For the other parameters, we used the values indicated in Table 3-1.

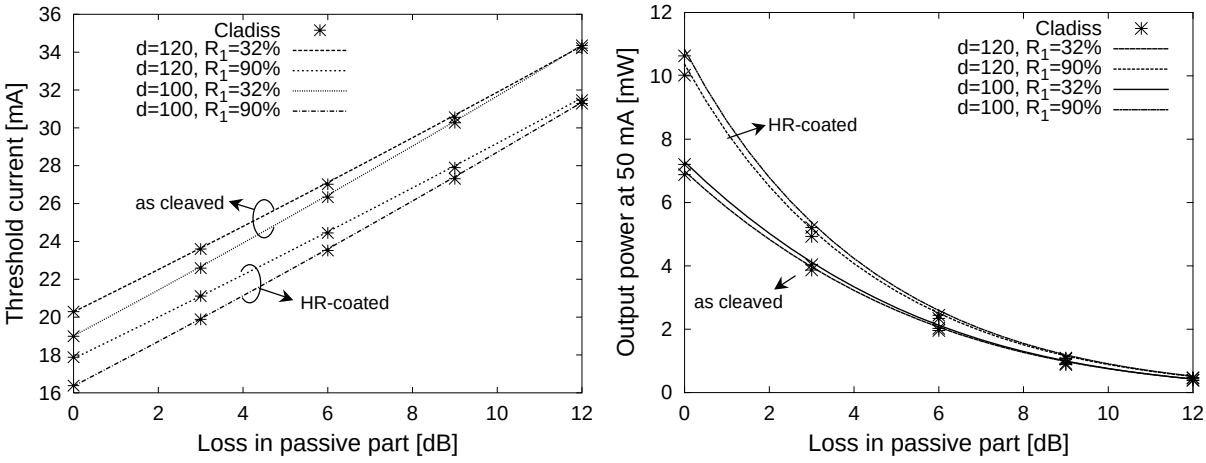

Fig. 3-5 Comparison between the threshold current (left) and the output power at 50 mA drive current (right), calculated using a rigorous laser model (CLADISS) - represented by the crosses - and using the above derived rate equations, as function of the loss in the passive cavity, for different laser parameters. This calculation was carried out for a laser with a bulk active layer with thickness $d = 100$ nm and $d = 120$ nm.

Some general trends may be seen from these pictures:

- The threshold current increases and the output power decreases strongly with increasing cavity loss.

- The threshold current decreases and the output power increases when applying a HR-coating to one facet. However, as was already seen from Fig. 3-4a, the effect on the output power becomes much less important when the cavity loss increases.
- For low loss cavities, the threshold current decreases and the output power increases when the active layer thickness is decreased from 120 nm to 100 nm. However, when the cavity loss increases, the difference becomes smaller and for $\alpha_p = 12$ dB, the threshold currents are almost the same.

From Fig. 3-5a, it is obvious that the threshold current calculated using formula (3-35) agrees very well with the value obtained from CLADISS. The output power at the right facet shown in Fig. 3-5b, was calculated following:

$$P_2 = \frac{h\nu}{e}\eta_{ext,2}\left(I - I_{th}\right) \tag{3-42}$$

with $\eta_{ext,2}$ from (3-39). As can be seen from Fig. 3-5b, the output power calculated using the rigorous model is somewhat smaller than the value obtained from the rate-equations. The difference becomes larger when the loss of the passive cavity increases and when a high-reflective (HR) coating is applied to the left facet. This may be understood from Fig. 3-6. This figure shows the forward and backward travelling power, the total power and the electron density along the active part of the laser cavity for two different lasers: one with no HR-coating applied and with no loss in the passive cavity, the other one with HR-coating and with a high loss passive cavity. All the characteristics were calculated using CLADISS except for the total power, which was also calculated using the travelling wave model that was used to derive (3-37). When deriving the rate equations, we assumed a uniform electron density in the active part of the laser cavity. From Fig. 3-6a, it is apparent that this is a very good approximation for a laser with a low-loss passive cavity. Moreover, we see that the total travelling power calculated using the rate-equations and calculated using the rigorous model is almost identical in this case. However, for the laser in Fig. 3-6b this is no longer the case: due to carrier depletion, there is an asymmetry in the electron density, resulting in a non uniform gain and a difference between the traces representing the total power along the cavity, calculated using CLADISS and calculated using the simple model.

In general however, the discrepancy between the rigorous and the simple model is small and the general trends predicted by our laser model and CLADISS are the same. Therefore, the rate-equation approach will be useful to predict the static laser characteristics and to optimise a PAL design towards threshold current or output power.

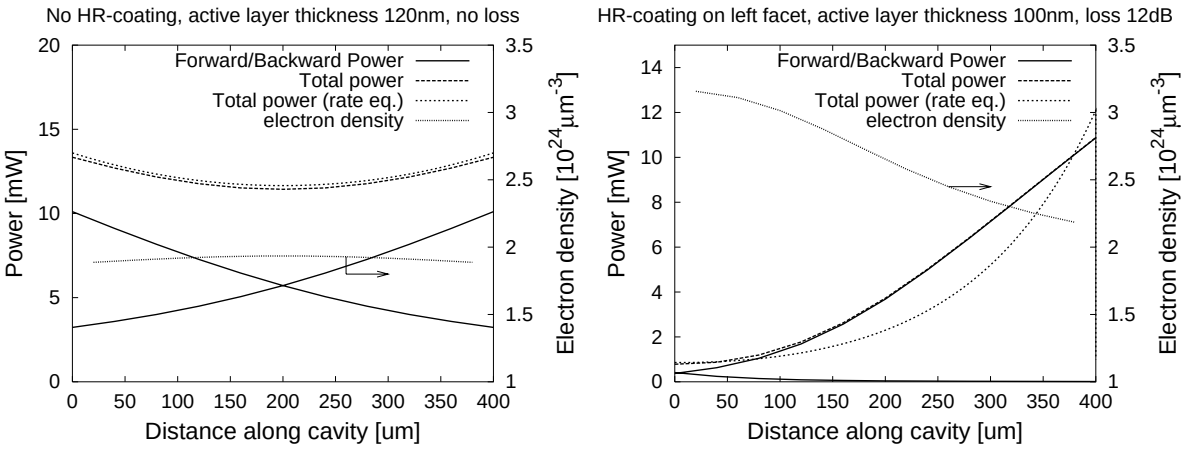

Fig. 3-6 Power density and electron density along the active part of a laser. The left picture is for a laser with no loss in the passive cavity and with no HR-coatings applied. The right picture is for a laser with a 12 dB passive cavity loss and a 90 % HR-coating.

As an illustration, we calculated the threshold current and the threshold current density of a laser as function of the length of the amplifier, for different values of the cavity loss. For the modal gain we used the relation obtained from experimental results for a $3\,\mu m$ wide ridge laser with the same cross-section as the amplifiers to be used in the monolithically integrated PAL (see chapter 4, section 1.1). The results are depicted in Fig. 3-7. These were for a laser with one HR-coated facet ($R_1 = 0.9 / R_2 = 0.32$). If no HR-coating is applied, the cavity loss is increased by approximately 2.5 dB. Also for the internal loss ($\alpha_s = 4.5$ cm^{-1}) and the internal efficiency ($\eta_i = 0.85$), we used experimentally obtained values.

As shown in Fig. 4-6, the gain saturates with increasing current density. Therefore, the threshold condition cannot be obtained when the amplifier is shorter than a certain minimum length, which depends on the total cavity loss. Further, Fig. 3-7 shows that the optimal amplifier length for minimising the threshold current increases from $150\,\mu m$ for the cavity with no loss to $800\,\mu m$ for the 12 dB loss cavity. However, one may also notice that the threshold current increases only slightly with increasing amplifier length, while the threshold current density decreases strongly. Therefore, it may be favourable to use a longer amplifier, thereby reducing the possibility of additional gain reduction due to active layer heating.

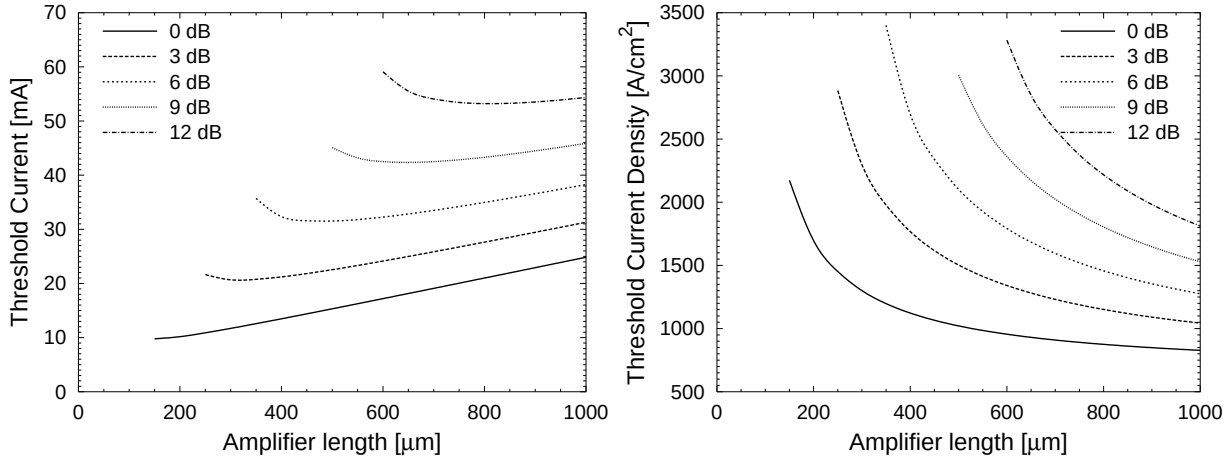

Fig. 3-7 Threshold current and threshold current density as function of cavity length. The loss of the passive cavity is varied between 0 and 12 dB

We also calculated the current and the current density needed to obtain an output power of 2 mW. These are depicted in Fig. 3-8. Since the internal loss is very small, the differential quantum efficiency is almost independent of the cavity length (e.g. for a 6 dB loss cavity loss, $\eta_{ext,2}$ decreases from 14.4% to 11.9 % for the amplifier length increasing from $100\,\mu m$ to $1000\,\mu m$). Therefore, the curves in Fig. 3-8 are almost identical to these in Fig. 3-7, except for a shift depending on the cavity loss.

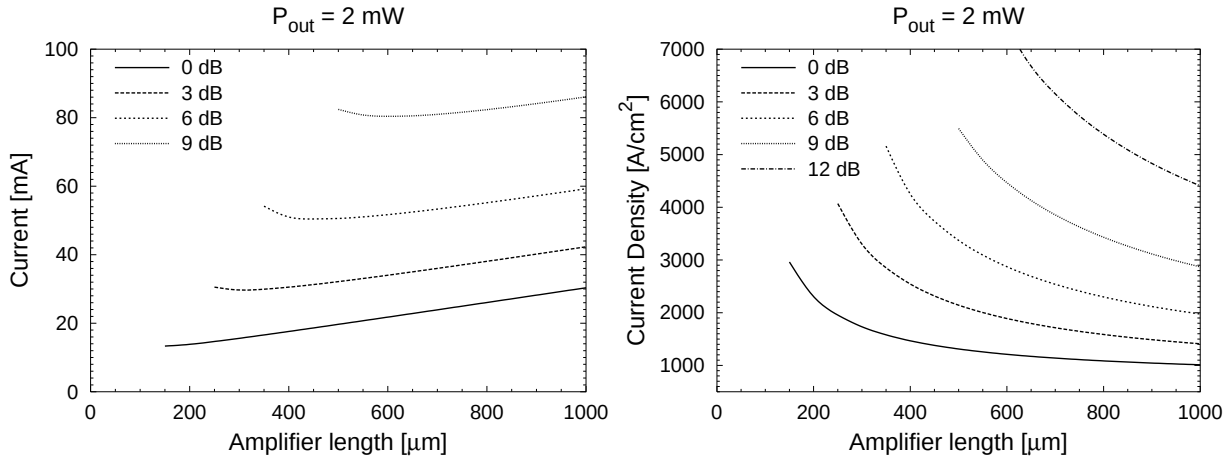

Fig. 3-8 Current and current density for an output power of 2 mW as function of cavity length. The loss of the passive cavity is varied between 0 and 12 dB

2.3 Side Mode Suppression Ratio

2.3.1 Multi-mode rate-equations

Until now, the rate-equations were derived for a single lasing mode. If several lasing modes are considered, a rate-equation for each mode can be written down, yielding:

$$\begin{aligned} S_i^{\#}(t+\tau_L) &= f_i^{\,2} R_1 R_2 \exp\left[2(\Gamma g_i - \alpha_s)L_a\right] S_i^{\#}(t) + K_i R_{sp,i}^{'} \\ &\approx \left[1 + 2(\Gamma g_i - \alpha_s - \alpha_m - \alpha_{p,i})L_a\right] S_i^{\#}(t) + K_i R_{sp,i}^{'} \end{aligned} \tag{3-43}$$

Note that the loss in the passive cavity, f_i, may depend on the mode number. For non-lasing modes, the spontaneous emission factor K_i is somewhat smaller than the value defined by eq. (3-27), but for moderate cavity losses, this effect is negligible.

If we restrict ourselves to the stationary behaviour, the photon number in each lasing mode may be calculated by combining (3-43) with eq. (3-26), which defines the spontaneous emission coefficient $R_{sp,i}^{'}$:

$$S_i^{\#} = \frac{L_a}{L} \frac{Kn_{sp}}{\left(\dfrac{\alpha_s + \alpha_{p,i} + \alpha_m}{\Gamma g_i}\right) - 1} \tag{3-44}$$

From (3-36) and (3-39), we obtain the following relation between the output power and the photon density:

$$\begin{aligned} P_{2,i} &= h\nu \frac{\eta_{ext,2}}{\eta_i} \mathrm{v}_g g_{th,i} V_a S_i \\ &= \mathrm{v}_g h\nu (\alpha_{p,i} + \alpha_m) \xi_2 S_i^{\#} \end{aligned} \tag{3-45}$$

(3-44) together with (3-45) may be used to estimate the required gain difference $\delta g = g_i - g_0$ to obtain a good side mode suppression ratio. If we define T as the required ratio between the output powers ($T = S_0/S_1 = P_{2,0}/P_{2,1}$), δg is given by:

$$\delta g / g_{th} = T \frac{L_a}{L} \frac{Kn_{sp}}{P_{2,0}} \mathrm{v}_g h\nu (\alpha_{p,0} + \alpha_m) \xi_2 \tag{3-46}$$

For a given output power and a given value of T, the required gain difference δg increases with increasing cavity loss. Further, there is a hidden dependence on L_a, through the term $(\alpha_{p,0} + \alpha_m)$. Eq. (3-46) seems to indicate that there is a strong dependence on the length of the passive cavity through the factor L_a/L. However, one has to take into account that for a long cavity laser, the amount of modes within a given wavelength interval increases by the inverse of this factor.

If the modes are located far away from each other, as is the case for modes in different passbands of the Phased-Array, the required gain difference δg to obtain single mode operation must arise from the spectral dependence of the gain or the cavity loss. In the following paragraph, we use this observation to calculate the minimum free spectral range, which is necessary to avoid multi-passband lasing. The modes within a single passband however, experience an enhanced single-longitudinal mode stability due to a strong non-linear wave-mixing

effect. This effect is important in long-cavity lasers because the longitudinal mode spacing is very narrow and is described in more detail in 2.3.3.

2.3.2 Required FSR to prevent multi-passband lasing.

Practical demultiplexers typically show a periodical behaviour, with a free spectral range $\Delta\lambda_{FSR}$. For both grating and Phased-Array demultiplexers the *FSR* is given by

$$\Delta\lambda_{FSR} = \lambda_c / m \tag{3-47}$$

with λ_c the central wavelength of the demultiplexer and *m* the grating order*. If the difference in gain experienced by two modes in a different passband of the demultiplexer is smaller than the difference required to obtain a good SMSR as calculated in the previous paragraph, multi-passband lasing (MPB) will occur.

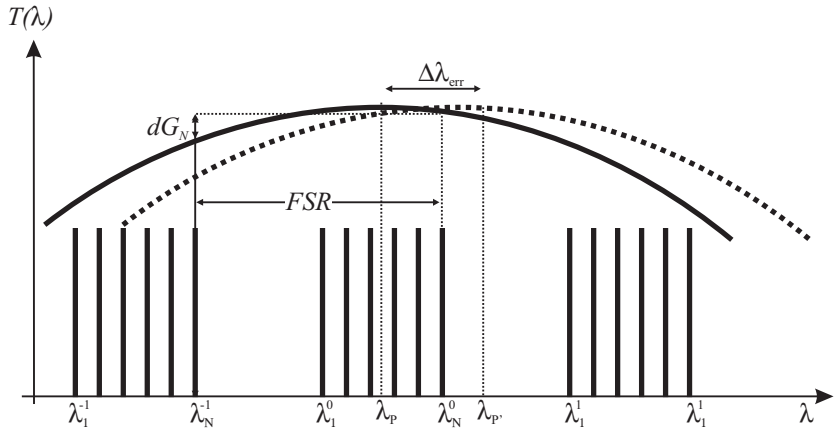

Fig. 3-9 Multi-passband lasing mechanism

This is illustrated in Fig. 3-9. The different wavelength channels are denoted as λ_j^i with *i* indicating the passband number and *j* the channel number within each passband. $i = 0$ denotes the central (desired) passband.

If we assume that the gain peak ($\lambda = \lambda_p$) coincides with the central wavelength of the multiplexer, the worst SMSR-condition occurs for the wavelengths λ_1^0 and λ_N^0 at the outer edge of the passband. If we define the normalised gain as $G_j^i = g_j^i / g_{th}$, with g_{th} obtained from eq.(3-5), then, to prevent MPB, the normalised gain difference $dG_N = G(\lambda_N^0) - G(\lambda_N^{-1}) = G_N^0 - G_N^{-1}$, has to be larger than the required minimum gain difference $dG_{\min}$ to obtain a good SMSR:

---

* For Phased-Array demultiplexers, the grating order is in fact the modified grating order given by $m = M \dfrac{n_g}{n_{eff}}$ (see chapter 2, section 4.1)

$$G_N^0 > G_N^1 + dG_{\min}$$

or (3-48)

$$dG_N > dG_{\min}$$

with $dG_{\min} = \delta g_{\min} / g_{th}$ and $\delta g_{\min}$ obtained from (3-46).

An analogous condition may be obtained for $dG_1 = G_1^0 - G_1^1$.

If we, for convenience, expand the gain spectrum around its maximum yielding a parabola, G may be written as

$$G = G_p - \left[2\frac{(\lambda - \lambda_p)}{\Delta\Lambda} \right]^2 \tag{3-49}$$

From (3-48)-(3-49) and using $\lambda_j^{i+1} = \lambda_j^i + \Delta\lambda_{FSR}$ we obtain the following condition for obtaining a good SMSR:

$$\left| \lambda_j^0 - \lambda_c \right| < \frac{\Delta\lambda_{FSR}}{2} - \frac{(\Delta\Lambda)^2 dG_{\min}}{8\Delta\lambda_{FSR}} = \frac{\Delta\lambda_{FSR} - \Delta\lambda_G}{2} \tag{3-50}$$

indicating that the useful range of the FSR is decreased by an amount $\Delta\lambda_G = (\Delta\Lambda)^2 dG_{\min} / 4\Delta\lambda_{FSR}$.

In practise however, due to fabrication tolerances*, it will be very difficult to force the gain peak wavelength to coincide with the central wavelength of the demultiplexer. If we assume that the gain peak wavelength is shifted to a value $\lambda_{p'}$ with $\lambda_{p'} - \lambda_c = \Delta\lambda_{err}$ and want to make sure that the gain for channel λ_j^0 is larger than the gain for channel λ_j^1 in the next passband, the following condition is derived from Fig. 3-9:

$$\lambda_{p'} - \lambda_1^0 < \lambda_1^1 - \lambda_{p'} - \Delta\lambda_G \tag{3-51}$$

with $\Delta\lambda_G$ as defined in (3-50) added to guarantee a good SMSR. After some manipulation this condition may be rewritten as:

$$\Delta\lambda_{err} < \frac{1}{2}(\Delta\lambda_{FSR} - N\Delta\lambda_{CS} - \Delta\lambda_G)$$

or, as a condition on the free spectral range: (3-52)

$$\Delta\lambda_{FSR} > 2\Delta\lambda_{err} + N\Delta\lambda_{CS} + \Delta\lambda_G$$

---

* This uncertainty is determined primarily due to the uncertainty on the absolute material peak gain but also due to the uncertainty on the exact threshold carrier density, since, with increasing threshold gain and carrier density, the gain peak wavelength shifts towards lower wavelength due to band filling effects.

An uncertainty $\Delta\lambda_{err} \approx 10$ nm seems unavoidable. Often however, the uncertainty is even larger. Consequently, from (3-52) it may be seen that a large FSR may be necessary to prevent MPB-lasing. Such a large FSR considerably increases the size of the multiplexer (see chapter 2, section 4.1). For that purpose, Doerr has proposed and demonstrated the use of a chirped Phased-Array to avoid MBP-lasing [30]. Chirping of the multiplexer destroys the periodicity of the transfer, by suppressing the transmission through the passbands next to the central passband. This adds only a small loss, does not increase the size of the laser and requires no additional manufacturing steps. Furthermore, by choosing the position of the central passband with respect to the gain peak, the linewidth enhancement factor α may be optimised as is sometimes done for DFB-lasers.

2.3.3 Single longitudinal mode stability

As demonstrated in the previous paragraph, eq. (3-46) is useful to calculate the SMSR of lasing modes that are spaced far away from each other. However, it cannot be used to explain the experimentally observed strong single mode stability in multi-wavelength lasers. Due to their long cavity, the longitudinal mode spacing is very narrow, ranging from only 1.76 GHz in [7] to 7.5 GHz for the most compact device published up to now [8]. Since the typical filter bandwidth of the multiplexer is between 50 GHz and 150 GHz, there are several modes around the filter peak wavelength that show only a very small net gain difference and one would expect these lasers to be multi modal. However, side mode suppression ratios over 40 dB have been observed experimentally (e.g. see [9] or chapter 5). Originally, it was thought that additional filtering arising from Fabry-Pérot cavities caused by internal reflections selects the longitudinal mode at which the laser oscillates [10]. In the past, such a theory was successfully used to explain the spectral characteristics of lasers with deliberately induced damage centres along the cavity [11]. However, while for more recent devices the intra-cavity reflections could almost completely be removed by using an improved monolithic integration technology [9], they even show a better SMSR. It turns out that not these reflections but the combined effect of a strong self induced carrier modulation and the intra-cavity filter are responsible for this excellent SMSR: beating of neighbouring modes modulates the carrier density at the mode-spacing frequency Ω. Since the modulation of the carrier density also produces a variation of the dielectric constant, both a dynamic gain lattice and a dynamic phase lattice will be produced by the wave beating. The phase grating will scatter laser radiation at a frequency ω_0 in the same direction, with a Stokes' shift Ω, and as a consequence generates an asymmetric contribution to the gain spectrum such that the gain is enhanced for modes lying on the long-wavelength side but reduced for the shorter-wavelength modes.

This model was proposed by Bogatov [12] and could explain well experimental results in lasers and travelling wave amplifiers with an inter-mode spacing limited to a few GHz [18][19][22][23][24]. The strength of this interband effect decreases rapidly when the longi-

tudinal mode spacing becomes comparable to the reciprocal of the carrier lifetime ($\tau_e \approx 1$ ns). In that case, intraband dynamics such as carrier heating and spectral hole burning, which affect the shape of the carrier density distribution in energy space, but not the total carrier density, become increasingly important. These intraband dynamics are governed by the small intraband relaxation times (50 fs ~ 1 ps) implying that they have a low efficiency but at the same time a large bandwidth (> 1 THz) [21][25]. Several authors have tried to estimate the relative importance of the intra- and interband wave mixing effects starting from a density matrix approach [14][15][16] [17] [20]. From all these contributions, it became clear that, in the frequency range we are considering here ($\Omega < 100$ GHz), the effects arising from spectral hole burning and carrier heating are negligible compared to the interband effect arising from the self-induced carrier density pulsation.

To make an estimation of its strength, we calculate the gain difference experienced by two modes with electric field strengths E_0, E_1. In this paragraph, E_i denote the real electric fields, given by

$$\begin{aligned} E_0 &= E_{00}\exp(j\omega_0 t) + \text{cc} \\ E_1 &= E_{10}\exp(j\omega_1 t) + \text{cc} \end{aligned} \tag{3-53}$$

and normalised so that the number of photons in the active part in each mode is given by $S_i^{\#} = |E_i|^2$.

The total photon number is given by $S^{\#} = S_0^{\#} + S_1^{\#}$. However, if the photon density at a certain axial position of the cavity is considered, the beat signal $E_0 E_1$ between both modes has to be taken into account:

$$\left(S^{\#}/V\right)_z = \left(S_0^{\#} + S_1^{\#}\right)/V + \left(2E_0E_1/V\right)_z \tag{3-54}$$

Using (3-53), this beat signal is given by

$$E_0 E_1 = E_{00}E_{11}^{*}\exp(j\Omega t) + \text{cc} \tag{3-55}$$

with the beat frequency $\Omega = \omega_0 - \omega_1$.

The beat signal will induce a variation of the carrier density, $N = N_0 + \delta N$, with N_0 the carrier density without the beat signal, yielding for the carrier density rate-equations:

$$\begin{aligned} \frac{dN_0}{dt} &= \frac{I}{eV_a} - R(N_0) - \mathrm{v}_g \Gamma g \left(S_0^{\#} + S_1^{\#}\right)/V_a \\ \frac{d\delta N}{dt} &= -\frac{\delta N}{\tau_e} - \mathrm{v}_g \Gamma \frac{\partial g}{\partial N}\delta N \left(S_0^{\#} + S_1^{\#}\right)/V_a - 2\mathrm{v}_g \Gamma g\, E_0E_1/V_a \end{aligned} \tag{3-56}$$

Eq. (3-56) reveals that also δN will vary with the beat frequency and inserting (3-55) into (3-56) yields:

$$\delta N = -\frac{2\mathrm{v}_g \Gamma g}{V_a} \frac{E_{00}E_{10}}{j\Omega + 1/\tau_{eff}} \exp(j\Omega t) + \mathrm{cc} \tag{3-57}$$

with the effective carrier recombination time given by

$$\frac{1}{\tau_{eff}} = \frac{1}{\tau_e} + \mathrm{v}_g \Gamma \frac{\partial g}{\partial N} \left(S_0^{\#} + S_1^{\#}\right) / V_a \tag{3-58}$$

This carrier density variation affects in turn the complex dielectric constant, which will also be modulated with the beat frequency, yielding for the complex non-linear polarisation:

$$\begin{aligned} P_{NL} &= \delta\varepsilon(t)\left(E_{00}\exp(j\omega_0 t) + E_{10}\exp(j\omega_1 t)\right) \\ &= \frac{\partial \varepsilon}{\partial N}\delta N(t)\left(E_{00}\exp(j\omega_0 t) + E_{10}\exp(j\omega_1 t)\right) \end{aligned} \tag{3-59}$$

By solving (3-59) and retaining only terms proportional to $\exp(j\omega_0 t)$ and $\exp(j\omega_1 t)$ one obtains:

$$P_{NL} = \delta\varepsilon_0 E_{00}\exp(j\omega_0 t) + \delta\varepsilon_1 E_{10}\exp(j\omega_1 t) \tag{3-60}$$

with

$$\begin{aligned} \delta\varepsilon_0 &= -\frac{\partial \varepsilon}{\partial N}\frac{2\mathrm{v}_g \Gamma g}{V_a}\frac{|E_{10}|^2}{(j\Omega + 1/\tau_{eff})} \\ \delta\varepsilon_1 &= -\frac{\partial \varepsilon}{\partial N}\frac{2\mathrm{v}_g \Gamma g}{V_a}\frac{|E_{00}|^2}{(-j\Omega + 1/\tau_{eff})} \end{aligned} \tag{3-61}$$

The additional gain induced by this polarisation is proportional to the imaginary part of the variation of the dielectric constant and after inserting the linewidth enhancement factor $\alpha = -\mathrm{Re}(\partial\varepsilon/\partial N)/\mathrm{Im}(\partial\varepsilon/\partial N)$, which relates the real and the imaginary part of the dielectric constant, one finally obtains:

$$\begin{aligned} \delta g_0 &= -C\frac{\partial g}{\partial N}\frac{2\mathrm{v}_g \Gamma g}{V_a}\frac{\alpha\Omega + 1/\tau_{eff}}{\Omega^2 + 1/\tau_{eff}^2}|E_{10}|^2 \\ \delta g_1 &= C\frac{\partial g}{\partial N}\frac{2\mathrm{v}_g \Gamma g}{V_a}\frac{\alpha\Omega - 1/\tau_{eff}}{\Omega^2 + 1/\tau_{eff}^2}|E_{00}|^2 \end{aligned} \tag{3-62}$$

C is a constant approximately equal to 0.5, introduced to account for the imperfect overlap between both modes [12].

The gain difference experienced between both modes is given by:

$$\delta g_1 - \delta g_0 = C\frac{\partial g}{\partial N}\frac{2\mathrm{v}_g \Gamma g}{V_a\left(\Omega^2 + 1/\tau_{eff}^2\right)}\left[\alpha\Omega\left(|E_{10}|^2 + |E_{00}|^2\right) + \frac{1}{\tau_{eff}}\left(|E_{10}|^2 - |E_{00}|^2\right)\right] \tag{3-63}$$

The second term within the square brackets implies that the higher intensity mode receives more gain than the lower intensity mode. This effect enhances the domination of one mode and the suppression of the other modes.

From the first term the before mentioned asymmetry of the non-linear gain is clearly visible: the higher frequency mode will receive less gain than the lower frequency one ($\Omega = \omega_0 - \omega_1$) and the amount of asymmetry is governed by the linewidth enhancement factor α. If the power in the second mode is much lower than the power in the main mode $\left(|E_{00}|^2 >> |E_{10}|^2\right)$, the gain difference $(\delta g_1 - \delta g_0)$ is proportional to $\frac{\alpha\Omega + 1/\tau_{eff}}{\Omega^2 + 1/\tau_{eff}^2}$. The latter is depicted in Fig. 3-10 for representative values of the effective carrier lifetime τ_{eff} and the linewidth enhancement factor α.

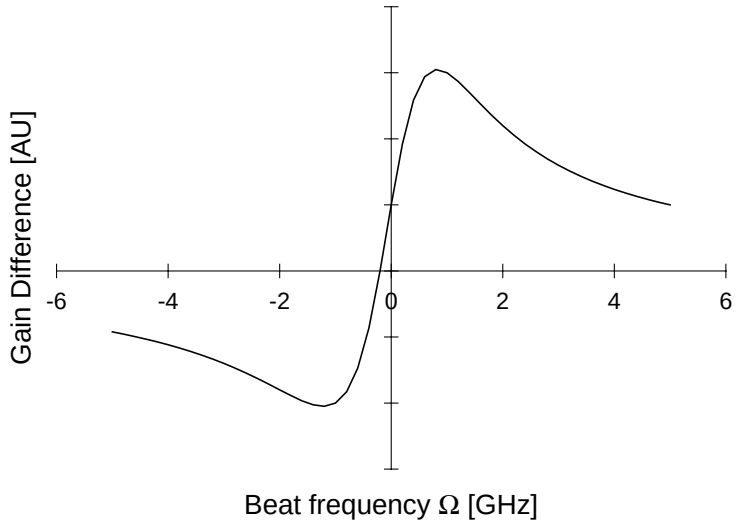

Fig. 3-10 The factor $\left[\left(\alpha\Omega + 1/\tau_{eff}\right)/\left(\Omega^2 + 1/\tau_{eff}^2\right)\right]$ with τ_{eff} = 1 ns and $\alpha = 5$

If this carrier induced intermodulation effect is combined with a suitable intra-cavity filter, single longitudinal mode operation may be obtained: when the laser is first turned on, operation in multiple modes will occur and the carrier density will vary according to the beat frequencies. However, as shown by (3-63), this carrier density pulsation will favour the highest intensity mode and the laser will choose one mode to operate at. Due to the frequency dependent term in (3-63), this mode will be placed at the low frequency side (high wavelength) side of the intra-cavity filter).

Using (3-63), Doerr [13] derived a design rule, which ensures single-longitudinal mode stability of long-cavity lasers. It is derived by postulating that the power change induced by the non-linear gain is larger than the power added by the spontaneous emission:

$$\delta g S^{\#} >> \frac{L_a}{L} g K n_{sp} \tag{3-64}$$

Using (3-63) and setting the maximum detuning equal to the 3dB-bandwidth of the filter $(\Omega = \Delta\omega_{3dB})$ one obtains:

$$\Delta\omega_{3dB} << \mathrm{v_g}\left(\pi S^{\#}\right)^{2/3}\left(\frac{\alpha\Gamma g'}{Kn_{sp}V_a LL_a}\right)^{1/3} \tag{3-65}$$

with $g' = dg/dN$ and $S^{\#}$ the number of photons in the active part of the cavity, which is related to the output power by (3-45). In Fig. 3-11, eq. (3-65) is depicted, as function of the output power, using parameters that are relevant for the hybrid lasers discussed in chapters 5 & 6 ($\Gamma = 0.245$, $V_a = 400\mu m \times 2.5\mu m \times 120nm$, $n_g = 3.56$, $n_{sp} = 1.5$ and $g' = 2.2\times10^{-20}\mathrm{m}^2$). The result, when depicted as function of the output power, is independent of the cavity loss.

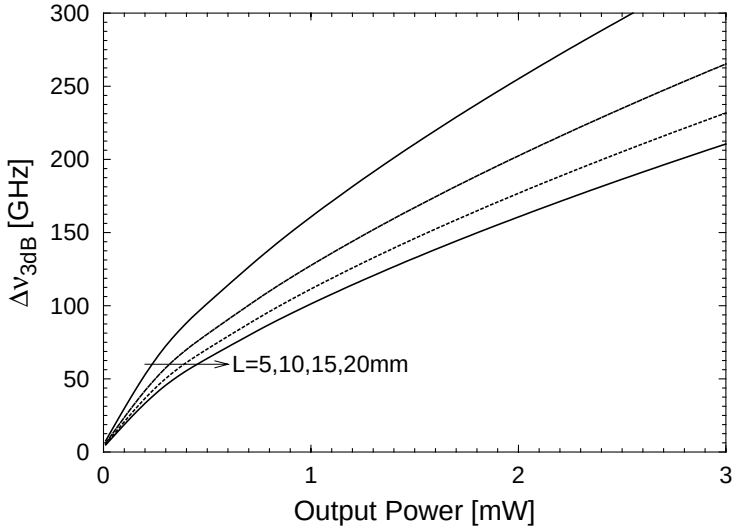

Fig. 3-11 $\Delta\nu_{3dB}$ calculated from eq. (3-65)

From a stability analysis of the single mode operation of a long-cavity laser with an intra-cavity filter, it was demonstrated that there is a stability region near the peak of the filter [33] (somewhat shifted to the lower frequency side). As long as a lasing mode stays in this region, all other modes will be suppressed effectively. However, if the operating mode is moved with respect to the filter such that it exits this region, the lasing will switch to another mode somewhere else in the stability region. This mechanism prevents effectively rapid mode hopping.

Effects not included in the model (intra-cavity reflections, multi-transverse moding, spatial hole burning) will distort the stability region. For that reason, it is important that this region is as wide as possible. This may be obtained by both decreasing the cavity length and decreasing the filter bandwidth. However, for practical multiplexers, there is a trade-off between both conditions: decreasing the filter bandwidth will typically increase the cavity length considerably and vice versa as demonstrated already in chapter 2. From the above-mentioned model, it was empirically found that minimising $L^3\omega_{3dB}$ maximises the stability region. This relation was used in chapter 2 for optimising the demultiplexer design.

2.4 Linewidth

The linewidth of a Fabry-Pérot laser containing a passive section has been calculated by Henry [31]. He obtains:

$$\Delta\nu = \frac{v_g \Gamma g n_{sp} K\left(1+\alpha^2\right)}{4\pi S^{\#}}\left(\frac{L_a}{L}\right)^2 \tag{3-66}$$

This is the same expression as obtained for a normal laser except for the additional factor $(L_a/L)^2$, indicating that the linewidth of long cavity lasers may be substantially reduced. Using expression (3-45) which relates the output power to $S^{\#}$, (3-66) may be reformulated as function of the output power, yielding:

$$\Delta\nu = h\nu\left(\alpha_p+\alpha_m\right)\xi_2 \frac{v_g^2 \Gamma g_{th} n_{sp} K\left(1+\alpha^2\right)}{4\pi P_2}\left(\frac{L_a}{L}\right)^2 \tag{3-67}$$

Fig. 3-12a shows the linewidth versus the inverse output power. The value of the loss in the passive cavity was varied between 5 dB and 14 dB. For the other parameters, we used the values indicated in Table 3-1. As expected from (3-67) the linewidth is inversely proportional to the output power and increases with increasing cavity loss due to the increasing modal gain Γg_{th} (note that the factor $\xi_2 K$ is rather independent of the cavity loss).

For obtaining Fig. 3-12b, the value of the linewidth enhancement factor was varied between 3 and 9.

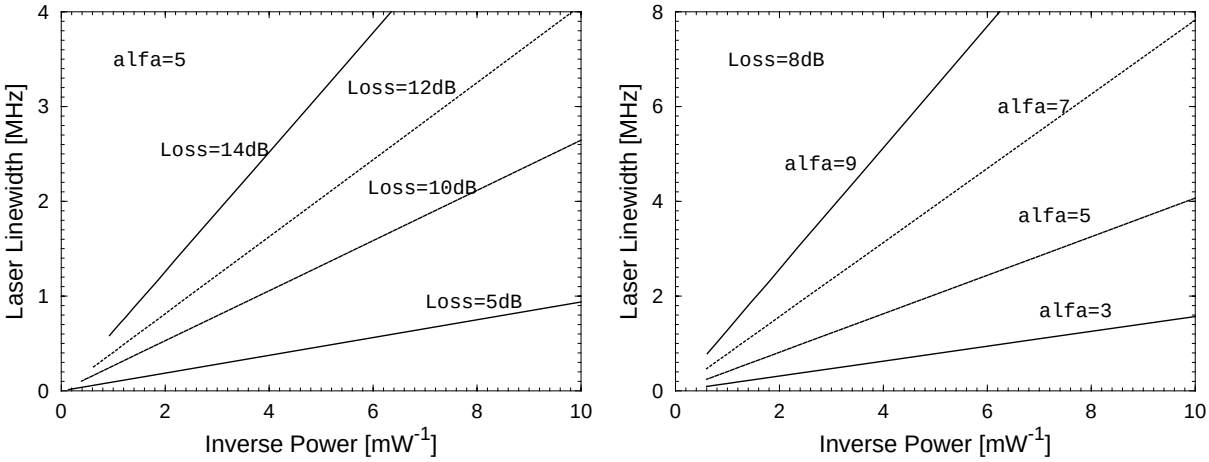

Fig. 3-12 Laser linewidth as function of inverse output power with varying cavity loss (left) or varying linewidth enhancement factor (right)

2.5 Dynamic Properties

In this section, the small signal response of a long cavity laser is analysed, starting from the rate equations derived in paragraph 2.1:

$$S(t) = \left[1+2\left(\Gamma g-\alpha_s-\alpha_m-\alpha_p\right)L_a\right]S\left(t-\tau_L\right)+\Gamma K R_{sp}^{'}/V_a \tag{3-68}$$

and

$$\frac{dN}{dt} = \frac{I - I_{th}}{eV_a} - \frac{1}{\tau_e}(N - N_{th}) - \mathrm{v}_g g S \tag{3-69}$$

In the last equation the recombination rate $R(N)$ was expanded around the threshold carrier density according to:

$$R(N) = R(N_{th}) + \frac{1}{\tau_e}(N - N_{th}) \tag{3-70}$$

with the carrier lifetime τ_e given by:

$$\frac{1}{\tau_e} = \left.\frac{dR(N)}{dN}\right|_{N=N_{th}} = A + 2BN_{th} + 3CN_{th}^2 \tag{3-71}$$

The gain is split into a linear and a non-linear part:

$$g = g_L(1 - \kappa_s S) \tag{3-72}$$

with κ_s the gain compression coefficient.

To derive the small signal modulation response of the laser, a small sinusoidal modulation ΔI is applied to the mean current $\langle I \rangle$ according to:

$$I(t) = \langle I \rangle + \mathrm{Re}(\Delta I \exp(j\omega t)) \tag{3-73}$$

If $|\Delta I| << \langle I \rangle$ the rate equations may be linearised around their stationary values, yielding also sinusoidal variations of the carrier density and the photon density:

$$\begin{aligned} N(t) &= \langle N \rangle + \mathrm{Re}(\Delta N \exp(j\omega t)) \\ S(t) &= \langle S \rangle + \mathrm{Re}(\Delta S \exp(j\omega t)) \end{aligned} \tag{3-74}$$

Eqs. (3-73)-(3-74) are now inserted into the rate equations (3-68)-(3-69), yielding for the photon rate equation:

$$(1 - \exp(-j\omega\tau_L) + \gamma)\Delta S = 2\Gamma L_a \frac{\partial g}{\partial N}\langle S \rangle \Delta N \tag{3-75}$$

with

$$\gamma = \frac{V_a K R_{sp}'}{\Gamma \langle S \rangle} + 2\Gamma L_a g_L \kappa_s \langle S \rangle \tag{3-76}$$

and we used:

$$\frac{\partial g}{\partial S} = -\kappa_S g_L \tag{3-77}$$

and

$$2\left(\Gamma g-\alpha_s-\alpha_p-\alpha_m\right)L_a=-\frac{KR_{sp}^{'}}{\left\langle S^{\#}\right\rangle} \tag{3-78}$$

The carrier rate equation yields:

$$\left(j\omega+\frac{1}{\tau_e}+\mathrm{v}_g\frac{\partial g}{\partial N}\langle S\rangle\right)\Delta N=\frac{\Delta I}{eV_a}-\mathrm{v}_g g\Delta S \tag{3-79}$$

Combining equations (3-75) and (3-79) gives us the following relation:

$$\begin{aligned}\left[\left(1-\exp\left(-j\omega\tau_L\right)+\gamma\right)\left(j\omega+\frac{1}{\tau_e}+\mathrm{v}_g\frac{\partial g}{\partial N}\langle S\rangle\right)+2\Gamma L_a\frac{\partial g}{\partial N}\langle S\rangle\mathrm{v}_g g\right]\Delta S \\ =2\Gamma L_a\frac{\partial g}{\partial N}\langle S\rangle\frac{\Delta I}{eV_a}\end{aligned} \tag{3-80}$$

Setting

$$\omega_r^2=\frac{L_a}{L}\langle S\rangle\Gamma g\frac{\partial g}{\partial N}\mathrm{v}_g^2 \tag{3-81}$$

and using (3-45), (3-80) one obtains:

$$\frac{\Delta P_2}{\Delta I}=\eta_{ext,2}\frac{1}{\left[\frac{1}{\omega_r^2\tau_L}\left(1-\exp\left(-j\omega\tau_L\right)+\gamma\right)\left(j\omega+\frac{1}{\tau_e}+\mathrm{v}_g\frac{\partial g}{\partial N}\langle S\rangle\right)+1\right]} \tag{3-82}$$

when $\omega\tau_L<<1$* this reduces to the familiar form

$$\frac{\Delta P_2}{\Delta I}=\eta_{ext,2}\frac{1}{\left[\left(\frac{j\omega}{\omega_r}\right)^2+\frac{j\omega}{\omega_d}+1\right]} \tag{3-83}$$

with the resonance frequency ω_r as defined in (3-81) and the damping frequency ω_d given by:

$$\omega_d=\frac{\omega_r^2}{\gamma/\tau_L+1/\tau_e} \tag{3-84}$$

To verify this model, we calculated the small-signal response of some lasers using a rigorous laser model (CLADISS, [2]) and compared the results with those obtained from the rate-equation model. For the differential gain, we used $g'=2.0\times10^{-20}\mathrm{m}^2$. For the recombination coefficients, we used experimentally obtained values (chapter 4, Table 4-4, first column). The

* If we for example want $\omega\tau_L<0.1$ the frequency ν has to be smaller than 1.9 GHz for a 400 μm long laser and smaller than 75 MHz for a typical long cavity laser with a length of 10 mm

gain compression factor was set to $\kappa_p = 2.5$ W^{-1} (or $\kappa_s = 3.34\times10^{-23}$m^3) and the other values were taken from Table 3-1. Fig. 3-13a shows the small signal response of a 400 μm long short-cavity laser (no external cavity) with the facets as cleaved ($R_i = 0.32$). The current was varied from 30 mA to 90 mA. The output power increased thereby from 1.7 mW to 15.3 mW. There is a good agreement between the results obtained from the rate-equations and those obtained from CLADISS. Fig. 3-13b shows analogous results for a long-cavity laser ($L_a = 400\,\mu m$, $L_p = 10$ mm). The loss of the passive cavity was 5 dB and an HR-coating was applied to the facet at the amplifier side ($R_1 = 0.90$). In this case, the bias current was varied from 50 mA to 110 mA, corresponding with an output power increase from 2.1 mW to 9.0 mW. The results obtained from the rate-equations were shifted down by 10 dB for clarity. From these results, it is obvious that the modulation frequency decreases considerably due to the long cavity length. Further, one sees that a resonance peak arises, at a frequency approximately equal to the inverse of the cavity roundtrip time $1/\tau_L = v_g/2L$. This may also be seen from the denominator of eq. (3-82), which shows that the response is somewhat periodic. Again, there is a good agreement between the rate-equation model and the results obtained from CLADISS, although the rate-equation model seems to overestimate the damping somewhat at lower frequencies.

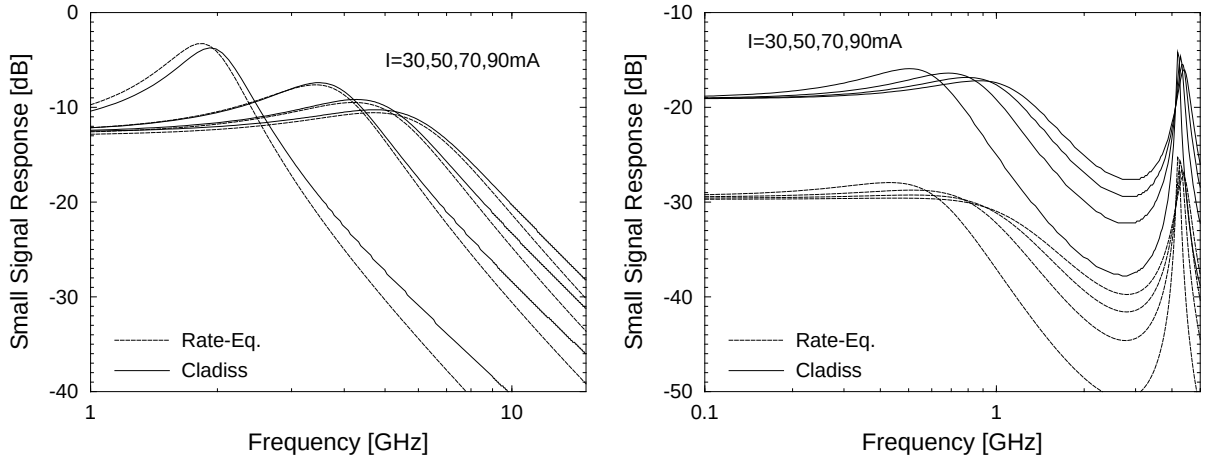

Fig. 3-13 a) Calculated small-signal response of a short-cavity laser for four different bias-currents. b) Calculated small-signal response of a long-cavity laser with a 5 dB loss in the passive cavity. For clarity, the results obtained from the rate-equations are shifted down by 10 dB.

Fig. 3-14a shows the small signal response as function of the cavity length ($I = 70$ mA). This figure shows more clearly the periodicity of the resonance peaks. For $L_p = 20$ mm, the first peak arises already at $\nu \sim 2.2$ GHz and the second peak falls together with the first resonance peak of the characteristic for $L_p = 10$ mm. Fig. 3-14b shows the influence of the damping factor. This figure shows that the overestimation of the damping in the rate-equation model

does not originate from a difference in the damping coefficient. Even for $\kappa_p = 0$, the effect is visible.

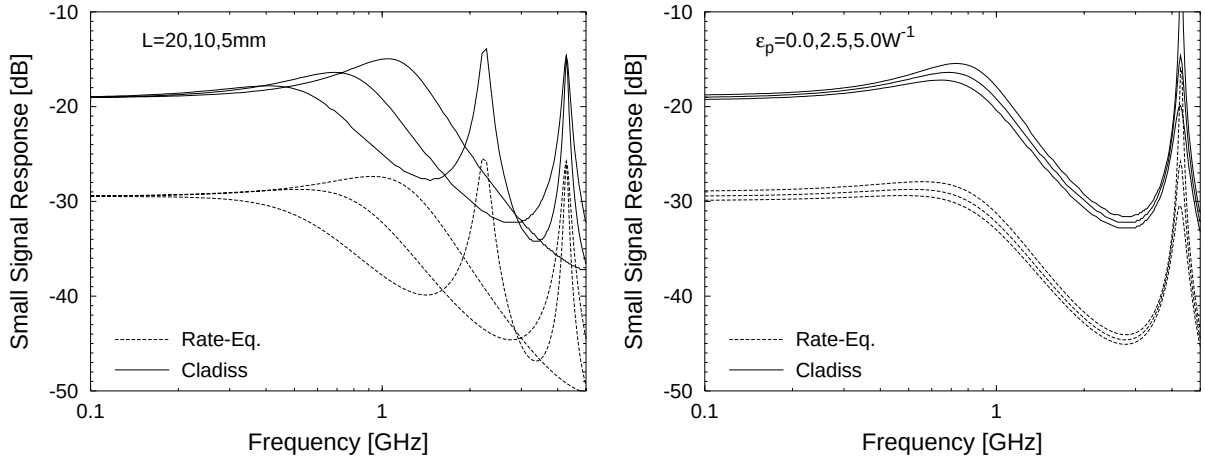

Fig. 3-14 a) Calculated small-signal response of a long-cavity laser with the cavity length varied (ε_p =2.5 W^{-1}). b) Calculated small-signal response of a long-cavity laser with the damping factor varied (L_p =10 mm). For clarity, the results obtained from the rate-equations are shifted down by 10 dB.

Fig. 3-15a shows the 3-dB bandwidth as function of the drive current, with the loss of the passive cavity varied (calculated using CLADISS). As expected, the bandwidth increases with increasing drive current and for a given drive current, with decreasing cavity loss. However, if we depict the bandwidth as function of the output power (taken at the passive facet), the bandwidth increases strongly with increasing cavity loss. This effect stems from the much higher photon densities in the high loss cavities.

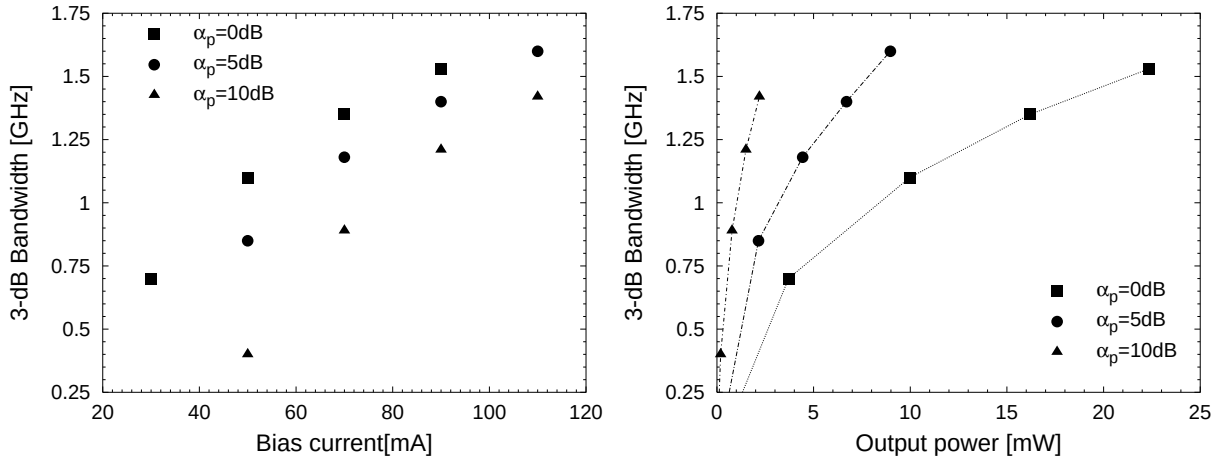

Fig. 3-15 3-dB bandwidth obtained from CLADISS for different values of the cavity loss, as function of the bias current (left) and as function of the output power (right).

3 Multi-wavelength lasers with common amplifier

3.1 Multi-channel rate equations

In this section, the rate equation description is extended to describe the full multi-wavelength source with multiple amplifiers attached at the input side of the multiplexer and a booster amplifier at the common output waveguide as depicted in Fig. 3-1a. As explained at the beginning of section 2, studying this complete set of equations is only necessary when a common output amplifier is used. Without the latter, the coupling between the channels is negligible and the single channel rate-equations of section 2.1 adequately describe the operating characteristics of the laser. However, if a common amplifier is used, all channels operate on the same carrier reservoir when traversing this amplifier and we have to consider the complete set of rate-equations describing all signal amplifiers and the common amplifier.

In the following, the subscripts c and a denote parameters and properties for the signal amplifiers and for the common amplifier respectively. The subscript i, ranging from 1 to N, denotes the channel number, N being the total number of channels.

The photon number rate equations are given by

$$S_i^{\#}(t) = f_i^2 R_1 R_2 G_{a,i}^2 G_{c,i}^2 S_i^{\#}(t-\tau_L) + K_i R_{sp,i}^{'} \qquad 1 < i < N \tag{3-85}$$

with

$$\begin{aligned} G_{c,i} &= \exp\left[(\Gamma g_{c,i} - \alpha_s) L_c\right] \\ G_{a,i} &= \exp\left[(\Gamma g_{a,i} - \alpha_s) L_a\right] \end{aligned} \tag{3-86}$$

and

$$\begin{aligned} g_{c,i} &= g_{c,i}(N_{c,i}, \nu_i) \\ g_{a,i} &= g_{a,i}(N_{a,i}, \nu_i) \end{aligned} \tag{3-87}$$

$S_i^{\#}$ is here considered to be the sum of the number of photons in the signal amplifier and the common amplifier for the *i*-th channel.

The carrier densities in the signal amplifiers and the common amplifier are respectively governed by the equations:

$$\begin{aligned} \frac{dN_{c,i}}{dt} &= \frac{I_{c,i}}{eV_c} - R(N_{c,i}) - \mathrm{v}_g g_{c,i} S_{c,i} \qquad 1 < i < N \\ \frac{dN_a}{dt} &= \frac{I_a}{eV_a} - R(N_a) - \sum_{i=1}^{N} \mathrm{v}_g g_{a,i} S_{a,i} \end{aligned} \tag{3-88}$$

With $S_{a,i}, S_{c,i}$ the mean photon densities for channel *i*, in the common and signal amplifier respectively. Since $S_{a,i}$ and $S_{c,i}$ are easily calculated from $S_i^{\#}$, the total photon number for the *i*-th channel, eq. (3-85) and (3-88) represent a set of 2*N*+1 coupled non-linear equations with 2*N*+1 variables:

$$\begin{matrix} S_i^{\#} & 1<i<N \\ N_{c,i} & 1<i<N \\ N_a & \end{matrix} \tag{3-89}$$

The threshold currents may be determined from the condition

$$f_i^{\,2} R_1 R_2 G_{a,i}^2 G_{c,i}^2 = 1 \qquad 1<i<N \tag{3-90}$$

and setting the photon densities to zero in (3-88). A suitable relation between the currents applied to the signal channels and the current applied to the common amplifier has to be chosen. Typically, I_a is set to a fixed value or equal to the signal channel current.

To prove the validity of this model, we solved the equations for a laser consisting of two 400 µm long amplifiers with a passive cavity in between (Fig. 3-16, "laser 1"). The loss of this passive cavity was varied between 0 dB and 18 dB. The results are compared with values obtained from CLADISS [2] (Fig. 3-17). The results for a laser with one 800 µm long cavity (Fig. 3-16, "laser 2") are also included.

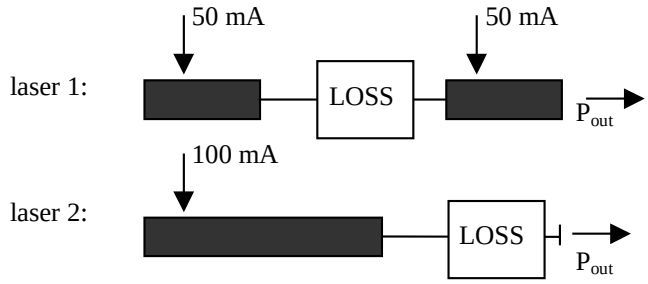

Fig. 3-16 Schematic layout of "laser 1" and "laser 2"

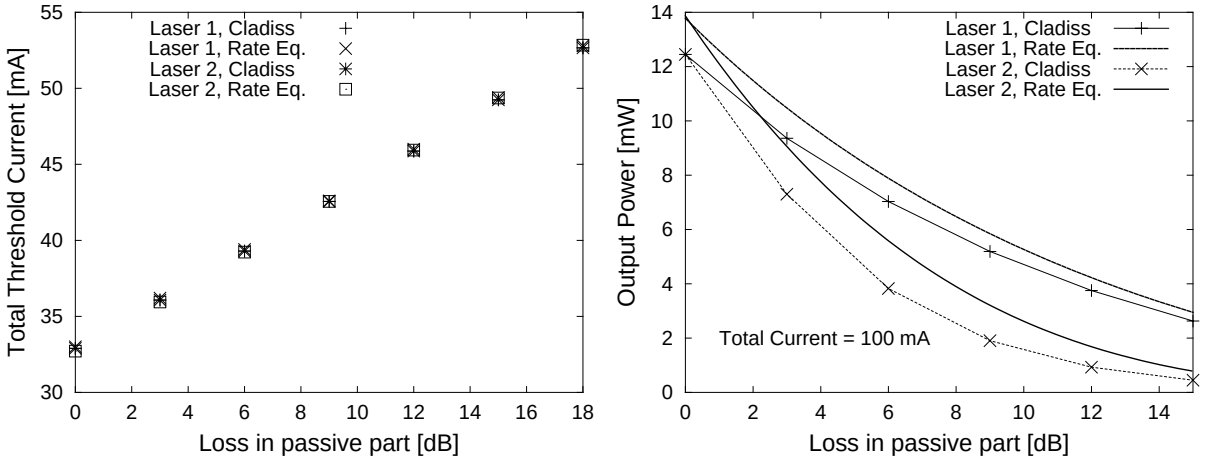

Fig. 3-17 a) Threshold current for laser 1 and laser 2 (shown in Fig. 3-16), calculated using a rigorous laser model (CLADISS) and using the rate-equations. b) The output power when the total drive current is 100 mA.

Fig. 3-17a shows that the values for the threshold current calculated from equations (3-88)-(3-90) are equal to the values obtained from CLADISS. Further, it shows that the threshold currents are equal for both laser types. From Fig. 3-17b, one may see that CLADISS predicts a decreasing output power with increasing cavity loss and this decrease appears to be stronger for the single-amplifier laser ("laser 2") than for the laser with two amplifiers. The rate-equation model predicts a similar behaviour. However, the output power is again slightly overestimated as was already noticed in section 2 (e.g. see Fig. 3-6). Still we believe that this model may be very useful for optimising the laser design.

Fig. 3-17b reveals that a common amplifier may be very useful: with the same total current applied and the same total amplifier length, the two-section laser has a significantly higher output power than the single section laser when the loss in the passive cavity increases. The origin of this behaviour may be understood as follows: since the total cavity loss is identical for both devices, also the required threshold gain calculated from (3-90) and the corresponding threshold carrier density will be the same. From the carrier rate equations (3-88), one derives easily that in such a case, with the same current density applied in both cases, the mean photon density in both lasers is also identical. However, as shown in Fig. 3-18, to obtain a comparable output power level in the single and the double amplifier design, the first requires a much higher mean photon density level.

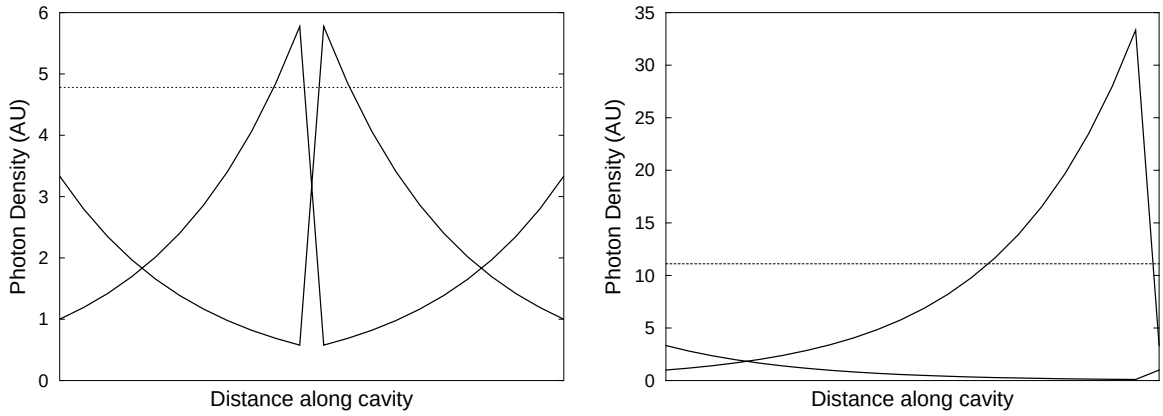

Fig. 3-18 Forward and backward travelling photon densities in a two-amplifier design (left) and single-amplifier (right) design for the same output power level. The horizontal line shows the average photon density, indicating clearly the higher average power density level in the one-amplifier design ("laser 2")

In an actual two-amplifier design, the total cavity loss may be higher due to the additional active-passive interface. However, even in that case it may be favourable to use a second amplifier as shown in Fig. 3-19. The solid line in this figure depicts the output power of an 800 μm long single-amplifier laser. The other lines represent the output power of a double amplifier laser, taking into account an increasing active-passive transition loss ($f_t = 0$, 1, 4 dB). For an active-passive transition loss of 1 dB, which is typical for monolithically integrated PICs, the double amplifier design is better as soon as the passive cavity loss surpasses

1.5 dB (indicated by the first arrow). Hybridly integrated PICs, with a typical transition loss of 4 dB to 6 dB, may have very low additional cavity losses (even below 1.5 dB), which makes that it is less obvious that a second amplifier is useful.

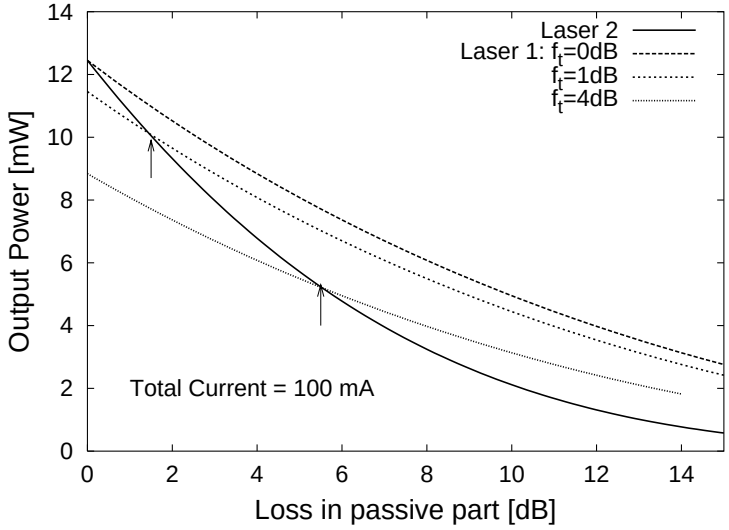

Fig. 3-19 The solid curve shows the output power for a laser consisting of one 800 μm long amplifier and a passive cavity versus the loss in the passive part (including the loss of one active passive transition). The other curves represent the output power for a laser with two 400 μm long amplifiers and a passive cavity in the middle, respectively in the cases where the active/passive transition loss f_t is negligible, 1 dB and 4 dB.

3.2 Signal distortion and crosstalk from carrier density changes in the common amplifier

When multiple channels are operated simultaneously, a change in the power level of a single channel results in a carrier density change in the common amplifier as can be seen directly from the corresponding rate equation:

$$\begin{aligned}\frac{dN_a}{dt} &= \frac{I_a}{eV_a} - \frac{N_a}{\tau_e} - \sum_{i=1}^{N} v_g g_{a,i} S_{a,i} \\ &\approx \frac{I_a}{eV_a} - \frac{N_a}{\tau_e} - v_g g_a S_a\end{aligned} \tag{3-91}$$

In the second equation, $S_a = \sum S_{a,i}$ is the total photon density in the common amplifier and we assumed the gain to be constant for all channels.

The carrier density change in turn will affect the amplifier gain, resulting in signal distortion and crosstalk between all channels.

To illustrate this, Fig. 3-20 shows the per channel output power as function of the drive current of the signal amplifiers ($I_{c,i}$), which is assumed to be equal for all channels. The bias current of the common amplifier (I_a) was kept at a constant value, indicated in the figures.

L_a denotes the length of the common amplifier and the length of the signal amplifiers was 400 μm. The loss of the passive cavity was set at 6 dB and N is the number of channels. The other parameters were as indicated in Table 3-1. From all three figures, it is obvious that the output power decreases considerably with increasing channel number. The non-linearity in the curves arises from the fact that only the total gain $g_a + g_{c,i}$ is clamped. The gain of the individual amplifiers depends on the total photon density within the respective amplifiers.

The various options for the drive current combinations may be compared by looking at the output power for a constant per channel drive current $I_{tot,i} = I_{c,i} + I_a/N$. For example, for $N = 4$ and $I_{tot,i} = 50$ mA, we find, in the case of $L_a = 400\,\mu m$, I_a = 30 mA, $P_{2,i} = 1.8$ mW ($I_{c,i} = 42.5$ mA). This is lower than the value we found for a single amplifier device with $I_{tot,i} = 50$ mA (2.50 mW, see Fig. 3-5). In the case of $L_a = 400\,\mu m$, I_a = 50 mA, we find $P_{2,i} = 2.7$ mW ($I_{c,i} = 37.5$ mA).

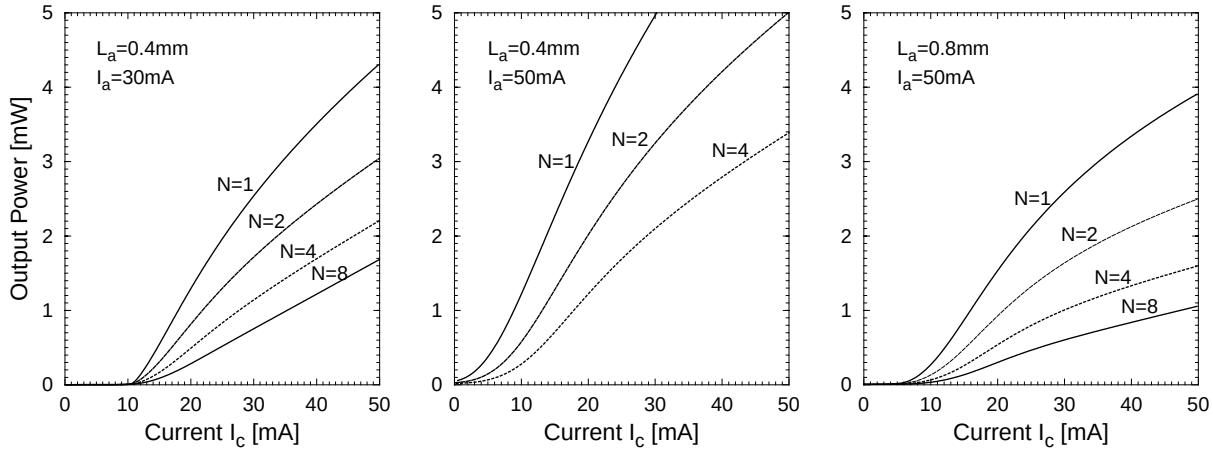

Fig. 3-20 Per channel output power versus signal amplifier current for a multi-channel laser. The bias current of the common amplifier (I_a) was set at a fixed value. The length of the signal amplifiers was 400 μm. L_a denotes the length of the common amplifier.

The carrier density change is governed by an effective time constant

$$\frac{1}{\tau_{eff}} = \frac{1}{\tau_e} + \mathrm{v}_g \frac{\partial g_a}{\partial N_a} S_a \qquad (3\text{-}92)$$

which, depending on the carrier density and the power level, may vary from a few nanoseconds to values as low as 200 ps. Therefore, the gain fluctuations induced by photon density changes, will affect both the static and the dynamic properties of the multi-wavelength laser.

In [26], the channel crosstalk and the induced power penalty generated in a travelling wave amplifier for intensity modulated multi-channel transmission was theoretically investigated. It was shown that the power penalty due to the channel crosstalk initially increases with increasing number of channels. However, when the channel number increases further, the

power penalty decreases again due to the fact that the crosstalk depends on the total power level (cf. eq. (3-91)), which shows a decreasing deviation probability with increasing channel number. In a multi-wavelength laser, the same effect may occur, at least if the number of simultaneously operated channels is high enough.

Next to the crosstalk due to the carrier density variation, gain nonlinearities will induce an additional penalty. When multiple wavelength channels are passing through the common amplifier, wave mixing products will be generated. Since the channel spacing is typically larger than or equal to 100 GHz, the gain nonlinearities that are relevant here arise from fast intraband effects as explained in paragraph 2.3.3, contrary to the interband effects, which are important for obtaining single longitudinal mode operation but work only on a short frequency range. If more than two channels are operated simultaneously, their wave mixing product may overlap with other channels thereby causing channel power fluctuations [27]. These may only be avoided by choosing an unequal channel spacing or by completely removing the common amplifier*.

In the next two paragraphs, we describe two methods to avoid crosstalk induced by the carrier density saturation in the common amplifier, one based on an electronic feed forward scheme, which was already described in literature and one novel method, developed in the context of this work.

3.3 Electronic compensation

To avoid crosstalk and signal distortion, the carrier density has to be kept constant. If the gain of the amplifiers is approximated by

$$g(N) = a(N - N_0) \qquad a = \frac{\partial g}{\partial N} \tag{3-93}$$

with N_0 the transparency carrier density and a the differential gain, a constant carrier density level may be obtained by adding a current component proportional to the total power level to the bias current. If

$$I(t) = I_0 + a v_g (\tau_e I_0 - e V_a N_0) S_a \tag{3-94}$$

the solution to (3-91) is given by

$$N(t) = \frac{\tau_e I_0}{e V_a} \tag{3-95}$$

* Actually, even if no common amplifier is used, wave mixing products are observed in the spectrum of simultaneously operated multi-wavelength lasers (e.g. see [29] or this work, chapters 5 & 6). These wave-mixing products are generated in the passive output waveguide and are much smaller than those arising from a common amplifier. Shortening the length of the output waveguide may easily reduce the strength of the wave mixing products.

which is a constant.

Several authors have proposed to use such a compensation technique [3][4][5]. In [4], a feedback scheme is used: the total output power is measured and a suitable current component, proportional to this level, is added to the amplifier bias current. In the same article, the authors propose to measure the voltage across the amplifier instead of the output power level as an indication for the carrier density level but they did not carry out such an experiment. In [5], a feed forward scheme was demonstrated: a signal proportional to the sum of the electrical channel drive currents is added to the amplifier bias current. Since this sum is approximately proportional to the total power density in the common amplifier, the carrier density can be kept constant. Bit error measurements performed on a four channel MWL, modulated with 622 Mb/s non-correlated signals, showed error free operation for the electronic compensated device, while the non-compensated device had high error floors for each channel.

3.4 Gain clamping mechanism

Instead of using an electronic compensation scheme, we proposed a new approach to clamp the gain of the common amplifier, thereby avoiding the carrier density fluctuations. This method does not require any external electronic equipment and no alteration of the fabrication process. Only a minor modification of the device layout is needed.

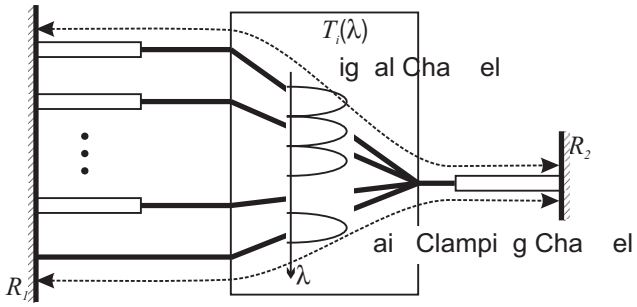

Fig. 3-21 Multi-wavelength laser with gain clamped output amplifier.

As shown in Fig. 3-21, one of the amplifiers at the input side of the multiplexer is replaced by a passive waveguide. If the common amplifier is pumped and the signal amplifiers are left unpumped, lasing will occur on the clamping channel as soon as the round trip gain for this channel reaches unity. If the current I_a to the amplifier is further increased, the power in the clamping-channel will increase but the gain and the carrier density in the shared amplifier will remain clamped at their threshold level given by (compare to eq. (3-90)):

$$\Gamma g_{a,0}(N_{th}) = \Gamma g_{a,0} = \alpha_s + \frac{1}{2L_a}\ln\frac{1}{f_0^2 R_1 R_2} \tag{3-96}$$

If now the signal amplifiers are turned on, laser action will be achieved on these channels as soon as their round trip gain reaches unity. However, due to the laser operation on the gain-clamping channel, the gain in the shared amplifier will remain constant, and no crosstalk

between the channels will occur. The amplifier gain, required to facilitate laser operation of the signal channels, is given by:

$$\Gamma g_{c,i} = \alpha_s + \frac{L_a}{L_c}\alpha_s + \frac{1}{2L_c}\ln\frac{1}{f_i^{\,2}R_1R_2} - \frac{L_a}{L_c}g_{a,i} \approx \alpha_s + \frac{1}{L_c}\ln\left(\frac{f_0}{f_1}\right) \qquad (3\text{-}97)$$

For the second equality, we assumed that the gain of the common amplifier is approximately constant for every channel ($g_{a,0} \approx g_{a,i}$). Since also the transmission loss through the multiplexer is almost constant for every channel ($f_0 \approx f_i$), the required threshold current for the signal channels will be only a few mA above the transparency current.

From the carrier rate equations for the signal amplifiers (3-88), we obtain the following relation between the photon density and the current:

$$S_{c,i} = \frac{I_{c,i} - I_{c,i,th}}{eV_c \mathrm{v}_g g_{c,i}} \qquad (3\text{-}98)$$

This is the same relation as for a standard, one-section laser. However since the threshold gain $g_{c,i}$ now is much lower (cf. eq. (3-97)), the LI-curve will be much steeper, or, in other words, the external differential quantum efficiency is much higher. From the carrier rate-equation for the common amplifier, it is easy to derive that this amplifier remains clamped as long as the total power in all signal channels is smaller than the power in the gain-clamping channel when none of the signal channels is pumped. Therefore, in practice the total output power of such a device is limited to the maximum power that may be delivered by one channel. At first sight, this is a severe limitation. However, in practical devices, due to mutual heating and due to saturation of the common amplifier, the maximum power obtained under simultaneous operation is never much higher than the maximum power under single channel operation.

Fig. 3-22 illustrates the gain clamping under static operation. For clarity, we consider a laser with only two channels. In the left column, the drive currents of respectively the common amplifier and the two signal amplifiers are shown while the right column depicts the corresponding output powers, which were calculated using the rate-equation model described in the previous paragraphs. The x-axis is a time scale. Its unit is irrelevant but it is considered to be large enough to allow neglecting the time derivatives in the equations describing the behaviour of the laser.

- In the interval *t*=[0,75], the current to the common amplifier is increased, until the output power in the gain-clamping channel reaches a value of 2 mW. From now on, the current to the common amplifier is kept constant.
- Starting from *t*=75, the bias current to the first signal amplifier is increased. Between *t*=75 and *t*=170, the power in the gain-clamping remains constant. However, at *t*=170, the current to the signal reaches its threshold value and the power in the signal channel starts to increase, while, as expected from eq. (3-91), the power in the gain clamping channels decreases with the same amount.

- From *t*=190 on, the current to the second signal channel is first increased monotonously and subsequently modulated a few times around the value $I_{c,2} = 6$ mA. As long as this current is smaller than its threshold value, the output power of the gain clamping channel and the first signal channel remain constant. As soon as the power in the second channel starts to increase, the power in the gain clamping decreases further. However, the power in the first signal channel remains unchanged, due to the fact that the output amplifier gain is clamped. Note that , although $I_{c,2}$ is only slightly modulated, this has a large impact on the output power level in this channel
- From *t*=375 on, the current to the first signal channel is modulated a few times and finally increased further to $I_{c,1} = 7$ mA, while $I_{c,2}$ is held constant. At *t*=475, the power in the gain clamping channel falls to zero and the common amplifier is no longer clamped. The latter is clearly visible from the power in the second signal, which starts to decrease, and from the decrease of the external differential efficiency of the first signal channel.

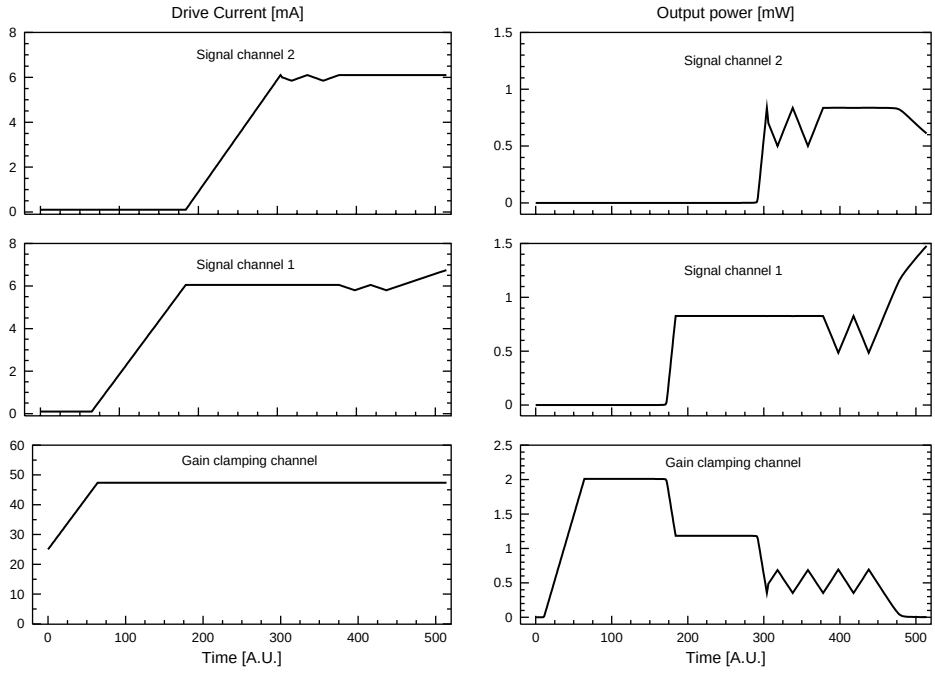

Fig. 3-22 Example illustrating the clamping of the gain of the common amplifier.

To investigate the gain clamping under dynamic conditions, we assume a single-amplifier long-cavity laser in which a modulated signal S_1 is injected[2], as shown in Fig. 3-23, and investigate the change ΔN of the carrier density under influence of this signal. If the gain clamping principle works also under dynamic operation, this change should be very small.

[2] For our study, it is not important whether this signal originates from an external source or from another channel of the multi-wavelength laser.

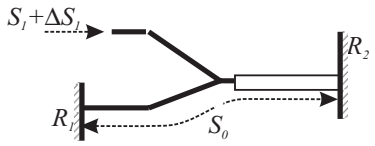

Fig. 3-23 a) Long cavity laser with injected signal.

The carrier density and the photon density rate-equations for this laser are respectively given by:

$$\frac{dN}{dt} = \frac{I}{eV_a} - \frac{N}{\tau_e} - \mathrm{v}_g g(S_0 + S_1) \tag{3-99}$$

and

$$S_0(t) = \left[1 + 2\left(\Gamma g - \alpha_s - \alpha_m - \alpha_p\right)L_a\right]S_0(t - \tau_L) + \Gamma K R_{sp}' / V_a$$

where we supposed the gain to be equal for both signals.

If we again write the carrier density and the photon densities as

$$\begin{aligned} N(t) &= \langle N \rangle + \mathrm{Re}(\Delta N \exp(j\omega t)) \\ S_i(t) &= \langle S_i \rangle + \mathrm{Re}(\Delta S_i \exp(j\omega t)) \end{aligned} \tag{3-100}$$

the rate-equations may be linearised around their steady-state conditions, yielding for the carrier rate equation:

$$\left(j\omega + \frac{1}{\tau_e} + \mathrm{v}_g \frac{\partial g}{\partial N}\left(\langle S_0 \rangle + \langle S_1 \rangle\right)\right)\Delta N = -\mathrm{v}_g g(\Delta S_0 + \Delta S_1) \tag{3-101}$$

From the photon rate-equation, we find:

$$\left(1 - \exp(-j\omega\tau_L) + \gamma\right)\Delta S_0 = 2\Gamma L_a \frac{\partial g}{\partial N}\langle S_0 \rangle \Delta N \tag{3-102}$$

with γ as defined in (3-76).

Combining (3-100) and (3-101) and using again the definition for ω_r as in (3-81), finally yields:

$$\frac{\Delta N}{\Delta S_1} = -\frac{\mathrm{v}_g g\left(1 - \exp(-j\omega\tau_L) + \gamma\right)}{\left(1 - \exp(-j\omega\tau_L) + \gamma\right)\left(j\omega + 1/\tau_{eff}\right) + \omega_r^2 \tau_L} \tag{3-103}$$

with $1/\tau_{eff}$ as defined in (3-92).

For an unclamped amplifier on the other hand we find:

$$\frac{\Delta N}{\Delta S_1} = -\frac{\mathrm{v}_g g}{\left(j\omega + 1/\tau_{eff}\right)} \tag{3-104}$$

Both relations are depicted in Fig. 3-24 together with the denominator of (3-103), which is proportional to the power density variation under influence of a current modulation $\Delta S_0 / \Delta I$

(see 3-24). It is obvious that in the frequency region where the small-signal response of the amplifier is important, the carrier density variation of the clamped amplifier is smaller than that of the unclamped amplifier.

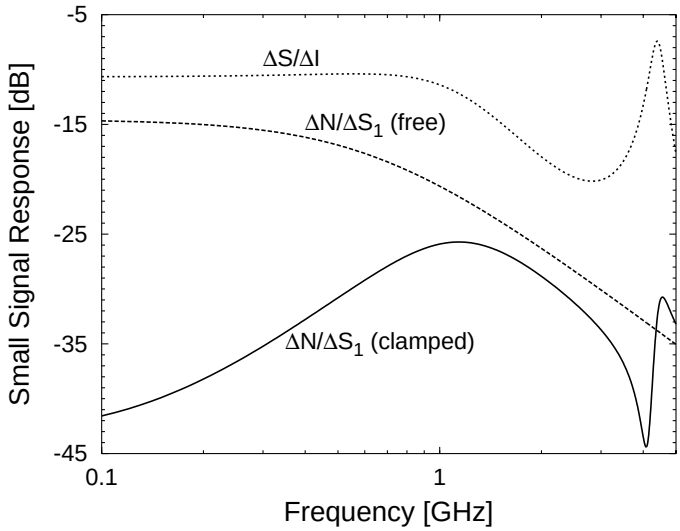

Fig. 3-24 Modulation of the carrier density ΔN in a clamped and in an unclamped long-cavity laser (10 mm) under influence of an external signal ΔS_1. For reference, also the modulation of the photon density of the laser ΔS_0 under influence of a current modulation ΔI is depicted.

4 Conclusion and design rules

To conclude this chapter, we summarise some design rules, obtained from the results described above. The "optimal design" however depends strongly on the exact application for the laser and therefore it is important to define the envisaged operating circumstances and the minimum requirements before actually initiating the design process.

Common amplifier

If the laser is employed as a wavelength selectable source and only one channel is used at a time, it may be favourable to include a common output amplifier. If the cavity loss stems mainly from the transmission through the demultiplexer and the loss at the transition between the active and passive waveguides is small, a second amplifier may, for a given total drive current, give rise to a higher output power (e.g. see Fig. 3-19). The second amplifier can also be used to locate the lasing mode reliably in the centre of the stability region for single longitudinal mode operation near the centre of the filter passband. This decreases the chance for mode hopping considerably (see 2.3.3 or [27]). Further, if multiple common amplifiers are attached to the output side of the demultiplexer, it is possible to change the central wavelength of the device by turning on the right amplifier. If no common amplifier is used on the other hand, extremely high suppression of the ASE-noise is obtained due to the filtering of the multiplexer.

If multiple channels are modulated together, the advantage of the common amplifier is less apparent. By choosing the drive currents adequately, it is still possible to obtain a higher output power per channel (for a given total current per channel). However, if the channels are modulated, gain-compression induced crosstalk will arise. This crosstalk can be avoided by clamping the gain of the common amplifier as was explained in paragraph 3.4. However, as for every gain-clamped amplifier, this limits the total output power of the laser. Another possibility would be to use an electronic feed forward scheme (see paragraph 3.3). This option has the drawback of requiring additional electronics and careful adjustment. A further problem is that there are strong wave mixing products generated in the common amplifier. Therefore, we believe that in general it is not useful to employ a booster amplifier if multiple channels are operated together. This is in particular the case for the hybridly integrated devices, where the loss of the active-passive transition is large compared to the total cavity loss.

Cavity length

To allow for high-speed operation, it is important to shorten the length of the cavity as much as possible (see paragraph 2.5). The accuracy on the channel spacing on the other hand, is determined by the longitudinal mode spacing (see also chapter 1, Table 1-2). For a 10% accuracy, in a 100 GHz system, the minimum cavity length is ~4.5 mm. In a 50 GHz system, this already becomes 9.0 mm. Another drawback of minimising the cavity length is that the chirp under modulation increases. However, for the cavity lengths, which are practically attainable, the chirp is still much lower than that of a standard short-cavity single mode laser.

When designing the Phased-Array laser, it is in particular important to minimise the length of the access waveguides. This allows decreasing the filter bandwidth considerably while keeping the total cavity length constant (see also chapter 2, section 4.2), which will ensure an enhanced single longitudinal mode stability. To avoid wave-mixing products in the oscillation spectrum, also the length of the passive output waveguide should be minimised.

Multi-passband lasing

Chirping of the Phased-Array is undoubtedly the best way to prevent multi-passband lasing [27]. Otherwise, the free-spectral range has to be increased considerably so that the selectivity of the amplifier gain profile is sufficient to choose lasing in only one passband (see paragraph 2.3.2). Further, it is also favourable to increase the length of the amplifiers (cf. eq. (3-46)). If a large free spectral range is used, it may be useful to fill the complete FSR uniformly with channels. Afterwards, one may select the channels that best meet the expectations with respect to wavelength and operating characteristics. If a hybrid integration approach is used, this selection can be accomplished by attaching the amplifier array (with a limited number of amplifiers) to the right access waveguides.

Reflections

Intra-cavity reflections may destroy the gain-compression induced single longitudinal mode stability. Therefore, they should be reduced as much as possible. Further, we believe that

the anomalous behaviour of the lasers in some circumstances (see chapters 5 & 6) was caused by external reflections. Although their effect was not systematically investigated in the context of this work, we believe that an isolator should be used to avoid back-reflections and to provide stable laser operation.

5 References

[1] K. Petermann, "Laser diode modulation and noise", Kluwer Academic Publishers, 1988

[2] P. Vankwikelberge, G. Morthier, R. Baets, "Cladiss - A longitudinal Multi-Mode Model for the analysis of the static, dynamic and stochastic behavior of diode lasers with distributed feedback", IEEE JQE, Vol. 21, pp 1985-1963, 1985

[3] T. E. Darcie, R. M. Jopson, A. A. Saleh, "Electronic compensation of saturation-induced crosstalk in optical amplifiers", El. Lett., Vol. 25, 235-236, 1989

[4] K. O. Nyairo, I. H. White, C. J. Armistead, P.A. Kirkby, "Multiple channel signal generation using multichannel grating cavity laser with crosstalk compensation", El. Lett., Vol. 28, pp. 261-263, 1992

[5] C. R. Doerr, C. H. Joyner, M. Zirngibl, L. W. Stulz, H. M. Presby, "Elimination of signal distortion and crosstalk from carrier density changes in the shared semiconductor amplifier of multifrequency signal sources", IEEE PTL, Vol. 7, pp. 1131-1133, 1995

[6] C. van Dam, "InP-based Polarisation independent wavelength demultiplexers", PhD Thesis, Delft University of Technology, The Netherlands, 1997

[7] C. R. Doerr, "Direct modulation of long-cavity semiconductor lasers", IEEE JLT, Vol. 14, pp 2052-2061, 1996

[8] M. R. Amerfoort, J. B. D. Soole, C. Caneau, H. P. Leblanc, A. Rajhel, C. Youtsey, I. Adesida, "Compact arrayed waveguide grating multi-frequency laser using bulk active material", El. Lett., Vol. 33, pp 2124-2126, 1997

[9] C. H. Joyner, C. R. Doerr, L. W. Stulz, J. C. Centanni, M. Zirngibl, "Low-Threshold Nine-Channel Waveguide grating router-based continuous wave transmitter", IEEE JLT, Vol. 17, 647-651, 1999

[10] C. H. Joyner, M. Zirngibl, J. P. Meester, "A multifrequency waveguide grating laser by selective area epitaxy", IEEE PTL, Vol. 6, 1277-1279, 1994

[11] L. F. De Chiaro, "Damage-induced spectral perturbations in multi-longitudinal mode semiconductor lasers", IEEE JLT, Vol. 11, 1659-1669, 1990

[12] A. P. Bogatov, P. G. Eliseev, B. N. Sverdlov, "Anomalous interaction of spectral modes in a semiconductor laser", IEEE JQE, Vol. 11, 510-515, 1975

[13] C. R. Doerr, M. Zirngibl, C. H. Joyner, "single longitudinal-mode stability via wave mixing in long-cavity semiconductor lasers", IEEE PTL, Vol. 7, pp 962-964, 1995

[14] A. A. Tager, "Side-Mode Suppression for long DBR lasers", IEEE PTL, Vol. 7, pp 866-868, 1995

[15] A. Uskov, J. Mork, J. Mark, "Wave mixing in semiconductor laser amplifiers due to carrier heating and spectral hole burning", IEEE JQE, Vol. 30, pp 1769-1781, 1994

[16] G. R. Gray, G. P. Agrawal, "Importance of Self-Induced Carrier-Density Modulation in Semiconductor Lasers", IEEE PTL, Vol. 4, pp 1216-1218, 1992

[17] I. Koltchanov, S. Kindt, K. Petermann, S. Diez, R. Ludwig, R. Schnabel, H. G. Weber, "Analytical theory of terahertz four-wave mixing in semiconductor-laser amplifiers", Appl. Phys. Lett., Vol. 20, pp 2787-2789, 1996

[18] J. Manning, R. Olshansky, D. M. Fye, W. Powazinik, "Strong influence of nonlinear gain on spectral and dynamic characteristics of InGaAsP lasers", El. Lett., Vol. 21, pp 496-497, 1985

[19] L.V.T Nguyen, M. J. L. Cahill, A. J. Lowery, D. Novak, P. C. R. Gurney, D. D. Sampson, "Effects of carrier-induced modal intermodulation on dynamic spectral characteristics of multimode Fabry-Perot lasers", Opt. Quant. Elec. , Vol. 28, pp 1067-1080, 1996

[20] M. Yamada, "Theoritical analysis of nonlinear optical phenomena taking into account the beating vibration of the electron density in semiconductor lasers", J. Appl. Phys., Vol. 66, pp 81-89, 1989

[21] T. Lee, C. A. Burrus, J. A. Copeland, A. G. Dental, D. Marcuse, "Short-Cavity InGaAsP Injection Lasers: Dependence of Mode Spectra and Single-Longitudinal-Mode Power on Cavity Length", IEEE JQE, Vol. 18, pp 1101-1113, 1982

[22] T. Mukai, T. Saitoh, "Detuning characteristics and conversion efficiency of nearly degenerate four-wave mixing in a 1.5-um travelling-wave semiconductor amplifier", IEEE JQE, Vol. 26, pp 865-874, 1990

[23] W. F. Sharfin, J. Schlafer, E. S. Koteles, "Observation of mode beating and self-frequency locking in a nearly single-mode semiconductor laser", IEEE JQE, Vol. 30, pp 1709-1712, 1994

[24] F. Favre, D. LeGuen, "Four-wave mixing in travelling-wave semiconductor laser amplifiers", IEEE JQE, Vol. 26, pp 858-864, 1990

[25] G. P. Agrawal, "Gain nonlinearities in semiconductor lasers: theory and application to distributed feedback lasers", IEEE JQE, Vol. 23, 860-868, 1987

[26] K. Inoue, "Crosstalk and its power penalty in multichannel transmission due to gain saturation in a semiconductor laser amplifier", IEEE JLT, Vol. 7, 1118-1124, 1989

[27] C. R. Doerr, C. H. Joyner, L. W. Stulz, J. C. Centanni, "Wavelength selectable laser with inherent wavelength and single-mode stability", IEEE PTL, Vol. 9, 1430-1432, 1997

[28] C. R. Doerr, R. Monnard, C. H. Joyner, L. W. Stulz, "Simultaneous CW operation of shared angular dispersive element WDM-lasers", IEEE PTL, Vol. 10, 501-503, 1998

[29] C. R. Doerr, C. H. Joyner, L. W. Stulz, "Multifrequency laser with reduced intracavity wave mixing", IEEE PTL, Vol. 11, 635-637, 1999

[30] C. R. Doerr, M. Zirngibl, C. H. Joyner, L. W. Stulz, "Chirped waveguide grating router multifrequency laser with absolute wavelength control", IEEE PTL, Vol. 8, 1606-1608, 1996

[31] C. H. Henry, "Theory of spontaneous emission noise in open resonators and its application to lasers and optical amplifiers", IEEE JLT, Vol. 4, 288-297, 1986

[32] K. Ujihara, "Phase noise in a laser with output coupling", IEEE JQE, Vol. 20, 814-817, 1984

[33] C. R. Doerr, "Theoretical stability analysis of single mode operation in uncontrolled mode-selection semiconductor lasers", IEEE PTL, Vol. 9, 1457-1459, 1997

CHAPTER 4

DESIGN, FABRICATION AND CHARACTERISATION OF SUB-COMPONENTS FOR THE PHASED-ARRAY LASER

Chapter 4

Design, fabrication and characterisation of sub-components for the Phased-Array laser

As explained in chapter 1, the monolithic integration scheme based on a selective area epitaxial growth process incorporates amplifiers with a ridge type cross-section, to facilitate an easy coupling with the ridge type passive waveguides to be used for the Phased-Array demultiplexer. Also the amplifiers provided by Optospeed SA, used for the development of the hybridly integrated PICs (chapter 5 and 6), were of the ridge type. Therefore, section 1 of this chapter discusses the advantages, disadvantages and general operating characteristics of ridge type lasers and amplifiers. In paragraph 1.1, the general theoretical background is presented. Paragraphs 1.2 & 1.3 describe the more specific aspects concerning the design and the characterisation of respectively the amplifiers developed for the monolithic integration technology and the ones provided by Optospeed in more detail.

Section 2 discusses the design and characterisation of the passive waveguides employed in the context of this work. Again, the passive waveguides developed for the monolithically integrated Phased-Array laser (paragraph 2.1) and the ones used for the hybridly integrated laser (paragraph 2.2), are presented separately.

In section 3, the coupling loss arising from hybridly integrating two InP chips is calculated and the influence of misalignment errors is discussed. Finally, section 4 describes shortly the transition between the active and the passive waveguides in the monolithic integration scheme.

1 Ridge lasers

1.1 Theoretical description of ridge type lasers

Fig. 4-1 shows a cross-sectional view of a typical ridge laser. An active layer with thickness t_a is embedded in between n- and p-doped cladding layers. Sometimes additional film layers are used, as indicated in the figure. Both bulk and quantum well active layers may be employed. The ridge provides an effective, self-aligned lateral current confinement and waveguiding. The apparent advantage of this laser structure compared to others is its ease of fabrication. Only one growth step and no current blocking layers are required. However, the etching depth, which determines the lateral index contrast, is a very sensitive parameter. It has been found that a minimum effective index step is necessary to compensate for the refractive index reduction in the centre of the ridge, induced by the carrier injection [1]. Moreover, the weaker lateral electrical confinement causes higher threshold currents and,

while for buried laser structures the active layer is surrounded by transparent InP-current blocking layers, in ridge lasers the tails of the lateral optical mode profile extend into the absorbing active layer stack what will reduce the modal gain.

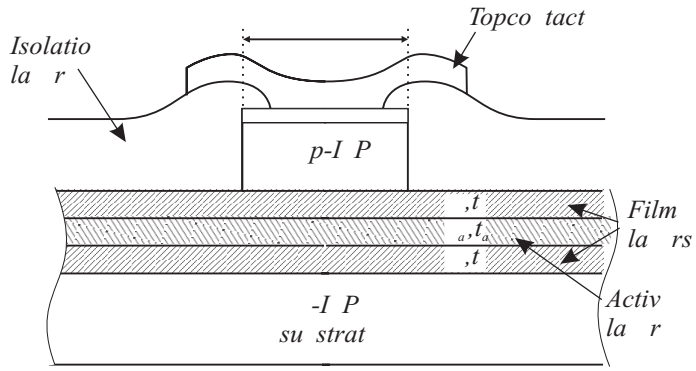

Fig. 4-1 Cross-sectional view of ridge laser

The exact solution of the lateral current flow and the carrier distribution in the active layer requires solving the 2-D current continuity relations. This can only be done using numerical tools. However, to gain some insight in the operation of a ridge-type laser and for design purposes, several approximate models were developed [1][2][3]. In these models, the effective index method is used to reduce the 2D-problem to an equivalent 1D one. This is justified by the fact that the active layer thickness is generally much smaller than the lateral dimensions. Furthermore, the models mostly do not take into account the influence of the optical field on the carrier distribution and consequently they are only strictly valid in the subthreshold regime. However, for traditional laser structures, the models can also be used in the above threshold regime since the effects of carrier density saturation will be limited as long as the output power is not too high.

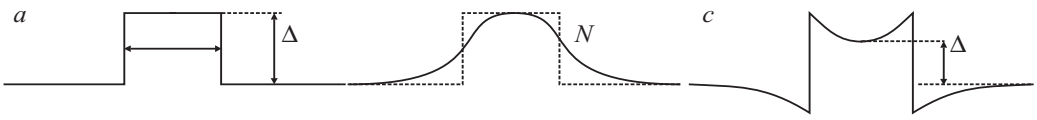

Fig. 4-2 Schematic view of a) built-in effective index profile $n_{eff}(y)$ b) Injected carrier density $N(y)$ c) Induced effective index profile $n'_{eff}(y)$

For a typical ridge waveguide with straight walls, the shape of the effective index profile is rectangular, as depicted in Fig. 4-2a. If a bias current is applied, carriers are injected in the active layer and the resulting lateral distribution of the carrier density is mainly determined by carrier outdiffusion (Fig. 4-2b). Due to the carrier injection, the refractive index is reduced and the effective index profile becomes M-shaped as shown in Fig. 4-2c. Thereby, the built-in optical contrast Δn_{eff} is reduced to an effective value $\Delta n'_{eff}$. Depending on the magnitude of the original built-in index contrast and the anti-guiding effect, the effective index contrast

$\Delta n'_{eff}$ may even become negative, resulting in strong radiation losses, which enhance the threshold current and reduce the differential efficiency.

To evaluate this anti-guiding effect, the diffusion equation for the carries in the active layer has to be solved. Taking into account bimolecular recombination and Auger processes, the latter is given by:

$$D_{eff}\frac{\partial^2 N}{\partial y^2}-\frac{N}{\tau}-BN^2-CN^3+G=0 \qquad \textbf{(4-1)}$$

D_{eff} is the effective diffusion coefficient, which equals twice the hole diffusion coefficient D_p [1]. The generation rate $G(y)$is given by

$$G(y)=\frac{I(y)}{\mathrm{W}Lqt_a} \qquad (4\text{-}2)$$

where L denotes the laser length and t_a is the active layer thickness. The current injection $I(y)$ can be approximated well by a step function

$$I(y)=\begin{cases} I & |y|\le W/2 \\ 0 & |y|>W/2 \end{cases} \qquad (4\text{-}3)$$

This is justified by the fact that the ridge effectively confines the current in lateral direction. Moreover, as already mentioned, the thickness of the film layer and the active layer are much smaller than the lateral dimensions and these layers are not intentionally doped what will limit the current spreading further. In [10], a model is presented, which allows taking into account the current spreading in the film layers.

In [2], (4-1) is solved by introducing an effective carrier life time

$$\frac{1}{\tau_{eff}}=A+BN+CN^2 \qquad (4\text{-}4)$$

which is assumed to be constant over the whole active layer. In that case, equation (4-1) may be solved very easily. Subsequently, the current is written as a sum of a lateral current representing the amount of current escaping from the region beneath the ridge and the recombination current, which effectively contributes to the laser action. This model can give insight in the effect of the leakage currents but gives no information over the mode profile and the minimum effective index contrast Δn_{eff} , which is required to obtain laser operation.

In [1] the carrier diffusion profile is calculated without making the approximation (4-4), using Jacobian elliptic functions. Although this calculation is more involved than the one presented in [2], it gives a better estimation for the threshold gain and more physical insight. From the solution for the carrier diffusion profile $N(y)$, the resulting complex effective index profile $n'_{eff}(y)$ (Fig. 4-2c) is obtained:

$$n'_{eff}(y) = n_{eff}(y) + \Gamma\left(\frac{\partial n_{re}}{\partial N}N + j\frac{\partial n_{re}}{\partial N}N\right) = n_{eff}(y) + \Gamma\left(\beta N + \frac{j}{2k_0}a(N - N_0)\right) \quad (4\text{-}5)$$

$n_{eff}(y)$ is the square built-in effective index profile as depicted in Fig. 4-2a. Γ is the transverse confinement factor* and a and N_0 describe the optical gain as function of the carrier density, in the usual linear approximation. β is the anti-guiding parameter, which may also be expressed as function of the linewidth enhancement factor α as $\beta = -\alpha\frac{a}{2k_0}$ (with $\alpha = -(\partial n_{re}/\partial N)/(\partial n_{im}/\partial N)$).

Once the carrier induced effective index profile $n'_{eff}(y)$ has been found, the eigenmodes of the waveguide described by this profile have to be found. If the index profile is replaced by a staircase approximation, they may be readily calculated using a complex 1D-mode solver (see chapter 2). Subsequently, the modal gain is obtained from the complex part of the propagation coefficient: $g_{\mathrm{mod}} = 2\,\mathrm{Im}(\beta)$. The threshold current is found by equating the modal gain and the total cavity loss.

Demerlier [3] used a similar approach as the one outlined above. However, to obtain the carrier diffusion profile, equation (4-1) is not solved analytically as in [1] but numerically, which allows to include also the effects of stimulated recombination in the above threshold regime. The algorithm that he developed will be used in the following paragraphs for comparing experimental results with theoretical modelling and for parameter extraction.

1.2 Ridge lasers developed for the monolithic integration technology based on selective area growth

Often, the thickness of the layer stack formed by the active layer and the film layers (cf. Fig. 4-1) is chosen to maximise the transversal confinement factor Γ_a of the active layer. For the example depicted in Fig. 4-3, this would lead to a total active layer stack thickness of ~400 nm. However, from the monolithic integration scheme as outlined in chapter 1, it may be seen that this layer stack also forms the guiding layer for the passive waveguides (but with the thickness reduced by a factor 1.5 due to the selective area growth process). To obtain low loss passive devices, it would be advantageous that this guiding layer is as thick as possible (this will be explained in more detail in section 2 of this chapter). Furthermore, in [4] it was noted that a broadened active layer stack, although it may lead to a reduced confinement in the active layer, also reduces the confinement factor in the cladding layers (e.g. see Fig. 4-3).

---

* In general, the value of Γ beneath the ridge differs from the value besides the ridge. Mostly, this effect is neglected, however, taking it into account thus not complicate the analysis.

Consequently, the internal laser loss originating from free-carrier absorption in the cladding layers decreases, resulting in an increased external differential efficiency and improved overall laser characteristics.

For these reasons, we investigated the influence of the film layer thickness on the operating characteristics of ridge-type lasers, both theoretically and experimentally*.

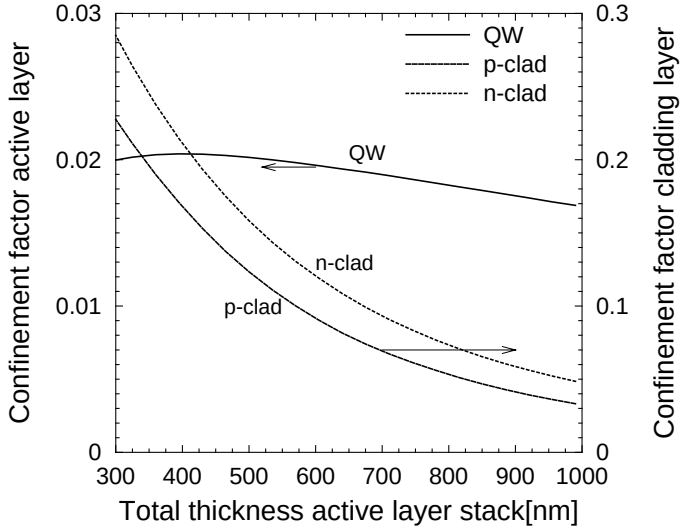

Fig. 4-3 Confinement factor in the active layer (10 nm quantum well) and cladding layers of a laser as function of the total thickness of the active layer stack. The layer stack is formed by a 180 nm Q1.25 layer with an embedded quantum well and surrounded with Q1.1 layers. The width of the latter was varied between 50 nm and 400 nm. The calculation was performed using a 2D-mode solver and the etching depth was chosen in such a way that the lateral index contrast remained constant at $\Delta n_{eff} = 0.024$.

1.2.1 Experimental results

Starting from the layer structure depicted in Table 4-1, lasers with different widths (2.5, 3, 5, 7 and 9 μm) and different etch depth were fabricated.

The most relevant results are summarised in Table 4-2. As usual, the etching depth is denoted with respect to the top of the first film layer. The length of all lasers was 500 μm.

* The lasers were fabricated by T. Van Caenegem. He also measured the LI-characteristics for obtaining the data summarised in Table 4-2. The gain measurements depicted in Fig. 4-4 & Table 4-3 were performed by us.

thickness [nm]	layer	[cm^{-3}]	layer
160	InGaAs	p++	contact layer
1550	p-InP	2x10^{18}	top cladding layer
50	p-InP	0.5x10^{17}	
50	InP	n.i.d.	
355	Q1.1	n.i.d.	top film layer
45	Q1.25	n.i.d.	
100	5 InGaAs QWs +Q1.25barriers*	n.i.d.	active layer
45	Q1.25	n.i.d.	bottom film layer
355	Q1.1	n.i.d.	
50	InP	n.i.d.	substrate
	n-InP	n+	

* The QWs were 8 nm thick, the barriers 15 nm

Table 4-1 Layer structure of the lasers fabricated for verifying the thick waveguide layer concept.

etch depth	Δn_{eff}	W	I_{th}	η_{ext}
+60 nm	0.009	all widths	no laser operation obtained	
-20 nm	0.015	< 5 μm	no laser operation obtained	
		5 μm	50 mA	35 %
		7 μm	51 mA	30 %
-100 nm	0.024	2.5 μm	20 mA	32 %
		3 μm	19 mA	34 %
		5 μm	25 mA	34 %
-200	0.038	2.5 μm	30 mA	27 %
		3 μm	32 mA	28 %

Table 4-2 Main results obtained from lasers fabricated for verifying the thick waveguide layer concept. The differential external efficiencies are single-sided values.

The best operation characteristics are obtained for the lasers with Δn_{eff} =0.024 (etched 100 nm into the quaternary layer), which show very high differential external efficiencies and rather low threshold currents. The lasers with lower optical contrast showed no laser operation at all (Δn_{eff} =0.009) or only for the broader structures (Δn_{eff} =0.015). This may be explained by the anti-guiding effect described in paragraph 1.1. The deeper etched lasers (Δn_{eff} =0.038) showed laser operation but with an increased threshold current and lower external differential efficiency. From measuring the spectral gain (see below), we believe that this stems from an enhanced internal loss. Several reasons may be responsible for this. The most likely are an increased scattering loss at the waveguide-polyimide interface or damage to the quantum

well layers due to the etching process. Other possible causes for the reduced differential efficiency of the deeper etched lasers are an increased confinement in the absorbing top-cladding layer or the fact that they are no longer operating in a single transversal mode.

For some of the lasers of Table 4-2, we determined the gain spectrum from the resonances in the spontaneous emission spectrum, using the Hakki-Paoli method [5]:

$$g_{net}(\lambda) = \frac{1}{L}\left(\ln\left(\frac{1}{R}\right) + \ln\left(\frac{r^{1/2}-1}{r^{1/2}+1}\right)\right) \qquad (4\text{-}6)$$

$r = r(\lambda)$ is the peak to valley ratio of the measured Fabry-Pérot resonances. $g_{net} = g_{\mathrm{mod}} - \alpha_{\mathrm{int}}$ is the net gain, which is equal to the distributed mirror loss $\alpha_m = 1/L \ln(1/R)$ at threshold (for R=0.32 and $L = 500\mu m$, $\alpha_m \approx 23$ cm^{-1}). g_{mod} is the modal gain, which can be accurately described by $g_{\mathrm{mod}} = \Gamma g_{mat}$ in buried laser structures. For the ridge lasers described here, this is only a rough approximation and it is better to calculate the modal gain directly from the modified effective index profile as described in paragraph 1.1. Fig. 4-4 shows the gain spectrum for a $3\,\mu m$ wide laser (Δn_{eff}=0.024). The threshold current and external differential efficiency of this laser were respectively 19 mA and 34%. In the region far above the lasing wavelength (the below bandgap region), the material gain is zero and the net gain is equal to the internal loss α_{int}. For this particular laser the internal loss was very low (~4.5 cm^{-1}).

In total five lasers were characterised in this way and the results are summarised in Table 4-3 and Fig. 4-5. In Fig. 4-5a the peak gain as function of the bias current is given for the four lasers with Δn_{eff}=0.024. The gain is limited by the threshold value $g_{net} \approx 23\,\mathrm{cm}^{-1}$. In Table 4-3, the parameters A and I_0 are given, which were obtained from fitting the linear part of the curves in Fig. 4-5a to a function $g_{\max} = A(I - I_0)$. The last column shows the transparency current for the modal gain $I'_0 = I_0 - \alpha_{\mathrm{int}}/A$. Fig. 4-5b depicts the wavelength of the gain maximum.

The operating characteristics of the lasers were not uniform. For example, laser #2 is identical to laser #3 but its threshold current is much higher. This is reflected in a higher internal loss and a lower value for A. Also the threshold current for laser #1 (29 mA) is higher than for the best lasers with this ridge width (which was 20 mA, see Table 4-2), which again may occur from an increased internal loss for this laser. Lasers #3, 4 & 5 are comparable to the best in their series. The internal loss for lasers #3 and #4 is very low (as expected, it is somewhat lower for the broader laser). As denoted already above, the internal loss for the deeper etched laser (#5) is somewhat higher again.

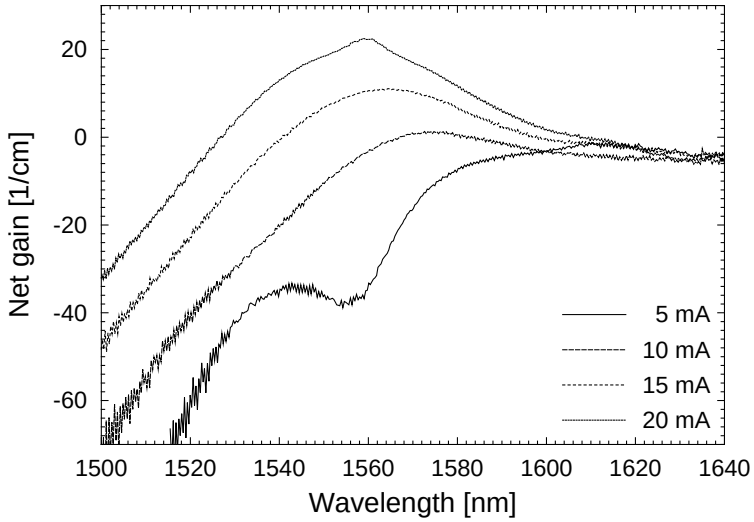

Fig. 4-4 Optical gain spectrum of a 3 μm wide laser (Δn_{eff} =0.024), measured using the Hakki-Paoli method

#	Δn_{eff}	W	I_{th}	η_{ext}	α_{int}	A	I_0	I'_0
1	0.024	2.5 μm	29 mA		10.5 cm^{-1}	1.5	15 mA	8 mA
2	0.024	3.0 μm	33 mA		13 cm^{-1}	1.4	18 mA	8.7 mA
3	0.024	3.0 μm	19 mA	34 %	4.5 cm^{-1}	2.1	10 mA	7.9 mA
4	0.024	5.0 μm	25 mA	35 %	2.3 cm^{-1}	1.5	10 mA	8.5 mA
5	0.038	3 μm		32 %	11 cm^{-1}			

Table 4-3 Summary of optical gain measurements. The gain spectrum for laser #3 is shown in Fig. 4-4. ([A]=$cm^{-1}mA^{-1}$)

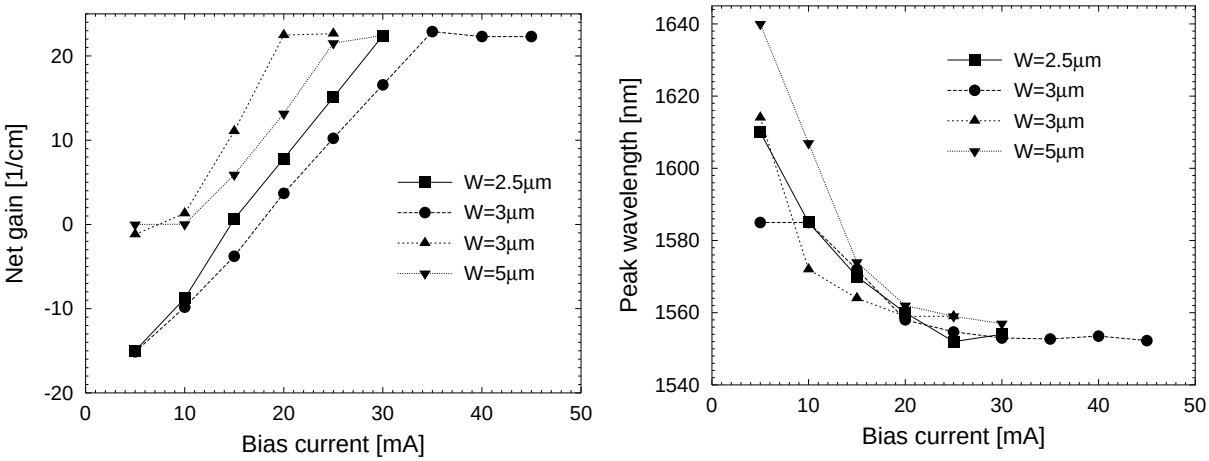

Fig. 4-5 Summary of optical gain measurements for a series of lasers with varying ridge width and Δn_{eff} =0.024

1.2.2 Calculation of modal gain

Using the model described in paragraph 1.1 of this chapter, we calculated the modal gain of a 500 μm long laser diode with the layer structure of Table 4-1. By fitting the measured gain parameters for laser #3 of Table 4-3 ($A = 2.1$ cm^{-1}mA^{-1}, $I'_0 = 7.8$ mA) to the simulated curve, we obtained values for the differential gain ($a = 4.63\times10^{-16}$ cm^{-2}) and the transparency carrier density ($N_0 = 1.2\times10^{-18}$ cm^{-3}) of the quantum well layers that are comparable to values reported in literature. Using these values, we calculated the modal gain for a 5 μm wide laser, which is also shown in Fig. 4-6a. From this curve, the transparency and threshold current for this laser are estimated to be respectively $I_0^{'} = 10$ mA and $I_{th} = 24$ mA, which agree reasonably well with the experimentally obtained values shown in Table 4-3 for laser #4.

To investigate the influence of the lateral optical index contrast on the laser characteristics, we calculated the modal gain as function of the drive current. Δn_{eff} was varied from Δn_{eff} =0.009 to Δn_{eff} =0.038 as in Table 4-2. The results are depicted in Fig. 4-6b. To obtain a modal gain of $g_{\mathrm{mod}} = 26$ cm^{-1} (the threshold gain for a 500 μm laser with $R = 35$ % and $\alpha_{\mathrm{int}} = 5$ cm^{-1}), the required current increases from 18 mA for the device with the highest lateral index contrast to 23 mA for the one with $\Delta n_{eff} = 0.009$. This difference is less than expected from the observation that none of the devices with the lowest lateral index contrast showed laser operation. Probably this is caused by the fact that we used a linear gain model for the QWs. Such a model is only valid in a limited range. A logarithmic model describes the gain accurately over a wider range and will give rise to an additional saturation of the modal gain curve.

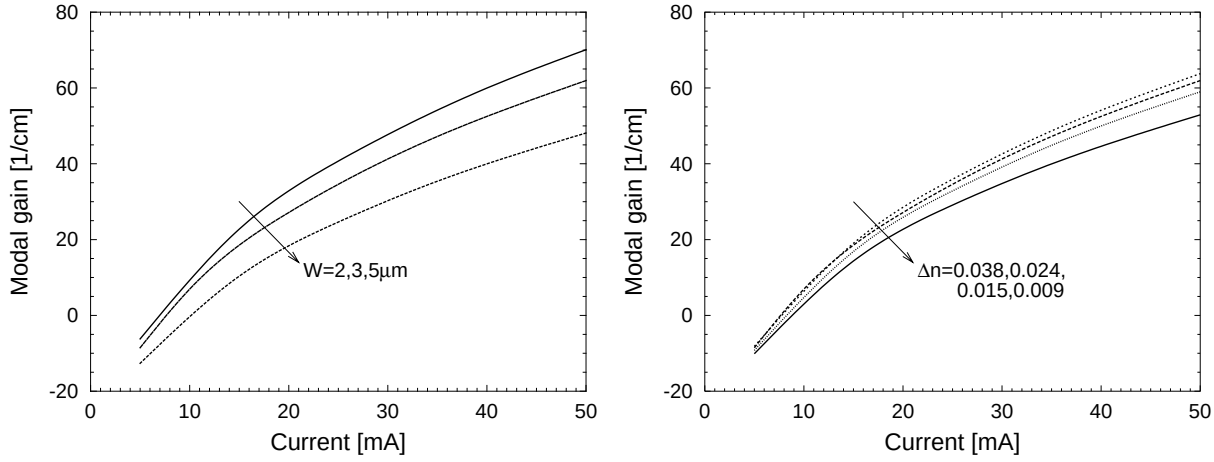

Fig. 4-6 Simulated modal gain as function of bias current for a 500 μm long laser diode with the layer structure of Table 4-1. In the left figure the width is varied for a fixed contrast ($\Delta n_{eff} = 0.024$) while in the right figure the contrast is varied for fixed width (3 μm).

1.2.3 Use of etch stop layer

From the experimental and theoretical results discussed in the previous paragraphs, it is obvious that the etching depth is a very critical device parameter. Therefore, it would be advantageous if the upper film layer could be used as a stop layer for a selective etch process, while maintaining the optimal lateral index contrast (Δn_{eff} =0.024) as it was found from the measurements described in paragraph 1.2.1. This might be obtained by reducing the thickness of the guiding layer somewhat as illustrated in Fig. 4-7. For this figure we calculated the lateral optical index contrast as function of the etching depth for a laser structure identical to the one of Table 4-1 but with varying thickness t_f of the Q1.1 film layers. The optimal layer thickness for the Q1.1 layer appears to be ~230 nm, resulting in a total layer thickness of 650 nm. For this layer thickness, the lateral index contrast Δn_{eff} =0.024 is obtained by stopping the etching process upon the upper film layer. As may be seen from Fig. 4-3, reducing the thickness of the film layers results in a somewhat increased confinement factor in the absorbing cladding layers. However, since also the confinement factor of the QWs is slightly increased, we believe that this will not affect the laser characteristics considerably.

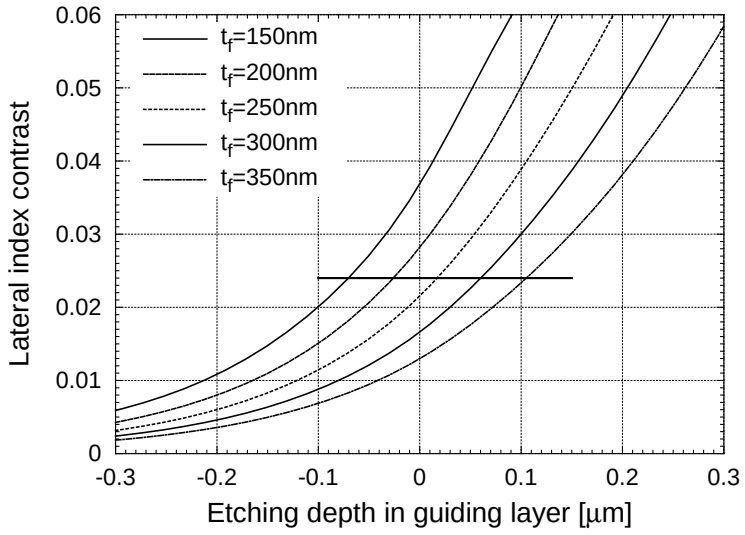

Fig. 4-7 Lateral optical index contrast for the laser of Table 4-1 as function of the etching depth, with the thickness of the Q1.1 film layers varied from 150 nm to 350 nm. The horizontal line indicates the optimal optical index contrast (Δn_{eff} =0.024)

1.3 Semiconductor amplifiers for hybrid integration

For realising the hybridly integrated PICs (see chapters 5 & 6), reflective semiconductor amplifiers (RSOA) are needed. These are amplifiers, which have one highly reflecting facet and one facet with negligible reflection. The latter is obtained by angling the waveguide towards the facet and by applying an AR-coating. We designed the RSOAs in co-operation with Optospeed SA [6][7], which also fabricated them. The design and operating characteristics of these devices is outlined in the next paragraph (1.3.1). We made similar amplifier and laser

arrays in our own facilities. These were used for testing the permanent bonding procedure developed for the hybrid integration process (chapter 6). The fabrication and characterisation of these amplifiers is discussed in paragraph 1.3.2.

1.3.1 Design and operating characteristics of the RSOA-arrays fabricated by Optospeed SA

The transversal cross-section of the amplifiers fabricated by Optospeed SA, could not be chosen freely since the arrays were part of a larger batch, containing also amplifiers for other customers. As shown in Fig. 4-8, a Q1.55 bulk active layer provides the required gain. The Q1.27 film layer on top, with thickness t_f, serves as an etch stop layer. Two different series of amplifiers were fabricated, one with an active layer thickness $t_a = 100$ nm and one with $t_a = 120$ nm. An AR-coating was applied to the slanted facet, the opposite facet was HR-coated.

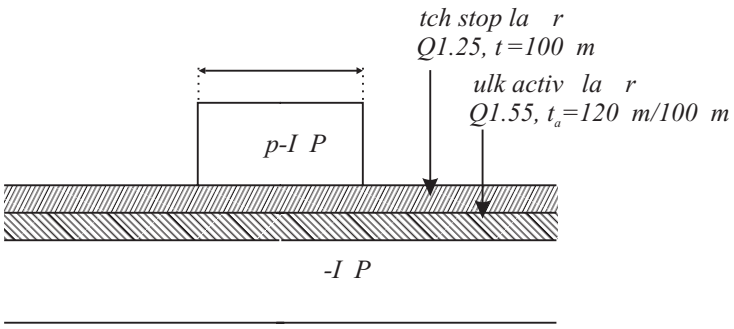

Fig. 4-8 Transversal cross-section of Optospeed RSOAs

From preliminary experiments (see chapter 5), it was found that slanting the waveguide by 5 degrees could not completely reduce residual reflections at the amplifier facet. For that reason, we choose an angle of 10 degrees for the final design. The slanting was obtained by bending the waveguide following a sinusoidal curve, described by:

$$h(z) = \frac{H}{L} z - \frac{H}{\pi} \sin\left(\pi \frac{z}{L} \right) \tag{4-7}$$

z is the distance along the axis, h is the height of the curve with respect to the axis, L is the length of the amplifier and H is determined by the angle at the facet following:

$$H = \frac{L}{2} \tan(\alpha) \tag{4-8}$$

In this way the bend radius is adiabatically increased to its maximum value at $L/2$ and again decreased. The apparent advantage of this structure compared to a curve with constant radius combined with a single straight waveguide, is that no offsets are required, which would be difficult to implement in an active stripe.

The stripe is tapered from 2 μm at the HR-coated facet to 3 μm at the slanted facet. This relaxes the coupling tolerances somewhat and reduces further the residual reflections as may be seen from Fig. 4-9. This figure depicts the calculated reflection for the amplifier as function of the angle with the facet. The effect of the AR-coating is not included in this figure. One may see that the residual reflection of the first order mode is relatively high for the employed angle. However, in the smallest part of the RSOA, the modal gain of the first order mode is much smaller than that of the zeroth order mode, so we believe that this will not compromise the operation of the PICs built from these amplifiers.

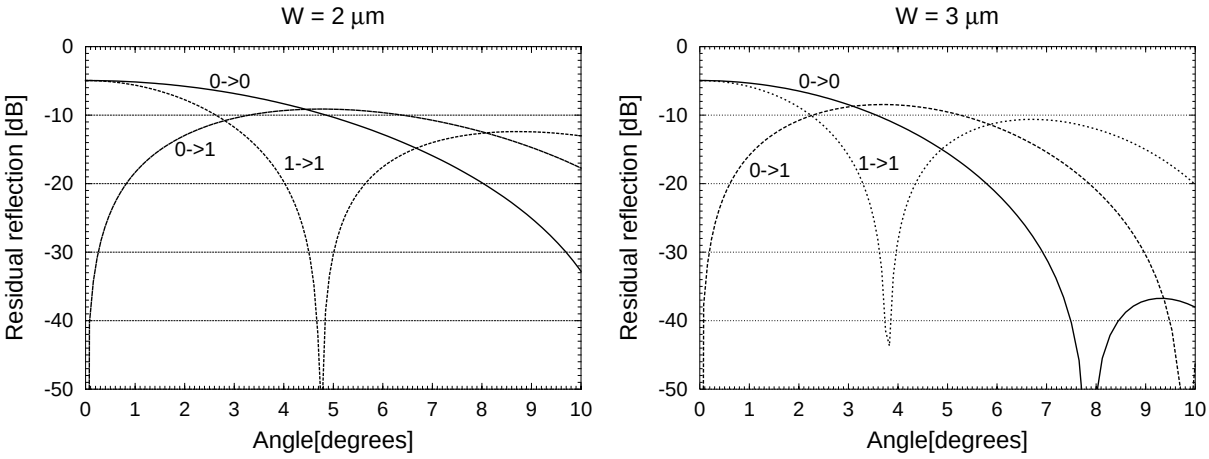

Fig. 4-9 Calculated residual reflection of the RSOA with cross-section as shown in Fig. 4-8 for both $W = 2\mu m$ and $W = 3\mu m$ (t_a = 120 nm).

Each array contained 10 RSOAs, thereby providing some redundancy against fabrication errors since only 8 working amplifiers are required for the realisation of the hybrid Phased-Array laser. The RSOA-length was 400 μm. Fig. 4-10a shows the LI-curves of one array. As

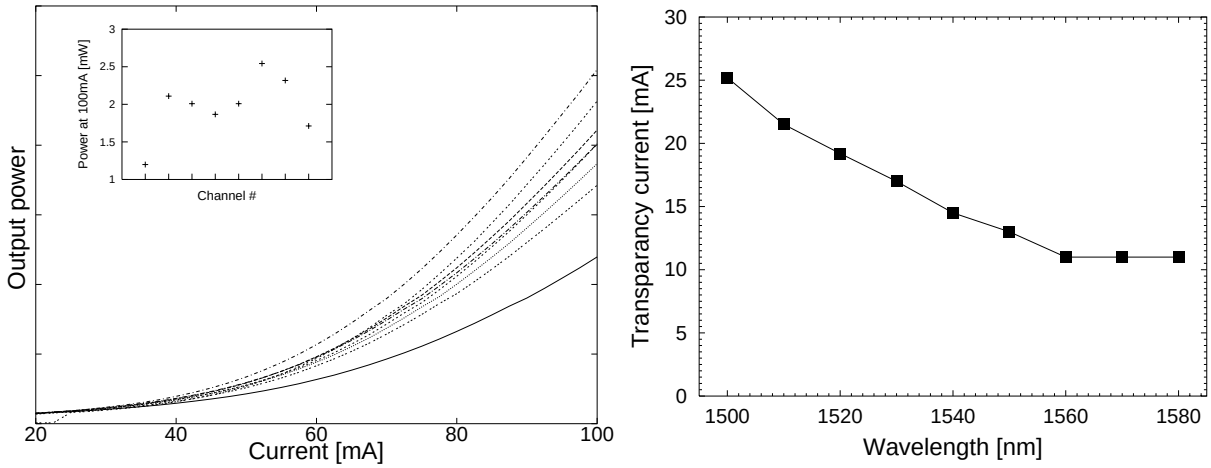

Fig. 4-10 a) LI-curves of RSOAs b) Transparency current as function of wavelength

may be seen from the inset, the output power at 100 mA varies from 1.2 mW to 2.5 mW. This particular array was mounted on a silicon substrate using a conductive epoxy. Fig. 4-10b shows the transparency current of the amplifiers versus the wavelength. We measured this

current by operating the SOA as a detector [8][9]. Chopped light from a tunable laser was injected in the waveguide. If the bias current of the diode is below the transparency current, the detection of the signal arises from absorption of injected electrons. At a bias above the material transparency point, the detection arises from stimulated emission, while at the point of transparency, the detected signal becomes zero and changes its polarity.

Fig. 4-11 shows the spontaneous emission spectrum, measured for different values of the bias current. The peak of the noise spectrum shifts from 1550 nm towards 1500 nm with increasing current. The actual gain peak may be expected to be located somewhat towards higher wavelengths but will show the same behaviour*. From the ripple in the ASE-spectrum, we estimate the residual reflection of the slanted facet to be lower than 30 dB.

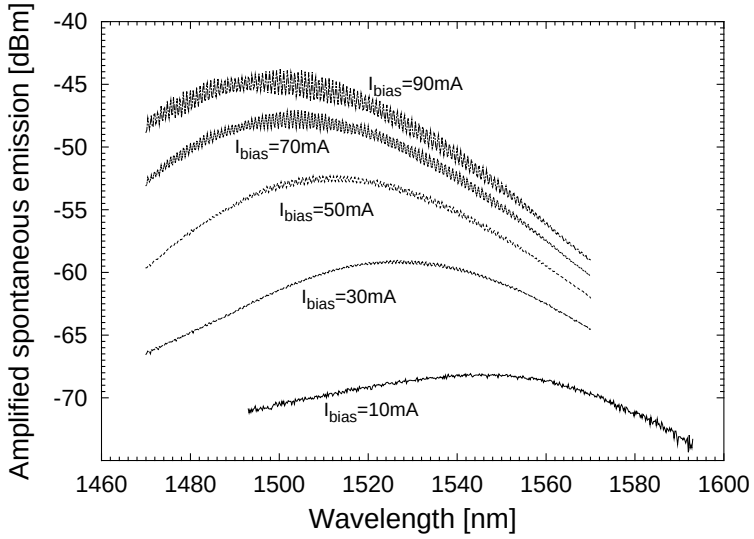

Fig. 4-11 Spontaneous emission spectrum of RSOAs

We also measured the small signal response of the amplifiers. Fig. 4-12a shows the scheme of the measurement setup. A standard current source (1) provides the bias current I_{bias}. This current is combined with a signal coming from a signal generator (Rode & Schwartz SMT, 5 kHz ~ 3 GHz), using a suitable bias tee (3) and applied to the SOA using a high-frequency probe with a built-in 45 Ohm series resistor (R_{ext}). The internal series resistance of the SOA was approximately 5 Ohm. The amplitude of the applied signal was varied between 10 mV and 100 mV, however this had no influence on the measured response. The measurement results are summarised in Fig. 4-12b, c, & d.

Fig. 4-12b shows the small signal response of an RSOA mounted on a Silicon substrate, for different bias currents. The solid lines were fitted using a 1-pole transfer function. In Fig. 4-12c, the 3-dB bandwidth is shown as function of the bias current. Also, the effective carrier

* This is verified by the fact that the operating wavelength of the best hybridly integrated devices (I_{th} ~35 mA) is around 1535 nm and for higher loss devices shifts gradually towards lower wavelength (see chapters 5 & 6)

lifetime $\tau_{eff}\,(=1/(2\pi\nu_{3dB}))$ is shown in this figure. By fitting the latter to the definition $1/\tau_{eff} = A+2BN+3CN^2$ (see chapter 3)* and taking into account the relation between the bias current and the carrier density ($I/eV_a = R(N)$ with $R(N) = AN + BN^2 + CN^3$), we obtained values for the mono-molecular, the bimolecular and the auger recombination coefficients *A*, *B* & *C*, which agree reasonably well with values reported in literature. However, due to the fact that the amplifiers has a ridge type cross-section, it is difficult to determine the effective width that has to be used to calculate the active layer volume V_a. As depicted in Table 4-4, the latter has a strong influence on the values of the recombination coefficients so there remains some uncertainty about their exact magnitude.

In Fig. 4-12d, the small signal response of the RSOA is compared with the small signal response of a comparable RSOA mounted on a glass substrate. It appears that the high-frequency roll-off is somewhat steeper for the RSOA on the silicon substrate. This may stem from a parasitic capacitance to the conductive silicon substrate†. However, it could as well be caused by the slightly different interconnection pattern. Due to the low thermal conductivity, the output power of the amplifiers mounted on the glass carriers was considerably lower compared to that shown in Fig. 4-10 for the amplifiers on a silicon substrate. Therefore, the amplifiers on the glass carriers were no longer used.

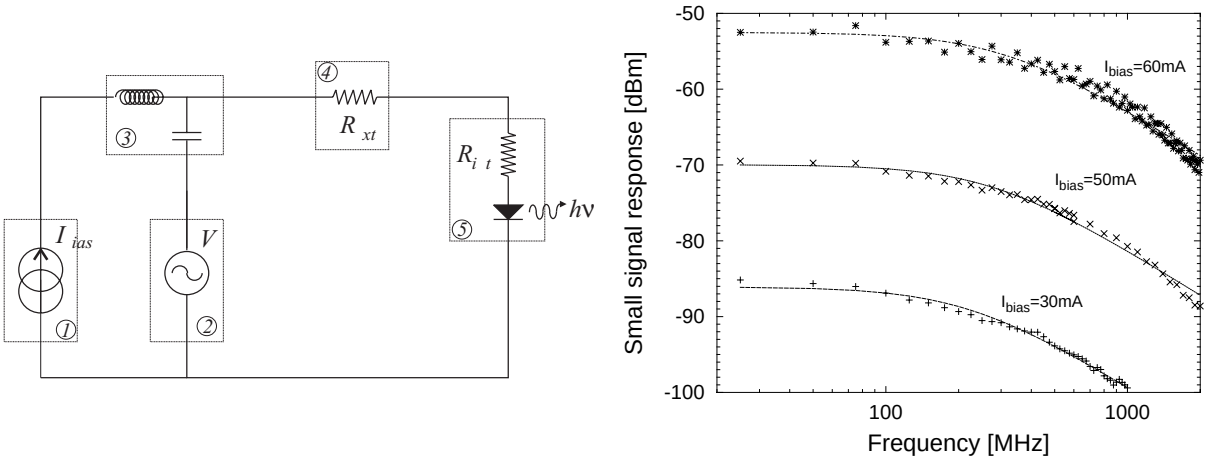

Fig. 4-12 a) Setup for measuring small signal response. b) Small signal response of RSOA for different bias currents.

* We thereby neglected the influence of the term $v_g gS$ what is justified by the fact that the output power is low.

† The substrate was covered with a dielectric layer SiN (300 nm) and a gold interconnection pattern.

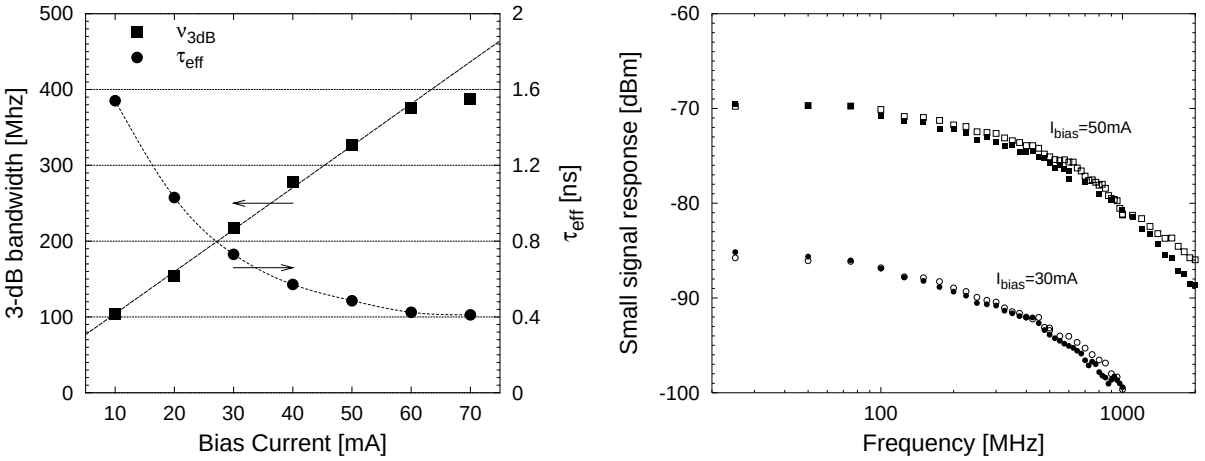

Fig. 4-12 c) 3-dB bandwidth and effective carrier lifetime, as function of bias current. The dashed line is a least squares fit to the 3-dB bandwidth. The solid line was obtained by fitting a calculated curve to the measured results for τ_{eff} from which we obtained the values for A, B & C in the first column in Table 4-4. d) Comparison between small signal response from RSOA mounted on a Silicon substrate (closed symbols) and on a glass substrate (open symbols)

	$W = 2.5\mu m$ $d = 120nm$	$W = 3.0\mu m$ $d = 120nm$	$W = 2.5\mu m$ $d = 100nm$
A, $10^{-8}s^{-1}$	2.5	1.4	3.1
B, $10^{-16}m^3s^{-1}$	1.0	1.2	1.1
C, $10^{-40}m^6s^{-1}$	0.43	0.57	0.25

Table 4-4 Values for the monomolecular, the bimolecular and the auger recombination coefficients, obtained from fitting a calculated curve to the experimentally obtained values for τ_{eff}, shown in Fig. 4-12c.

1.3.2 Design and operating characteristics of the RSOA-arrays fabricated at INTEC

For testing the permanent bonding procedure for hybridly integrated PICs (chapter 6), many devices were necessary. Therefore, we developed a mask set suitable for fabricating both RSOA-arrays and laser arrays. The design of the RSOA-arrays was similar to the design described in the previous paragraph. However, both the width of the waveguide at the highly reflecting facet (2.0, 2.5, 3.0, 3.5 μm) and at the slanted facet (2.5, 3.0, 3.5, 4.0 μm) were varied. Next to the RSOAs, the mask contained also laser arrays with varying ridge width (2.0, 2.5, 3.0, 3.5, 4.0, 5.0 μm).

Several batches of these amplifiers and lasers were manufactured. The fabrication procedure is described in more detail in appendix 1 of this chapter. The cross-section was similar to that depicted in Fig. 4-8. The operating characteristics of the first lasers that were fabricated were not very good. For that reason we measured the optical gain spectrum, from which the

internal loss was extracted (cf. paragraph 1.2.1). The result is shown in Fig. 4-13a. The LI-curve of this laser ($W = 3\mu m$, $L = 600\mu m$) is shown in Fig. 4-13b. The peak gain increases again linear $g_{\max} = A(I - I_0)$ with $A =$ 1.14 (mA.cm)$^{-1}$ and $I_0 = 35$ mA.

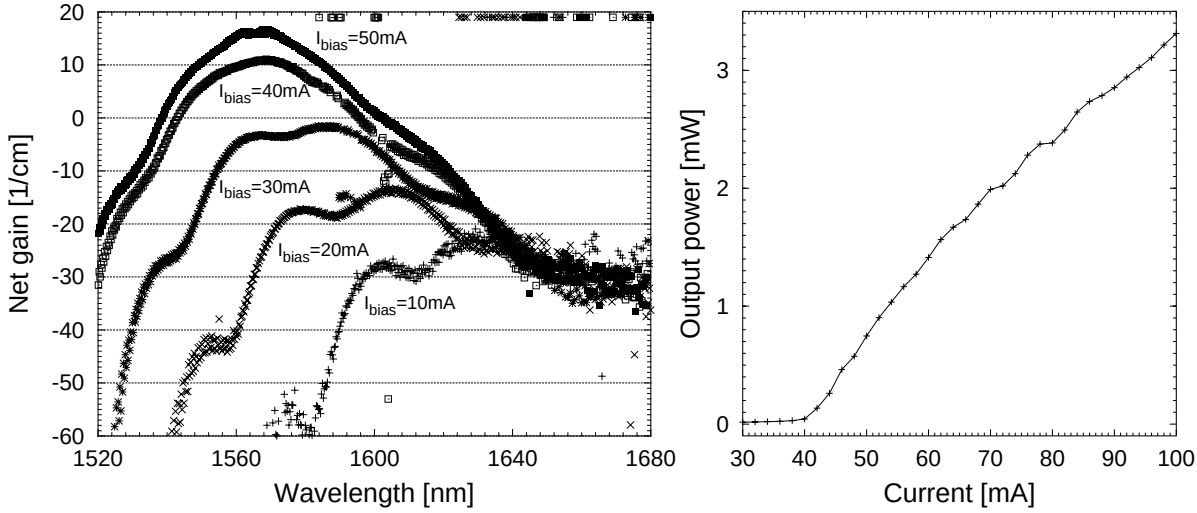

Fig. 4-13 Net gain versus wavelength for different bias currents (left) and LI-curve (right) of laser with bulk-active layer ($W = 3\mu m$, $L = 600\mu m$)

The measured internal loss increases slightly from 25 cm^{-1} at $I_{bias} = 10$ mA to 30 cm^{-1} at 50 mA. Using the same approach as outlined in paragraph 1.2.2, we estimated the differential gain ($a = 1.91\text{x}10^{-16}$cm^{-2}) and the transparency carrier density ($N_0 = 0.925\text{x}10^{-18}$cm^{-3}) of the bulk active layer. Similar values were obtained from the results presented in Fig. 4-15 and Fig. 4-16. As expected, the differential gain obtained here - for a bulk active layer - is lower than the value obtained for the QWs of paragraph 1.2.

The high internal loss and the low differential gain may explain the relatively high threshold current and the low external differential efficiency. However, from fitting the formula for the external differential efficiency $\eta_{ext} = \eta_{\text{int}} / (1 + \alpha_{\text{int}} / \alpha_m)$ to the measured value ($\eta_{ext} = 13\%$) with $R = 32\%$, we believe that also the internal differential efficiency is low (< 0.7).

For fabricating these lasers, a wafer with an InP-top cladding layer of only $1\,\mu m$ was employed. In Fig. 4-14 the calculated absorption in this top-cladding layer versus its thickness is depicted (the exact layer structure of these amplifiers and the material parameters that were used for the simulation may be found in Table 4-5). For obtaining the upper curve, also the loss due to the Titanium contact was taken into account. Titanium has a large real part of the refractive index, allowing the optical mode profile to extend far into this strongly absorbing layer*. The lower curve is the calculated loss for the case where the Titanium contact layer is replaced by an ideal metal layer. If also the absorbing InGaAs layer is omitted, the

* n (Ti) = 3.7 + j 4.5 (e.g. compare to gold: n (Au) = 0.18 + j 10.2) [12]

absorption loss in the cladding layers stays almost constant at 2 cm^{-1}, the value to which both curves in Fig. 4-14 saturate.

The inset of Fig. 4-14 shows the most relevant part of the curves in more detail. The calculated absorption decreases from 6 cm^{-1} to 2 cm^{-1} when increasing the thickness of the cladding layer from $d_{cl} = 1.0\,\mu m$ to $d_{cl} = 1.5\,\mu m$. The dips in the calculated curves have a period of $\lambda_0/(2n_{cl})$ and are caused by a resonance effect in the top-cladding layer.

thickness [nm]	layer	[cm^{-3}]	α [cm^{-1}]
40	Ti	-	364830
200	InGaAs	p++	8500
d_{cl}	p-InP	$2x10^{18}$	40
50	p-InP	$0.5x10^{17}$	10
50	InP	n.i.d.	0
70	Q1.27	n.i.d.	0
100	Q1.55	n.i.d.	0
2000	InP	n	0

Table 4-5 Layer structure of RSOA-amplifiers fabricated at INTEC (d_{cl} was 1 μm for the first wafer and 1.5 μm for following wafers).

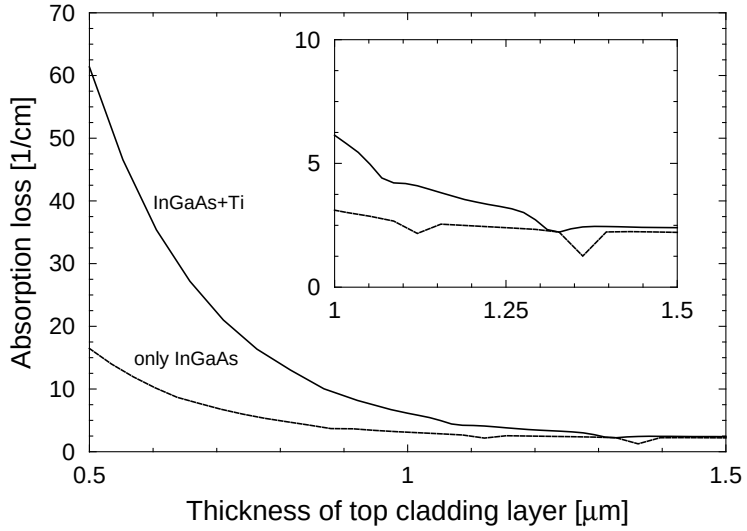

Fig. 4-14 Internal loss versus the top cladding layer thickness for the laser structure depicted in Table 4-5 with $W = 2\,\mu m$.

Although the calculated loss in the top cladding layer cannot completely explain the high value of the measured internal loss, a new wafer with a thicker cladding layer was grown. Results of the characterisation of a series of lasers fabricated using this wafer ($t_a = 120$ nm, $t_f = 70$ nm) are presented in Fig. 4-15 and Fig. 4-16. The first figure shows the threshold current and the threshold current density for lasers with varying stripe width and cavity length under CW operation (T=18°C). In Fig. 4-16, the threshold current and threshold current den-

sity of the 400 μm long lasers under pulsed operation are given (pulse duration 0.1 μs, duty cycle 1 %). It is apparent that, due to the heating of the active layer, the threshold current increases considerably under CW operation. We also measured the threshold current density of broad area lasers under pulsed operation. For 400 μm and 600 μm long lasers, we found respectively $J_{th} = 1365\, A/cm^2$ and $J_{th} = 1090\, A/cm^2$. The first value is indicated in Fig. 4-16b by the horizontal line, which shows that in the ridge lasers a considerable part of the current is lost due to the anti-guiding effect described in paragraph 1.1. As expected this effect is more important for the smaller ridges.

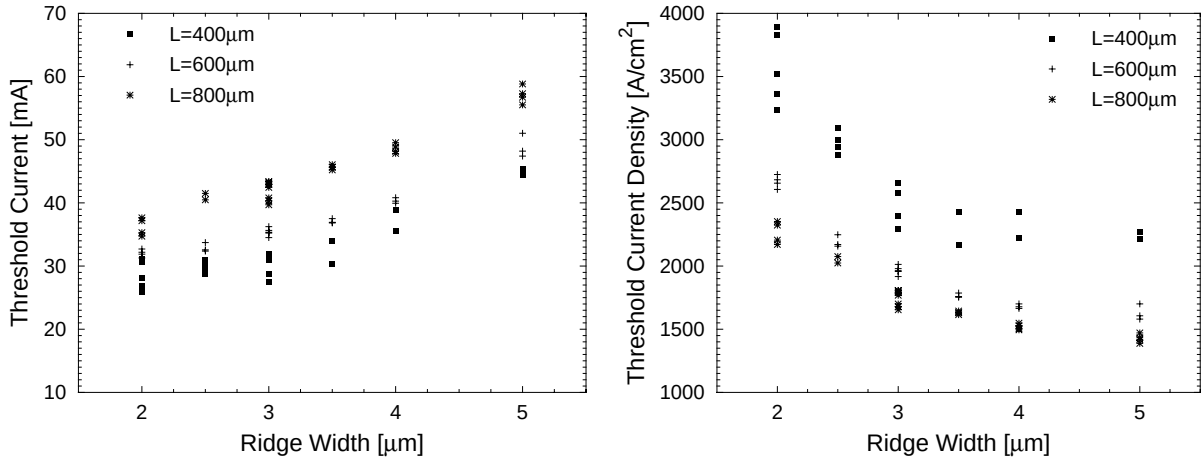

Fig. 4-15 Threshold current (a) and threshold current density (b) as function of waveguide width for CW-operated lasers.

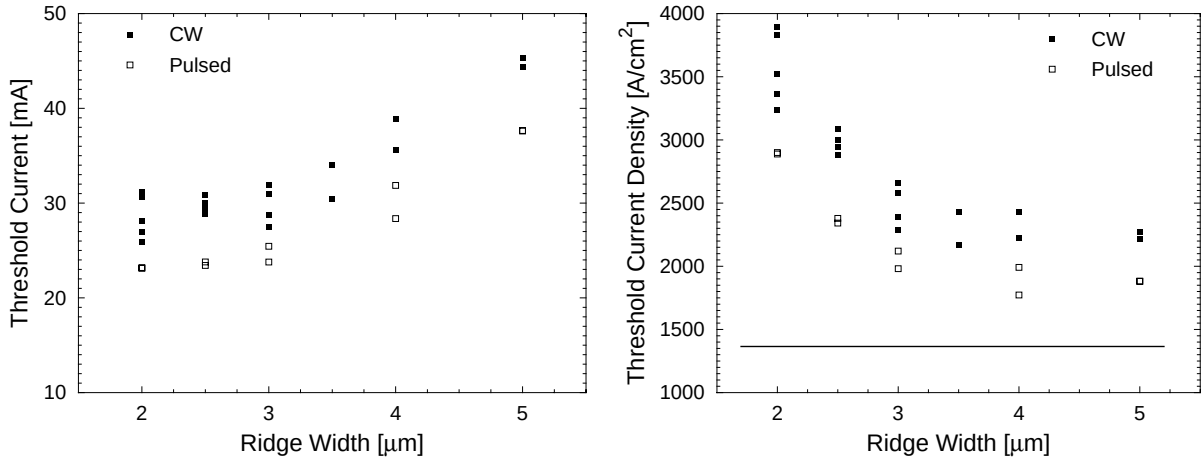

Fig. 4-16 Threshold current (a) and threshold current density (b) as function of waveguide width for lasers under pulsed and CW operation (cavity length $L = 400 \mu m$). The horizontal line in the right picture denotes the threshold current density of broad area lasers with the same cavity length (pulsed).

Although the threshold currents for these lasers were reasonable good, the external differential efficiency* was very low (< 7%), resulting in a maximum output power between 1 mW and 3 mW (compare with Fig. 4-10a, which shows the ASE-emitted from the amplifiers fabricated by Optospeed). The 400 μm long lasers showed a thermal rollover behaviour at output powers below 1 mW. Under pulsed operation, this thermal rollover was not seen but the external differential efficiency remained low (<10%). We tried to extract the internal loss from the values for the external differential efficiency for different lengths. However, due to the large scatter of the values, this was not possible. We believe that the internal loss is high but this cannot completely explain the extremely low external differential efficiency. Also the internal differential efficiency must be low. It is not yet clear how this has to be explained. Note that the threshold current density for the broad-area lasers has a rather normal value.

2 Design and characterisation of passive waveguides

Passive waveguides were studied in the context of both the monolithic integration scheme and the hybrid integration scheme. The waveguides employed for the monolithically integrated PAL had doped cladding layers, which may increase the propagation loss. This effect was investigated experimentally and theoretically (paragraph 2.1). The waveguides employed for realising the passive InP- chips for the hybridly integrated PICs had a cross-section already extensively described in literature. Therefore, we will only present some typical measurement results here (paragraph 2.2).

All the losses, which are reported in this section, were measured using the Fabry-Pérot method [16]. This method gives reliable values for losses in the range 0.5 dB ~ 4 dB. The reproducibility of independent measurements of the same waveguide is about 0.1 dB/cm. On several occasions, we also compared measurements performed by us and performed at the Delft University of Technology. These showed almost the same reproducibility (e.g. see Fig. 4-21 or [17]). The main uncertainty is the value of the facet reflection coefficient. In most cases, we used the values $R_{TE} = 35\%$ and $R_{TM} = 25\%$ for respectively TE and TM polarised light†. Further, for wider, multi-modal waveguides, the uncertainty is larger since the measured value may dependent on the precise excitation of the modes. In most cases only the losses for TE polarised light were measured since this is the polarisation that is relevant for both the monolithically and hybridly integrated lasers.

* All external differential efficiencies are single-sided values

† Changing the value for R from 36% to 32%, changes the extracted propagation loss by 0.5 dB

2.1 Passive waveguides for the monolithically integrated Phased-Array laser

As explained already in chapter 1 and in paragraph 1.2 of the current chapter, the layer stack forming the guiding layer for the passive waveguides of the monolithically integrated PICs is identical to the film layer in the active part, except for a reduction of the layer thickness by a factor 1.5. For that reason, a layer structure as depicted in Table 4-6 was fabricated. This layer stack is almost identical to the one used for the lasers described in paragraph 1.2.1 (cf. Table 4-1), except for a reduced top-cladding height and, of course, for the decrease of the thickness of all layers.

thickness [nm]	layer	[cm^{-3}]	α [cm^{-1}]
200	p-InP	$2x10^{18}$	40
50	p-InP	$0.5x10^{18}$	10
50	InP	n.i.d.	0
250	Q1.1	n.i.d.	0
45	Q1.25	n.i.d.	0
100	5 InGaAs QWs +Q1.25barriers*	n.i.d.	0
45	Q1.25	n.i.d.	0
250	Q1.1	n.i.d.	0
50	InP	n.i.d.	0
	n-InP	n	1

* In this case, the QWs were only 2.5 nm thick and transparent at $\lambda = 1.55\mu m$.

Table 4-6 Layer structure of the passive waveguides originally employed for the monolithic integration process.

The measurement results for straight waveguides with different stripe widths are shown in Fig. 4-17. Waveguides with two different etching depths (res. 120 nm and 320 nm into the quaternary layer) were fabricated*. The large scatter is caused by dust particles that were already on the wafer before the start of the processing. The high loss waveguides all had defects. Consequently, we believe that only the waveguides with the lowest losses are relevant here.

Usually, due to the increasing scattering loss, one expects the waveguide loss to increase strongly with decreasing waveguide width. This is indeed the case for the waveguides of Fig. 4-17b, however, for the waveguides of Fig. 4-17a the loss of the best waveguides is almost constant around 1.5 dB/cm, independently of the waveguide width. Probably, this is caused by the absorption loss in the p-doped cladding layer. We calculated this absorption loss using a 2D complex mode solver and the results are shown in Fig. 4-18. The three curves

* These waveguides were fabricated at INTEC (epitaxial growth + RIE) by T. Van Caenegem. The measurements were partly performed by us and partly by TVC.

respectively denote the absorption in the p-doped top cladding, the n-doped substrate and the total absorption. For the free-carrier absorption in the p-doped cladding layer, we used the values presented in paragraph 2.4 of chapter 2. Values for the absorption of n-doped InP layers are less well known, but it is generally accepted that they are much lower than for p-doped layers. Here we choose rather arbitrarily $\alpha = 1$ cm^{-1} for the n-doped layers (see Table 4-6).

As one may see from the left picture, the absorption loss for the shallower etched waveguide increases strongly with increasing waveguide width. This is caused by an increasing confinement in the absorbing top-cladding layer. Apparently, this effect compensates for the decreasing scattering loss, resulting in an overall more or less constant propagation loss. Note that, although their intrinsic loss is much lower compared to that for the p-doped layers, the n-doped layers may account considerably to the total loss. This originates from the much larger confinement of the optical mode in the substrate. For the deeper etched waveguides (Fig. 4-18b), almost the same effect is seen for the absorption in the p-doped cladding. However, when taking also into account also the substrate loss, the total loss remains almost constant as function of the waveguide width in this case.

Although the results of Fig. 4-18 may qualitatively explain the experimentally obtained loss values, the calculated values are much higher than the measured values*. The values we used for the absorption coefficient of the p-doped cladding layers, have been reported by several authors (see chapter 2). This could indicate that the actual doping levels were lower than the ones indicated in Table 4-6.

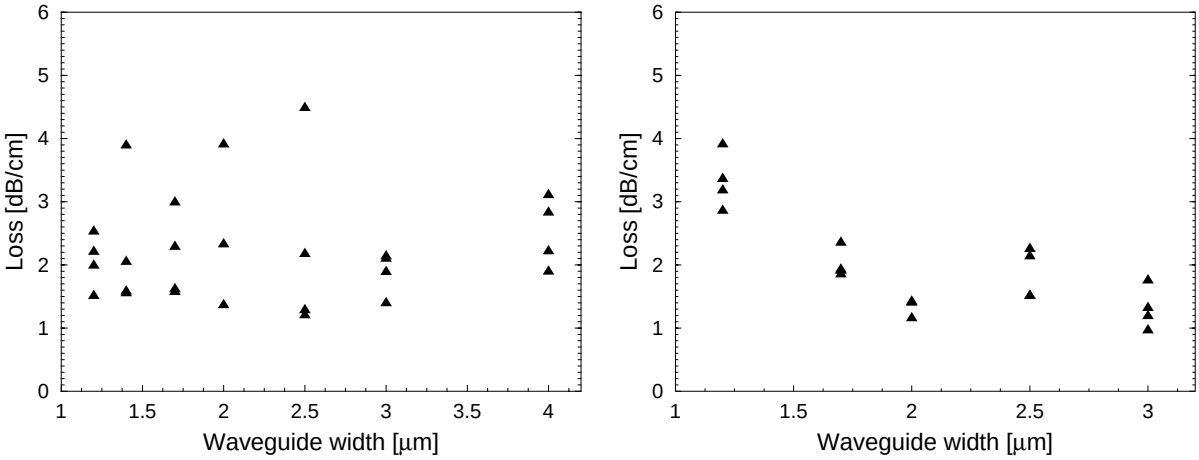

Fig. 4-17 Measured propagation losses for waveguides etched 120 nm (left) and 320 nm (right) into the guiding layer

* The measured values were denoted in dB/cm, the calculated ones in 1/cm.

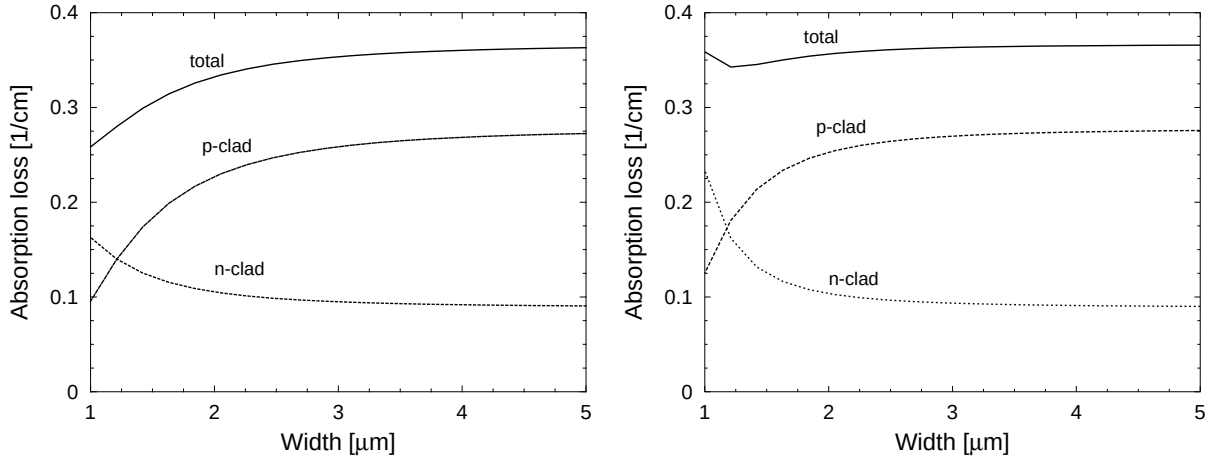

Fig. 4-18 Simulated absorption loss for a waveguide with the layer structure of Table 4-6, etched 120 nm (left) and 320 nm (right) into the guiding layer versus the waveguide width.

By comparing the measurements from Fig. 4-17a and Fig. 4-17b we see that, as expected, the scattering losses are somewhat higher for the deeply etched waveguides. However, overall the losses are very low and this waveguides are considered suitable for use in a complex PIC.

We also measured the losses of curved waveguides (only for the waveguides etched 120 nm into the quaternary layer). Bends with radius $R = 500\mu m$ showed negligible radiation losses. Bends with radius $R = 250\mu m$ showed excess losses of 2.3 dB ($W = 3\mu m$) to 3.7 dB ($W = 1.4\mu m$).

As explained in paragraph 1.2.3, it would be advantageous if the thickness of the Q1.1 film

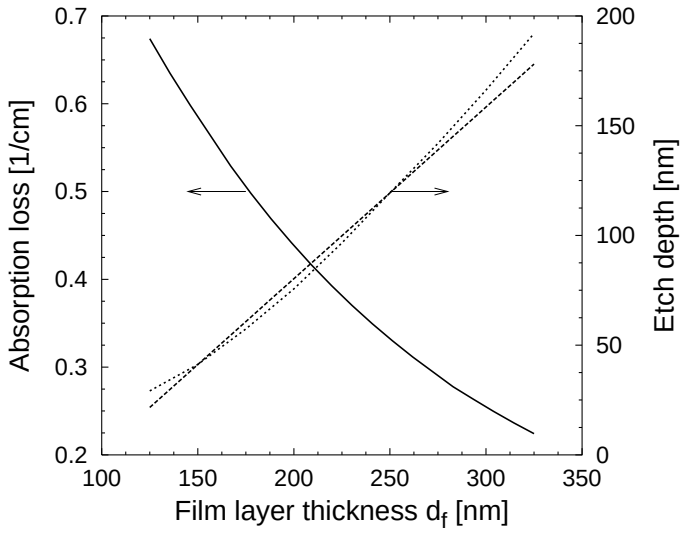

Fig. 4-19 Calculated absorption loss in the p-doped cladding layer of the passive waveguide for the monolithically integrated PAL, as function of the film layer thickness. The etching depth is varied to keep the lateral index contrast constant (the curved line represents the etching depth needed to obtain this, the straight line represents the value that was actually used for the calculation).

layers could be reduced somewhat so that the top of the upper film layer can be used as a selective etch stop layer in the active region. As explained there, the optimal thickness for the film layers in view of the ridge laser fabrication procedure would be around $t_f \sim 230$ nm (in the active part) or $t_f \sim 150$ nm (in the passive part). Due to the reduction of the overall film layer thickness, we expect that the confinement of the optical modes in the absorbing cladding layers and hence the propagation losses will increase. To quantify this, we simulated the absorption loss in the cladding layers of a $2\,\mu m$ wide waveguide, as function of the thickness of the Q1.1 film layers. The etching depth was varied to keep the lateral index contrast constant. Fig. 4-19 shows that the estimated absorption loss increases from 0.33 cm^{-1} for $t_f \sim 250$ nm (the value for which the results of Fig. 4-17 were obtained) to 0.6 cm^{-1} for $t_f \sim 150$ nm.

Fig. 4-20 depicts the minimum bend radius for a $2\ \mu m$ wide waveguide with the structure depicted in Table 4-6, as function of the etching depth. The thickness d_f of the film layer was varied from 50 nm to 300 nm. The bend loss was calculated using the formula derived in chapter 2 (section 2.1.6) taking $\alpha = 0.01$ dB/90^0 as the maximum tolerable value. For the relevant thickness $d_f = 150$nm (indicated in bold in Fig. 4-20), the required etching depth to allow for a $500\,\mu m$ bend radius is ~50 nm.

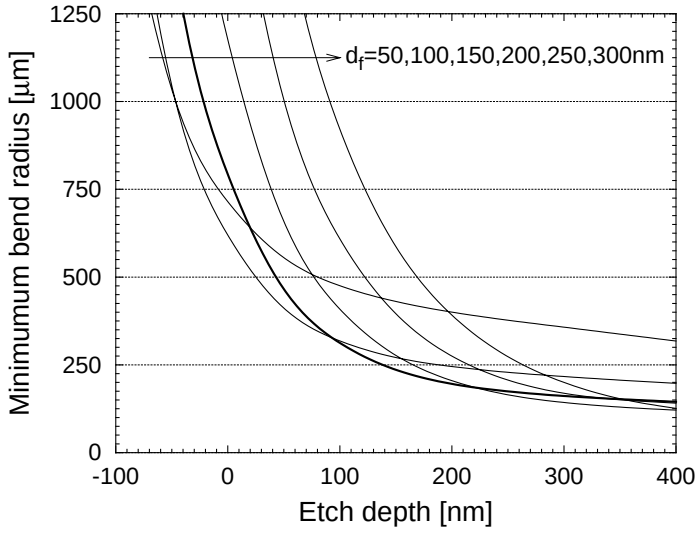

Fig. 4-20 Minimum bend radius for the waveguide structure depicted in Table 4-6 as function of the etching depth. The thickness d_f of the film layer is varied.

2.2 Characterisation of passive waveguides for hybridly integrated PICs

For the passive waveguide chips that were used to build the hybridly integrated PICs (chapters 5 & 6), in most cases a waveguide structure similar to the one depicted in Fig. 2.4 of chapter 2 was employed. The waveguides were fabricated at the Delft University of Technology, using a reactive ion etching process. For details on the manufacturing procedure, we

refer to [15]. The characteristics of this waveguide structure were already described by several authors (e.g. see [13][14]) and in chapter 2 of this work some of its properties were already discussed. The waveguides employed by us had a width of $2\,\mu m$. The most relevant remaining parameter is the etching depth, which determines the minimum bending radius that can be used. For the Phased-Array demultiplexers, typically a minimum bend radius of $500\,\mu m$ was employed. Therefore, as may be seen from Fig. 2.19a with $\log(k_0 R n_1) = 3.827$, an etching depth between 50 nm and 100 nm is required.

Fig. 4-21 shows the measured waveguide losses of reference waveguides on a chip, used for realising the gain-clamped Phased-Array laser (see chapter 5). Results of two independent measurements performed by us and one measurement performed at the Delft University of Technology, are presented. The propagation loss of the straight waveguides was extremely low (~0.6 dB/cm). From the results for the curved waveguides, it is obvious that the bends with radius $500\,\mu m$, which was also the minimum bend radius applied for the Phased-Array on this mask, will exhibit negligible excess losses.

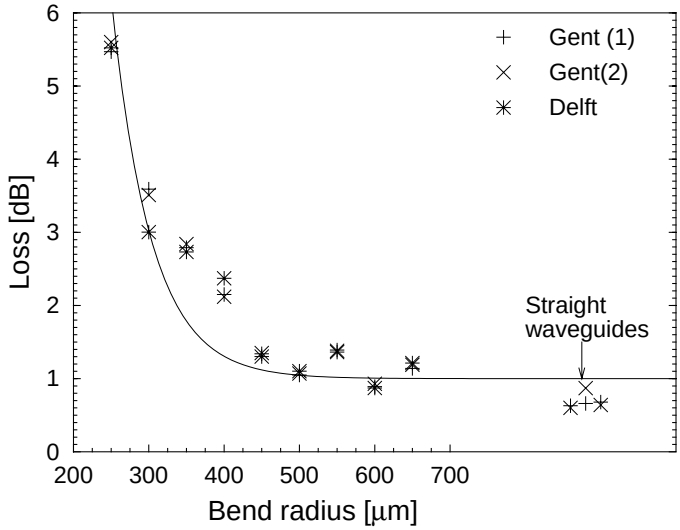

Fig. 4-21 Measured waveguide losses of curved and straight waveguides with cross-section as in Fig. 2.4 ($W = 2\,\mu m$). The solid line was calculated as explained in chapter 2, taking into account a scattering loss of 1dB.

3 Hybrid coupling

In the hybrid coupling scheme, the RSOA with the cross-section shown in Fig. 4-8 and a passive waveguide as described in paragraph 2.2 have to be coupled. To estimate the required alignment accuracy, we modelled the transmission efficiency between these two waveguides using *Fimmprop3D* (cf. chapter 2).

Both waveguides were tapered to $3\,\mu m$ at the facet and they had an AR-coating applied. If the alignment is optimised, the coupling efficiency between both waveguides is very high (96%). Fig. 4-22 shows the transmission efficiency as function of the longitudinal distance

between both waveguides. The effective index of the medium in between both waveguides was chosen to be $n=1$ and $n=1.5$, the latter simulating the case where epoxy is applied between both waveguides. For this calculation, the near field is expanded in its plane wave components, which are successively propagated through the gap and recombined at the interface with the second waveguide. *Fimmprop3D* does not allow the use of absorbing or transparent boundaries, so the power reaching the walls is reflected back into the calculation window. This may be seen from the small ripple in the curves of Fig. 4-22 for the larger gap widths (for this calculation, the window was approximately $30\,\mu m \times 40\,\mu m$).

From these calculations, it is apparent that applying the epoxy may considerably enhance the coupling efficiency. Furthermore, this effect becomes more important with increasing distance between both chips. This has been experimentally verified. From visual inspection, we estimated the distance between two hybridly coupled chips to be less than $2\ \mu m$. Note that in the case with the epoxy applied between both chips, the actual distance between both waveguides is somewhat shorter compared to the case without the epoxy, due to the reduced angle of the laser beam in the free space region with respect to the optical axis.

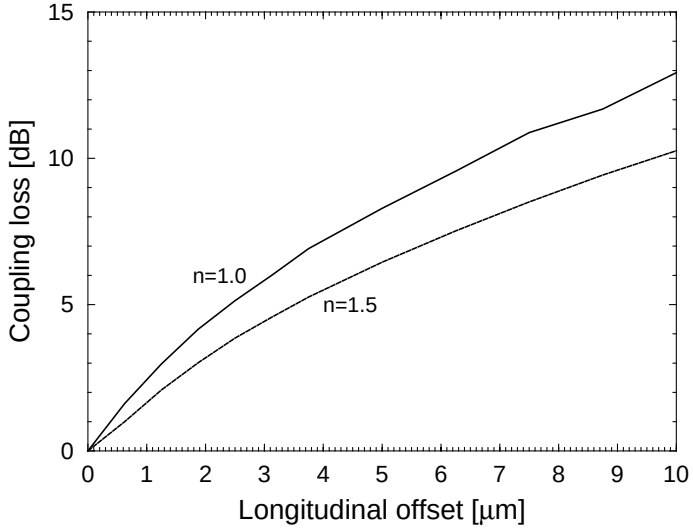

Fig. 4-22 Transmission efficiency between both waveguides as function of the longitudinal displacement d_{gap}, with the refractive index of the medium in between both waveguides equal to $n=1$ and $n=1.5$.

Fig. 4-23 shows the transmission efficiency as function of the lateral displacement. For $d_{gap}=0$, we find a 1 dB down tolerance of $\pm 0.6\mu m$ and $\pm 0.22\mu m$ in horizontal and vertical direction respectively.

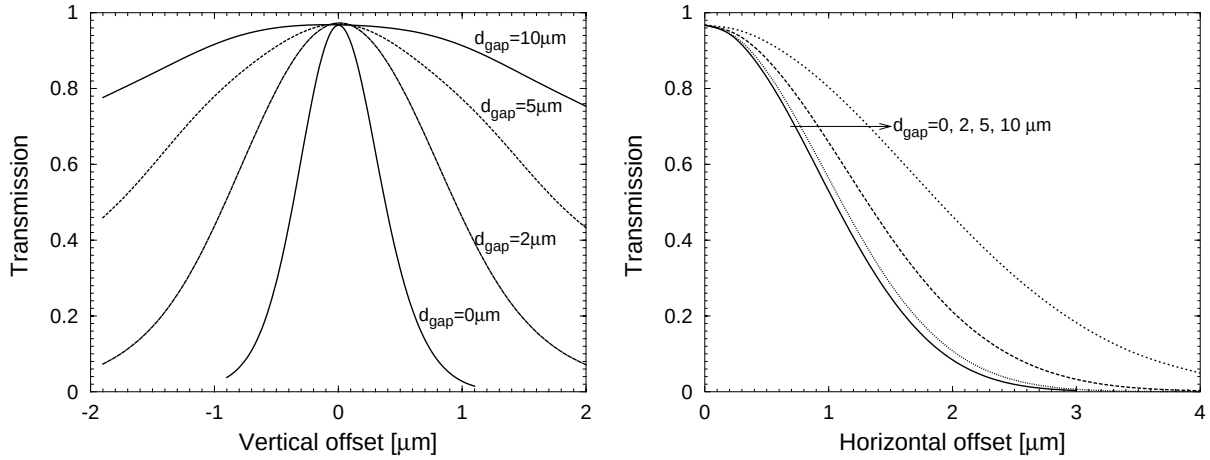

Fig. 4-23 Transmission efficiency as function of lateral displacement in vertical (left) and horizontal (right) direction. The distance between both chips (d_{gap}) is varied.

In Fig. 4-24a the results from Fig. 4-23 are summarised. This figure shows that, although the

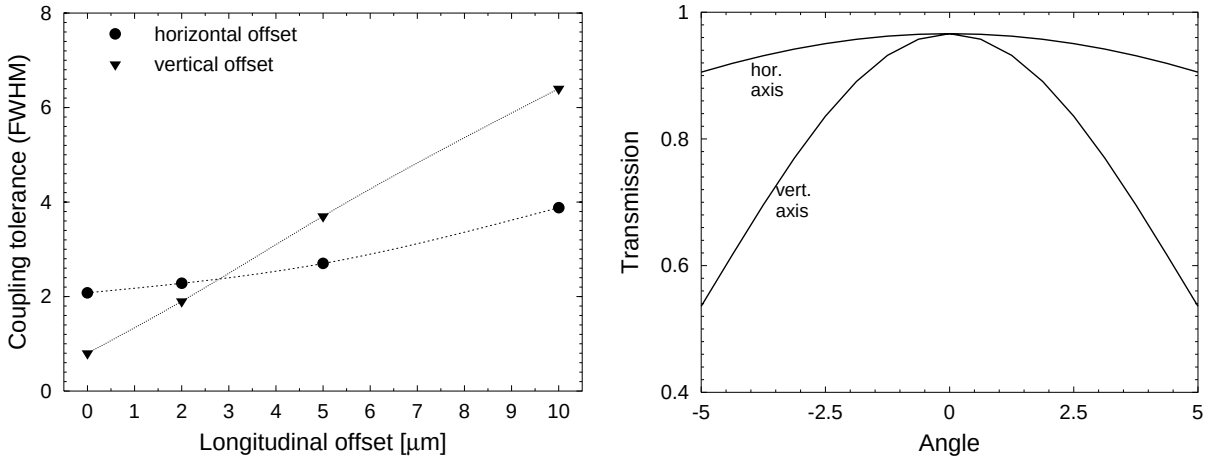

Fig. 4-24 a) Summary of simulations shown in Fig. 4-23. b) Transmission as function of the angle around a vertical and horizontal axis.

vertical alignment is much more critical at zero distance between both chips, its FWHM for the smallest gaps that can be obtained in practice (1 to 3 μm) is almost the same as that for the alignment in horizontal direction. This effect originates from the much wider far field in the vertical direction compared to that in the horizontal direction for both waveguides* and was also seen from experimental results (see chapter 5). Fig. 4-24b shows the transmission as function of an angular misalignment. One sees that the penalty arising from a misalignment around the horizontal axis is rather small. Experimentally, it has been seen that a small mis-

* We calculated $\theta_H = 27^0$ and $\theta_V = 52^0$ for the FWHM of the far field of the amplifier waveguide in respectively horizontal and vertical direction. For the passive waveguide, we found $\theta_H = 27^0$ and $\theta_V = 72^0$.

alignment (~1 degree) of both chips in the upwards direction may even improve the coupling efficiency, probably because this allows to bring both waveguide ends closer together while the misalignment penalty remains small (see also chapter 6).

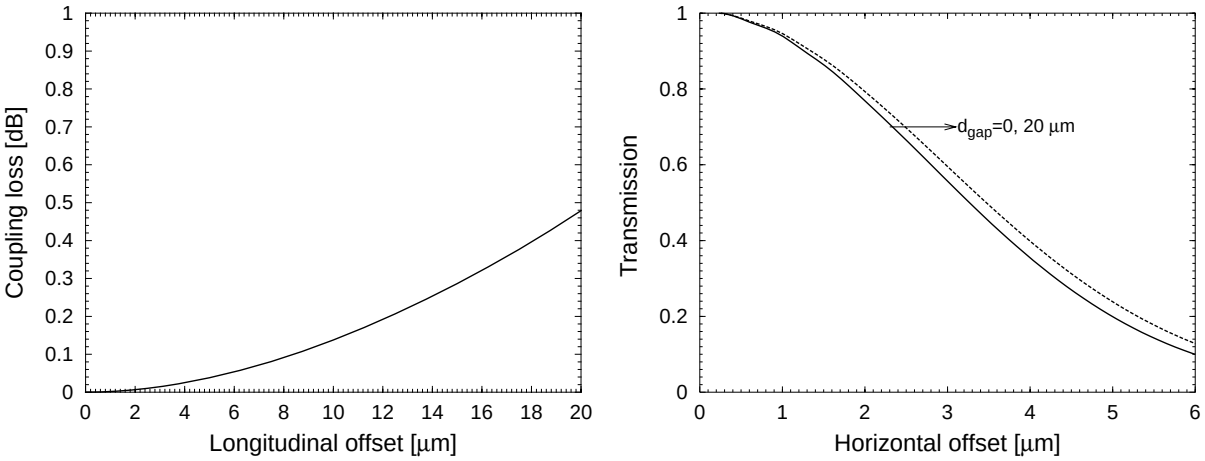

Fig. 4-25 a) Transmission efficiency as function of the distance d_{gap} between two identical low contrast waveguides. b) Transmission efficiency as function of the lateral offset between both waveguides.

For comparison, we calculated the coupling loss between two typical low contrast waveguides, having a 7x7 μm^2 square core with refractive index $n_{co}=1.454$, embedded in uniform cladding layers with $n_{cl}=1.444$. The results are summarised in Fig. 4-25. For $d_{gap}=0\,\mu m$, we find a 1 dB down tolerance of $\pm 1.8\mu m$ for a misalignment in horizontal or vertical direction. More importantly, even for a distance $d_{gap}=20\,\mu m$ between both waveguides, the transmission efficiency decreases by less than 0.5 dB. For comparison, for the high-contrast waveguides we employed, the gap allowed for a reduction in transmission power less than 1 dB, is 0.4 μm.

The most straightforward option to relax the coupling tolerances between hybridly coupled InP-chips is obviously to incorporate spot-size converters in both the active and passive waveguides. However, these may also complicate the processing scheme considerably. Therefore, as an intermediate option, one may try to reduce the width of the far field in the vertical direction (the far field in the horizontal direction is already reasonable small). This may be accomplished by reducing the refractive index of the guiding layer of the waveguides. If the Q1.3 film layer (n=3.395) of the passive waveguides is replaced by a Q1.1 layer (n=3.29), the far field width reduces from $\theta_V = 72^0$ to $\theta_V = 55^0$ (in vertical direction) and the coupling loss decreases from 4 dB to 3 dB (for an air gap of 2 μm). By reducing the refractive index of the film layer to n=3.25, which may be obtained by using diluted waveguides as proposed in [18], the far field width and the coupling loss decrease further to $\theta_V = 47^0$ and 2 dB respectively. However, while for the waveguide with the Q1.1 film layer it

is still possible to employ a minimum bend radius of 500 μm, this will be difficult for the waveguide with n=3.25, due to the small optical contrast with the substrate. Another way to reduce the far field width of the waveguides is to use a graded index core layer. The type of waveguide that is used for the monolithic integration is a first step in that direction: this waveguide has a central Q1.25 layer surrounded by Q1.1 layers. Its far field width is $\theta_V = 53^0$.

4 Transition between active and passive waveguides in the monolithic integration scheme

In the monolithic integration scheme as it was outlined in section 3 of chapter 1, the active waveguides are defined using a wet chemical etching process, while the passive waveguides for the demultiplexer are defined by a reactive ion etching process (dry etching). During the etching of one type of waveguides, the other type is covered using a suitable masking layer. The transition is made in the planarly grown region (= passive region). In practice however, it is not possible to perfectly align both masks. If there is a gap between both masks (Fig. 4-26a), the waveguides will be etched twice as deep in the transition region. If both masks overlap, as shown in Fig. 4-26b, no waveguides will be defined in the transition region.

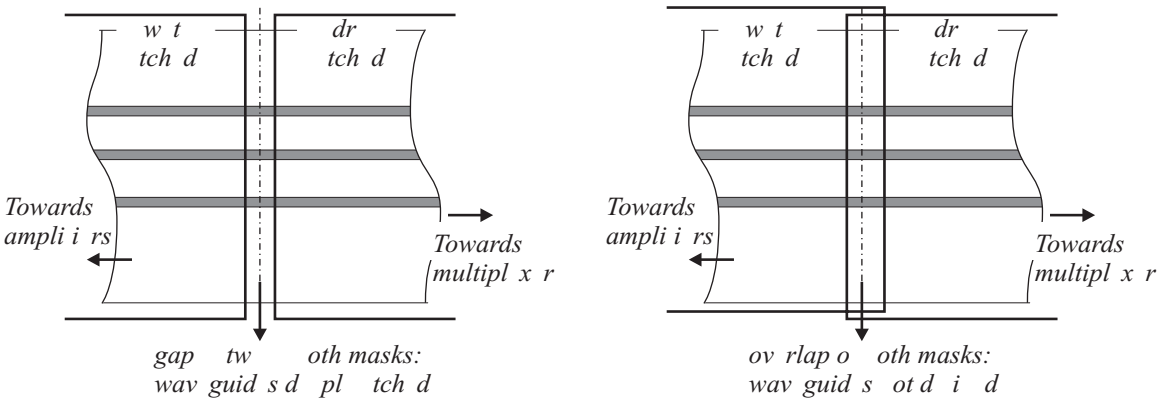

Fig. 4-26 Transition between wet and dry etched region in the monolithic integration scheme.

To model the loss arising from this mask misalignment, we used an eigenmode propagation expansion method for the case of Fig. 4-26a (deeper etched waveguides) and a BPM solver for the case of Fig. 4-26b (short free space propagation). The results are depicted in Fig. 4-27a & b for respectively a 2 μm wide waveguide and a 3 μm wide waveguide. From these one may see that for small misalignment errors, the error arising from a short free-space propagation section is less severe than the one arising from a deeper etched waveguide. Further, we believe that the latter also will give rise to an increased back reflection, which may be disadvantageous for the single mode stability as was explained in chapter 3. Therefore, it was decided to misalign both masks intentionally by a small amount to make them overlap as shown in Fig. 4-26b.

Further, it may be seen from the calculated results in Fig. 4-27 that it is advantageous to use a wider waveguide in the transition region. The latter is a rather general conclusion that applies to a wide range of different types of discontinuities between waveguides such as a lateral offset, waveguide intersections or a chip-to-chip coupling between two waveguides and stems from the fact that the broader waveguides have a smaller far field width. In the particular case of Fig. 4-27, the transition loss is reduced by almost a factor of three by tapering the waveguides from 2 to 3 μm in the transition region.

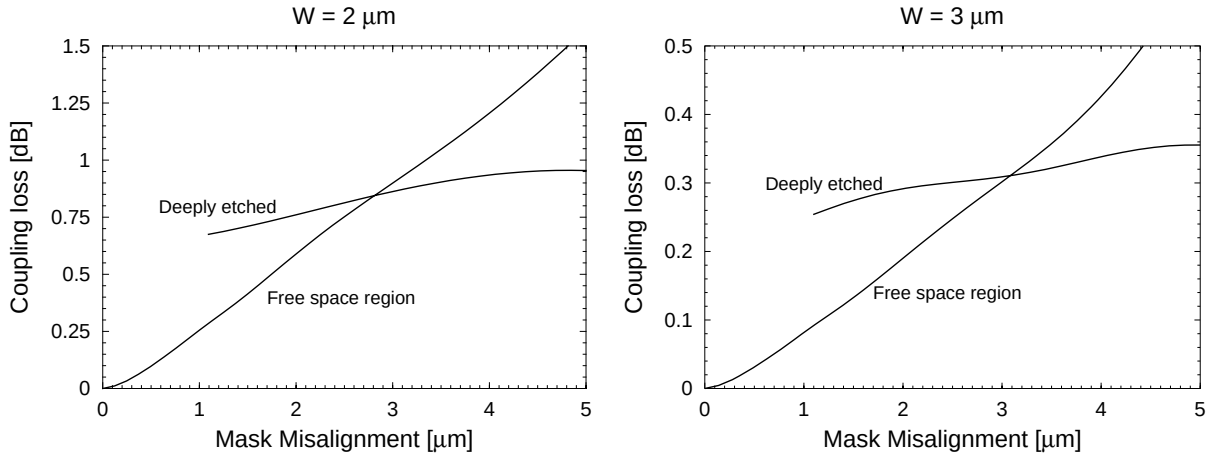

Fig. 4-27 Loss arising from the transition between the wet and dry etched region versus the misalignment error between both masks for a 2 μm wide waveguide (left) and a 3 μm wide waveguide (right).

5 References

[1] M. C. Amann, B. Stegmuller, "Threshold current analysis of InGaAsP-InP ridge-waveguide lasers", IEE Proc. J, Vol. 133, 341-348, 1986

[2] G. J. Letal, J. G. Simmons, J. D. Evans, G. P. Li, "Determiniation of active-region leakage currents in ridge-waveguide strained-layer quantum well lasers by varying the ridge width", IEEE JQE, Vol. 34, 512-517, 1998

[3] J. Demerlier, G. Morthier, R. Baets, "The influence of lateral carrier diffusion on the behaviour of ridge waveguide active MMIs", IEEE/LEOS Symposium Benelux Chapter Proceedings, Mons, Belgium, 227-230, 1999

[4] D. Garbuzov, R. Menna, H. Lee, R. Martinelli, J.C. Connolly, L. Xu, S.R. Forrest, "Broadened waveguide, low loss 1.5um InGaAsP/InP and 2um InGaAsSb / AlGaAsSb laser diodes", pp 551-554, 1997

[5] P. Verhoeve, "Object oriented measurement and parameter extraction methodologies for opto-electronic components", PhD Thesis, University of Gent, Belgium, 1998

[6] Optospeed SA, http://www.optospeed.ch

[7] J. Eckner, "Semiconductor Optical Amplifiers: Optimization of Polarization and Monolithical Integration in Ridge Waveguide Bulk InGaAsP/InP", Diss. ETH No 12792 (1998)

[8] G.E. Shtengel, D.A. Ackerman, "Internal optical loss measurements in 1.3um InGaAsP lasers", El. Lett., Vol. 31, 1157-1158, 1995

[9] P. A. Andrekson, N. A. Olsson, T. Tanbun-Ek, R. A. Logan, D. Coblentz, H. Temkin, "Novel technique for determining internal loss of individual semiconductor lasers", El. Lett., Vol. 28, 171-172, 1992

[10] G. Morthier, P. Vankwikelberge, "Handbook of distributed feedback laser diodes", Artech House, Inc., Boston, 1997

[11] F. Vermaerke, "Ontwerp en realisatie van hoogperformante InGaAs/AlGaAs halfgeleider laserdiodes", Ph. D. Thesis, Unversity of Gent, Belgium, 1996

[12] M. A. Ordal, L. L. Long, R. J. Bell, S. E. Bell, R.R. Bell, R. W. Alexander, C. A. Ward, "Optical properties of the metals Al, Co, Cu, Fe, Pb, Ni, Pd, Pt, Ag, Ti and W in the infrared and far infrared", Appl. Optics, Vol. 22, pp 1099-1119, 1983

[13] M. R. Amersfoot, "Phased-Array wavelength demultiplexers and their integration with photodetectors", PhD. Thesis, Delft University of Technology, The Netherlands, 1994

[14] L. H. Spiekman, "Compact Integrated optical components for telecommunication networks", PhD. Thesis, Delft University of Technology, The Netherlands, 1996

[15] Y. S. Oei, L. H. Spiekman, F. H. Groen, I. Moerman, E. G. Metaal, J. W. Pedersen, "Novel RIE-process for high quality InP-based waveguide structures", Proc. 7th Eur. Conf. On Integr. Opt. (ECIO'95), April 3-6, 1995, Delft, The Netherlands, pp 205-208

[16] G. Walker, "Simple and accurate loss measurement technique for semiconductor optical waveguides", El. Lett., Vol. 21, 581-583, 1985

[17] F. Goussaert, J. Veldeman, "Phased-Array laser voor WDM-toepassingen: ontwerp en realisatie van teststructuren", Afstudeerwerk Universiteit Gent, 1995-1996

[18] A. Rigny, C Ramus, A. Bruno, Y. Rafle, H. Sik, G. Post, M. Carre, A. Carenco, "Taper-assisted polarisation compensation in efficiently fibre-coupled InP demultiplexer", El. Lett., Vol. 32, 1885-1886, 1996

Appendix 1: Ridge laser fabrication procedure

In this section, we shortly introduce the processing scheme that was employed for fabricating the ridge type lasers and amplifiers. For more detailed information we refer to [11].

Step 1

Epitaxial growth of layer structure using a metal organic vapour deposition process (MOVPE).

Step 2

Definition of a SiO_2 pattern defining the ridges. The latter are subsequently etched using a combination of a reactive ion etching process (RIE) and a wet selective etch, which allows to determine exactly the etch depth.

Step 3

An isolating polyimide layer is deposited over the whole wafer and subsequently etched open above the ridges using a photo-resist mask. The opening in the polyimide is $1\,\mu m$ smaller than the ridges. This requires a very critical photo-lithographic step.

Step 4

Deposition of the Ti-Au top contact and electro-plating. For obtaining a good contact the wafer typically has a highly doped 150 nm InGaAS contact layer.

Step 5

Etching away polyimide that is not covered with a metal contact, to facilitate cleaving.

Step 6

Substrate thinning (to $150\,\mu m$) and polishing.

Applying of bottom contact

Step 7

Cleavage of arrays

CHAPTER 5

DEVELOPMENT OF HYBRIDLY COUPLED PHASED-ARRAY MULTI-WAVELENGTH LASERS

Chapter 5

Development of hybridly coupled Phased-Array multi-wavelength lasers

1 Introduction

During the last decade, the maturing of wavelength division multiplexed communication systems has created a strongly increasing demand for complex photonic integrated circuits that can provide multiple optical functions in one compact fibre connected module. For years one believed that only fully monolithically integrated photonic circuits in InP would yield the large versatility in device design and functionality that is needed to fabricate such a photonic integrated circuit (PIC). InP chips can provide optical gain, absorption and a fast refractive index change, all in a very compact size. Moreover, due to their suitability for mass production, monolithically integrated PICs promise to be cheap. However, although there have been numerous laboratory demonstrations of monolithically integrated PICs, even "simple" devices, such as a laser integrated with a monitor diode, have proved to be unattractive for exploitation*. The reason is the complex epitaxial growth and processing required, which makes it very difficult to achieve high yield, good uniformity and reliability in monolithic devices. Moreover, monolithic integration does not provide a solution for the fibre alignment and attachment problem although this may account for over 90 % of the component cost.

In the mean time, due to the growth of the optical network and the stronger competition between the carriers, the demand for cheaper and more reliable optoelectronic components has exploded. Therefore, as an alternative for the monolithically integrated PICs, several companies developed a hybrid integration technology. Starting from well-established technologies such as silica waveguide fabrication, V-groove etching and spot-size converted laser diodes, complex hybridly integrated components could be made commercially available in only a few years and at the moment it seems that at least for the coming years, only this type of components will be able to fulfil the demand for opto-electronic integrated circuits.

For the development of the Phased-Array multi-wavelength laser in the context of this work, an analogous evolution has been seen. While originally the plan was to fabricate a monolithically integrated PAL, that option soon proved to be more difficult than expected. For

---

* At this moment, the DFB-laser with electro-absorption modulator seems to be the only integrated component that is widely exploited. Only very recently also the DBR-laser, which may be considered as an amplifier integrated with two passive grating sections, has become commercially available.

that reason, we developed an alternative, hybrid integration technology, based on the butt coupling of an InP amplifier array and an InP waveguide chip. To avoid reflections at the chip-to-chip interface, the waveguides are slanted towards the facet. This approach differs considerably from most other hybrid integration technologies, which are currently employed, due to the fact that only InP-based chips are employed. Further, only standard components, which require no complicated processing, or components, which are commercially available, are used. At this moment, spot-size converted laser diodes are no such components so they were not used (in a later stage, they may obviously be incorporated in the coupling scheme). Furthermore, the modules realised in the context of this work were only intended for laboratory use and for use in a system demonstrator. Therefore, the more complicated processing and the increased loss associated with passive alignment techniques are not paid of by large volumes here and we decided to use an active alignment approach.

From these restrictions, one may have the impression that our goal was not very challenging and that this coupling approach will have only a limited applicability. However, we believe that, at the development stage, there is a great need for a technology, which circumvents the very time-consuming and expensive processing associated with monolithic integration technologies. And although the approach was initially only intended to deliver some first experimental results, meanwhile some very performant modules have been realised and a permanent bonding technique for the chips was developed (see chapter 6). Currently we believe that this technology may be developed further such that it can be used for fast prototyping of complex PICs and for the realisation of complete modules, which may be used in a demonstrator setup or even for commercial applications.

In the following section, a review of the currently deployed hybrid integration technologies will be given. In section 3, our own hybrid coupling technology is discussed and in section 4 experimental results for the hybridly coupled Phased-Array laser are presented. The experimental verification of the gain-clamping principle for multi-wavelength lasers, which was proposed for the first time in the context of this work and already theoretically introduced in chapter 3, is discussed in section 5.

While the hybrid coupling approach was developed having Phased-Array multi-wavelength lasers in mind, nevertheless the technique is directly applicable to other situations as well. This is illustrated in section 6 where we for the first time present experimental results for a digitally tunable laser using a ring resonator as the wavelength selective element.

2 Overview of currently deployed hybrid integration technologies

The term "hybrid optical integration" spans a range of techniques to copackage active and passive optical elements and the necessary electronic driver circuitry, on a single substrate. Conventionally, transmitters and receivers are housed in metal packages and assembled using multiple ceramic or diamond piece parts that are actively aligned and laser welded. As long as the volumes were low, the reliability of the components was regarded to be more

important than a low price. However, with the increasing demand of optoelectronic components, lower cost assembly techniques are becoming essential. One way to obtain this goal, is to replace the expensive diamond substrates by cheaper ones. Paragraph 2.1 explains why silicon could be the preferred alternative. Another way to realise cheaper modules is to employ passive alignment techniques as discussed in paragraph 2.2 or non-hermetically sealed packages (paragraph 2.3). Paragraph 2.4 summarises some of the remaining difficulties and in paragraph 2.5 some typical examples of currently deployed heterogeneous integration technologies are presented.

2.1 Silicon as the preferred optical bench

Several materials have been used as a substrate for optoelectronic components. The most widespread examples are diamond, silicon and silicon carbide, alumina (Al_2O_3) and aluminum nitride (AlN). Diamond (20 W/cmK) and silicon carbide (3.5 W/cmK) have the highest thermal conductivity. However, these materials are expensive and not very suitable for accurate micro machining. Alumina and aluminum nitride are the cheapest materials but they have a much lower thermal conductivity (0.5, res. 0.7 W/cmK) and they are also not very amenable for high-precision manufacturing techniques. For silicon on the other hand, a broad range of very accurate processing technologies is available. With the development of lasers, which are able to operate reliably at high temperatures without cooling and with reduced threshold current, the limited thermal conductivity of silicon (1.57 W/cmK) forms no longer a problem. Moreover, its thermal expansion coefficient ($2.33 \times 10^{-6} K^{-1}$) is intermediate to that of InP ($4.5 \times 10^{-6} K^{-1}$) and silica ($0.55 \times 10^{-6} K^{-1}$) so that the stresses due to thermal expansion will be shared by the active (typically InP) and the passive (typically Silica) components. Due to its use in the semiconductor industry, silicon wafers can be easily obtained and they are relatively cheap and robust. They are also well characterised and the manufacturing equipment is widely available.

These three factors - satisfactory thermal properties, excellent micromachining possibility and widespread material availability and knowledge - have made silicon the preferred material for optical hybrids. The additional advantage that silicon is also an excellent substrate material for the fabrication of highly performant passive waveguides could only further enhance the success of the silicon optical bench technology.

2.2 Passive optical alignment

The cost associated with active optical alignment is believed to dominate the cost of optoelectronic components [6]. Although a hybrid integration technology facilitating passive alignment may require more complex substrate and device processing, the increase in cost incurred at wafer processing is, in large volumes, greatly outweighed by the reduction in the final assembly cost, resulting in a net lowering of the component price [22]. In general, several techniques are combined to facilitate passive optical alignment:

- *Anisotropic etching*: the anisotropic etching properties of silicon are commonly used to fabricate precision V-grooves. These allow for accurate alignment of a fibre (or a fibre array) with an optoelectronic component. Sometimes, the V-groove technique is combined with alignment features on the optoelectronic component to compensate for the statistical variation in the V-groove width ([2], see also the examples described at the end of this section). Next to fabricating V-grooves, the etching properties of silicon may also be used to place ball lenses with very high precision [20] and for etching mirrors, which facilitate a simple alignment of a photo diode and an optical fibre or an optoelectronic component [3].
- *Flip chip mounting*: for the accurate vertical alignment of optoelectronic components, flip-chip technology has proven to be indispensable. Moreover, due to their smaller physical size and the very low inductance, solder bumps have an inherent advantage compared to wire bonds. For the lateral alignment, one may again rely on the self-aligning properties of the solder bumps. However, also other techniques were developed, such as precision micromachining, in order to fit parts together precisely [22], or optical methods [16]. The latter are similar to the method of aligning photo masks during photolithography in that they use visual alignment patterns for reference and an expensive precision stage for the alignment (but do not require precise optical processing).
- *Spot size converters*: by the development of lasers amplifiers with integrated beam size expanders, the required alignment tolerances can be reduced significantly, both in lateral and in longitudinal direction (due to the better confinement of the beam) and additional lenses in the optical train [20] are no longer required. The tolerances for the alignment of a standard laser diode and a lensed fibre may be below 0.5 μm. Current tolerances for the alignment of SOAs integrated with spot-size converters (1 dB reduction in transmission) are better than ± 2 μm in horizontal and vertical directions and 20 μm in axial direction [16] (see also chapter 4, section 3).

2.3 Non-hermetic packaging

Devices in a plastic package may be extremely cheap compared to their hermetically sealed metal counterparts, since the assembly may be automated and the raw materials are cheap [23]. However, non-hermetically packaging techniques require the whole component to be encapsulated in silicone or a similar material to prevent water condensation [21]. If lenses have to be used in the optical train [20], this is not possible due to the index-matching effect of the silicone. With the advent of good quality beam-expanded laser diodes and amplifiers, these lenses are no longer needed, thereby opening the way to non-hermetically packaging techniques.

2.4 Remaining difficulties

Fig. 5-1 presents an overview of the previous paragraphs. Although several very successful hybridly integrated modules have been demonstrated, some difficulties remain to be solved. The most apparent one relates to the tight tolerances required when processing the components for the hybrid PICs. Although the basic building blocks, such as the V-grooves for the

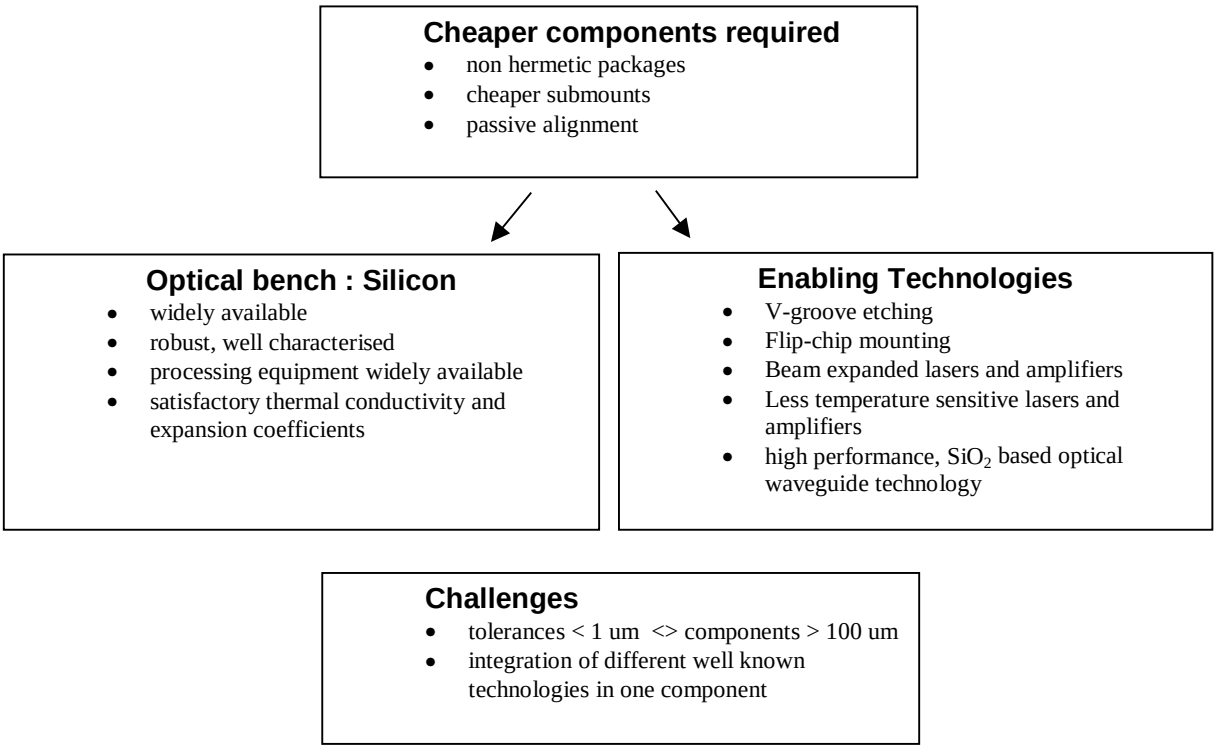

Fig. 5-1 Summary of drives and challenges for Silicon bench technologies

fibre-alignment, are an order of magnitude larger than those of electronic IC's, a similar fabrication accuracy (0.1-1 µm) must be obtained. In particular the high-precision lithography may be compromised by he large features.

Another essential question is how to integrate the electrical interconnect pattern with the silicon motherboard. Due to its conductivity, silicon cannot be used as the dielectric material for microstrip line structures. The easiest alternative is to cover the silicon with a dielectric and to use coplanar waveguides [16]. However, when a more dense interconnect pattern is required or for line rates over 2.5 Gbit/s, microstrip lines are indispensable. For that purpose, complete microstrip structures (ground plane, dielectric and signal plane) have been formed on the silicon motherboard. Another way to circumvent the problem is to position the small optical silicon hybrid on a larger motherboard, containing the electronic circuitry [7][8].

As a last problem, we want to mention the so-called "statistical yield limit". Several components and processes cannot be defined with absolute accuracy. Examples are the dimensions of the amplifier and the laser diode chips, which are determined by the cleavage process (typical variation $5\,\mu m$ per facet), the absolute fibre diameter and its concentricity, which, even for well controlled processes, may vary over several hundred nanometres, the depth of the V-grooves and the flip-chip mounting. All these processes introduce a statistical variation of the alignment accuracy. Consequently, the device performance will vary in a statistical way also.

2.5 Examples

a) Fibre Array Alignment Procedure (ETH Zurich)

Due to small process variations, the exact width of a V-groove, which is used for passively aligning an optical fibre with an optoelectronic chip, may vary. Since the height of the core of the optical fibre with respect to the surface of the silicon substrate is determined by the width of the groove, these process variations generally imply a variation of the optical coupling efficiency. Hunziker [2] has proposed an interesting approach to circumvent this problem. The idea is illustrated in Fig. 5-2. The optical self-alignment is based on an etched indentation on the optoelectronic chip, which fits in the same silicon V-groove as the fibre. The alignment in both horizontal and vertical direction is thereby defined by a single parameter *D*, the distance between the waveguide centre and the alignment edge. This approach has been successfully applied to amplifier arrays with standard amplifiers and with angled amplifiers.

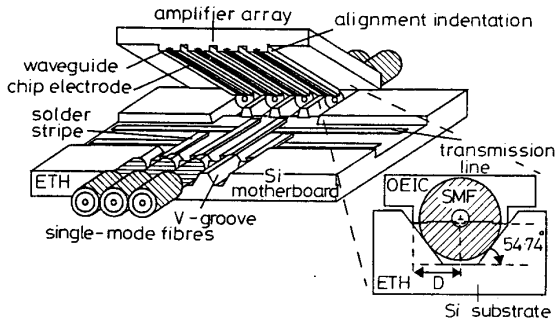

Fig. 5-2 Principle of self-aligned flip-chip packaging (from [2])

b) Optical transmitter module (Nortel)

Fig. 5-3 shows a SEM-picture of a typical hybrid transmitter module as it is widely applied and commercially exploited today [4]. It contains a ridge waveguide laser and a monitor diode passively aligned on a silicon optical bench. The laser incorporates a patterned metal-

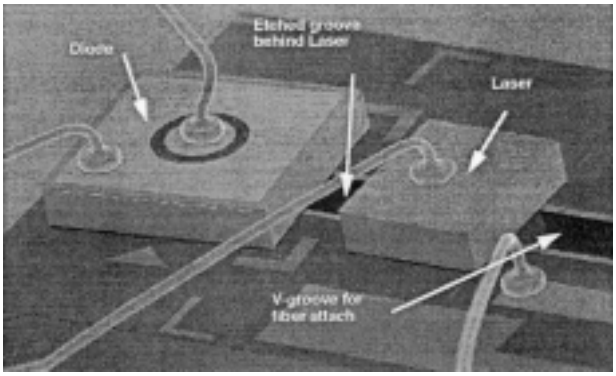

Fig. 5-3 Optical transmitter module (from [4])

lisation, which matches that on the silicon bench. A flip chip bonding process is used to mount the laser diode to the optical bench. This positions it relative to the etched V-groove

in front of the laser. This V-groove is used for location of a lensed single mode fibre. To the rear of the transmitter, another groove is etched, which reflect the light exiting the back facet of the transmitter onto the photo diode. After completing the assembly, the whole module is put into a ceramic package.

This alignment procedure has been successfully implemented in a volume production environment and forms the basis of a commercially available, low-cost optical transmitter. Reliability tests using devices without any pre-screening have demonstrated an excellent stability during storage at extreme temperatures and up to 7000 temperature cycles. Similar approaches for both transmitter and receiver modules were demonstrated by other manufacturers [9][10][11][12][13][18].

An important aspect of the fabrication of this type of modules is that part of the optical assembly and the characterisation can be done before dicing the silicon wafer (e.g. the die bonding of laser and detector). This means that fibre optic modules can be made leveraging on methods developed for electronics. In [9], a manufacturing process allowing making approximately 350 modules on a batch comprised of a single wafer is presented. The chips are burned in while still in the whole wafer and they can be tested and screened prior to further assembly to reduce the cost.

c) Hybrid optical bench incorporating passive waveguides (NTT)

One of the most prominent and most complete hybrid integration schemes is the hybrid planar lightwave circuit (PLC) platform developed by NTT [14][15][16][17][18][19][21] and illustrated in Fig. 5-4. Instead of an ordinary substrate, a silicon substrate with terraced regions is used. The optical waveguide with a core embedded in a thick cladding layer is formed only on the ground plane of the substrate. The terraced surface acts as an optical bench and as a heat sink for the active devices (amplifiers, laser diodes and waveguide detectors). The lateral alignment of the optoelectronic devices is achieved by index alignment: marks are formed on both the silicon terrace and the active device and the placing of the chip is carried out as shown in Fig. 5-4 (accuracy ± 1 μm). Since the height from the surface to the waveguide core centre is designed to be identical to the height of the active layer of an active device, the alignment in vertical direction (accuracy ± 0.5 μm) is carried out simply by placing the chip on the solder surface. The amplifiers and lasers employ spot size converters [24], keeping the average coupling loss below 4 dB. This is a combined effect from different alignment errors: misalignment of the marks on both the optical bench and the optical devices, misalignment of the marks with respect to each other, vertical misalignment and variation on the length of the chips due to cleaving inaccuracy [19].

Since the passive optical waveguides end in the middle of the chip, AR-coating of their facets is difficult. Therefore, they are angled as may be seen from Fig. 5-4. A special saw-toothed structure is necessary because the active devices have no angled waveguides and emit perpendicular to their facet [14]. Electronic circuits are formed by coplanar waveguides on the

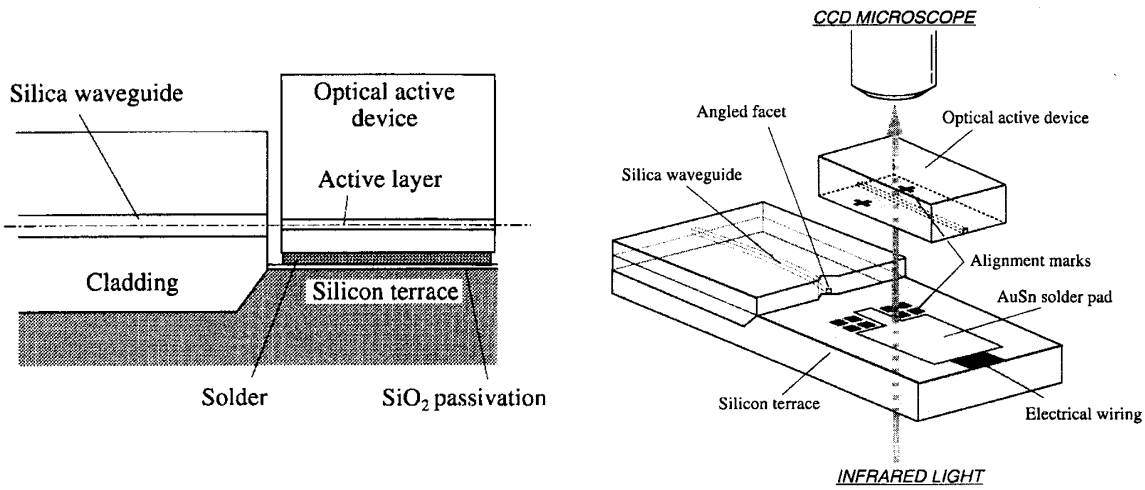

Fig. 5-4 Hybrid PLC platform developed for integrating low contrast passive waveguides (silica on silicon) with InP optical active devices (from [19]).

overcladding layer of the passive waveguides. They are connected to electrodes on the silicon terrace with gold wires [16].

Using this PLC platform technology, transceiver chips incorporating a 1.55/1.30 demux, a receiver and a laser diode, intended for use in FTTH-applications (fibre to the home), have been made commercially available (Fig. 5-5a). In addition, gate-switches with two arrays of four SOA-gates are available (Fig. 5-5b) by now [16].

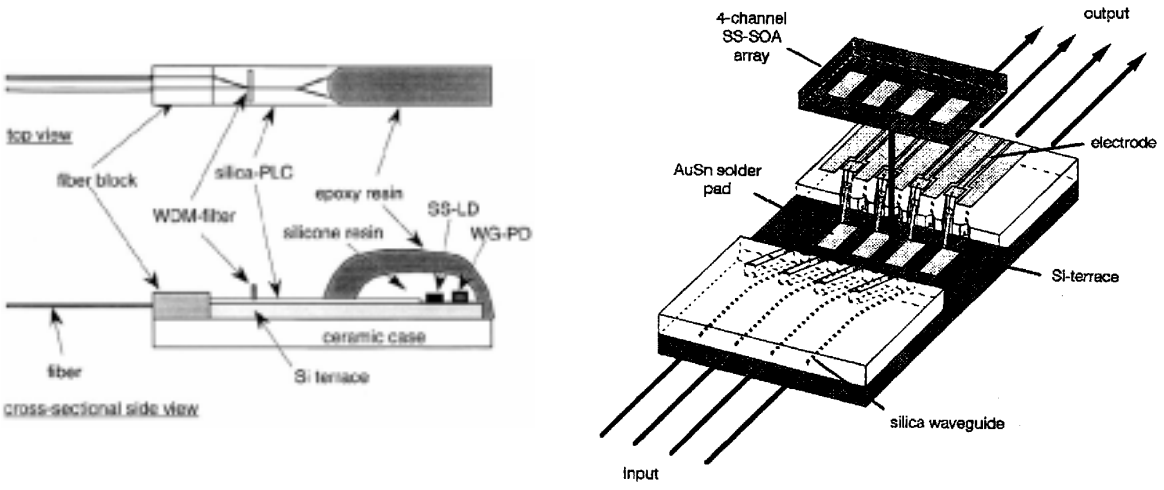

Fig. 5-5 a) Plastic module for a Spot-size converted laser diode (SS-LD) and waveguide photo diodes mounted on a PLC platform (from [21]). b) Optical gate array (from [16]).

One of the most important advantages of monolithically integrated InP PICs compared to Silica-based technologies is that, due to the higher index contrast, a lot more devices may be fabricated on a single substrate. Silica based technologies were regarded to be not suitable for realising PICs integrating a large number of different optical functions. However this problem has been circumvented recently, by the development of a PLC to PLC direct attachment technique. Using this approach, an eight channel wavelength selector module was

fabricated, by connecting two conventional PLCs, each containing a Phased-Array demultiplexer, on either side of an optical gate array (identical to the one of Fig. 5-5b), using a UV curable adhesive [17].

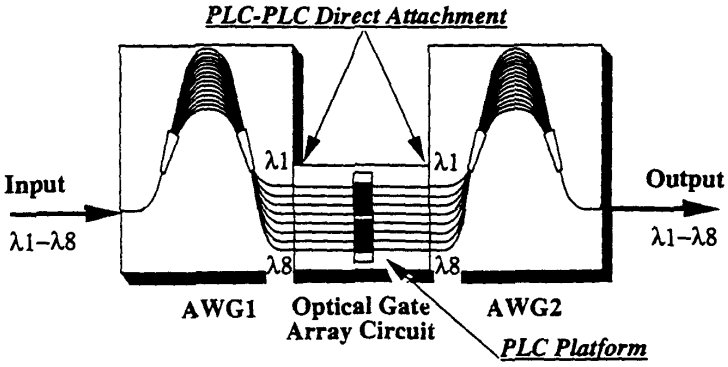

Fig. 5-6 Direct PLC to PLC attachment technique (from [17]).

3 Our approach

This section describes the hybrid coupling technology as it was developed in the context of this work. Fig. 5-7 demonstrates how a hybrid PIC is realised in practice. An amplifier array is butt coupled with an InP-based passive optical chip using precision translation stages. The coupling is carried out by looking at the gap between both chips through a microscope

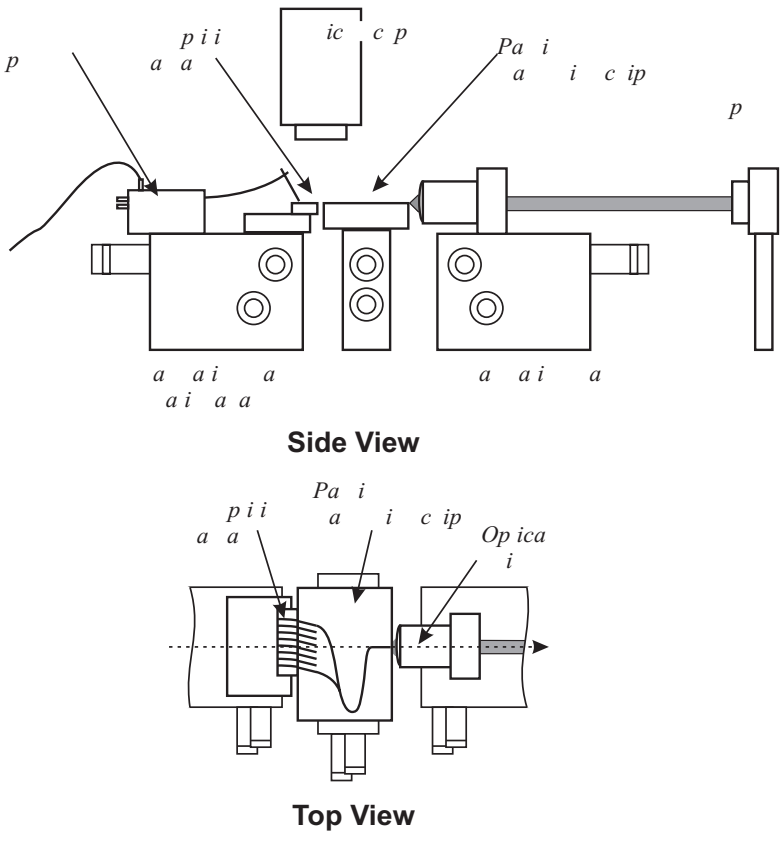

Fig. 5-7a Setup for hybridly coupling an amplifier array and a passive waveguide chip

and by monitoring the output power using an infrared camera and a power meter. The first translation stage is equipped with three electrostrictively-controlled actuators that position the stage along the x-, y- and z-axes. Three other actuators allow changing the angular position of the device along the three rotational axes. Similar to standard waveguide coupling experiments, the Lloyd interference fringes may be used to adjust the height of both chips. The lateral alignment of the waveguides is carried out by visual inspection and then further optimised by inspecting the output power. To optimise the coupling in the longitudinal direction, the chips are brought in physical contact. This also automatically optimises the (angular) alignment around the vertical axis as sketched in Fig. 5-8. The angular alignment around the horizontal axes is more difficult. If only one waveguide has to be connected, the optimisation of the alignment around the axis parallel to the waveguides may be skipped. However, if multiple channels have to be coupled, the alignment around this axis is very critical and is carried out by monitoring the output power from waveguides at the outer edges of the chip. A drawback of the setup used is that the rotation centre of the three rotational axes does not coincide with the position of the amplifier facet, which means that following every adjustment of one of the angular positions, all the other positions have to be readjusted. The optimisation around the horizontal rotational axis perpendicular to the optical axis is the most time consuming process and is carried out by changing the angle around this axis in small steps. For every step, the positions with respect to all other axes have to be optimised again. Fig. 5-7b shows a photograph of the measurement setup.

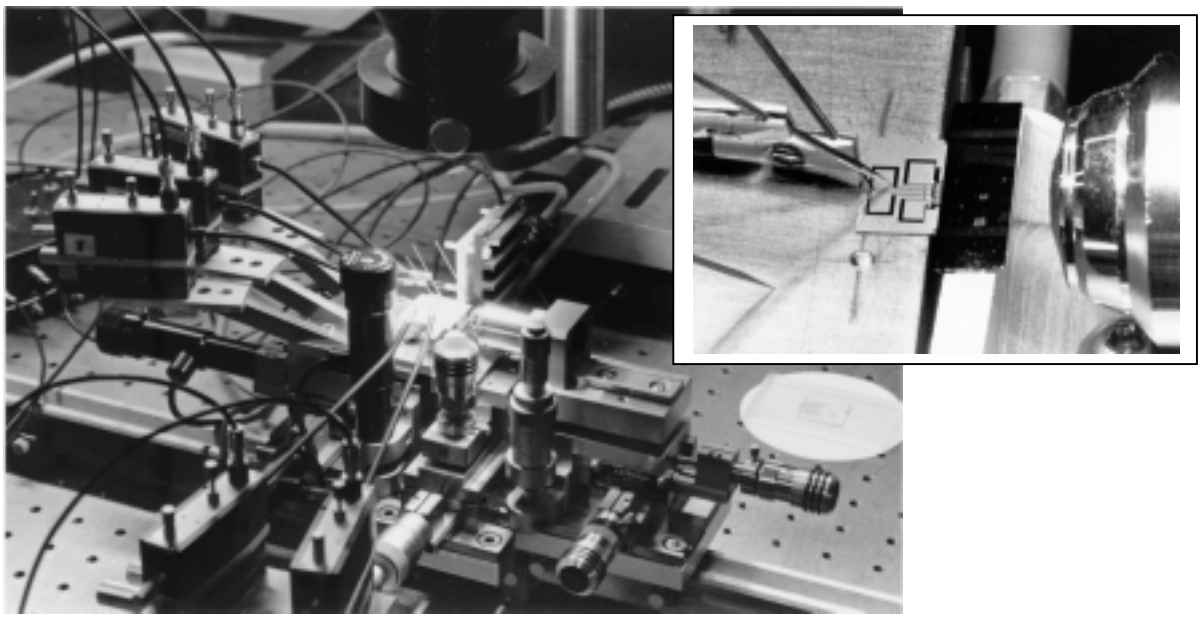

Fig. 5-7b Photograph of the optical bench used for the hybrid coupling of two chips

It is difficult to estimate the time needed for completing the whole coupling process, however when starting from a more or less pre-aligned setup*, one typically needs between 10

* The pre-alignment may be carried out by visual inspection or using simple means such as a spirit level.

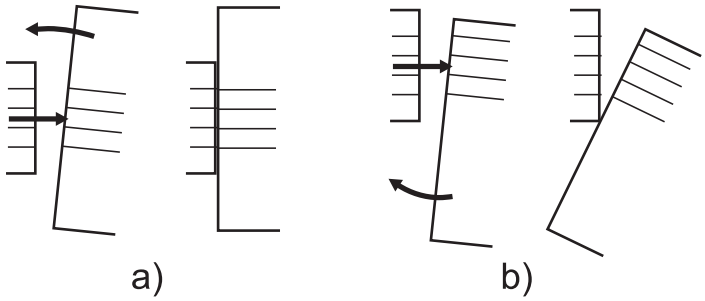

Fig. 5-8 Angular alignment: (a) by bringing both chips in physical contact, they will align themselves automatically. (b) In some cases however, for example when the access waveguides are located at the edge of a large waveguide chip, complete misalignment will follow upon pushing both chips together.

minutes and half an hour for coupling one channel. If multiple channels have to be coupled simultaneously, the time to obtain a reasonable transmission efficiency increases rapidly, sometimes to several hours. This is partly caused by the fact that the hysteresis of the actuator controlling the angular alignment around the optical axis was much larger than the accuracy needed, which made the coupling rather a random trial-and-error process than a directed optimisation. In principle, the whole procedure might be automated what would alleviate the coupling process considerably.

Since both chips are in physical contact with each other and, as shown in Fig. 5-8, part of the alignment is obtained due to this contact, the facets of both chips have to be completely flat. Small dust particles may inhibit a successful coupling. More important is the quality of the cleave itself: for determining the cleavage plane, a small scratch is always required. However, at that place, the cleavage plane will be corrugated and this corrugation will inhibit the chip-to-chip butt coupling. To avoid this problem, the scratch has to be made as far as possible form the waveguide region and this zone has to be removed from the chip by a second cleave, perpendicular to the first one. Obviously, also other facet corrugation occurring from the cleavage process should be avoided.

For most applications, reflections at the interface between both chips have to be minimised as much as possible. Taking into account a single pass loss of 2 dB for the passive waveguide chip, a 5 dB loss at the outer facet of the passive waveguide chip and a 4 dB loss arising from the transition between both chips, the maximum feedback to the amplifier from the passive waveguide is limited to -17 dB (see also Fig. 5-9). Therefore, the residual reflection from the amplifier facet, back into the amplifier will have to be much lower than this value. Such low values may be obtained by applying a high

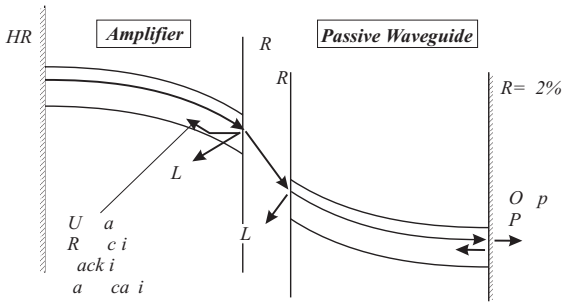

Fig. 5-9 Losses occurring in hybridly coupled PIC.

quality anti-reflection (AR) coating. However, the deposition of such a coating requires a very tight, in-situ control of the layer thickness and the refractive index [26]. This does not correspond with our aim to simplify the processing as much as possible. Therefore, a more simple AR-coating is used, having typical reflection values varying between 0.5 % and 3 %. To reduce the reflection further, the waveguides are slanted towards the facet (by 5 degrees for the first experiments, by 10 degrees for later experiments). This guarantees that the largest part of the light reflected at the facet will not be guided back into the guide but will be lost in the substrate.

As already mentioned, no vertical beam expanders were used, to keep the device processing simple. Consequently, the vertical alignment tolerances are extremely tight (see also chapter 4, section 3). Even a small thermal expansion of one of both chips will result in a change of the coupling efficiency as long as both chips are not permanently bonded. Such a thermal expansion may, for example, originate from changing one of the drive currents. In practice, it has been seen that the (non-permanently fixed) hybrid coupling is stable enough to do several experiments at a constant current (measurement of optical spectrum, small-signal modulation response, laser linewidth …). However, when the current is changed over more than 10 mA, the coupling efficiency is sometimes seen to change. Moreover, in such cases it is often difficult to distinguish between effects caused by the changing coupling efficiency and effects inherent to the device itself.

Realising a novel PIC, using the coupling procedure outlined above, requires simply the fabrication of a new passive optical waveguide chip for which only one lithographic step is needed. The amplifier arrays are standardised and may be fabricated in large quantities or are commercially available. Therefore, only one mask level has to be designed and it is obvious that the hybrid coupling allows for a very fast development cycle.

4 Realisation of a hybridly coupled Phased-Array laser

4.1 Demonstration of the feasibility of the hybridly coupling approach

To demonstrate the feasibility of the approach, arrays with four buried heterostructure amplifiers, slanted by 5 degrees at the facet were fabricated. The active layer consisted of four InGaAs Quantum Well layers surrounded by Q1.1 material. Amplifiers with varying width ($1.5\,\mu m$, $2.5\,\mu m$, $3.5\,\mu m$) were manufactured and the bend radius applied was $1000\,\mu m$. For the experiments described here, an array with $1200\,\mu m$ long and $3.5\,\mu m$ broad amplifiers was employed (tapered to $4.5\,\mu m$ at the facet). The facets were coated but from Fabry-Pérot measurements on waveguides coated at the same time, the facet reflection of straight guides was estimated to be still around 5%.

For a first experiment, the amplifier array was coupled with a similar array of passive waveguides. The waveguides were defined using the same mask as used for defining the amplifier ridges and wet etched into a quaternary guiding layer with a bandgap wavelength

of 1.1 μm . The loss was approximately 3 dB/mm, which is too high for good passive devices but was suitable for this experiment since only very short waveguides were used. The minimum threshold current obtained for the coupled cavity consisting of an amplifier and a passive waveguide was 60 mA, the corresponding output power at 150 mA was 1.60 mW. This output power is not so much higher than the amplified spontaneous emission obtained from the amplifier at that current, but from the optical spectrum and the LI-characteristics it was obvious that laser operation between the outer facets of the coupled cavity was obtained.

Subsequently, the same amplifier array was coupled with a Phased-Array demultiplexer, as shown in the photograph of Fig. 5-10. The passive waveguides for the multiplexer were defined by reactive ion etching (RIE) and had the cross-section already described in chapters 2 & 4 (600 nm Q1.3 guiding layer, InP top cladding layer, etched 150 nm into the guiding

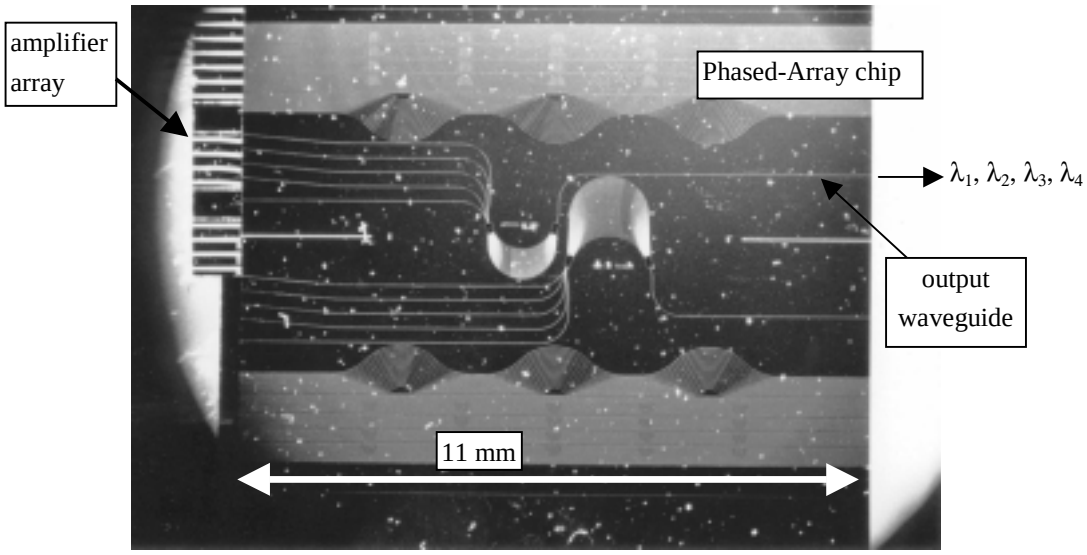

Fig. 5-10 Photograph of first hybridly coupled PAL laser (amplifiers slanted by 5 degrees at the facet).

layer). The Phased-Array demultiplexer had four channels with a frequency spacing of 400 GHz. The excess loss compared to a straight waveguide was 2.5 dB, resulting into a total insertion loss of 4 dB for the multiplexer.

The minimum threshold current for the Phased-Array laser realised employing this passive waveguide chip was 90 mA, the maximum output power 0.42 mW (at 180 mA). Laser operation in all four channels was obtained and it was possible to switch between different channels without changing the optical alignment. However, due to heating of the amplifiers, simultaneous operation of multiple channels could not be obtained. The superimposed oscillation spectra from two channels are shown in Fig. 5-11a.

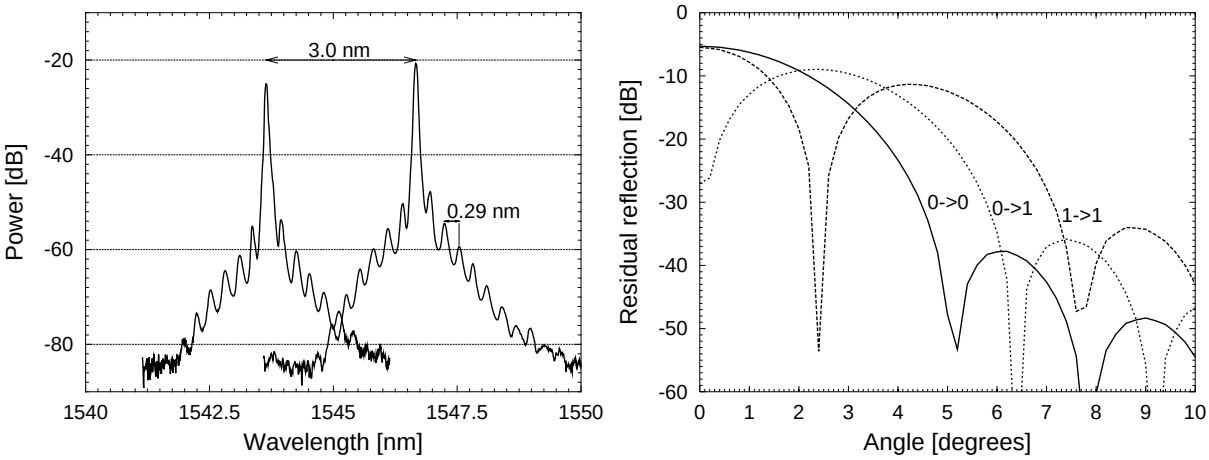

Fig. 5-11 (a) Superimposed oscillation spectra of first hybrid PAL. (b) Calculated residual reflection at amplifier-waveguide interface as function of the angle between the waveguide axis and the facet.

The longitudinal modes from the MWL itself ($\Delta\nu \sim 3$ GHz) are not visible in this figure due to the limited resolution (0.1 nm) of the spectrum analyser. The fringes that are visible in the oscillation spectra are caused by the residual reflection at the amplifier-waveguide interface*. This indicates that the residual reflection is still rather high. Fig. 5-11b shows that the residual reflection into the amplifier from the zeroth order mode to itself should be low enough at the design value of 5 degrees. However, the reflections from the zeroth order mode to the first order mode and from the first order mode to itself are much higher, indicating that these may be responsible for the ripple in the oscillation spectra of Fig. 5-11. Moreover, due to the dip at 5 degrees, it is obvious that the exact value of the residual reflection of the zeroth order mode will be very sensitive to process variations.

From the above-described experiments, involving amplifiers slanted by 5 degrees, we could demonstrate the feasibility of the hybrid coupling approach for realising complex devices. However, from the oscillation spectra, it became apparent that the residual reflection at the interface between both chips is still too high. Therefore, we decided to increase the slanting angle from 5 to 10 degrees.

4.2 Phased Array Laser realised by hybrid coupling

As described in the previous paragraph, slanting of the waveguides by 5 degrees was not enough to suppress the residual reflection back into the amplifiers completely. Therefore, we decided to design a new amplifier array incorporating gain sections slanted by 10 degrees towards the facet. The array was designed in close co-operation with and fabricated by Optospeed SA [27]. Although only eight working amplifiers per array were necessary, each chip contains ten amplifiers, thus providing some redundancy against processing errors.

* This may be concluded from the distance between the fringes that agrees well with a Fabry-Pérot cavity with the same length as the amplifier.

The distance between each amplifier is $250\,\mu m$ and they are tapered from 2 to $3\,\mu m$ at the angled facet. The back facet is HR-coated, the facet that forms the interface with the passive chip is AR-coated. The gain is provided by a bulk InGaAsP active layer and has its peak between 1500 and 1540 nm, depending on the carrier density (design value was 1550 nm). The basic operating characteristics of these amplifiers were already described in chapter 4.

The first series of amplifiers were mounted on an alumina carrier using a conductive epoxy. As already mentioned in paragraph 2.1 of the current chapter, this kind of ceramic substrate has a small thermal conductivity. Moreover, the setup, which was used for the initial experiments, had no temperature controlled device holder. For later experiments, the alumina carrier was replaced by a Silicon substrate and the possibility to control the device temperature was added to the setup. Most experiments reported here were obtained using the chips mounted on the Silicon substrate. The earlier results may be found in [28][29][30].

To facilitate the butt coupling with a passive waveguide, the amplifiers are mounted with their slanted end protruding about $100\,\mu m$ beyond the carrier edge, as shown in the schematic drawing of Fig. 5-7. For both the alumina and the silicon carriers, the chips were wire-bonded to bond pads on the substrate. These bond pads in turn, were connected with larger gold pads thereby allowing for easy probing.

The passive waveguide chips were fabricated at the Delft Technical University, based on epitaxial layer structures grown in Gent. A suitable mask (Fig. 5-12) was designed, containing a series of test waveguides and four Phased-Array demultiplexers, which are identical two by two. Each Phased-Array incorporates 8 access waveguides angled by 10 degrees towards the facet. The characteristics of the Phased-Arrays are summarised in the following table (the largest Phased-Arrays in Fig. 5-12 are the ones with the 200 GHz channel spacing):

	Type 1	Type 2
channel spacing	400 GHz	200 GHz
FWHM	150 GHz	75 GHz
FSR	28 nm	29.4 nm
# waveguides	~ 48	~ 96
minimum bend radius	500 µm	500 µm
waveguide width	2 µm	2 µm
spacing at star coupler	0.6 µm	0.6 µm
input waveguide spacing	5 µm	5 µm

Table 5-1 Characteristics of Phased-Arrays on hybrid PAL mask

The waveguides were defined in a layer stack formed by a 600 nm thick Q1.3 film layer and a 300 nm InP top layer using a reactive ion etching process. Different chips were manufactured, with etching depth varying between 50 nm and 150 nm into the quaternary film layer. The waveguide loss for a $2\,\mu m$ wide straight waveguide varied between 0.5 and 2.0 dB/cm

(see chapter 4). Due to the varying etching depth, also the central wavelength of the different chips varied from chip to chip. Fig. 5-13 shows a photograph of a hybridly coupled PAL.

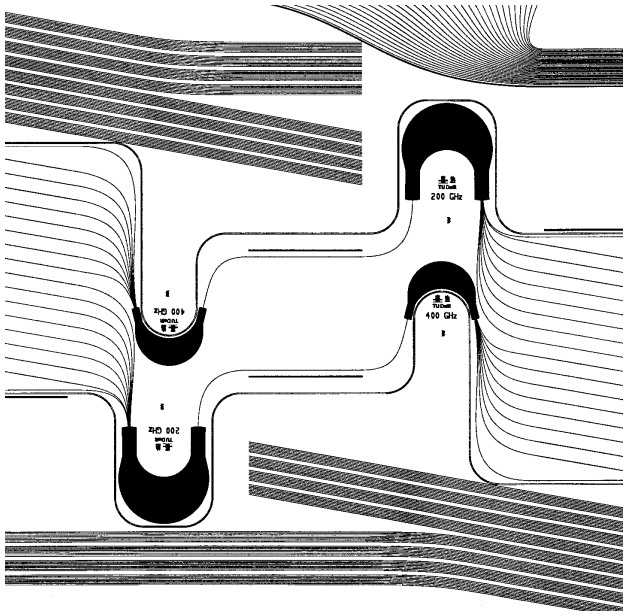

Fig. 5-12 Passive waveguide mask

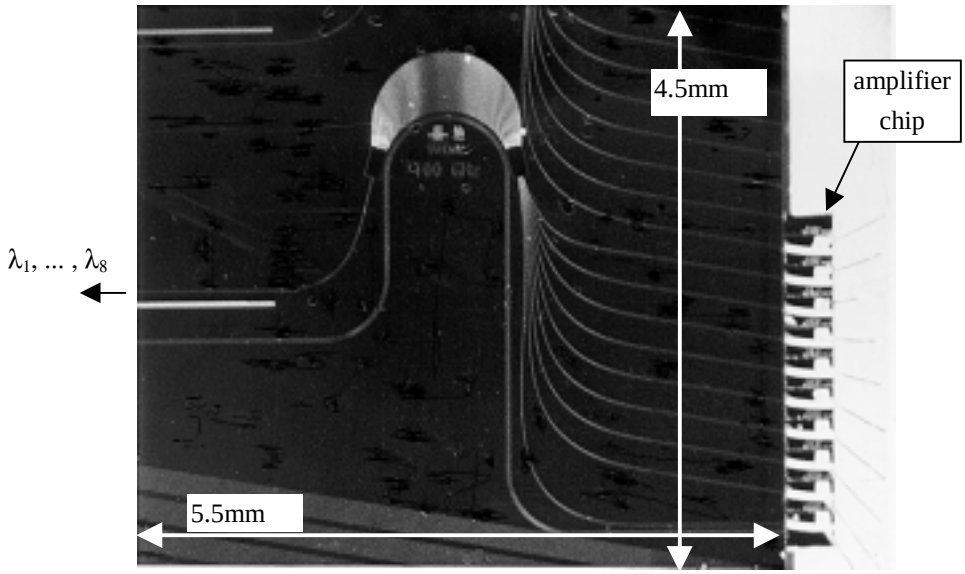

Fig. 5-13 Photograph of hybridly coupled PAL.

4.2.1 Transition loss and coupling tolerances

By comparing the ASE emitted by an amplifier on its own and by the same amplifier coupled with a waveguide angled by 10 degrees over the whole length of the passive waveguide chip (Fig. 5-14a), the transition loss was estimated to be between 4 and 5 dB. For lasers formed by an amplifier and a waveguide slanted at one facet (Fig. 5-14b) external differential efficiencies between 8 % and 12 % were measured, together with minimum threshold current values of 28 mA (Fig. 5-15). Taking into account the above mentioned transition loss and a 1 dB

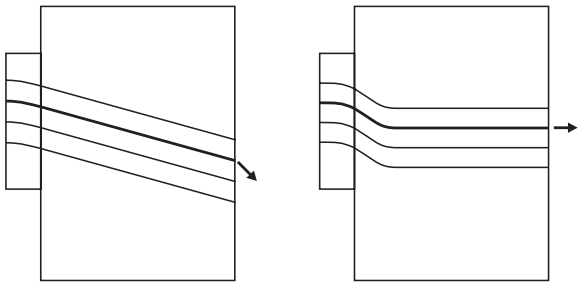

Fig. 5-14 Schematic view of an amplifier array coupled with waveguides angled over the whole length of the passive waveguide chip (left) and with waveguides angled only towards the inner facet, thereby creating a laser cavity (right).

waveguide loss*, the experimental values for the external differential efficiency agree with the values predicted from theory (Fig. 3-4 in chapter 3).

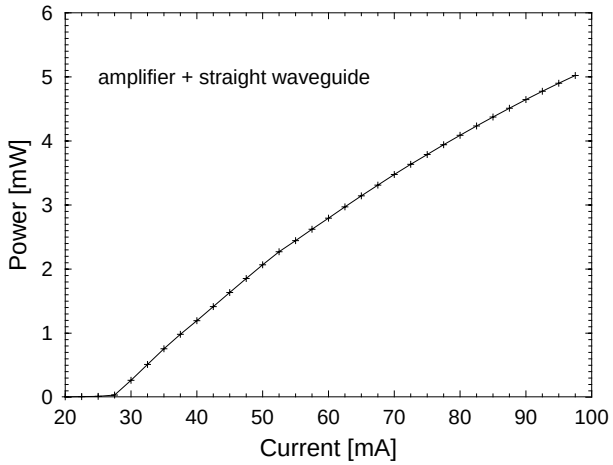

Fig. 5-15 LI-curve for an amplifier coupled with a straight waveguide

Again using a waveguide chip with waveguides angled over the whole length of the chip (left picture in Fig. 5-14), the tolerances for an alignment error were determined. Fig. 5-16a shows the misalignment tolerance for a displacement in the horizontal plane, for different widths of the gap between both chips. The angling of the waveguides is responsible for the asymmetry of the curves. Fig. 5-16b shows the influence on the coupling efficiency of a vertical displacement. Fig. 5-16d summarises the results from Fig. 5-16a and Fig. 5-16b. In Fig. 5-16c the maximum output power as function of a displacement along the optical axis is shown. The solid line in this figure represents the calculated transmission already presented in chapter 4 (section 3).

* The length of the waveguides was approximately 5 mm.

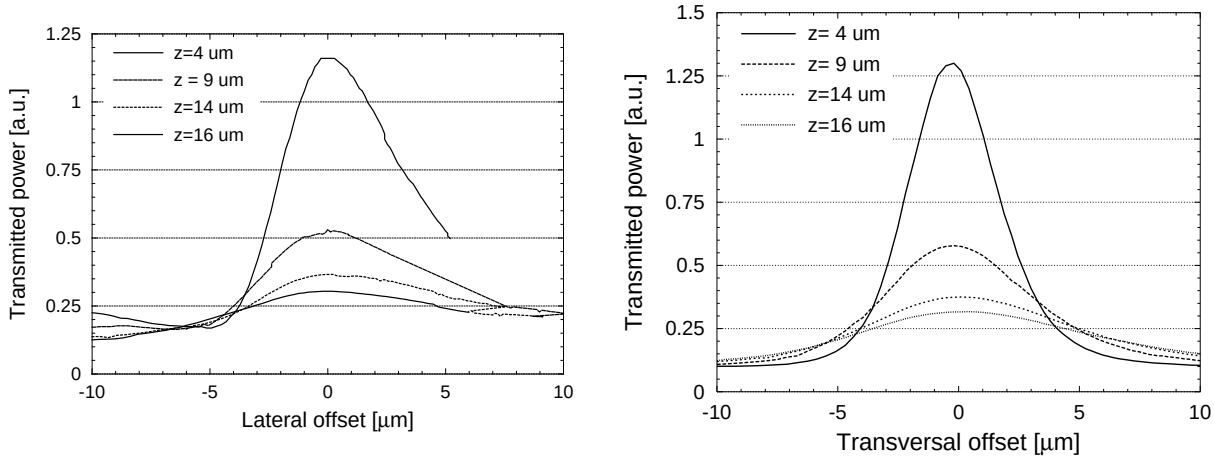

Fig. 5-16 Misalignment tolerances for a displacement in lateral (a) and transversal direction (b). The different curves are for increasing distance (z) between both chips.

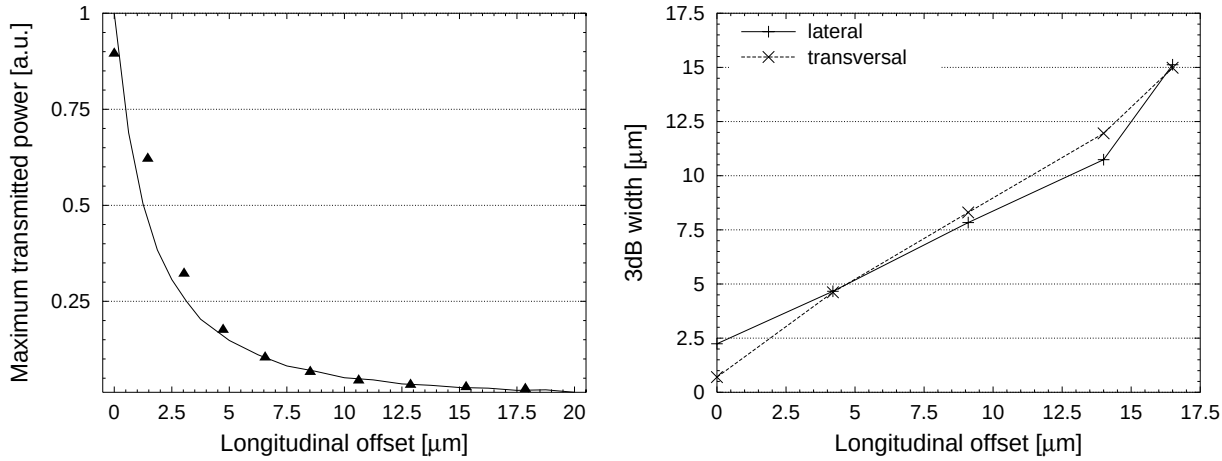

Fig. 5-16 c) Maximum transmission as function of the longitudinal displacement. d) Summary of Fig. 5-16a & b: 3-dB tolerances for a misalignment in lateral and transversal direction. The values at zero longitudinal offset are simulated, the other values are calculated from the measured results shown in figures Fig. 5-16a & b.

We believe that the minimum distance that can be obtained between both chips is between 1 and 2 μm. From the results in Fig. 5-16, one may believe that the coupling tolerances are quite high. However, one has to take into account that an additional coupling loss of 3 dB has severe consequences for the operating characteristics of the device. In practice, an alignment accuracy much better than 1 μm is required.

4.2.2 Threshold current and output power of hybrid PAL

Fig. 5-17a shows superimposed LI-curves of 5 channels of the hybrid PAL shown in Fig. 5-13 (measured at room temperature). The threshold currents vary between 44 mA and 48 mA, the output power is around 1.5 mW (at 100 mA). Several of these LI-curves have one or more kinks. In most cases, these kinks are relatively small but also output power variations as large as 0.8 mW were measured (e.g. see channel 3). Originally, we believed that these

irregularities were caused by variations of the coupling efficiency due to a change of the amplifier temperature with increasing current. However, when characterising a permanently bonded hybrid PAL (see chapter 6), the same sort of irregularities were seen, albeit often in a less pronounced form. In that case, we could relate the discontinuities in the LI-curves with discontinuities in the wavelength (mode hops). For more information, we refer to paragraph 5.4 of chapter 6. In conclusion, we believe that the discontinuities in the LI-curves from Fig. 5-17a are caused by mode hopping as well as by changes in the coupling efficiency. This makes it difficult to draw conclusions from experiments involving a current sweep, as long as the coupling between both chips is not permanently fixed.

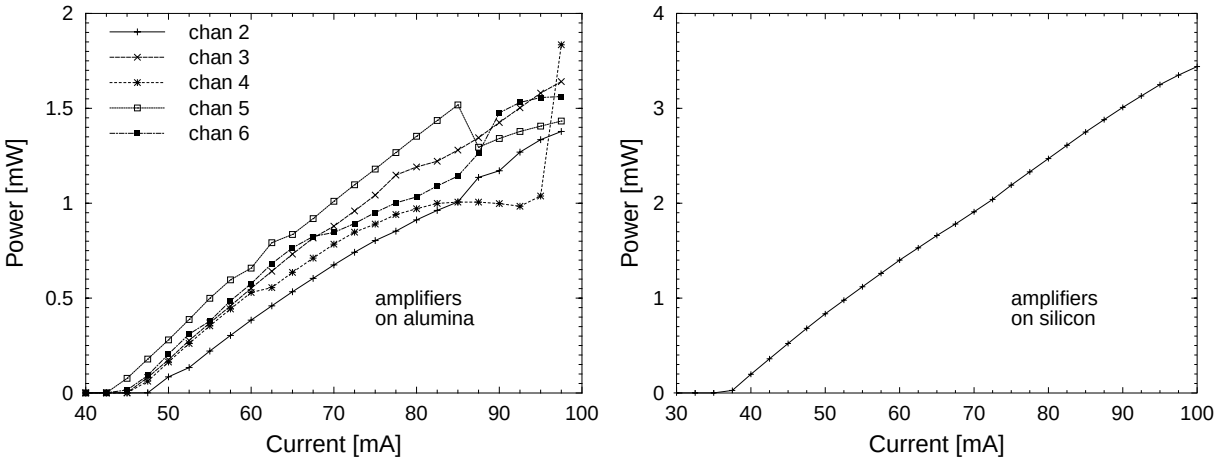

Fig. 5-17 a) Superimposed LI-curves of a PAL formed by hybridly coupling an amplifier array mounted on a alumina substrate and a Phased-Array with a 200 GHz channel spacing. b) LI-curve of a PAL formed by coupling an amplifier array mounted on a silicon substrate and the same passive waveguide chip as used for the left figure.

Fig. 5-17b shows an LI-curve measured from a PAL formed by hybridly coupling an amplifier array mounted on a silicon substrate and the same Phased-Array as used for obtaining Fig. 5-17a (measured at 19°C). Due to the better thermal conductivity of the silicon substrate compared to the alumina substrate, the output power increased to 3.5 mW (free space) and the threshold current decreased to 38 mA. By cooling to 16°C, the threshold current decreased even further, down to 32 mA. Simultaneous operation of four channels could be obtained*†. The maximum output power obtained in that case was 6.2 mW (each channel at 100 mA). These values are by far the best reported until now for PAL-lasers employing a bulk active layer [31][32]. In [33] a device employing a quantum well active layer was reported, exhibiting lower threshold current values (18 - 22 mA) but with comparable output power as the device reported here (at 100 mA).

---

* With the number of channels limited by the number of available current sources.

† With the amplifier array mounted on an alumina carrier, simultaneous operation of only three channels could be obtained.

4.2.3 Spectral characteristics

Fig. 5-18a shows the superimposed oscillation spectra of four channels spaced by 200 GHz, each of them individually operated (amplifiers mounted on silicon, 80 mA drive current per channel). The spectra were measured using a double-pass spectrum analyser with 0.1 nm resolution bandwidth (HP70951). Due to the additional filtering effect of the multiplexer, the ASE-noise originating from the amplifiers is suppressed by more than 60 dB. At the left side of the oscillation spectra, approximately 28 nm away from the main peak, small peaks caused by transmission of the ASE through the lower passband of the multiplexer are visible. These are suppressed by 40 dB*. Fig. 5-18b shows the oscillation spectrum of the same device with four channels operated simultaneously. The same features as for the spectra of Fig. 5-18a can be noticed. However, small additional peaks next to the main lines are visible. These are caused by intra-cavity wave-mixing. This wave-mixing occurs in the passive output waveguide [34][35]. This was already mentioned in chapter 3 and will be explained in more detail in the next chapter†. Fig. 5-18c shows the same oscillation spectrum in more detail and Fig. 5-18d depicts the total output power versus the per channel current for 4 channels operated simultaneously.

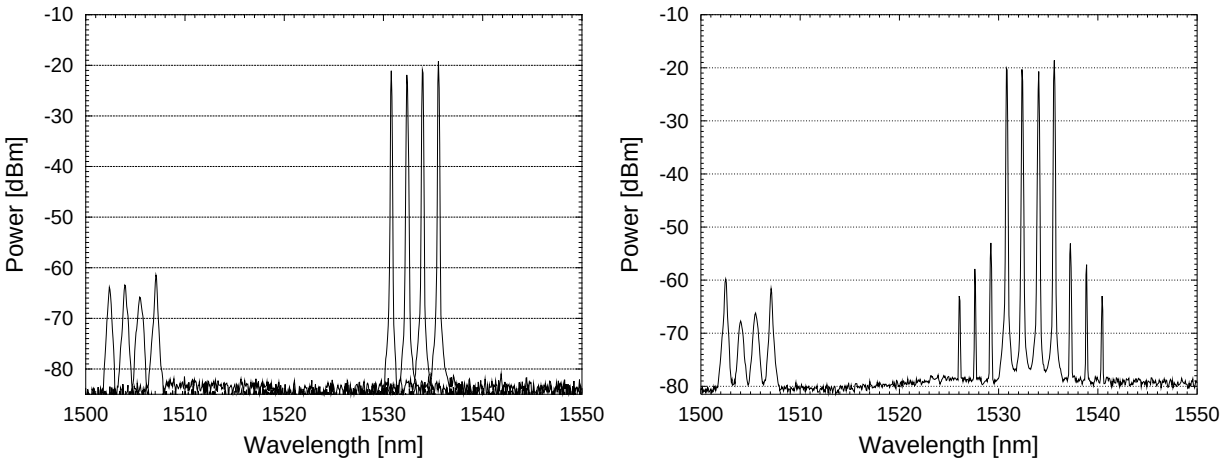

Fig. 5-18 a) Superimposed oscillation spectra of four individually operated channels of hybridly coupled PAL. b) Oscillation spectrum of four simultaneously operated channels.

Fig. 5-19 shows the oscillation spectra for a hybrid PAL, measured in identical circumstances as the one shown in Fig. 5-18b, but with the drive currents varied from 50 mA to 70 mA (per channel). These figures show that the side mode suppression ratio (SMSR) remains better than 35 dB, even for drive currents just above threshold. However, the oscillation spectra in Fig. 5-20 show that this is not always the case. For obtaining these spectra, the measurement

---

* The transmission through the higher order passband (not visible in Fig. 5-18) is suppressed even more.

† One might believe that these small peaks originate from side lobes of the intra-cavity filter. They do not, otherwise the peaks would also be visible in the oscillation spectra of the individually driven channels (Fig. 5-18a).

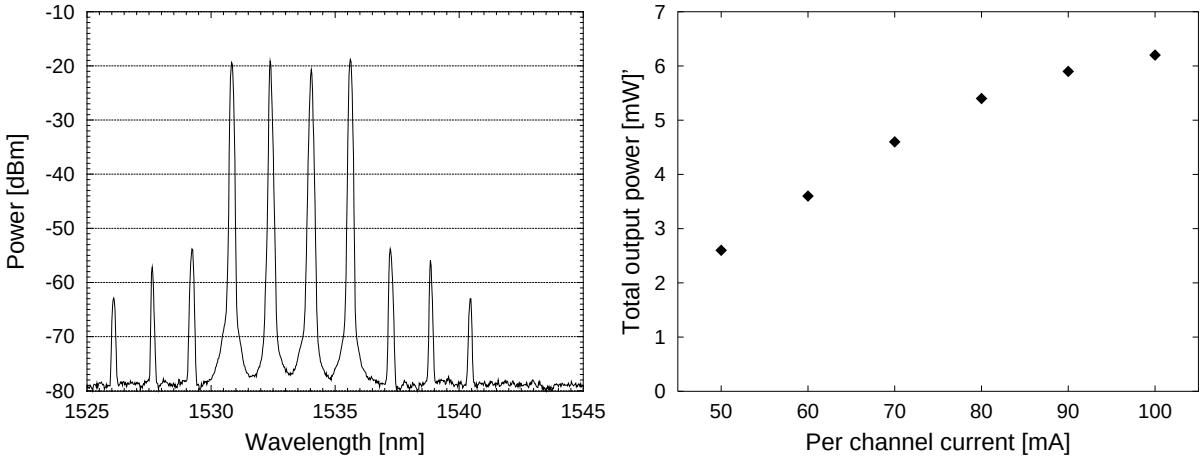

Fig. 5-18 c) Oscillation spectrum of 4 simultaneously operated channels. d) Total output power as function of per channel current for four channels operated simultaneously.

conditions were only slightly changed* but this had already a detrimental effect on the SMSR with respect to the lower passband modes. For some values of the drive current, the lasing in the third and fourth channel even switched completely to the lower passband. As described in chapter 3, this is caused by the fact that the gain peak of the amplifiers is located in between both passbands of the multiplexer. Since the exact position of the gain peak depends on the threshold carrier density, a slight change in the coupling efficiency between both chips may shift the lasing wavelength from one passband to another. Note that the oscillation spectra shown in Fig. 5-19 were measured using a double pass spectrum analyser, while these from Fig. 5-20 were measured using a single pass spectrum analyser. This explains the different form of the curves for low optical powers.

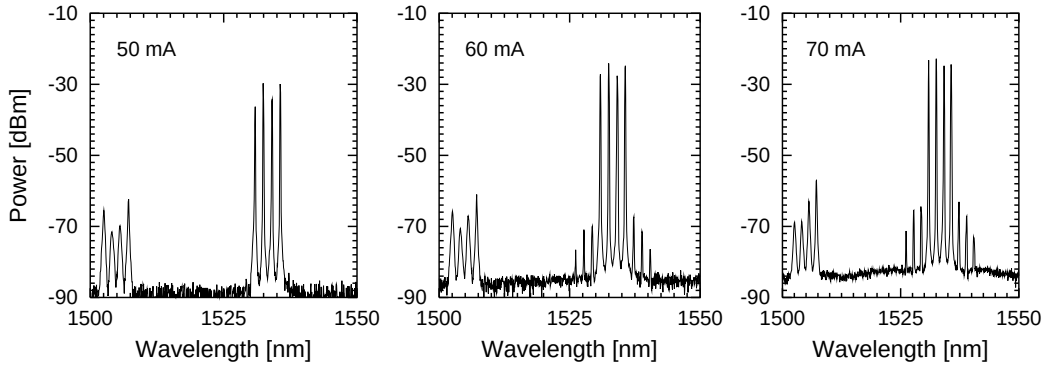

Fig. 5-19 Oscillation spectra of hybrid PAL at different drive currents showing good suppression of lower passband modes.

More in general, also for monolithically integrated devices, due to process variations influencing the exact location of the gain peak and the loss in the passive part, it will be very difficult to force the laser to operate in one particular passband, if no special measures are

* We slightly realigned both chips with respect to each other.

taken. The easiest way to circumvent the problem is to enlarge the Free Spectral Range of the Phased-Array. However, this may considerably enlarge the dimensions of the device. Therefore, a more elegant option is to chirp the Phased-Array, which suppresses the transmission through the passbands neighbouring the central passband (see also chapter 3, section 2.3.2).

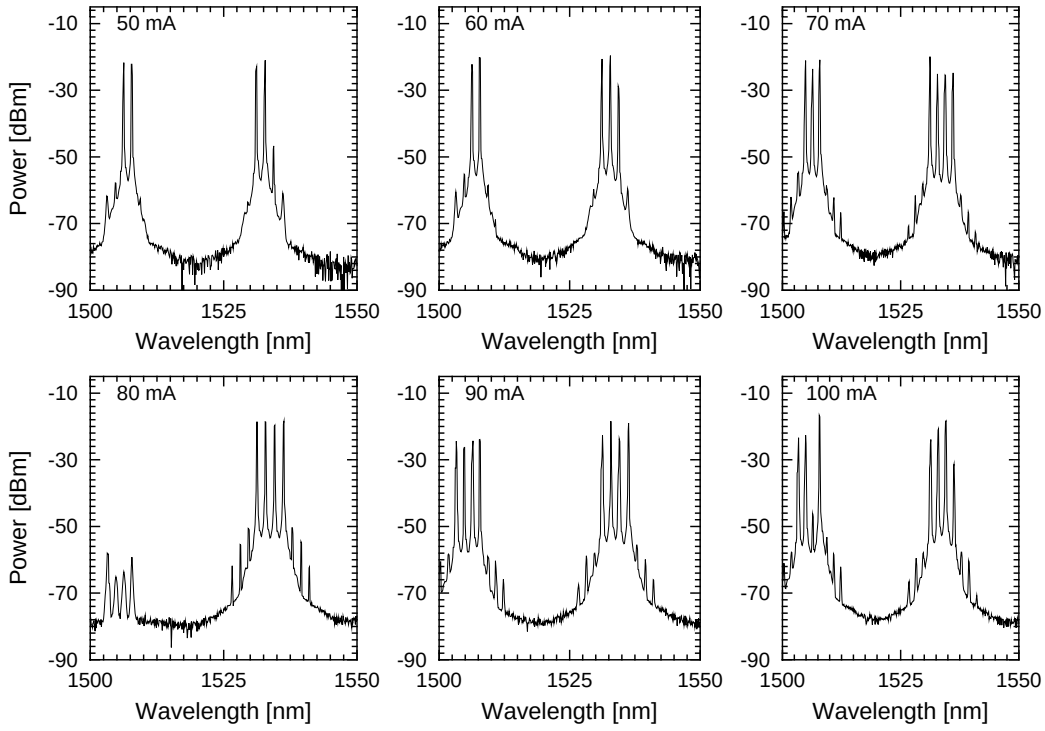

Fig. 5-20 Oscillation spectra of hybrid PAL at different drive currents showing multi-passband lasing

4.2.4 Longitudinal mode stability

For determining the longitudinal mode stability of both the 400 GHz PAL and the 200 GHz PAL, we used a Fabry-Pérot interferometer in combination with a band-pass filter. The free spectral range of the Fabry-Pérot interferometer was set at 0.4 nm, the bandwidth of the band-pass filter* at 0.1 nm. The finesse of the Fabry-Pérot interferometer was 77 (mirror reflectivity R=96%). Fig. 5-21 shows spectra obtained in this way for respectively a laser operating in a single longitudinal mode and for a laser showing multiple longitudinal mode operation.

Experiments performed under different operating conditions revealed that the Phased-Array laser with 200 GHz channel spacing is mostly operating in a single longitudinal mode. Some of the channels however show a mode hop at certain current values. Fig. 5-22a shows the frequency-current characteristic for two channels of the MWL. The characteristic for channel four shows no discontinuities. The other channel however, hops to a neighbouring longitu-

* For the band-pass filter we used the monochromator of a spectrum analyser

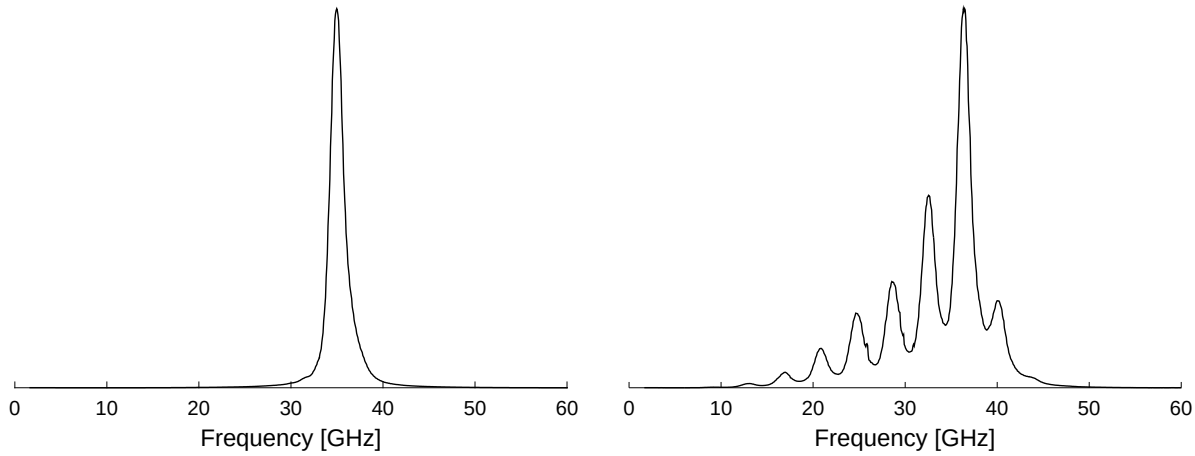

Fig. 5-21 Spectrum measured using FP-interferometer for (a) laser operating in a single longitudinal mode and (b) multiple longitudinal mode operation.

dinal mode around 90 mA. These characteristics show further that the frequency decreases with increasing current (±115 MHz/mA). Since a frequency decrease may be correlated with an increasing cavity length, the shift of the operating wavelength may be attributed to temperature effects (the experiments were performed at room temperature and with the amplifiers mounted on an alumina substrate).

As was explained in chapter 3, the lasing frequency is forced towards the lower frequency side of the intra-cavity filter, due to the carrier-induced modal intermodulation effect in the semiconductor amplifier. This may also be seen from Fig. 5-22a, which shows that the frequency jumps over approximately 8 GHz (two longitudinal modes) just above threshold. When the current is further increased, the lasing frequency is forced further to lower values due to the temperature increase of the amplifiers. At a certain moment, the lasing mode may leave its stability region: the wave mixing is no longer strong enough to suppress the lasing

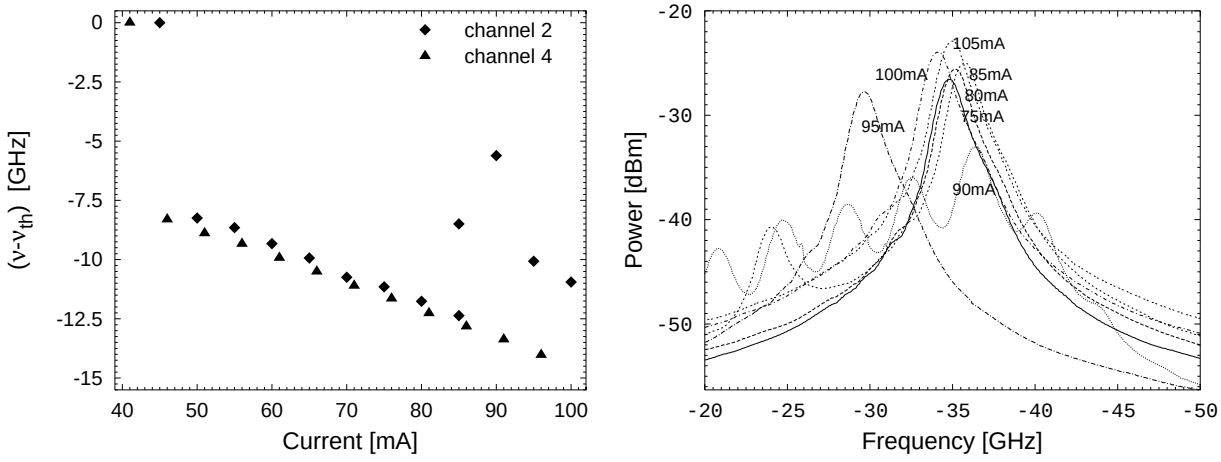

Fig. 5-22 a) Deviation of threshold value. b) Mode hop mechanism. The peak of the intra-cavity filter is placed, somewhat arbitrarily, at the frequency of the light emission just below threshold. However, we believe that the exact position of the intra-cavity filter will deviate less than half the longitudinal mode spacing (4 GHz) from this value.

at the centre of the filter and a new mode will appear. This mechanism is illustrated in Fig. 5-22b. For currents up to 85 mA, the lasing mode shifts gradually further to the low frequency side of the intra-cavity filter. At 90 mA, the wave-mixing effect is no longer strong enough to suppress the longitudinal modes at the centre of the intra-cavity filter and the lasing shifts by two longitudinal modes towards higher frequencies. Finally, at 100 mA, the lasing stabilises at a frequency, separated by one longitudinal mode from the original one.

We also determined the longitudinal mode spectrum of the hybrid multi-wavelength laser with 400 GHz channel spacing. In that case, multi-longitudinal mode lasing was observed for several operation conditions. This may be explained by the increased bandwidth of the 400 GHz Phased-Array demultiplexer (FWHM = 150 GHz) compared to the bandwidth of the 200 GHz Phased-Array (FWHM = 75 GHz). As may be seen from Fig. 5-23, the wave-mixing effect is not strong enough to suppress the lasing at frequencies further away from the main lasing frequency and contrary to the case shown in Fig. 5-22, these are also not suppressed by the intra cavity filter.

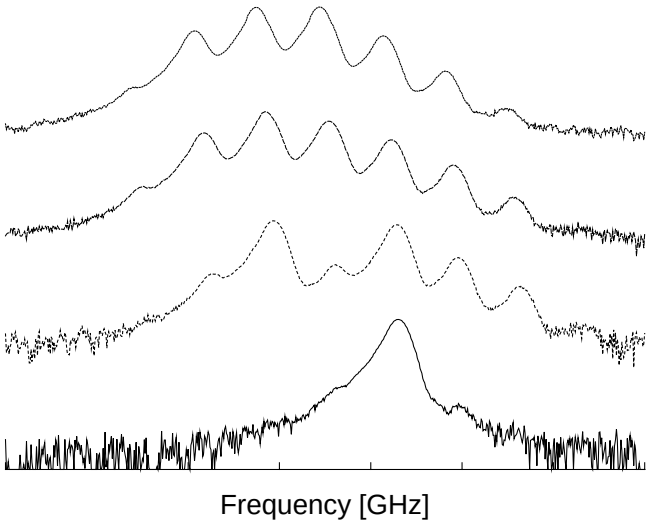

Fig. 5-23 Spectra from 400 GHz Phased-Array laser measured using a Fabry-Pérot interferometer. The lowest trace is measured at the threshold current and this peak indicates the centre of the intra-cavity filter. One may notice that with increasing current, the operating wavelength shifts to lower frequencies but the wave-mixing effect is not strong enough to suppress the higher-frequency longitudinal modes.

Table 5-2 summarises the results from these experiments. The longitudinal mode spacing allows estimating the cavity length. The difference in cavity length for channel 6 compared to channel 4 (both for the 200 GHz and 400 GHz PAL), may be explained by the difference in length of the respective access waveguides to the multiplexer.

$\Delta\nu_{CS}$ [GHz]	$\Delta\nu_{3dB}$ [GHz]	chan#	$\Delta\nu$ [GHz]	L [mm]*	$\Delta\nu/\Delta I$ **	λ_c [nm]
200	75	4	3.9	10.4	118	1508
200	75	6	4.1	9.8	114	1532
400	150	4	4.6	8.8	120	1535.5
400	150	6	4.8	8.4	-	1529

* The group index was estimated to be $n_g = 3.7$ ** [MHz/mA]

Table 5-2 Summary of FP-interferometer measurements

4.2.5 Dynamic measurements

We measured the small signal response of the PAL, using a high frequency probe with a built-in 45 Ohm matching resistor. The measurement setup was already shown in chapter 4 (Fig. 4-1). Fig. 5-24 shows the measured response for different values of the drive current. The vertical scale is in electrical dB (20log[x]). No isolator was used, which explains the irregular form of the curves. The 3-dB bandwidth varies from 500 MHz just above threshold ($I_{bias} = 50$ mA), up to 1100 MHz at a bias current of 90 mA. The corresponding output power values were 0.5 mW and 2.2 mW respectively.

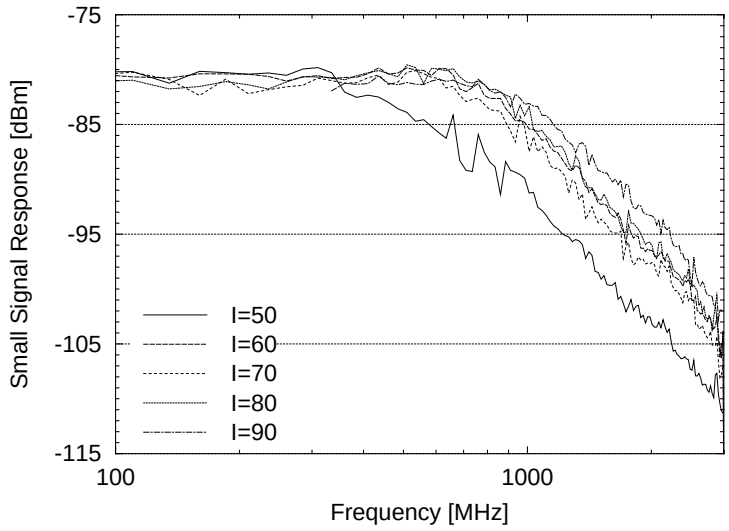

Fig. 5-24 Small signal response of hybridly coupled PAL for different drive currents.

From the results shown in Fig. 5-24, we believe that this device should allow for large signal modulation at 622 Mbit/s. However, eye diagrams measured for a single channel modulated with a 300 Mbit/s or a 600 Mbit/s pseudo-random signal were completely closed. In Fig. 5-25, the response of the laser for a pulse signal is presented. In most cases, the strongly damped waveform of the left picture was measured. However, in some cases, the laser exhibited large relaxation oscillations, as shown in the second picture, which was measured under quasi-identical circumstances as the first picture. We believe that this, seemingly randomly occurring, reduction of the damping is responsible for the closure of the eye. From

Fig. 5-22a, one may see that, near threshold, it takes some time for the laser to decide which longitudinal mode to operate at. This was also noticed in [36] and may probably explain this effect. Another reason could the switching of the laser frequency to a lower passband of the multiplexer. In Fig. 5-26a and Fig. 5-26b, oscillation spectra of the hybridly coupled PAL are presented, which were measured respectively without and with applying a data signal. Fig. 5-26b shows that indeed some of the power shifts to the lower passband when the laser is modulated. For more information on the large-signal modulation of the PAL we refer to chapter 6, where measurement results obtained from a permanently bonded hybrid PAL are presented. This laser showed no multi-passband lasing and the measured eye-diagrams are a lot better. In that case, we also determined the amount of eye-closure as function of the on-off ratio.

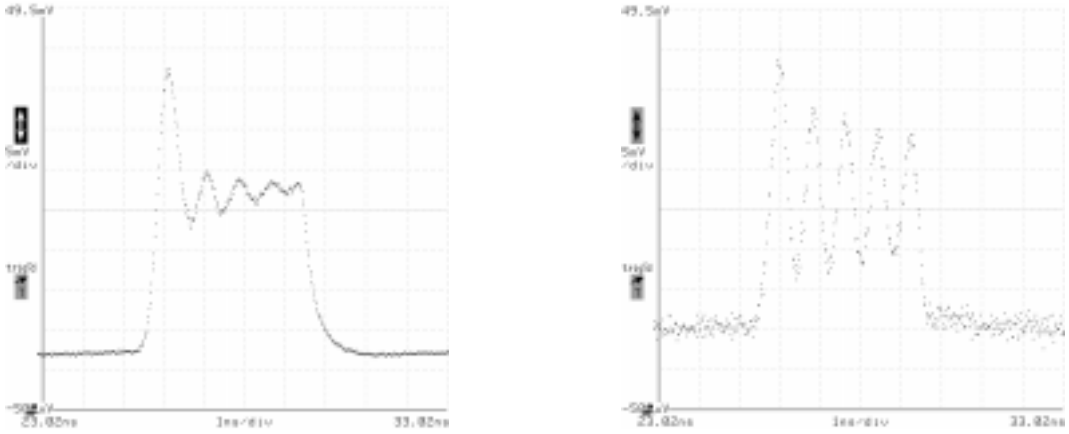

Fig. 5-25 Response of hybridly coupled multi-wavelength laser to square waveform measured under identical operating conditions, strongly damped (left) and with large relaxation oscillations (right).

Fig. 5-26c shows the right peak of the oscillation spectrum in more detail. A considerable broadening of the linewidth is noticed due to the modulation.

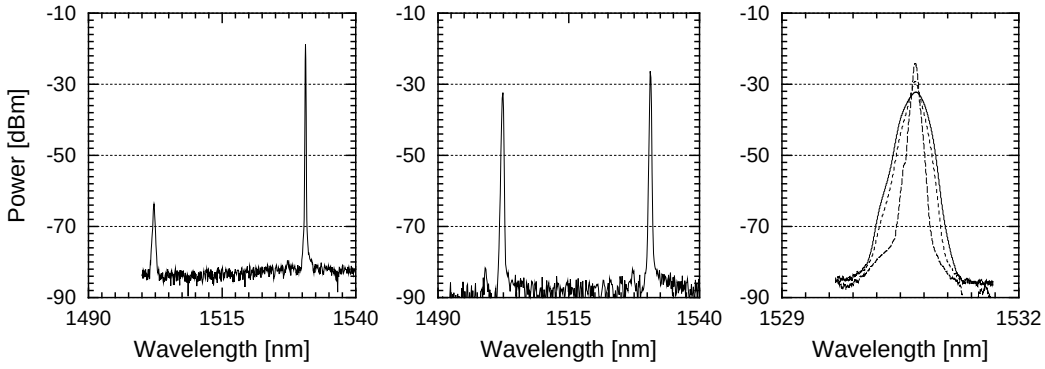

Fig. 5-26 a) Oscillation spectrum of PAL-channel without modulation. b) With pseudo-random data signal-signal (amplitude 3.3 V) applied. c) Broadening of the oscillation spectrum under modulation conditions. The smallest peak is measured under static conditions, the others with respectively a 2.2-Volt and 3.3-Volt PBRS signal applied.

5 Realisation of hybridly coupled Phased-Array laser with gain clamped common amplifier

As already noted in chapter 3, in some cases it may be beneficial to use a common amplifier at the output side of the device. For example, when the amplifiers were mounted on an alumina substrate, due to thermal crosstalk, we could not obtain simultaneous laser operation in more than three channels. By adding an output amplifier, this could be solved, because this amplifier allows reducing the drive current required for each channel, thereby also reducing the thermal crosstalk. However, when a common amplifier is used and multiple channels are operated together, gain variations in this amplifier can give rise to crosstalk between the channels. In order to prevent that, we proposed to clamp the gain of this amplifier by adding an additional passive waveguide at the input side of the multiplexer (Chapter 3, Fig. 3-). The lasing action on the channel formed by this waveguide and the common amplifier ("the gain-clamping channel") clamps the gain of the latter. Consequently, a variation of the power in one of the signal channels will induce a similar variation of the power in the gain-clamping channel, but the other signal channels will not be influenced.

To verify this idea experimentally, a new passive waveguide chip was developed, in co-operation with Delft Technical University. Fig. 5-27 shows the device layout. The laser is again realised using the hybrid coupling approach, so all the waveguides that have to be connected with a gain section are located at one side of the passive waveguide chip and angled by 10 degrees. The upper seven waveguides are for the signal channels, the lowest one is for the common amplifier. For characterising the device, a 90/10 MMI-coupler is incorporated in this channel, allowing splitting off some power to the left facet*. This waveguide is angled by 10 degrees to avoid reflections back into the laser cavity. The waveguide, which starts at the upper star coupler of the Phased-Array and ends perpendicular to the left facet, is the passive waveguide that forms - together with the common amplifier - the gain-clamping channel. The Phased-Array is identical to the 400 GHz device on the mask described in the previous section (Fig. 5-12 / Table 5-1). An identical layer structure as before was used (600 nm Q1.3 guiding layer, 300 nm InP cladding layer) and the waveguides were defined by RIE (etched approximately 100 nm into the quaternary layer)†. Extremely low waveguide losses were obtained (~ 0.5 dB/cm, see also chapter 4, paragraph 2.2), resulting in an estimated on-chip loss of less than 2 dB (including the MMI-coupler losses). The minimum bend radius applied was 500 μm and the total device size 5 x 4 mm^2.

---

* It is not possible to characterise the device by directly measuring the output power exiting the amplifiers, both because of the HR-coating applied to their back facet and because of the bond-wires connecting them with the substrate

† The layer structure was grown in Gent by MOCVD, the waveguides were etched at the University of Delft

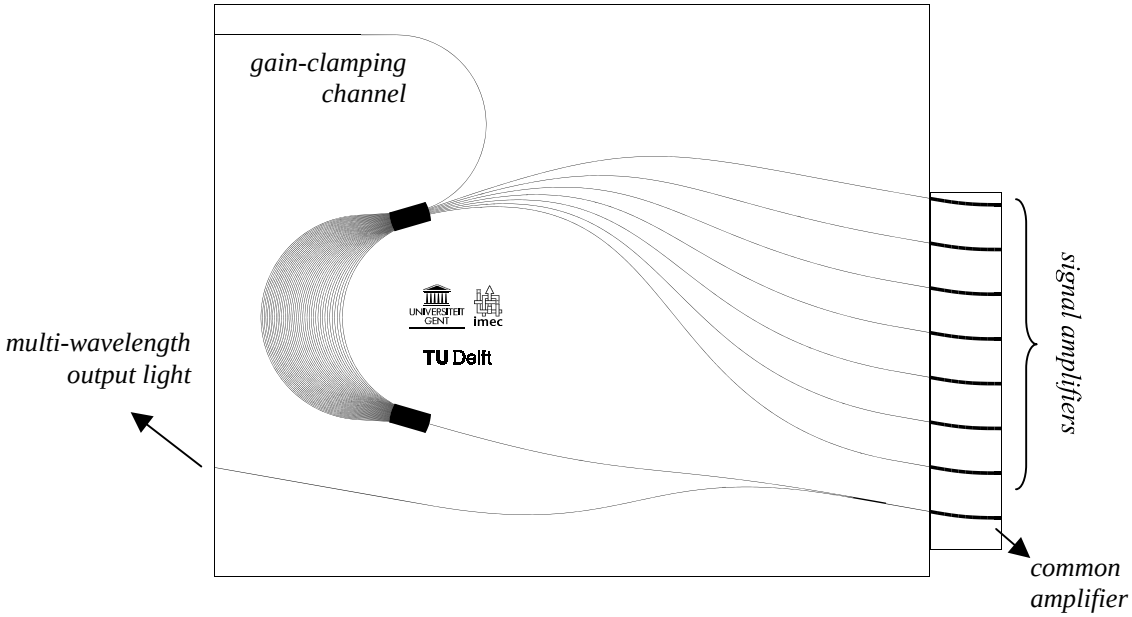

Fig. 5-27 Layout of the gain-clamped laser.

Using this passive waveguide chip, we realised a Phased-Array laser with common output waveguide. The threshold current for the gain-clamping channel was approximately 40 mA (T=19^{0}C). This is comparable with the 35 mA obtained for the Phased-Array laser without common amplifier described in the previous section, taking into account the additional loss of the MMI-coupler. The threshold current measured for the signal channels was between 14 mA and 16 mA (gain clamped operation), which is only a few mA higher than the measured transparency current at the operating wavelength (see chapter 4). Simultaneous, CW-laser operation of four signal channels and the gain-clamping channel was obtained. The oscillation spectrum is shown in Fig. 5-28. For this figure, the current to the common amplifier was 70 mA, the currents for the other channels 16.5 mA (except for the channel nearest to the common amplifier, which was pumped at 19 mA). The gain-clamping channel is operating in a lower passband of the Phased-Array due to the shift of the amplifier gain towards lower

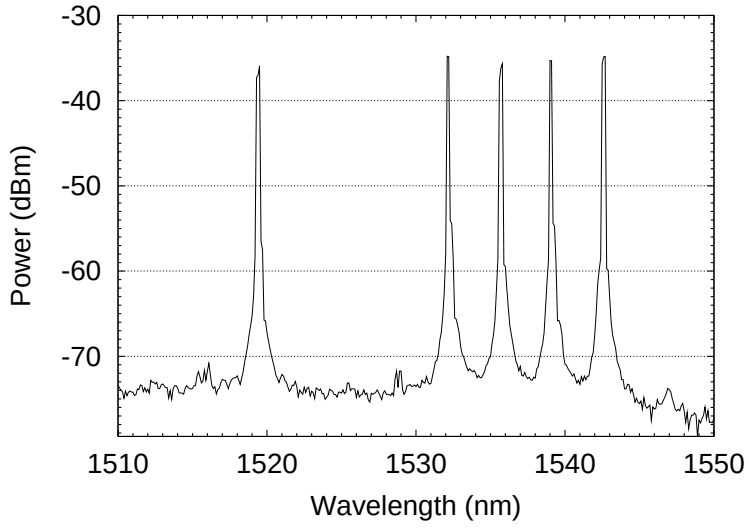

Fig. 5-28 Oscillation spectrum of gain-clamped Phased-Array laser

wavelengths with increasing current. No multi-passband lasing was observed in this case. The ASE-noise is suppressed by more than 35 dB (resolution bandwidth = 0.1 nm). For the PAL without common amplifier, we measured values better than 60 dB. The difference originates from the fact that the ASE-noise of the common amplifier is not suppressed by the intra-cavity filter here.

To demonstrate the gain clamping, we changed the power in one of the signal channels while keeping the other drive currents constant. To determine the power in each channel separately, a spectrum analyser was used.

Fig. 5-29a represents a measurement where only the common amplifier (50 mA) and one of the signal amplifiers were driven. The threshold current for the signal channel was 19 mA in this case. As expected, the power in the signal channel increases linearly with increasing drive current, while the power in the gain-clamping channel decreases. At 24 mA, the power in the gain-clamping channel falls completely to zero, implying that the gain of the common amplifier is no longer clamped and starts to saturate. This is immediately visible in the LI-curve for the signal channel, which shows a sublinear behaviour from this point on. Therefore, by varying the drive current of the signal amplifier by only 5 mA, the power in this channel can be changed from zero to the power that originally was available in the clamping-channel.

For obtaining Fig. 5-29b, the common amplifier and one signal amplifier (signal channel 2) were driven at a constant current, while the current to a second signal amplifier (signal channel 1) was changed. A higher loss passive waveguide chip was used, which explains the higher threshold current for the signal channel. It is obvious that the power in channel two is not influenced by the change in power in the other signal channel, which indicates that the gain of the common amplifier is clamped indeed.

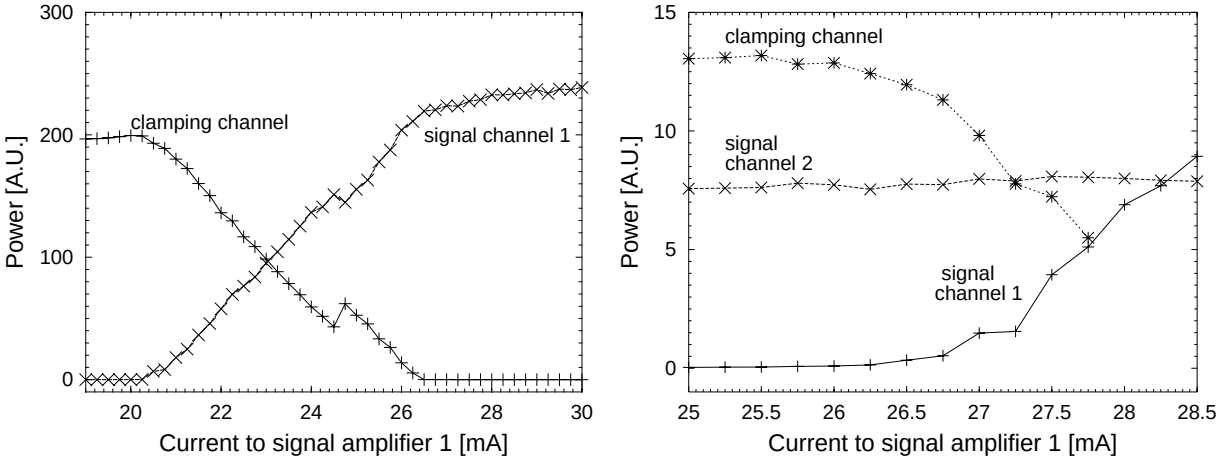

Fig. 5-29 Experimental verification of the gain-clamping. (a) Only one signal channel and the gain-clamping channel are driven. (b) In addition, a second signal channel is driven.

Although the above two pictures illustrate the gain clamping convincingly, we also performed several measurements, which were not that obvious. Fig. 5-30 illustrates two such

experiments. In the left picture, again the drive current of one of the signal amplifiers is increased while the drive current for a second signal channel is held constant. Although we expected the power in the latter to stay constant, in contrary it decreases monotonously. However, the effect of the gain-clamping is still visible: at 25 mA, the power in the gain-clamping channel becomes very low and there is a clear discontinuity visible in the direction of the LI-curves of both signal channels at that point. Because the power in the second signal channel (from which the drive current is held constant) decreases already before the drive current of the first channel reaches its threshold value, we believe that thermal crosstalk is responsible for the power decrease in the second channel. The dashed curves in the figure represent the power in the clamped signal channel and in the clamping-channel after filtering out the thermal effect. From these curves, the gain-clamping is much more obvious.

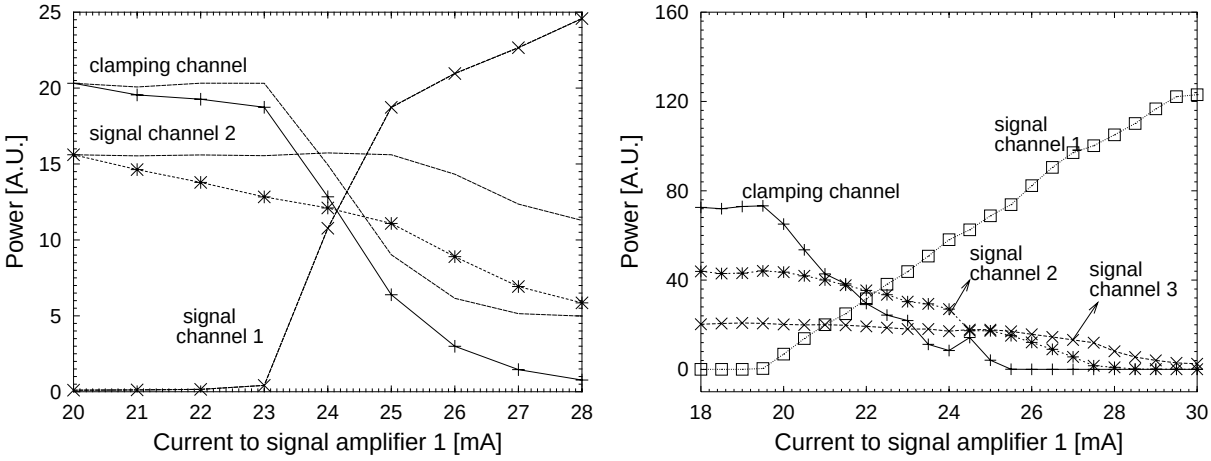

Fig. 5-30 Experimental verification of the gain-clamping. (a) Two signal channels and the gain-clamping channel are driven: thermal crosstalk seems to compromise the gain-clamped operation (b) Three signal channels and the common amplifier are driven. The power in the third signal channel stays constant but the power in the second channel starts to decrease as soon as the power in the first channel increases.

Fig. 5-30b shows a measurement where three signal amplifiers were driven (channels 2 and 3 held constant). Although the power in the second channel stays rather constant, this is not the case for the third channel. Moreover, contrary to the case of Fig. 5-30a, it is not obvious that this decrease may be attributed to thermal crosstalk. Several other experiments (one or more channels held constant) were performed that did not demonstrate the gain clamping either. There are different possible reasons for this anomalous behaviour:

- Thermal crosstalk between the amplifiers.
- Change of the coupling efficiency due to the increase of the drive current to one of the amplifiers
- The power per channel was determined from an oscillation spectrum measured for each current combination, using an optical spectrum analyser. Such an approach is very sensitive to environmental instabilities. It would be better to use a bandpass filter and a power meter.

- The Phased-Array had a 400 GHz channel spacing and 150 GHz 3-dB bandwidth. We have already demonstrated (see paragraph 4.2.4) that this bandwidth is to wide to force the laser to oscillate at a single longitudinal mode and it is very likely that also the gain-clamped laser exhibits multiple longitudinal mode operation. This effect may be responsible for additional instabilities in the LI-curves.

We could not yet determine the most important reason for the fact that the gain-clamping sometimes breaks down. Also the dynamic properties of the gain-clamped laser are not yet investigated. We believe that by permanently bonding both chips, applying the procedure outlined in the following chapter, it will be possible to obtain more conclusive results concerning the feasibility of the gain-clamping approach.

6 Realisation of a hybridly coupled tunable laser

To demonstrate that the hybrid coupling approach cannot only be used for realising Phased-Array lasers, we used the technique also for realising a completely different type of laser. Fig. 5-31a illustrates the device principle: the laser cavity is formed by a gain section, a ring resonator and a tunable Mach-Zehnder interferometer, together forming a digitally tunable laser. The operating principle is explained as follows:

The ring resonator has a fixed transmission function consisting of a series of narrow peaks as depicted in Fig. 5-31b. The radius of the ring determines the free-spectral range and the width of the peaks is function of the waveguide loss and the coupling ratio between straight waveguides and the ring. The reflective Mach-Zehnder interferometer (MZI) is formed by a 3dB coupler and two arms each containing a reflective SOA. The free-spectral range of the MZI is determined by the optical path length difference between both arms and is chosen to be much larger than the free spectral of the ring resonator. By changing the current to the gain sections in the MZI-arms, its central wavelength may be changed. If the gain section is pumped and the centre of the MZI is aligned with one of the peaks of the ring resonator,

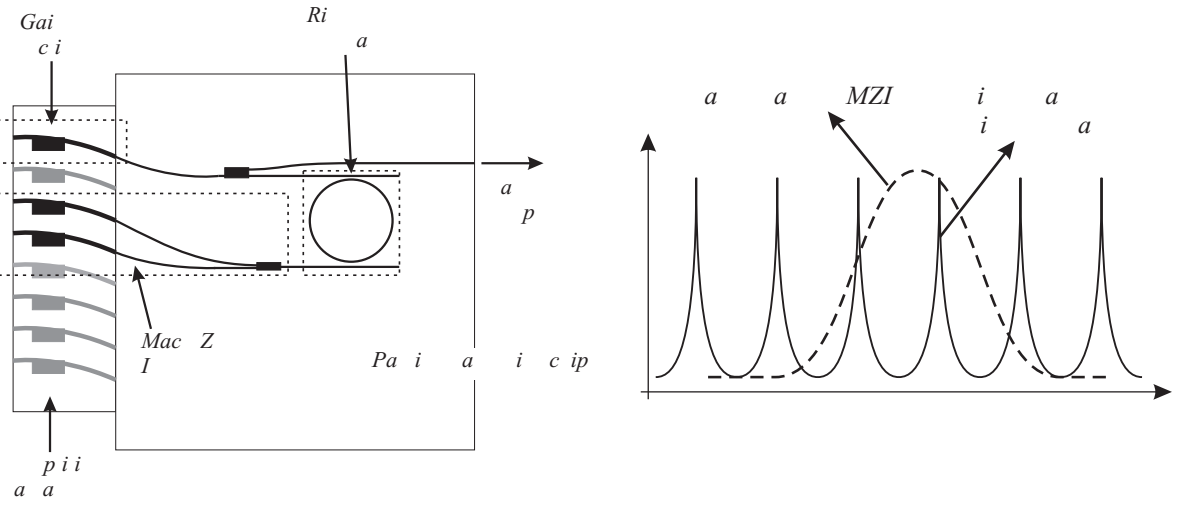

Fig. 5-31 a) Device principle of tunable ring laser. b) Transfer from ring resonator and tunable Mach-Zehnder interferometer (MZI).

laser operation at this wavelength may occur. By shifting the transmission wavelength of the MZI to a neighbouring peak, the operating wavelength is tuned in a digital way.

The tunable ring laser was proposed and theoretically investigated in [38]. We verified its operation experimentally, using the hybrid coupling technique. The passive waveguide chip was again fabricated by etching ridge waveguides into a 600 nm thick Q1.3 guiding layer covered with a 300 nm thick InP cladding layer. However, to allow for a bend radius of 125 μm, the waveguides were etched deeper than for the waveguides reported in the previous paragraphs (250 nm into the quaternary layer). The measured transfer through the ring resonator is depicted in Fig. 5-32a & b, for TM & TE polarised light respectively. The solid lines were fitted using a suitable model (see [37]). The much higher finesse and Q-factor for the TM-case originate from the fact that both the radiation loss in the ring and the coupling ratio are lower for TM-polarised light. This was verified experimentally and by simulations.

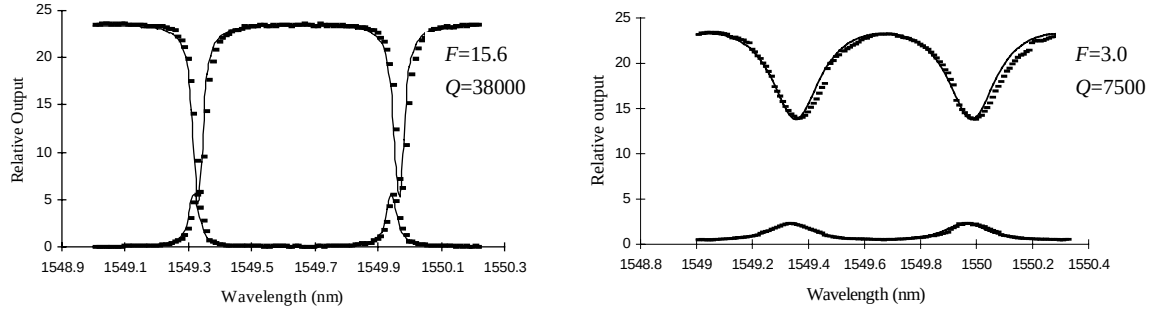

Fig. 5-32 Measured transfer of ring resonator for TM (left) and TE (right) polarisation. The solid lines were calculated. *F* and *Q* respectively denote the finesse and the Q-factor

An amplifier array similar to the one described in the previous section was employed. A minimum threshold current of 44 mA was obtained (with both amplifiers of the MZI at 35 mA). Although the cavity loss was smaller for TM-polarised light (see Fig. 5-32), the laser is operating in a TE-mode. We measured an output power of 0.4 mW*. Fig. 5-33 shows 15 superimposed oscillation spectra of this laser. For obtaining these, the gain section and one of the amplifiers in the MZI were driven with a constant bias current (60 mA and 35 mA respectively). The bias current of the other amplifier in the MZI was varied from 20 mA to 50 mA. The large variation in the output power level stems from the fact that no attempt was made for optimising the current settings. Nevertheless, laser operation in 12 separate channels was obtained, on a grid determined by the free spectral range of the ring resonator (~0.6 nm). For the best channels, a side mode suppression ratio better than 35 dB was measured.

The laser presented here is only tunable over a limited wavelength interval. By making the ring resonator tunable and replacing the MZI-filter with a second ring resonator, it should be possible, making use of the vernier effect, to realise a very broadly tunable laser. Such a laser

* This output power was measured from an angled output waveguide using an objective (NA=0.65), therefore we believe that the actual output power may be up to 3 or 4 times higher.

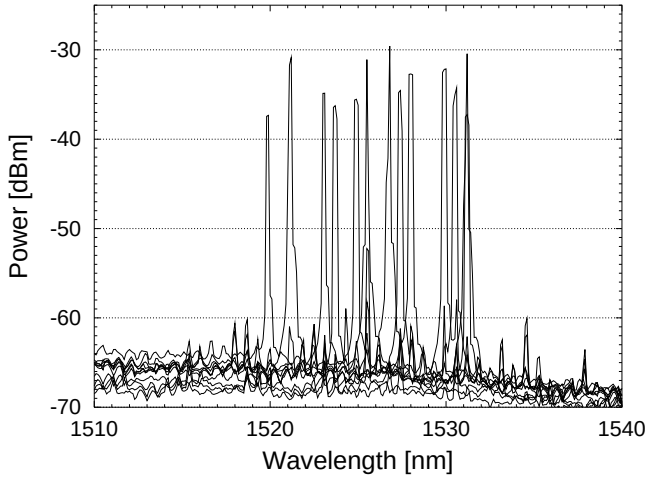

Fig. 5-33 Superimposed oscillation spectra of digitally tunable ring laser.

may possibly be more compact and easier to fabricate than more classical broadly tunable lasers based on Bragg gratings.

Another option could be to integrate an amplifier array with a resonator-based demultiplexer as shown in Fig. 5-34. Such a demultiplexer was demonstrated in [39] and is built by combining ring resonators with a slightly increasing radius. In that way it could be possible to realise an extremely compact multi-wavelength laser (the resonators employed in [39] had a radius of only 30 μm).

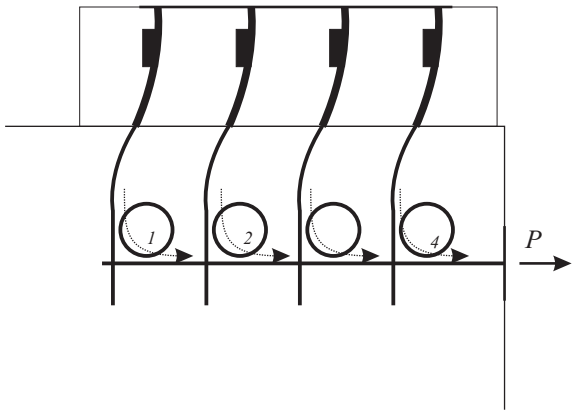

Fig. 5-34 Multi-wavelength laser by integrating amplifier array with ring resonator based demultiplexer.

7 References

[1] T. Van Caenegem, D. Van Thourhout, I. Moerman, P. Van Daele, R. Baets, P. Demeester, M. K. Smit, "Active-Passive integration by MOVPE Selective Area growth for multi-wavelength lasers", Proceedings 1995 IEEE/LEOS Benelux Chapter, Twente, The Netherlands

[2] W. Hunziker, W. Vogt, H. Melchior, D. Leclerc, P. Brosson, F. Pommereau, R. Ngo, P. Doussierre, F. Mallecot, T. Fillion, I. Wamsler, G. Laube, "Self-aligned flip-chip packaging of tilted semiconductor optical amplifier arrays on Si motherboard", El. Lett., Vol. 31, 488-490, 1995

[3] J. E. van der Linden, P. M. De Dobbelaere, P. P. Van Daele, M. B. Diemeer, "High-density and alignment-tolerant integration of monitoring photodetector arrays onto polymeric guided-wave components", IEEE Transactions on Advanced Packaging, Nov. 1999, VOL 2, No 4, pp. 534 - 540.

[4] P. M. Harrison, R. Cann, D. Spear, "Silicon V-Groove technology in the volume production of optical devices", LEOS '97, San Fransisco, WP5, 1997

[5] E. J. Murphy, "Integrated optical circuits and components - design and applications", Marcel Dekker, Inc., ISBN: 0-8247-7577-5

[6] R. A. Boudreau, "Passive alignment in optoelectronic packaging", OFC' 97, WB1

[7] R. G. Peall, B. J. Shaw, P. J. Ayliffe, H. F. M. Priddle, T. Bricheno, P. Gurton, "1 x 8 8 Gbit/s transmitter module for optical space switch applications", El. Lett., Vol. 33, 1250-1251, 1997

[8] R. G. Peall, B. J. Shaw, H. F. M. Priddle, M. C. Geear, A. Briggs, P. M. Harrison, A. Schmid, M. Bitter, J. Wieland, O. Zorba, R. Harcourt, "12 x 2.5 Gbit/s receiver array module", El. Lett., Vol. 32, 682-683, 1996

[9] R. A. Boudreau et al., "Single mode bidirectional links for fiber-in-the-loop and optical networks", LEOS '97, San Fransisco, WH1, 1997

[10] H. Asano, H. Kimura, G. Tohmon, T. Nishikawa, T. Uno, S. Morikura, "High performance optical receiver using hybrid integration photodiode module and preamplifier for passive optical network systems", LEOS '97, San Fransisco, WH4, 1997

[11] H. Han, R. W. Roff, R. A. Boudreau, T. P. Bowen, R. B. Wilson, "Pigtailed CATV PIN module packaged by passive alignment technology", LEOS '97, San Fransisco, WH5, 1997

[12] K. Tatsuno, T. Kato, T. Hirataka, K. Yoshida, T. Ishii, T. Kono, T. Miura, R. Sudo, M. Shimaoka, "High-performance and low-cost plastic optical modules for the access network applications", OFC' 97, WB3, 1997

[13] G. C. Joo, S. H. Lee, J. T. Moon, N. Hwang, M. K. Song, K. E. Pyun, "Optical coupling of a SMF to flip-chip bonded laser diode for low-cost subscriber's transmitter module", LEOS '97, San Fransisco, WP2, 1997

[14] I. Ogawa, Y. Yamada, H. Terui, "Reduction of waveguide facet reflection in optical hybrid integrated circuit using saw-toothed angled facet", IEEE PTL, Vol. 7, 44-46, 1995

[15] Y. Yamada, A. Takagi, I. Ogawa, M. Kawachi, N. Yoshimoto, "Silica-based optical waveguide on terraced silicon substrate as hybrid integration platform", El. Lett., Vol. 29, 444-446, 1993

[16] I. Ogawa, Y. Yamada, F. Ebisawa, F. Hanawa, T. Hashimoto, M. Yanagisawa, K. Shuto, T. Ohyama, Y. Akahori, A. Himeno, K. Kato, N. Yoshimoto, Y. Tohmori, "Hybrid integrated four-channel SS-SOA array module using planar lightwave circuit platform", El. Lett., Vol. 34, 361-363, 1998

[17] I. Ogawa, Y. Yamada, F. Ebisawa, K. Takiguchi, F. Hanawa, T. Hashimoto, A. Sugita, M. Yanagisawa, Y. Inoue, A. Himeno, K. Kato, Y. Tohmori, S. Mino, T. Ito, K. Magari, Y. Kawaguchi, "Lossless hybrid integrated 8-ch optical wavelength selector module using PLC platform and PLC-PLC direct attachment techniques", OFC'98, San Jose, USA, 1998

[18] S. Mino, T. Ohyama, Y. Akahori, M. Yanagisawa, T. Hashimoto, Y. Yamada, H. Tsunetsugu, M. Togashi, Y.Itaya, Y. Shibata, "High-Speed optoelectronic hybrid integrated transmitter module using a planar lightwave circuit (PLC) platform", IEEE PTL, Vol. 10, 875-877, 1998

[19] T. Hashimoto, Y. Yamada, M. Yanagisawa, K. Kato, Y. Tohmori, Y. Nakasuga, H.Terui, Y. Akahori, Y. Suzuki, "Multichip optical hybrid integration technique with planar lightwave circuit platform", IEEE JLT, Vol. 16, 1249-1258, 1998

[20] G. Nakagawa, K. Miura, S. Sasaki, M. Yano, "Lens-coupled laser diode module integrated on silicon platform", IEEE JLT, Vol. 14, 1519-1523, 1996

[21] M. Fukuda, F. Ichikawa, Y. Shuto, H. Sato, Y. Yamada, K. Kato, S. Tohno, H. Toba, T. Sugie, J. Yoshida, K. Suzuki, O. Suzuki, S. Kondo, "Plastic module of laser diode and photodiode mounted on planar lightwave circuit for access network", IEEE JLT, Vol. 17, 1585-1592, 1999

[22] G. E. Henein, D. J. Muehlner, J. Shmulovich, L. Gomez, M. A. Capuzzo, E.J. Laskowski, R. Yang, J. V. Gates, "Hybrid integration for low cost OE packaging PLC transceiver", LEOS '97, San Fransisco, ThB1, 1997

[23] J. Bell, D. Snyder, M. Yanushefski, R. Yang, J. Osenbach, M. Asom, "O-E transmitter packaging for broadband access systems", LEOS '97, San Fransisco, THB2, 1997

[24] N. Yoshimoto, K. Magari, T. Ito, Y. Kawaguchi, K. Kishi, Y. Kondo, Y. Kadota, O. Mitomi, Y. Yoshikuni, Y. Hasumi, Y. Tohmori, O. Nakajima, "Spots-size converted polarisation-insensitive SOA gate with a vertical tapered submicrometer stripe structure", IEEE PTL, Vol. 10, 510-512, 1998

[25] V. Vusirikala, S.S. Saini, R.E. Bartolo, R. Whaley, S. Agrawala, M. Dagenais, F. G. Johnson, D. Stone, "High butt-coupling efficiency to single mode fibers using a 1.55 um InGaAsP laser integrated with a tapered ridge mode transformer", LEOS 97, San Fransisco, WP3, 1997

[26] T. Saitoh, T. Mukai, "Recent progress in semiconductor laser amplifiers", IEEE JLT, Vol. 6, 1656-1664, 1988

[27] Optospeed SA, http://www.optospeed.ch

[28] D. Van Thourhout, J. De Merlier, T. Van Caenegem, K. Vandeputte, C. G. P. Herben, X. J. M. Leijtens, J. W. M. van Uffelen, M. K. Smit, I. Moerman, P. Van Daele, R. Baets, "Demonstration of multi-wavelength laser with a gain-clamped output amplifier", LEOS'98, Orlando, ThV2, 1998

[29] D. Van Thourhout, J. De Merlier, T. Van Caenegem, L. Vanwassenhove, I. Moerman, P. Van Daele, C.G.P. Herben, X.J.M. Leijtens, J.W.M. van Uffelen, M.K. Smit, R. Baets, "Elimination of crosstalk in the common output amplifier of a multi-wavelength source by gain clamping", OFC '99, San Diego , ThV2, 1999

[30] D. Van Thourhout, T. Van Caenegem, L. Vanwassenhove, I. Moerman, P. Van Daele, R. Baets, "Realisation of multi-wavelength Phased-Array laser by hybrid coupling of active and passive waveguide chips", Cleo Europe '98, Glasgow, CWB2, 1998

[31] M. R. Amersfoort, J. B. D. Soole, C. Caneau, H. P. Leblanc, A. Rajhel, C. Youtsey, I. Adesida, "Compact arrayed waveguide grating multi-frequency laser using bulk active material", El. Lett., Vol. 33, pp 2124-2126, 1997

[32] A. A. M. Staring, L. H. Spiekman, J. J. Binsma, E. J. Jansen, T. van Dongen, P. J. A. Thijs, M. K. Smit, and B. H. Verbeek , "A compact nine-channel multi-wavelength laser", IEEE PTL, Vol. 8, pp. 1139-1141, 1996

[33] C. H. Joyner, C. R. Doerr, L.W.Stulz, J. C. Centanni, M. Zirngibl, "Low-Threshold Nine-Channel Waveguide grating router-based continuous wave transmitter", IEEE JLT, Vol. 17, 647-651, 1999

[34] C. R. Doerr, R. Monnard, C. H. Joyner, L. W. Stulz, "Simultaneous CW operation of shared angular dispersive element WDM-lasers", IEEE PTL, Vol. 10, 501-503, 1998

[35] C. R. Doerr, C. H. Joyner, L.W.Stulz, "Multifrequency laser with reduced intracavity wave mixing", IEEE PTL, Vol. 11, 635-637, 1999

[36] C. R. Doerr, "Direct modulation of long-cavity semiconductor lasers", IEEE JLT, Vol. 14, pp 2052-2061, 1996

[37] B. Vanderhaegen, D. Van Thourhout, G. Sarlet, I. Moerman, L. Vanwassenhove, P. Vandaele, R. Baets, X. J. M. Leijtens, J. W. M. van Uffelen, M. K. Smit, "Loss measurements on InGaAsP ring resonator filters", ECIO' 99, Torino, Italy, pp. 381-384

[38] J. Demerlier, B. Vanderhaegen, "Ontwerp en realisatie van lasers voor multi-golflengte optische netwerken op basis van hybride chip-integratie", Afstudeerwerk Universiteit Gent, 1997-1998

[39] S. T. Chu, B. E. Little, W. Pan, T. Kaneko, S. Sato, Y. Kokubun, "An eight-channel add-drop filter using vertically coupled microring resonators over a cross grid", IEEE PTL, Vol. 11, 691-693, 1999

CHAPTER 6

DEVELOPMENT OF A HYBRID INTEGRATION TECHNOLOGY FOR MULTI-WAVELENGTH PHASED-ARRAY LASERS

CHAPTER 7

SUMMARY AND CONCLUSIONS

Chapter 6

Development of a hybrid integration technology for multi-wavelength Phased-Array lasers

1 Introduction

The experimental results presented in the previous chapter, proof that the hybrid coupling approach is useful for building complex photonic ICs. However, sometimes it is difficult to keep the coupling efficiency between both chips constant over longer time intervals or when the current changes. Moreover, as long as the chips are only temporarily coupled on an optical bench, it is not possible to use them in optical networks.

Therefore, we developed a permanent attachment technique for the hybridly coupled chips[1]. The procedure is similar to that used for attaching fibre arrays to polymeric or silica passive waveguide chips. In such a case, the fibres are arranged in a fibre array, which consists of a Silicon V-groove part and two reinforcement parts. The fibres are fixed in the grooves by a suitable adhesive. Subsequently, the fibre array and the waveguide array are attached to each other using a UV-curable adhesive. In order to obtain a stronger bond and to obtain high-quality end-faces, typically, the surface of the bond is enlarged by adding top and bottom plates [1]. In our case, the layer stack holding the fibres is replaced by the waveguide chip. Obviously, the much smaller dimensions of the InP waveguides will complicate the fixation considerably, not only due to the smaller alignment tolerances but also because of the fact that the smaller surface of the facets will limit the strength of the bond. Moreover, unlike the glass plates used to hold the fibre array, the InP chips are not transparent for UV-light[2].

In section 2 of this chapter, the procedure that we developed for bonding two hybridly coupled InP chips is described. The ultimate goal was to assemble a module, which can be used in the testbed setup built for the ACTS project APEX [5]. Therefore, the permanent fixation of both chips was not the only aspect that had to be investigated. In addition, a stable fibre-chip coupling and electrical connections had to be provided. The latter aspects however are

---

[1] The work described in this chapter was performed in strong collaboration with A. Van Hove. For more detailed information about the choice of the epoxies and the curing process, we refer to [2].

[2] For curing the epoxy UV-light with λ = 320 nm ~ 370 nm is used. In this wavelength range the absorption coefficient of InP is approximately 70 μm^{-1}.

not specific for hybridly integrated PICs and the solution we developed and which is discussed in section 3 of this chapter, can be used for monolithically integrated PICs as well.

Section 4 summarises the whole packaging procedure and in section 5, experimental results for a fully packaged hybrid PAL are presented. Some conclusions are given in the last section.

2 Permanent bonding of two hybridly coupled chips

2.1 Bonding procedure

The general procedure is outlined in Fig. 6-1a & b. Before starting the alignment process, the amplifier array chip is mounted on a silicon substrate, with the slanted end protruding approximately 100 μm beyond the edge of the silicon substrate. This substrate in turn is placed on a carrier, which has a U-shaped indentation at the front side. For the initial tests, this carrier was made out of copper. The carrier used in the final module is made out of aluminum. The waveguide chip is held by a vacuum needle, which fits in the indentation at the front of the carrier. In that way the amplifier chip and the waveguide chip may be aligned following a procedure similar to the one outlined in chapter 5 (active alignment by monitoring output power from passive waveguide chip).

Following this alignment step, the gap between both chips is widened again. Subsequently, a UV-curable epoxy ("epoxy 1") is applied (Fig. 6-1b), using an optical fibre tip mounted in a

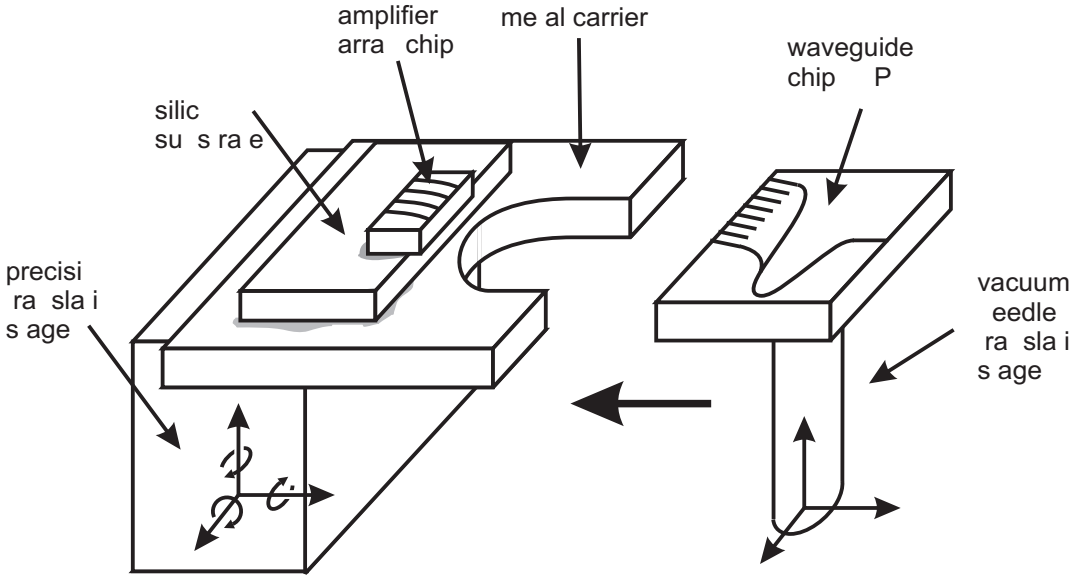

Fig. 6-1a This picture shows the amplifier sub-assembly, consisting of the amplifier array itself, the silicon substrate and the U-shaped carrier. The waveguide chip is held by a vacuum needle, fitting in between the legs of the carrier.

precision translation stage, and distributed over the facets by capillary forces. After realignment of both chips and optimisation of the output power, the epoxy is cured using a UV-

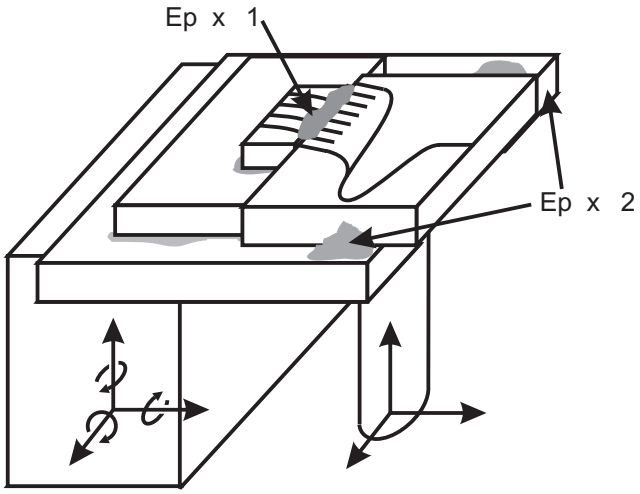

Fig. 6-1b This picture illustrates the location of epoxy 1, which holds both chips together, and epoxy 2, which stabilises the passive waveguide chip.

source with a flexible light guide. Finally, a second epoxy ("epoxy 2") is applied between the waveguide chip and the adapter plate to stabilise the PIC.

While the epoxy applied in between both chips ("epoxy 1") has to provide a very rigid and thermally stable bond, the epoxy used to stabilise the PIC ("epoxy 2") has to be flexible enough to take up displacements between the metal carrier and the InP waveguide chip. Therefore, it is obvious that two different kinds of epoxy need to be used. Their most important properties are summarised below.

"*Epoxy 1*"

- Optically transparent in the wavelength range around 1550 nm
- High glass-transition temperature (T_g). This ensures that the mechanical properties of the adhesive remain constant in the operational temperature ranges[1].
- Low thermal expansion coefficient
- Low shrinkage during curing
- Low elasticity
- Good adhesion to the chip facets (which are coated)
- At the transition between the amplifier and the waveguide, the energy density is very high[2]. This should not change the properties of the epoxy.

---

[1] Above the glass transition temperature, the thermal expansion coefficient may increase considerably while the elasticity modulus may drop over several decades. Generally, it is stated that the glass-transition temperature should be larger 95°C [1].

[2] If we take into account an output power $P_{out} = 1$ mW, a passive waveguide loss of 1 dB and a chip-to-chip coupling loss of 4 dB, the power exiting the amplifier is approximately $P_{amp} = 4.65$ mW. For an active cross-section of 4 μm^2, this yields a power density of $0{,}12 \times 10^6$W/cm^2. For the module presented in this chapter, the transition loss was much higher (~10 dB), yielding, for the same output

- The epoxy is distributed over the facets by capillary forces. If the viscosity of the epoxy is too low, the epoxy will leak off the facets. On the other hand, if the viscosity is too high, the epoxy will not be evenly distributed over the whole facet.
- Since the coupling efficiency can be kept constant over only limited time intervals, the curing has to be fast. This means that only UV-curing epoxies are applicable (see also paragraph 2.2.6)

"*Epoxy2*"

- High elasticity
- Since this epoxy has to fill the gap between both chips (20 to 30 μm), its viscosity has to be rather high.
- Good thermal conductivity: the central wavelength of the Phased-Array laser has to be adjusted by changing the temperature of the passive waveguide chip. However, the only direct contact between this chip and the thermoelectric cooler is through this epoxy.

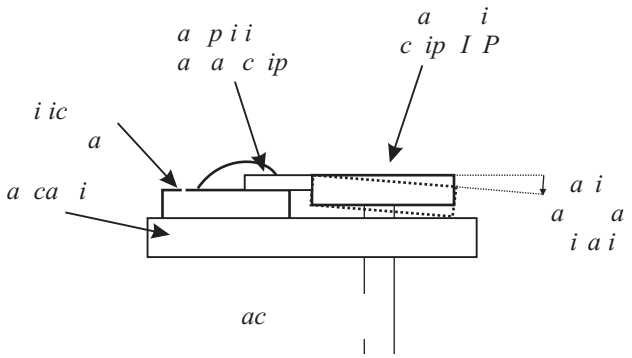

Fig. 6-2 Side view of hybrid coupling assembly.

Note that, as shown in Fig. 6-2, the stack formed by the amplifier chip, the silicon substrate and the epoxy, which is used to hold them in place, is 20 to 30 μm thicker than the passive waveguide chip, leaving some place for manipulation. However, since the waveguide chip is approximately 5 x 5 mm^2 large, the angular misalignment between the latter and the metal carrier may not be larger than 0.25 degrees to avoid contact between both chips.

2.2 Practical realisation

Following some successful initial tests, the epoxy "Vitralit 1505" (Panacol-Elosol) was selected for bonding both chips together ("Epoxy 1"). The epoxies of the Vitralit product range have a low shrinkage, a high glass transition temperature (T_g) and a high chemical and temperature resistibility. Their curing is initiated by UV-light. For some epoxies of the "Vitralit" product range, the curing continues even after removing the UV-source (dark cure). How-

---

power, P_{amp} = 18.5 mW or a local power density of 0.46×10^{6}W/cm^2. Note that most of this power is dissipated in the transition region.

ever, for the epoxy we used, this is not the case. The properties of the "Vitralit 1505"- epoxy are summarised below:

- *Viscosity* : 450 cps
- T_g : 150°C
- *Temperature range*: -40°C / + 180°C
- *Strength D*: 85 H_d
- *Curing*: UV-light (320 - 370 nm)
- No temperature curing / no dark cure
- Optically transparent (refractive index $n = 1.517$)
- Thermal expansion coefficient below T_g : 55 - 75 ppm/K
- *Applicability :* Glass, metal
- *Maximum curing depth :* 3 mm
- *Curing time:* 90s (layer thickness 0.5 mm, 60 mW/cm²)

To test the bonding procedure an extensive series of experiments was carried out. For these, we used either dummy chips or amplifier arrays and passive waveguide chips specially fabricated for this purpose. The most important observations regarding the bonding procedure and the properties of the employed epoxies are summarised below. For more detailed information about the bonding procedure and the epoxies applied we refer to [2].

2.2.1 Application of epoxy in between both chips

As already mentioned in paragraph 2.1, the epoxy is applied using a fibre tip, mounted in a translation stage (which was originally designed for laser probing). Usually two dots of epoxy are used, one at both ends of the amplifier array. By bringing both chips together, the epoxy is divided over both facets by capillary forces. The viscosity of the epoxy we used (450 cps) seems to be ideal for this procedure: higher viscosity epoxies have to be divided over the facet manually, lower viscosity epoxies do not stick to the facets. Moreover, when dipping the fibre tip in an amount of the epoxy on a glass plate, a small drop rests at the end of the fibre so that physical contact between the fibre and the chips may be avoided when depositing the epoxy on top of the latter.

2.2.2 Adhesion

From experiments using dummy chips, we learned that the adhesion of the epoxy to the chip facets was very good. When applying force to bonded chips with a large facet surface ($350\,\mu m \times 5$ mm), often one of the chips breaks instead of the epoxy bond itself.

The facet surface of the RSOA-chip used for assembling the multi-wavelength laser, is much smaller ($130\,\mu m \times 2.5$ mm) what decreases the global strength of the bond.

2.2.3 Index matching effect

On several occasions, we noticed that the coupling efficiency increased considerably by applying the epoxy in between both chips. This effect was most apparent in those cases where the coupling efficiency before applying the epoxy was low, due to a large gap between both chips[1]. The enhancement of the coupling efficiency may be understood from the fact that the far-field width of the waveguides is inversely proportional with the refractive index of the medium in between both chips (e.g. eq. 2-28 of chapter 2). In section 3 of chapter 4, this observation was theoretically verified using an eigenmode expansion propagation algorithm. From the results presented there, one may notice that the effect indeed becomes more important for an increasing gap width. In the limit, for an infinitesimal small gap, the coupling efficiency should become equal for both cases (with and without epoxy).

2.2.4 Distance and angle between both chips

Tests involving dummy chips or using the amplifier chips fabricated in house showed a high yield. However when we tried to bond the amplifiers provided by Optospeed SA to another chip, while following a procedure identical to that used for the test chips, it often occurred that the epoxy between the chip facets was not cured at all, even after very long UV-light exposure. We believe that this can be explained by a difference in the gap width. The dummy chips were cleaved manually and the amplifier chips we used for the tests showed often the "scratch" problem described in section 3 of chapter 5. The gap between such chips is, while being only a few micrometer, wider than the gap between the chips used for realising the PAL itself. The extremely narrow gap in the latter case may be the reason that, even when increasing the exposure times drastically, not enough UV-light reaches the epoxy between both chips to initiate the curing process.

Therefore, we tried to increase the gap between both chips in a controlled manner. This obviously decreases the coupling efficiency but it may increase the curing yield enough to compensate for that. However, for such an approach it is not possible to rely on the translation stages holding the chips, to widen the gap. When the chips are brought to a distance close enough to be a good compromise between increased yield and decreased coupling efficiency, the capillary forces originating from the epoxy in between both facets, are becoming much stronger than the force applied on the waveguide chip by the vacuum needle. As a result, both chips are pulled together and the gap between both chips is automatically minimised.

To circumvent this problem, we tried to corrugate the facet deliberately. By laser ablation [6] small grooves (width ~ $50\,\mu m$, depth 1 to $5\,\mu m$) were formed on the facet of the waveguide chip. Originally, the idea was that the larger accessibility for the light to the epoxy within

---

[1] This large gap in turn, may be caused by facet damage, dust particles in between both chips or by laser ablation applied to the passive waveguide facet, as discussed in paragraph 2.2.4.

the grooves themselves could provide an increased bonding strength. However, it turned out that the debris formed at the edges of the grooves by the ablation keeps the gap between both chips at a good value, resulting in an improved bonding yield and a tolerable transmission penalty. This approach was used for the module described in section 5 of the current chapter.

A related problem concerns the angle between both chips. It has been seen that a small upwards angle (< 1 degree) between both chips, as shown in Fig. 6-3b, may improve the transmission efficiency. This may be caused by the fact that in this way the gap between both chips is reduced while the negative effect from the angular misalignment is still very small (see also chapter 4, section 3). However, it has been seen that in such cases all of the epoxy is forced to the region below the edge of the chips, which cannot be reached by the UV-light, and the curing is inhibited. Illuminating the chips from below solved this, but complicates the setup considerably. In the situation shown in Fig. 6-3c, the curing is easy, but the penalty on the transmission efficiency is very high[1]. Therefore, we believe that an angular misalignment between both chips should be avoided as much as possible.

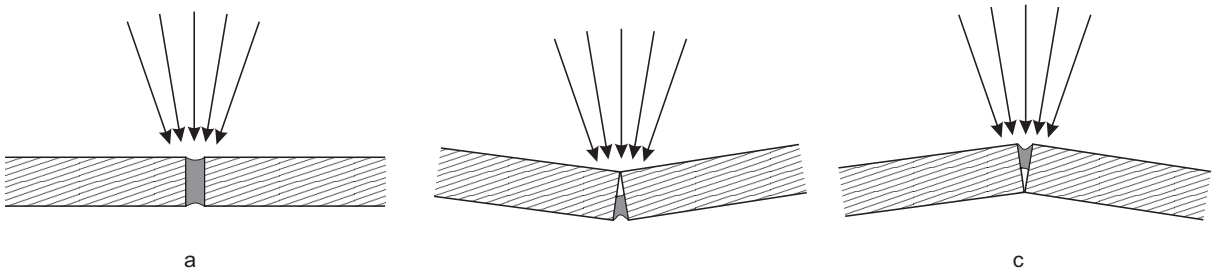

Fig. 6-3 Influence of angle on UV-light exposure

2.2.5 Radiation intensity

The amount of UV-light reaching the chip surface is obviously one of the most important parameters of the bonding process. The UV-source, which was employed (*EFOS Ultracure 100SS*), had a flexible light guide with a diameter of 6 mm. Its output power may be varied continuously up to approximately 10 Watt/cm^2. The energy reaching the epoxy is determined by the output power of the light guide and by its height with respect to the chip surface. This height was kept at approximately 15 cm for the first experiments. However, when the distance between the guide and the surface increases, the spot uniformity decreases, especially in the middle. Therefore, we decreased the distance to a few centimetres for the later experiments.

When exposing the chips to the UV-light, an important heating may occur due to the interaction of the radiation and the InP-chips. This may change the relative position of both chips during the exposure, finally resulting in a decreased or totally lost transmission. Therefore,

---

[1] An angle of 1 degree implies an increase of the gap by 2.5 μm (for an amplifier thickness of 150 μm).

the curing process is started at low radiation intensity (1 Watt or lower) and subsequently the power is gradually increased. The curing is carried out in short time intervals (~ 90 seconds), letting the chips cool down between each exposure. Typically, six time intervals were necessary to obtain a good bonding strength. However, also much longer exposure times were applied, especially in those cases were the narrow gap between both chips inhibited the curing process (see paragraph 2.2.4).

2.2.6 Temperature curing epoxies

As described in the previous paragraphs, the main problem with the bonding of the chips appears to be the accessibility of the epoxy in between both chips for the UV-radiation. This problem would be avoided if a room temperature curing epoxy could be used. Such an epoxy consists of two components, which form a stable bond when brought together. Unfortunately, it typically takes 24 hours before the curing is complete[1]. Since it is not possible to keep the coupling between both chips constant over such a long period, we regarded this type of epoxy impractical for the chip fixation. Nevertheless, two experiments were carried out, which may solve this issue.

The first of these experiments involved a temperature curing epoxy (EPO 301 from Epotek)(24 hours), with a viscosity (~150 cps) approximately equal to that of the UV-curing epoxy used for the experiments described in the previous paragraphs. This epoxy was applied to the chips and divided over the facets by capillary forces, just as before. The difference with the previously described procedure lies in the fact that, after bringing the chips together, a second, UV-curable, epoxy is applied on top of both chips (OG 142 from Norland). This epoxy has a very high viscosity (~ 9257 cps) what avoids its mixture with the first epoxy and it is immediately cured by UV-light exposure. In this way, the chip coupling can be held constant while the epoxy in between both chips reaches its ultimate strength. Only one such experiment was carried out until now. However, although the power dropped by 3 dB overnight, we believe that this procedure may form a good alternative for the procedure involving only the UV-curable epoxy, providing that the room temperature can be kept constant over a long enough time period.

For the second experiment, we used an epoxy that reaches already a relatively good bonding strength within one hour (EPO 302 from Epotek). This may be a reasonable period to keep the chip coupling constant. Also this experiment was successful. The drawback is that this specific epoxy had a high viscosity (5500 cps) and it had to be divided over the facet manually. In addition, although a reasonable bonding strength is reached within one hour, it takes much more time before the curing is complete.

---

[1] Alternatively, heating the epoxy may accelerate the curing. However, it is obviously not possible to place the complete optical bench into an oven.

2.3 Results from experiments, illustrating the bonding procedure

For illustrating some of the properties of the bonding procedure as it was outlined above, this paragraph presents the results of two experiments involving dummy chips. The experimental results from the hybridly integrated and packaged Phased-Array laser are discussed in section 5.1.

For the first test, we used the amplifiers angled by 5 degrees described in paragraph 4.1 of chapter 5, hybridly coupled with a passive waveguide chip incorporating a Phased-Array demultiplexer. Before applying the epoxy in between both chips, the threshold current and the output power of the laser were respectively 76 mA and 200 μW (at 100 mA). After applying the epoxy and before curing it, the output power increased to 450 μW, due to the index matching effect of the epoxy (see paragraph 2.2.3). Subsequently, due to the UV-curing the coupling efficiency decreased somewhat, but it stayed better than before applying the epoxy (I_{th} = 74 mA, P_{out} =220 μW, Fig. 6-4, trace A). For this experiment, the flexible epoxy for stabilising the PIC ("epoxy 2", see Fig. 6-1b) was not yet applied, so when removing the vacuum needle, the coupling efficiency decreased further (Fig. 6-4, trace B). However, by setting back the needle, the coupling efficiency could be increased again to its original value (Fig. 6-4, trace C).

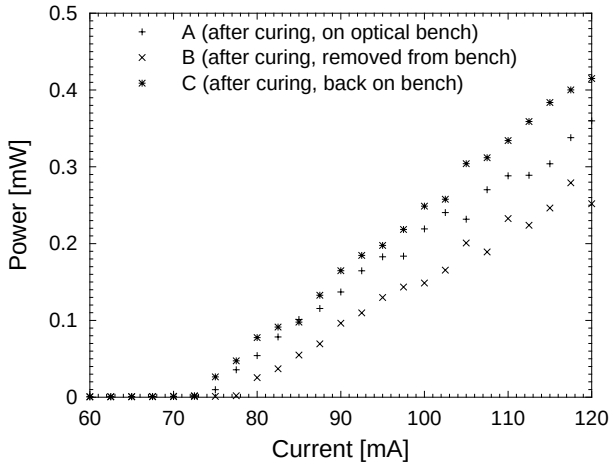

Fig. 6-4 Power versus current characteristics from permanently fixed hybrid PAL (5 degrees), after curing.

For a different experiment, an array of eight amplifiers (angled by 10 degrees at the facet) and a corresponding array with straight waveguides was employed. In this case, we did apply the stabilising epoxy between the metal carrier (copper) and the waveguide chip ("epoxy 2"). Fig. 6-5a shows the LI-curves for all 8 channels superimposed, as measured immediately following the finalisation of the complete bonding procedure. Before applying epoxy between both chips, the threshold currents were approximately 10 mA higher. From the difference between the LI curves for channels 1-4 and for channels 6-8, we believe that the angular alignment around the optical axis was not perfect. The amplifier of channel 5 was damaged. We measured the threshold current and the external efficiency of four channels of

this module several times during a 9 months period following the completion of the module. As may be seen from Fig. 6-5b, the characteristics of the module did not change considerably during this period. For comparison: the threshold current of a laser with an identical device structure and with the same length (800 μm) as the amplifiers used for this experiment was 50 mA.

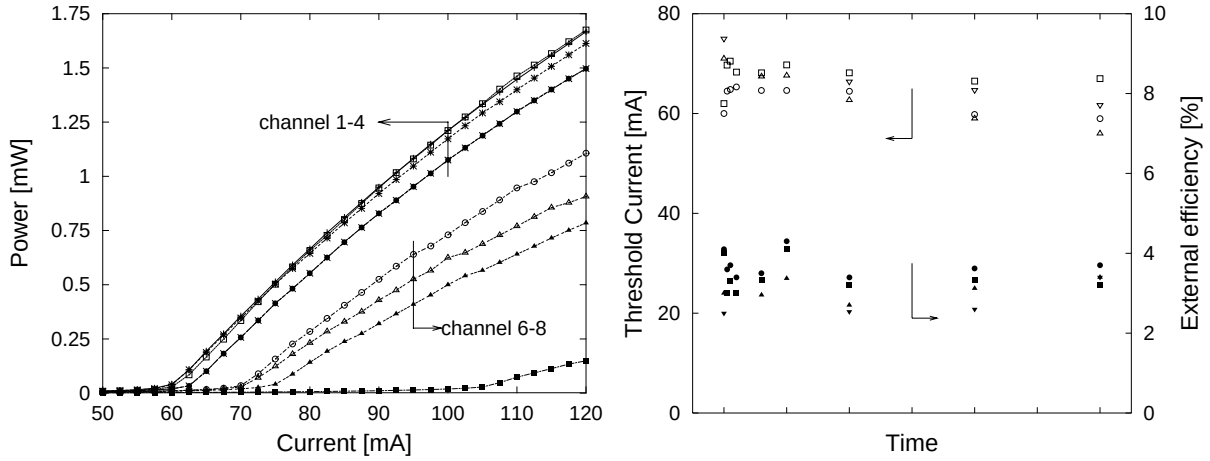

Fig. 6-5 Results of an 8 channel test module. The left picture shows LI-curves measured immediately following the completion of the fixation procedure. The right picture shows the threshold current (open symbols) and the external differential efficiency (closed symbols), measured over a 9 months time interval (the first 5 sets of measurements were performed in the days immediately following the bonding, the last three sets were each measured with a 3 months time interval).

3 Fibre-chip coupling and electronic connection

To be able to employ the laser in the APEX testbed, the assembled module needs to be packaged further to facilitate an easy optical and electronic access, as already mentioned in the introduction. For that purpose, we used the KAP10 laser package from Radians Innova [7]. This module contains a thermo-electric cooler and a translation stage holding the optical fibre and a coupling lens. The PIC itself must be mounted on a suitable adapter plate, which is also available from Radians Innova. However, none of the standard formats was convenient for mounting our specific device, so we had to design and manufacture one by ourselves.

Although the KAP10 module solves the optical coupling problem, we still had to find a means to provide the electronic signals to the multi-wavelength laser. As already mentioned, the laser was intended for use in the APEX testbed setup [5]. Therefore (see chapter 1, section 1.3), we had to be able to provide four 622 Mbit/s data signals to the multi-wavelength laser. For that purpose, the amplifiers were wire-bonded to bond pads on the silicon substrate. These bond pads in turn are connected with a larger gold pad to which a semi-rigid coaxial cable is attached. These are terminated with an SMA-connector and they are fixed to the substrate using a conductive epoxy. Although soldered connections would

provide a more reliable connection, they are more difficult to realise and require a more complicated substrate processing. Therefore, we believe that the use of epoxy is more in accordance with the idea of developing a technology useful for rapid device testing.

One of the drawbacks of the KAP-10 laser module is that it cannot be hermetically sealed. This makes that the laser cannot be cooled below a minimum temperature, depending on the environmental circumstances, to avoid water condensation. This may be a problem when using the device temperature to align the operating wavelength with the desired frequency grid.

4 Summary of packaging procedure

This section summarises the complete packaging procedure as it was outlined in the previous paragraphs

Device layout and dimensions

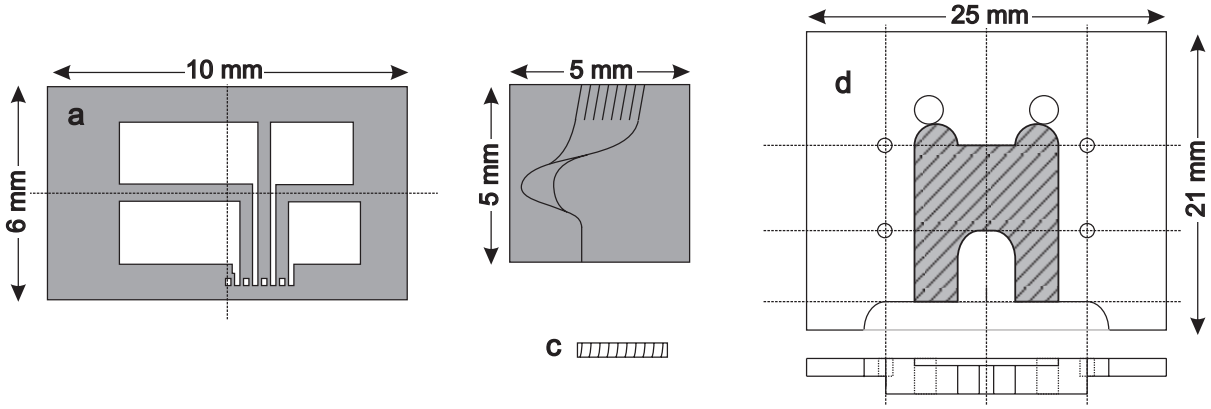

Fig. 6-6 Summary of layout and dimensions of parts used to assemble a hybridly coupled PIC.

Fig. 6-6 shows the parts, which have to be assembled to form the multi-wavelength laser. Parts (a), (b) and (c) are drawn to scale 8:1, part (d) to scale 2:1.

- (a): the silicon substrate, which is covered with a dielectric layer (Silicon-Nitride) and a gold interconnection pattern. (Dimensions: 6 x 11 x 0.250 mm^3). The pattern also contains alignment structures for making the amplifier mounting easier.
- (b): the InP passive waveguide chip with an 8-channel Phased-Array demultiplexer. (Dimensions : 5 x 5 x 0.350 mm^3)
- (c): the InP amplifier chip. (Dimensions : 2.5 x 0.400 x 0.130 mm^3).
- (d): the aluminum adapter plate. The U-shaped indentation is used for the vacuum needle that holds the waveguide chip. The shaded region in the middle is exactly as wide as the silicon substrate thereby allowing for an easy alignment of this substrate with respect to the optical axis. The two largest holes are used to screw the adapter plate onto the thermo-electronic element into the KAP10 laser module. The other holes are used to tighten the semi-rigid coaxial cables to the adapter plate.

First step: preparation of amplifier sub-assembly

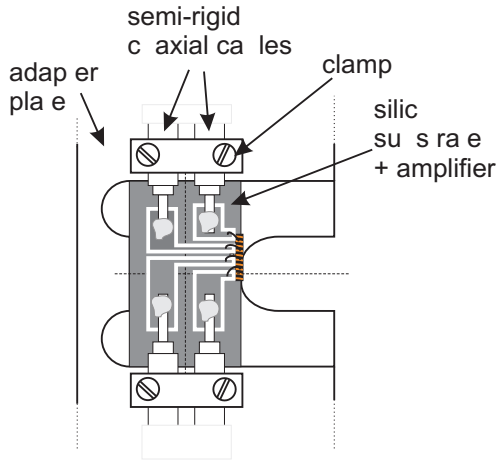

1. The amplifier array is mounted on the silicon substrate, using a conductive epoxy (the most recent devices were bonded using Indium-solder)
2. Wire bonding from amplifier array to substrate
3. Substrate is mounted in the adapter plate, using conductive epoxy
4. The semi-rigid coaxial cables are attached to the substrate using conductive epoxy and fastened to the adapter plate, using small clamp plates.

Second step: chip alignment and bonding

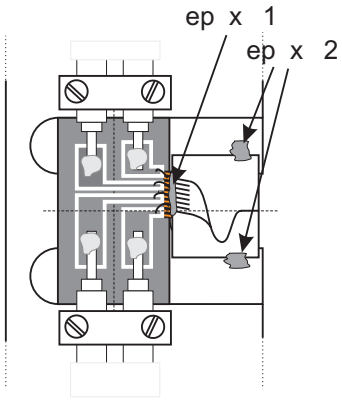

5. The waveguide chip, held by a vacuum needle, is aligned with the amplifier chip. The optimisation is carried out by monitoring the output power.
6. "Epoxy 1" is applied and cured
7. "Epoxy 2" is applied and cured
8. The vacuum needle is removed

Final step: insertion into the KAP-10 laser module

Finally, the adapter plate with the hybrid PIC is inserted in the KAP-10 laser module and the optical fibre is aligned with the output waveguide of the PIC. A typical fibre-chip loss of -5 dB is obtained. This is the same value as predicted by the manufacturer of the module. Fig. 6-7 shows a photograph of the completed module.

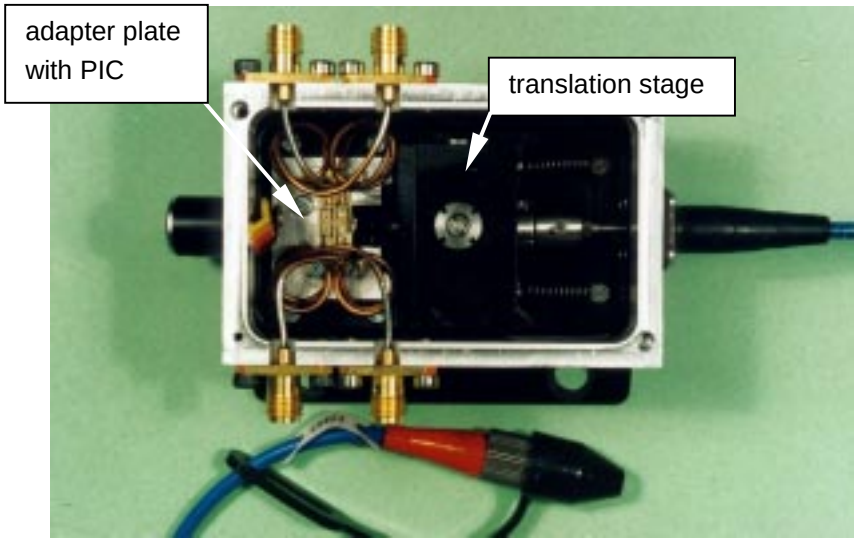

Fig. 6-7a) Photograph of hybrid PIC in KAP 10 laser module

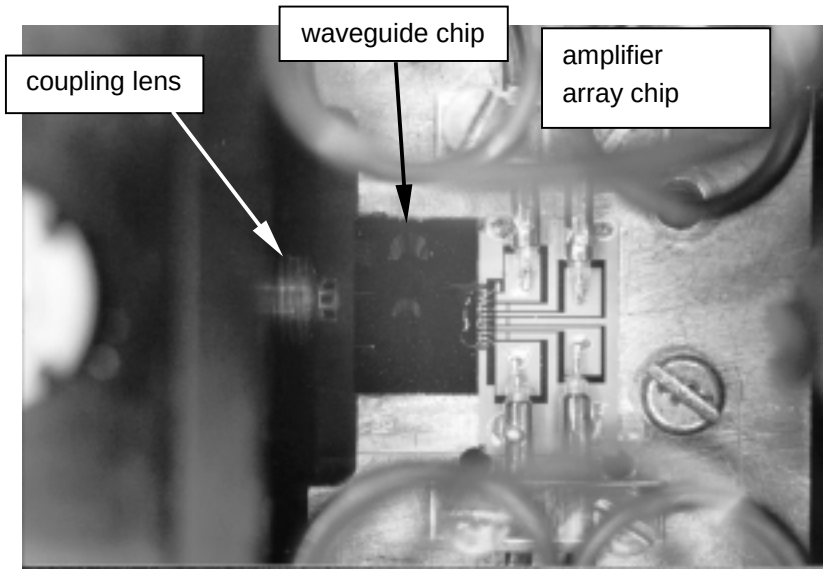

Fig. 6-7b Detail of packaged hybrid PIC

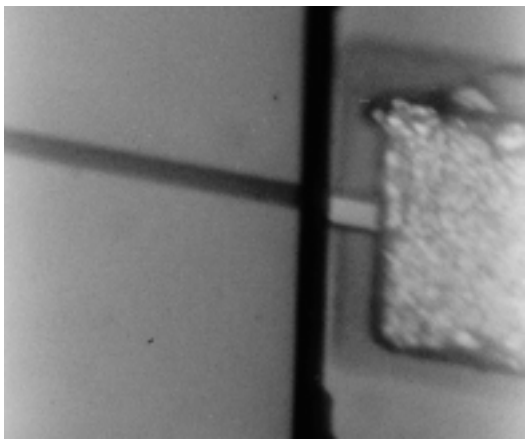

Fig. 6-7c Close-up of transition between both chips. The width of the passive waveguide (left part) is 3 μm

5 Experimental results

5.1 Introduction

In this section, we discuss the operation characteristics of a complete laser module as shown in Fig. 6-7a & b[1]. For realising the module, we used the same chips as those which were used for obtaining the results described in paragraph 4.2 of chapter 5 (the non-permanently coupled hybrid PAL). The amplifiers were mounted on a silicon substrate. The module was assembled as described in the previous paragraphs. Two small grooves were formed on the facet of the waveguide chip by laser ablation [6]. As described in paragraph 2.2.4, the debris formed at the edge of these grooves may be used to control the width of the gap in between both chips. A wider gap improves the accessibility to the epoxy between both chips for the UV-light, but at the same time reduces the coupling efficiency. In this particular case, the threshold increased from the values reported in the previous chapter (< 40 mA) to values over 80 mA for the best channels. However, by applying epoxy in between both chips, the threshold current decreased again, down to 52 mA for the best channel. For curing the epoxy, the light guide was placed 3 cm above the sample and the output intensity was set at 1 Watt. Although we believe that the curing was complete after approximately eight time intervals, the UV-radiation was set further for a total of twenty time intervals (100s/interval). For stabilising the module ("epoxy 2", see Fig. 6-5b), also a UV-curing epoxy was employed (UV-NOA from Norland). The assembly took place at room temperature (24°C)

Following the completion of the assembly, only three of the eight channels showed laser operation (channels 2, 3 and 4). Subsequently, the laser was intensively characterised. Unfortunately, during one of the experiments, channel 4 was destroyed. In an attempt to repair this channel, an additional amount of epoxy was applied on top of the interface between the amplifier chip and the waveguide chip. This did not result in a recovery of the damaged channel. However, due to the additional epoxy, we noticed a considerable improvement of the operating characteristics of channels 2 and 3. Moreover, also laser operation on channels 5 to 7 could be obtained now. We believe that this improvement is due to a better heat spreading, provided by the additional epoxy.

The next paragraphs describe the static and dynamic characteristics of this device. Some of the characteristics were measured before, and some after applying the additional epoxy on the facet. This will be mentioned where necessary.

5.2 Threshold current and output power

Fig. 6-8a shows LI-curves for channels 2 to 4, before the additional epoxy was applied. Both the free space and the fibre-coupled power were measured (respectively before and after

[1] Following the completion of this thesis, a new module was assembled with improved operating characteristics. The operating characteristics of this module are described in an appendix.

entering the PIC in the KAP10-laser module). A fibre coupling efficiency of -5.25 dB was obtained what is in agreement with the value predicted by the manufacturer of the module. Fig. 6-8b shows the LI-curves measured after applying the additional epoxy.

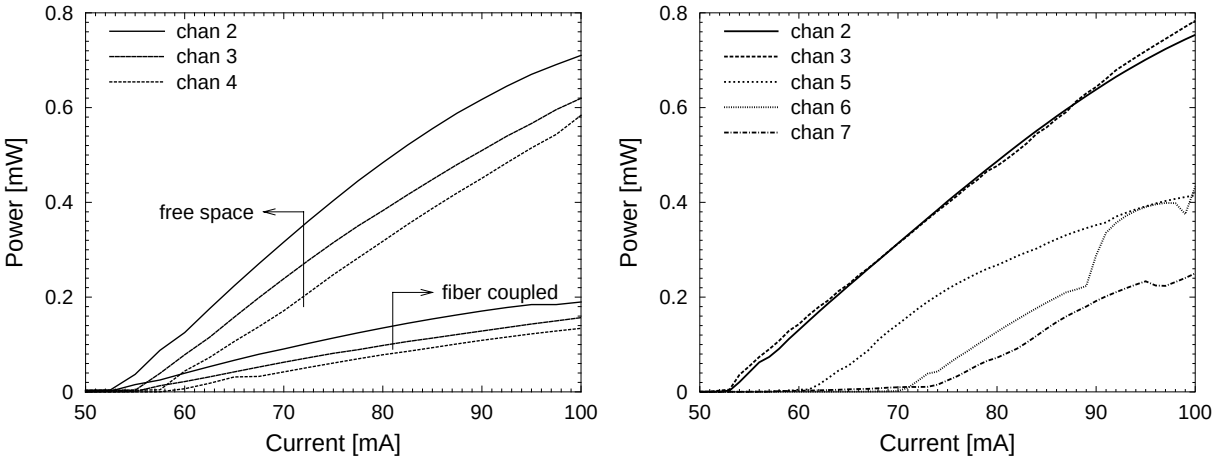

Fig. 6-8 LI-curves of permanently hybridly coupled MWL, before (left) and after (right) applying additional epoxy on the chip interface.

Fig. 6-8 shows that a fibre coupled power of 200 μW or approximately -7 dBm is obtained for channel 2. This is enough for the APEX testbed setup (a value of -10 dBm was specified, see chapter 1, paragraph 1.3). However, for most applications a higher output power is required what may be realised by improving the coupling to optical fibre. Values around 2.5 dB are commonly obtained by using a lensed fibre. Obviously, also the output power from the PIC itself is low. By improving the coupling efficiency between both chips, it should be possible to reach the same output power as for the non-permanently packaged PAL described in chapter 5 (> 3 mW). By increasing the length of the amplifiers, the maximum output power could be further increased.

Just above threshold, the maximum external efficiency is around 2.5 %. As may be seen from Fig. 3-4 in chapter 3, such a value corresponds with a total loss in the passive section of the laser of approximately 13 dB. Taking into account a 2 dB loss for the transmission through the Phased-Array, the chip to chip coupling loss is estimated to be 11 dB, which is 7 dB higher than the estimated value for the non-permanently packaged PAL. This high coupling loss may be attributed mainly to the increased gap width between both chips. From Fig. 5-16 in chapter 5, which shows the measured transmission as function of the longitudinal distance between both chips, one may see that a 7-dB penalty could be explained by an increase of the distance between both chips to 4.5 μm. From the calculated results in chapter 4 (section 3), almost the same value is obtained.

5.3 Spectral characteristics

Fig. 6-9a shows the oscillation spectrum of the hybridly integrated and packaged PAL with channels 2 to 4 operated simultaneously. Channel 2 was driven at 80 mA, the other channels

at 100 mA. In general, the same features occur as for the non-permanently coupled laser. However, due to the increased threshold current, the gain peak shifted towards a lower wavelength and compared to the spectra depicted in Fig. 5-18 of the previous chapter, the packaged PAL operates in a lower passband of the multiplexer. Due to the reduced output power, the side mode suppression ratio is reduced somewhat but is still better than 35 dB. Channels 2 to 4 operate reliably in a single passband of the Phased-Array.

Fig. 6-9b shows superimposed spectra of 6 channels (spaced by 200 GHz). Contrary to the first three channels, channels 5-7 show multi-passband lasing under some operation conditions. Their SMSR is also further reduced.

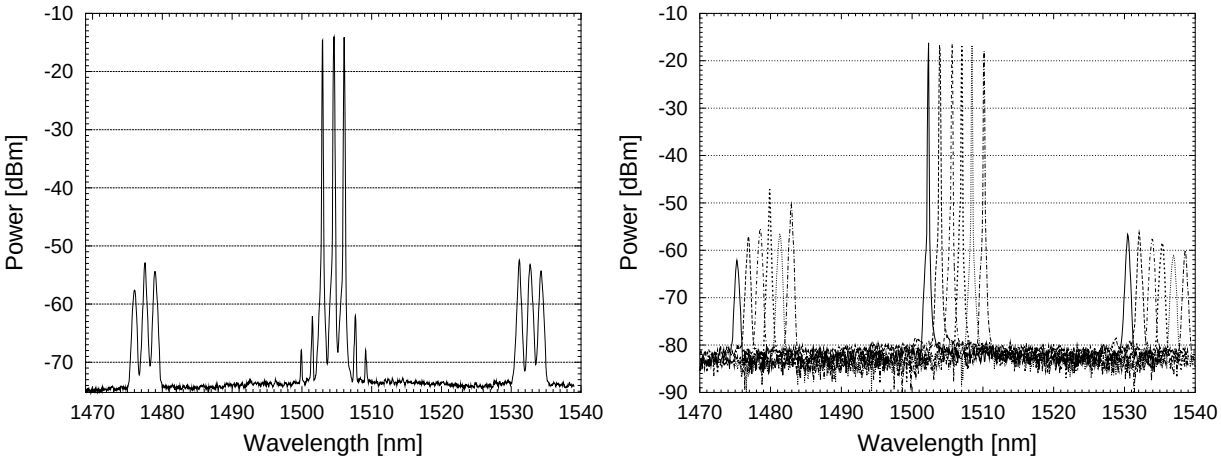

Fig. 6-9 a) Oscillation spectrum of channels 2-4 operated simultaneously (measured before applying additional epoxy). b) Superimposed oscillation spectra of channels 2-7 (measured after applying the additional epoxy, except for channel 4).

Fig. 6-10 shows a set of oscillation spectra, which illustrate the wave mixing in the common (passive) output waveguide. For obtaining the first two spectra, channels 2 and 3 were operated simultaneously, for the other two spectra, channel 4 was driven instead of channel 3. As one may see, contrary to the case of wave mixing in an amplifier, the strength of the effect is independent of the distance between the modes and it is symmetric. Table 6-1 summarises the results.

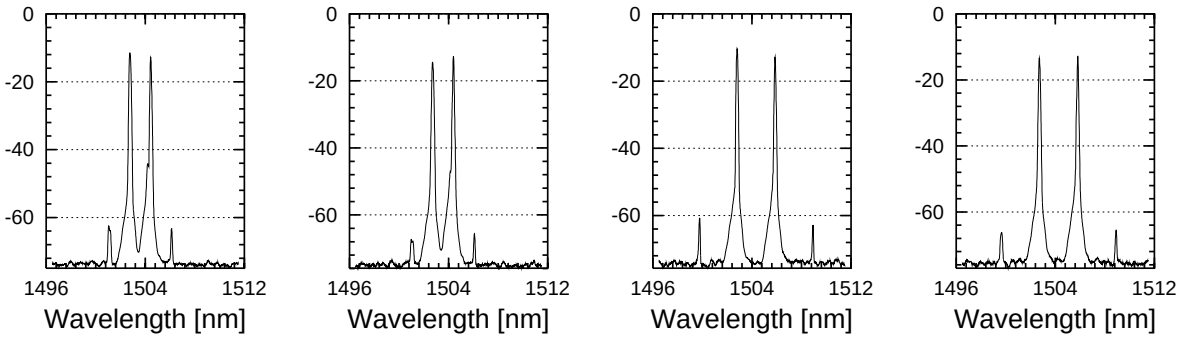

Fig. 6-10 Oscillation spectra from the packaged PAL, illustrating the wave mixing effect.

I_2 [mA]	I_3 [mA]	I_4 [mA]	P^-	P_2	$P_{3/4}$	P^+	$P_2^2 P_{3/4}/P^-$	$P_2 P_{3/4}^2/P^+$
100	100	0	-62.5	-11.8	-12.8	-63.4	26.2	26.0
80	100	0	-67.3	-14.4	-12.6	-66.0	25.8	26.3
100	0	100	-60.8	-10.5	-12.9	-62.8	26.8	26.6
80	0	100	-66.2	-13.5	-12.9	-65.6	26.4	26.2

Table 6-1 P_2 represents the power in channel 2, $P_{3/4}$ represents the power in channel 3 or channel 4, depending on which channel was driven. P^- and P^+ designate the power in the wave mixing mode respectively at the lower and the higher wavelength side. All powers are denoted in dBm.

The power in the wave mixing mode is given by [4]:

$$P_{2\lambda_1-\lambda_2} = \left(\frac{2\pi |n_2| l}{A_{eff} \lambda_0} \right)^2 P_{\lambda_1}^2 P_{\lambda_2} \qquad (1)$$

The last two columns of Table 6-1 are proportional to the term in brackets of equation (1). The mean value is 26.2. With the effective cross-section of the mode $A_{eff} = 2.0 \text{ x } 1.0\,\mu m^2$, the length of the passive waveguide $l = 3.0$ mm, and the power in the output waveguide $P_2 \approx 1.4$ mW, we find $n_2 \approx 4.5 \times 10^{-12}$ cm²/W. In [4] a value $n_2 \approx 0.9 \times 10^{-12}$ cm²/W is reported, obtained from a similar experiment. It has been found that the wave-mixing products may give rise to instabilities in the output power if they fall into a lasing mode [4]. We have not seen this effect until now, however, by shortening the length of the output waveguide, the power in the wave-mixing modes may easily be reduced to acceptable levels.

5.4 Longitudinal mode stability and tunability

Albeit in a less pronounced way than for the non-permanently coupled PAL, kinks were sometimes also observed in the LI-curves of the packaged module. To investigate the origin of those discontinuities, we measured the operating frequency using a high-precision wavelength meter (HP 86120B multi-wavelength meter), while scanning the current.

Fig. 6-11a shows such a measurement for channel 2 (at room temperature). Although the operating wavelength changes considerably, neither the LI-curve, nor the wavelength versus current curve show discontinuities. Only in the region just above threshold, it takes some time to choose the mode in which to lase. In this region, some amount of the power can also be found in lower passband modes ($2\,\mu W$ on a total of $12\,\mu W$). In the current interval from 60 mA to 100 mA, the operating wavelength changes by 0.13 nm[1], corresponding with a fre-

[1] The longitudinal mode spacing is ~ 4 GHz or 0.03 nm, so the operating wavelength changes over multiple modes spacings without hopping in this case.

quency change of 480 MHz/mA. This value is approximately 4 times as large as the value found for the non-permanently packaged PAL, using a Fabry-Pérot interferometer (see chapter 5). Probably, the higher loss in the coupling region is responsible for a heating of the passive chip. By cooling the module to 18°C, the wavelength change was slightly reduced, to 400 MHz/mA. Under all conditions, single longitudinal mode operation is obtained.

Fig. 6-11b presents similar results, taken from channel 4. However, in this case, there is a large discontinuity in the output power at 82 mA and a smaller one at 91 mA. By inspecting the wavelength scan, we see again the mode instability just above threshold, comparable to that of channel 2. However, two additional mode hops also appear, exactly corresponding with the location of the discontinuities in the LI-curve. It is interesting to note that, although for both mode hops the frequency changes by approximately the same amount, the effect on the LI-curve is much more pronounced for the first one compared to the second one.

When the device temperature was changed, the location and the amplitude of the kinks changed as well. Again, single longitudinal mode operation is obtained for most operating conditions.

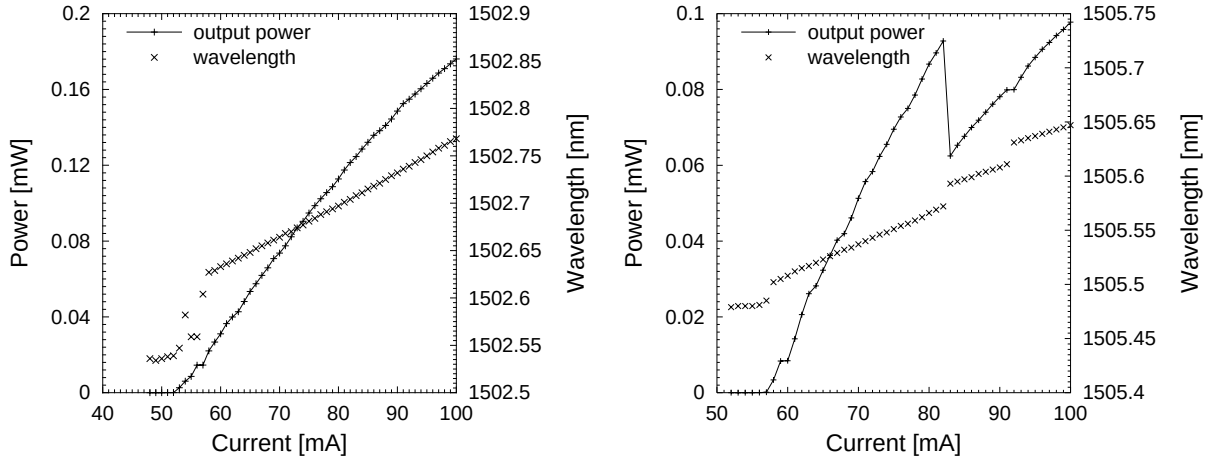

Fig. 6-11 Output power and operating wavelength measured as function of drive current for channel 2 (left picture) and for channel 4 (right picture)

Before the additional epoxy was applied, channel 3 showed the same type of discontinuities and mode hops as channel 4. However, with the epoxy, this channel behaved more like channel 2. The difference may possibly be explained by the change in output power. The strength of the wave mixing effect, which suppresses lasing in longitudinal modes next to the main mode, depends strongly on the photon density in the cavity.

5.5 Temperature tuning

In WDM-systems, the operating wavelength of the transmitter has to coincide exactly with that of the other employed network elements. Small deviations may already give rise to severe penalties at the receiver side. In practise however, due to process variations, it is diffi-

cult to obtain the required accuracy and one needs to use the device temperature for fine-tuning.

To investigate the tunability of the PAL-laser, we measured its wavelength and output power while changing the temperature. Again, a wavelength meter was used to determine the operating frequency and the built-in thermo-electric controller of the KAP10-laser module was used to change the temperature. The results are illustrated in Fig. 6-12. For obtaining the left picture, channel 2 was driven at 100 mA while the temperature was changed from 16^0C to 26^0C and back down to the original temperature. Opposite to what one would expect, the output power increases with increasing temperatures and reaches a maximum at approximately 24^0C. The same behaviour is seen for different bias currents and for the other channels. We believe that the coupling efficiency between both chips changes during the temperature scan due to mechanical stresses. The maximum at 24^0C may be explained by the fact that the module was assembled and cured at this temperature. Another reason could be that the coupling efficiency to the optical fibre changes when the temperature is changed. During the temperature scan, the operating wavelength changes by ~0.113 nm/K, which is typical for this sort of device. At 20.5°C (increasing temperature), the operating wavelength shifts to a neighbouring longitudinal mode what is also visible from a discontinuity in the curve representing the output power. In addition, at 26^0C, while the direction of the temperature sweep was changed, a mode hop occurred. The latter probably explains the hys-

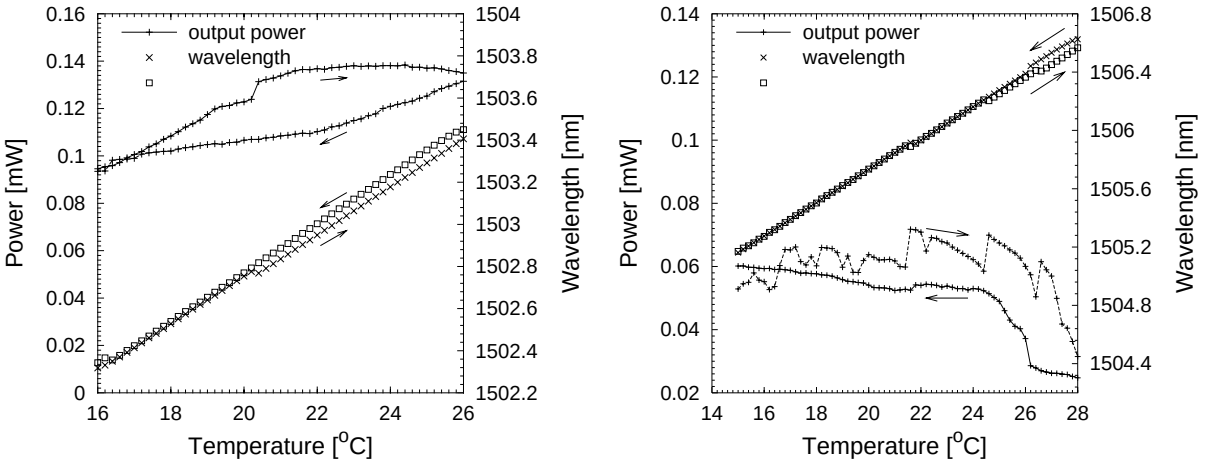

Fig. 6-12 Output power and operating wavelength measured as function of temperature for channel 2 (left picture) and for channel 4 (right picture). The arrows indicate whether the temperature is increased or decreased.

teresis observed in the power versus temperature characteristic.

Fig. 6-12b was measured from channel 4 (at 80 mA). Almost the same wavelength tuning (0.114nm/K) is obtained as for channel 2 and the output power again reaches its maximum around 24°C. However, similar to the case of the LI-curves shown in the previous para-

graph, a lot more discontinuities occur for channel 4 compared to channel 2[1]. The wavelength scan shows that again most of these discontinuities may be correlated with longitudinal mode hops.

In Fig. 6-13, the change of the junction voltage during the temperature scan is depicted, showing again the same discontinuities. Each time the operating wavelength jumps to another longitudinal mode, the junction voltage drops by approximately 1 mV. This again illustrates the fact that the PAL-laser does not always operate in the longitudinal mode with the lowest threshold carrier density. Instead, due to the carrier induced modal intermodulation, there is a stability region around the centre of the intra-cavity filter for each longitudinal mode to operate in. Only, when the lasing mode is moved far away from the centre of the filter and leaves the stability region, a mode hop will occur. This behaviour also explains the hysteresis noticed between the mode hops.

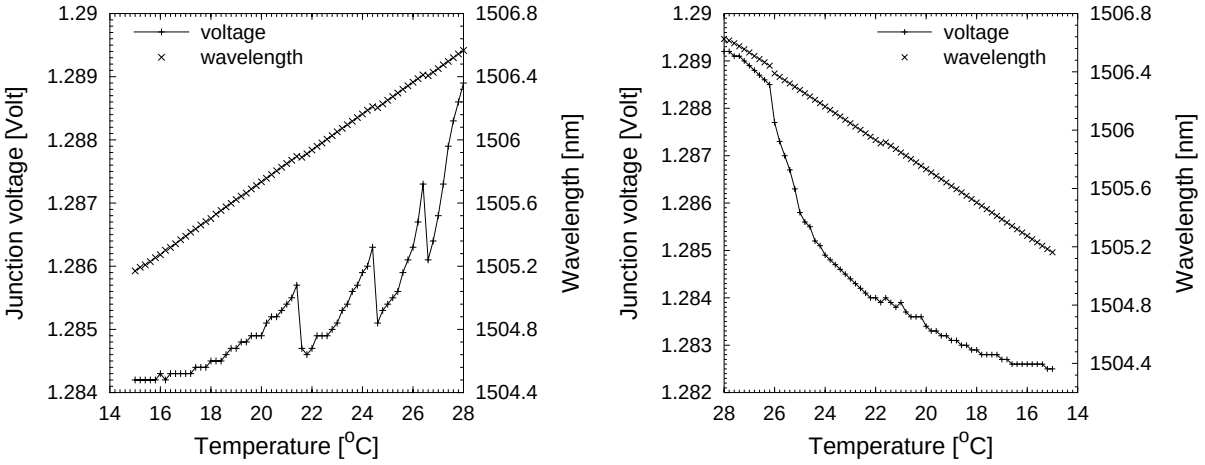

Fig. 6-13 Measurement of wavelength and junction voltage while the temperature is increased (left) and decreased (right)

From the experiments illustrated in Fig. 6-12 it is obvious that the power versus temperature characteristic is determined by the mechanical characteristics of the module, rather than by the intrinsic behaviour of the laser. If a changing fibre-chip coupling is responsible for this effect, the solution is trivial: one simply has to optimise the coupling at the operating temperature. However, another reason could be that mechanical stresses in the module itself change the coupling efficiency between both chips. A possible origin of these stresses is the difference in thermal expansion coefficient between the layer stack formed by the InP amplifiers and the silicon substrate and the epoxy between the InP waveguide chip and the aluminium carrier[2]. Although this epoxy was selected because of its flexibility, due to the long

[1] These measurements were performed before the additional epoxy was applied to the interface between both chips. Applying the epoxy considerably improved the operating characteristics.

[2] The thermal expansion coefficients for Silicon and InP are respectively $2.6\times10^{-6}K^{-1}$ and $4.5\times10^{-6}K^{-1}$. For epoxy, typical values between $20\times10^{-6}K^{-1}$ and $60\times10^{-6}K^{-1}$ are obtained.

lever, the angular momentum around the axis parallel to the amplifier facet may be large enough to induce a small rotation around this axis.

5.6 Linewidth

We measured the linewidth of the laser, using a delayed self-homodyne scheme with a 3.5 μs delay line. This method is expected to give results with an accuracy of 15 % for linewidths down to 250 kHz. For smaller linewidths, the laser coherence length becomes longer than the delay line and the measurement error increases rapidly (20% at 200 kHz).

Fig. 6-14a shows the linewidth as function of the drive current. The observed scatter is larger than the measurement error, which may be caused by a hop of the operating frequency to a neighbouring mode or by external reflections. Fig. 6-14b shows that the linewidth is inversely proportional to the output power as predicted theoretically (e.g. chapter 3).

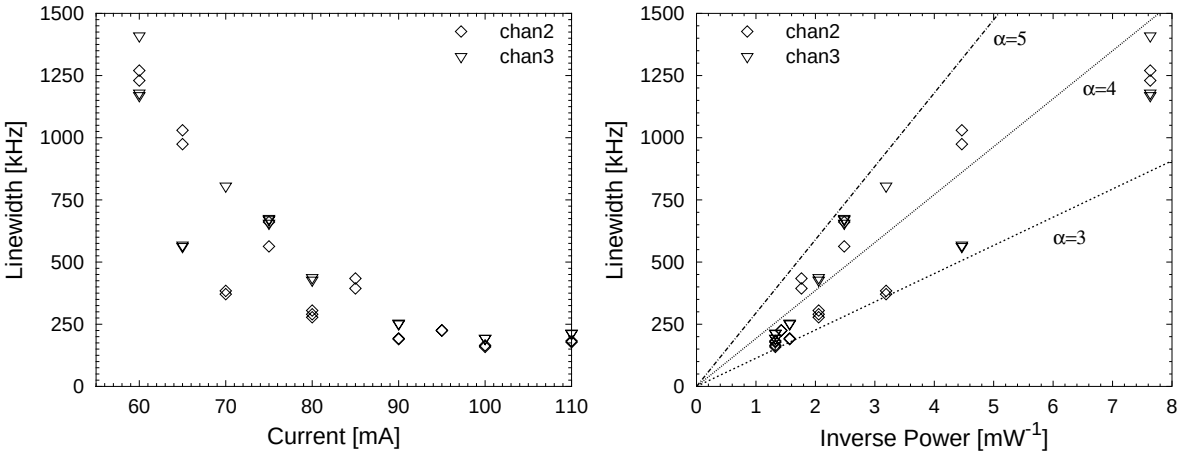

Fig. 6-14 a) Linewidth as function of drive current for channels 2 and 3. b) Linewidth as function of the inverse of the output power.

The lines in Fig. 6-14 were calculated using the formula obtained in chapter 3, using $L_a = 400\,\mu m$, $L = 10$ mm, $\Gamma = 0.245$, $n_g = 3.56$ and $n_{sp} = 1.5$[1]. The loss of the passive part was estimated to be 12 dB and the linewidth enhancement factor α was varied between 3 and 5 as indicated in the figure. Using a least squares fit, a value of 3.6 is obtained for α. This is a rather low value, however it is not unrealistic taking into account the high injection level and the fact that the device is operating at the low wavelength side of the gain peak. If the loss in the passive part is estimated to be 11 dB (13 dB) instead of the 12 dB used for Fig. 6-14, the fitted value for the linewidth enhancement factor increases (decreases) to 4.1 (3.2).

[1] n_{sp} is the population inversion factor, which has a value between 1.5 and 2.5 for a typical laser. Here we choose $n_{sp} = 1.5$ because of the high injection rate (For total inversion, $n_{sp} = 1.0$)

5.7 Small-Signal response

We measured the small signal response of the packaged module two times (see Fig. 4-12 for the measurement setup):

- The first time from channel 4, which was connected with a bias tee through the semi-rigid coaxial cable, attached to a bond pad on the silicon substrate. No matching resistor was employed. This measurement was performed before applying the additional epoxy, so the output power was relatively low. The results are shown in Fig. 6-15a.
- The small signal response was also measured from channel 2, using a high frequency probe with a 45 Ohm resistor incorporated in the probe head. This measurement was performed after having applied the additional epoxy (Fig. 6-15b).

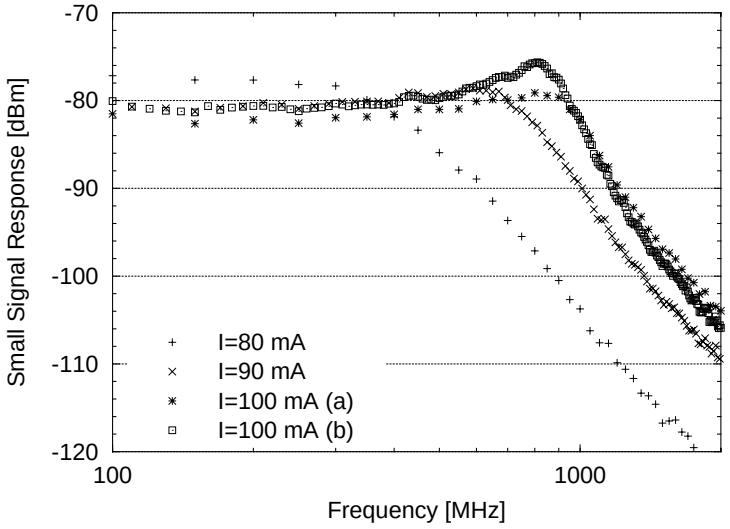

Fig. 6-15 a) Small signal response from channel 4, measured through semi-rigid coaxial cable.

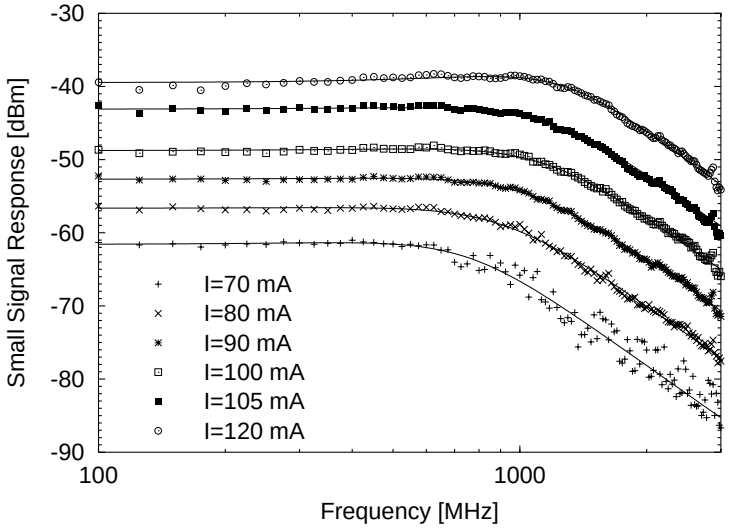

Fig. 6-15 b) Small signal response from channel 2, using high frequency probe.

The solid curves in Fig. 6-15b are fitted to the measured data using a conventional two-pole transfer function for the small-signal modulation response of a semiconductor laser:

$$H(j\omega)=\frac{A}{\left(j\frac{\nu}{\nu_r}\right)^2+j\left(\frac{\nu}{\nu_d}\right)+1} \tag{2}$$

The fitted values for the resonance frequency ν_r and the damping frequency ν_d are shown in Fig. 6-16. Not taking into account the measurement at I=105 mA, which seems to be anomalous, one sees that both the damping frequency and the 3-dB frequency are proportional with the drive current (and the output power). For small currents, this is also the case for the resonance frequency. For larger current values, the resonance frequency increases sublinearly. Note that there is a very good agreement with the simulated results presented in chapter 3 (Fig. 3-15).

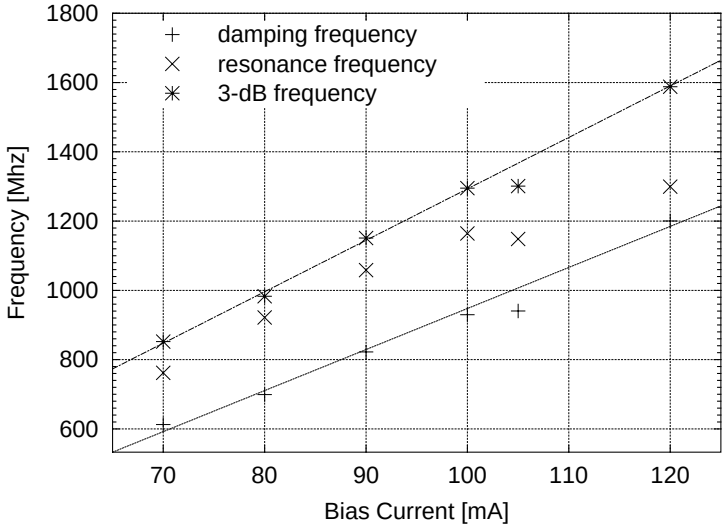

Fig. 6-16 Fitted values for the resonance frequency, the damping frequency and the 3dB-frequency obtained from fitting eq. (2) to the small signal response obtained from the packaged module.

Fig. 6-15a shows the small signal response from the packaged PAL measured without matching resistor. These are obviously not as good as those shown in Fig. 6-15b. The resonance frequency is lower, which may be explained by the limited output power from channel 4, and the high frequency roll-off is steeper, indicating a parasitic effect from the electrical circuit. The response for a bias-current of 100 mA was measured two times, in similar circumstances. Nevertheless, curve (b) (Fig. 6-15a) shows a strongly reduced damping at the resonance frequency. Possibly, this effect may be again attributed to a shift of the operating wavelength to a neighbouring longitudinal mode. As noted before, this may considerably influence the operating characteristics of the laser. Since no isolator was used, back reflection may be another cause for the distortion of the laser operation. Unfortunately, this chan-

nel broke down immediately after having performed this measurement so we could not further investigate this, nor the parasitic effect of the coaxial cable.

5.8 Large signal response

From the small-signal response shown in Fig. 6-15b, we believe that this Phased-Array multi-wavelength laser should allow for modulation with a 622 Mbit/s data-signal. To verify this, channel 2 was modulated with a pseudo random data signal using a high frequency probe (2^{31}). The optical/electrical conversion was performed through a 2.5 GHz detector. Fig. 6-17 shows eye diagrams obtained from a high-frequency oscilloscope. The operating conditions are denoted below the figures. The small arrows at the left side of the diagram indicate the off level.

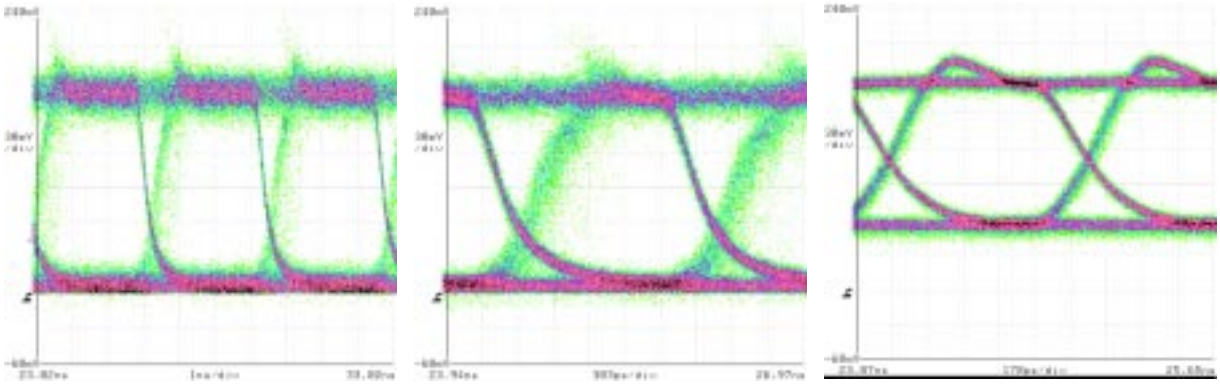

f = 300 MHz - I_{bias} = 75 mA
ΔV = 2 Volt - P_{on}/P_{off} = 14 dB

f = 600 MHz - I_{bias} = 75 mA
ΔV = 2 Volt - P_{on}/P_{off} = 14 dB

f = 1.0 GHz - I_{bias} = 90 mA
ΔV = 2 Volt - P_{on}/P_{off} = 4.9dB

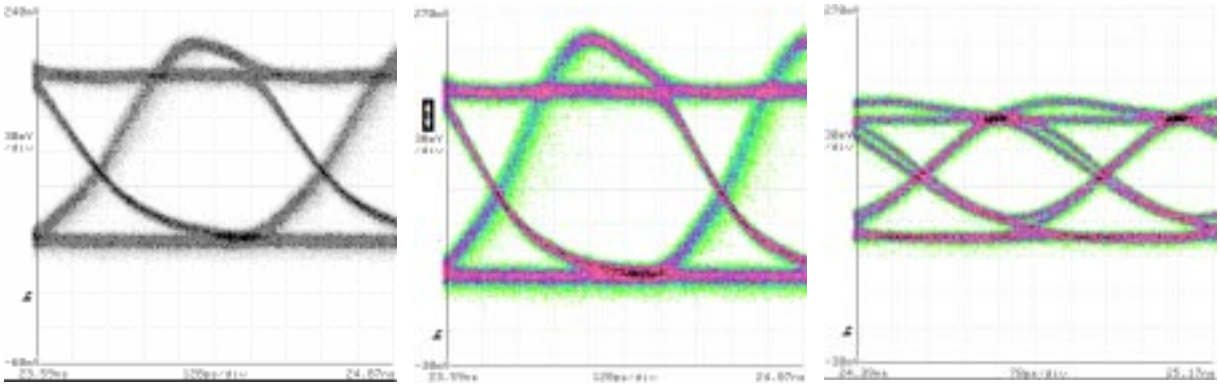

f = 1.22 GHz - I_{bias} = 90 mA
ΔV =2.3Volt - P_{on}/P_{off} =6.3dB

f = 1.22 GHz - I_{bias} = 100 mA
ΔV = 3Volt - P_{on}/P_{off} =6.7 dB

f = 2.5 GHz - I_{bias} = 100 mA
ΔV = 2Volt - P_{on}/P_{off} =3.6 dB

Fig. 6-17 Eye-diagrams measured from packaged PAL, channel 2, using high frequency probe.

The first eye diagram, measured for a 300 Mbit/s data-signal, shows a negligible turn-on jitter. Fig. 6-17b was measured at 600 MHz, with a high on/off ratio (14 dB)[1] and an off level

[1] For STM-1 transmission, an on-off ratio of 10 dB is recommended.

very close to the threshold level (I_{off} = 55 mA, I_{th} = 53 mA). In this case, the turn-on jitter occupies an important part of the centre of the eye and it is likely that this will result in a penalty on the bit-error rate. We believe that the turn-on jitter is caused by the mode instability just above threshold, which we have noticed to occur for all channels (see paragraph 5.4, Fig. 6-11). Also in [8], it was noted that it takes some time for the MWL to decide in which longitudinal mode to lase. The appearance of the turn-on jitter is rather digital: as soon as the off-level reaches a certain minimum level, it disappears completely. This is shown in Fig. 6-17c, which was measured for a reduced on-off ratio (5 dB). In [8], the direct modulation of a 16-channel multi-wavelength laser was demonstrated. Also in that case, the maximum on-off ratio was only 6 dB.

The lower row of Fig. 6-17 represents eye-diagrams measured at higher data-speeds and with varying on-off ratio. Remark the second figure in this row, taken for 1.22 GHz modulation, which has a reasonable on-off ratio and a low turn-off jitter.

6 Conclusion and discussion

Using the hybrid integration technology, we could realise very performant Phased-Array multi-wavelength lasers. The non-permanently coupled devices (chapter 5) exhibited the lowest threshold currents reported until now for devices employing a bulk active layer and had a high output power (> 3.5 mW at 100 mA, for single channel operation, > 6.2 mW for four channel operation).

The permanently integrated module discussed in chapter 6 had a higher threshold current but the best channels were oscillating reliably in a single passband of the Phased-Array and in a single longitudinal mode. Moreover, we measured an 1600 MHz 3dB bandwidth for small signal modulation, which is, to our knowledge, the best reported until now. The laser linewidth was below 1 MHz and, for moderate on-off levels (7 dB), good eye diagrams were obtained at data rates of 620 Mbit/s and 1.24 Gbit/s. The central wavelength of the laser is tunable by changing the device temperature (~0.11 nm/K).

In the introduction of chapter 5, we have shown that hybrid integration technologies are becoming increasingly important on world-scale. However, for applications such as the Phased-Array multi-wavelength laser, the widely applied silicon bench hybrids are not useful due to the large size of the devices fabricated in silica-on-silicon waveguide technologies. Therefore, the integration technology we developed incorporates only high-contrast InP-based components. Further, only standard devices, such as the passive waveguide chip or devices that are commercially available, such as the amplifier array, were used. This allows for very fast prototyping and a short development cycle. The results reported in chapters 5 & 6 and summarised above, proof that this hybrid integration technology is indeed a powerful tool for realising complex photonic ICs. By angling the waveguides towards the facet, we could effectively reduce the reflections at the interface between both chips to a negligible level. The main problem with the devices as they were used in the context of this work, is

the small tolerance for misalignment errors between both chips. In particular, the tolerance in longitudinal direction is very tight and only by bringing both chips extremely close together the transition loss is reduced to an acceptable level. However, this may be difficult because of facet corrugations. Further, the narrow gap between both chips may inhibit a successful curing of the UV-epoxy that is used for bonding them together (see chapter 6, paragraph 2.2.4). The most obvious way to increase the coupling tolerances is to use spot-size converters. However, incorporating them in the coupling scheme may complicate the fabrication of the devices. As an intermediate option, one could try to decrease the vertical far field width of the waveguides by using a guiding layer with a lower refractive index or with a graded index profile as was explained in section 3 of chapter 4.

The laser module, which is used to provide the coupling with an optical fibre, provides a very flexible way for characterising the PICs. A device on a suitable adapter plate can be mounted in the module and aligned with the fibre in only a few minutes. Some aspects of the packaging scheme, such as the electrical interconnection and the thermal properties however have to be investigated further. Possibly, it would be useful to bond the amplifiers on the substrate using a flip-chip technology. This will not only allow positioning the amplifiers more accurately but will also provide a better cooling and thereby reduce the thermal crosstalk between the amplifiers. For improving the yield, it would possibly be better to use smaller amplifier arrays, containing for example only four amplifiers. This will not only increase the yield of the amplifier arrays themselves but, because it is difficult to align eight amplifiers simultaneously, also the yield of the bonding process.

7 References

[1] E. J. Murphy, “Integrated optical circuits and components - design and applications”, Marcel Dekker, Inc., ISBN: 0-8247-7577-5

[2] A. Van Hove, Ph.D. Thesis, Ghent University, Belgium, 2000

[3] C. R. Doerr, R. Monnard, C. H. Joyner, L.W.Stulz, “Simultaneous CW operation of shared angular dispersive element WDM-lasers”, IEEE PTL, Vol. 10, 501-503, 1998

[4] C. R. Doerr, C. H. Joyner, L. W. Stulz, “Multifrequency laser with reduced intracavity wave mixing”, IEEE PTL, Vol. 11, 635-637, 1999

[5] ACTS AC332-APEX

[6] K. Naessens, A. Van Hove, T. Coosemans, S. Verstuyft, H. Ottevaere, L. Vanwassenhove, P. Van Daele, R. Baets, “Fabrication of Microgrooves with Excimer Laser Ablation Techniques for Plastic Optical Fibre Array Alignment Purposes.”, Laser Applications in Microelectronics and Optoelectronic Manufacturing V part of the SPIE’s Symposium on High-Power Lasers and Applications., January 2000

[7] Radians Innova, http://www.radians.sw

[8] R. Monnard, C. R. Doerr, M. Zirngibl, C. H. Joyner, L. W. Stulz, "Direct modulation of a multifrequency laser up to 16 x 622 Mbit/s", IEEE PTL, Vol. 9, 815-817, 1997

Appendix 1: 7-channel permanently integrated hybrid Phased-Array laser module

Following the completion of the thesis, a new module was assembled with improved operating characteristics, which are reported here.

For this module, the corrugation of the facet of the passive waveguide chip by laser ablation as it was described in paragraph 2.2.4, was omitted. Instead, a considerable amount of epoxy was applied on top of both chips. This epoxy is cured very fast and keeps both chips connected while the epoxy in between the chips is cured - during a much longer time. This procedure resulted in a considerably decreased threshold current and an increased output power with respect to previous modules (see Fig. 6-18a).

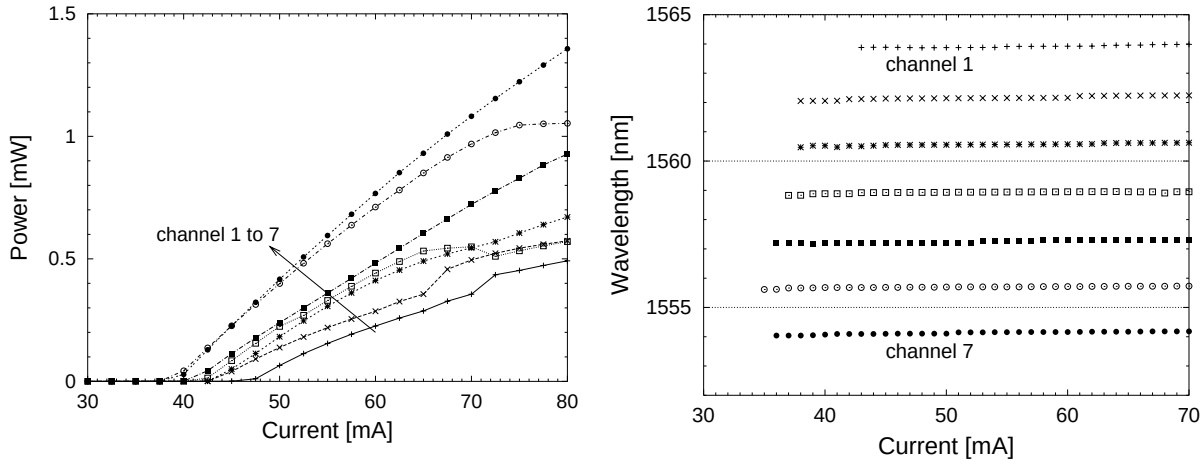

Fig. 6-18 LI-curves (left) and wavelength versus current (right) for improved module

Laser operation for 7 out of 8 channels could be obtained. Since the (non-operating) channel 8 was located immediately next to the best channel and the corresponding amplifier works well, we believe that the passive waveguide of this channel is defective.

Four channels (#2, #4, #6, #8) were terminated with SMA-connectors. One of these is the defective channel 8. The frequency spacing of the other electrically connected channels is 400 GHz. The absolute wavelength as function of the drive current is shown in Fig. 6-18b (measured at room temperature, using a HP 86120B wavelength meter). The frequency changes by 250 MHz/mA (2 pm/mA). No multipassband lasing has been observed.

Chapter 7

Summary and conclusions

The increasing complexity of optical telecommunication networks has created a need for more flexible laser sources, such as the Phased-Array multi-wavelength lasers that were investigated in the context of this thesis. At the moment this work was initiated, it was not yet obvious if such sources would be practical for use in real-world communication systems. Therefore, we investigated their properties both theoretically and experimentally.

In chapter 1, a review of the operating characteristics of current state-of-the-art multi-wavelength lasers was given. From this study, the most important advantages of Phased-Array multi-wavelength lasers appear to be the accurate channel spacing, the simplified characterisation and packaging procedure, the limited need for control equipment and the high side mode suppression ratio. The output power on the other hand is still considered to low for practical applications and de yield may be small due to the large chip surface. The fabrication itself however is simple since no fine-grid gratings are required and one fibre pigtail is shared by multiple channels. The main disadvantage at this moment, is the modulation bandwidth, which is limited due to the long cavity length. As an alternative, one could consider external modulation. Although this requires that the signals are demultiplexed again, still the use of a multi-wavelength laser may lead to a net lowering of the total number of devices required.

In chapter 2, the methods we used for analysing the waveguide structures and lasers that were studied in the context of this work were introduced. Further, we also discussed the synthesis of complex photonic IC's and pointed out some of the weaknesses of the methods that are currently available for that purpose. We also proposed an alternative knowledge driven approach, which focuses more on the manipulation of previously obtained data, rather than on field calculation as such. This was illustrated, using the design of a Phased-Array laser as an example. At the end of chapter 2, we also shortly introduced the operating principle of Phased-Array multiplexers and discussed their design. We thereby focussed on the trade-off arising from the fact that for obtaining a maximally stable laser operation, both the cavity length and the filter bandwidth should be minimised.

In chapter 3, we theoretically investigated long-cavity lasers such as the Phased-Array laser. In a first part, rate-equations for the photon and the electron density were established. Next, those were used to investigate the static characteristics, the longitudinal mode stability and the dynamic characteristics. We also investigated the effect of gain-suppression induced crosstalk in the common amplifier of such a laser and proposed a new approach to clamp the gain of this amplifier thereby preventing this sort of crosstalk. In addition, some general design rules for Phased-Array multi-wavelength lasers were given.

In chapter 4, the subcomponents of the Phased-Array laser - amplifiers and passive waveguides - were investigated. By comparing theoretical results with experimentally obtained ones, we could derive several intrinsic material parameters that were used for modelling the complete multi-wavelength laser. In this chapter, we also studied the transition between the active and the passive waveguides for both the monolithically and the hybridly integrated devices.

To be able to verify the results from the theoretical analysis described in chapter 3 with experimental results, we developed a hybrid integration technology that allowed to built complex photonic IC's, starting from standard components such as SOA-arrays and passive waveguide chips. Originally, the chips were only temporarily coupled on an optical bench. In that way we could realise some very performant Phased-Array lasers, having the lowest threshold current and highest output power reported until now for devices with a bulk active layer. Later, to improve the stability of the PICs and to make their use in optical networks possible, we developed a permanent bonding technique for the hybridly coupled chips, using a UV-curing epoxy. This allowed us to realise a fully packaged Phased-Array laser, with slightly higher threshold current but also with the highest modulation bandwidth reported until now for this sort of device (1600 MHz). The linewidth was below 1 MHz and completely open eye diagrams were measured at a data rate of 1.24 Gbit/s and an on-off ratio of 7 dB.

In our opinion, these results proof that a hybrid integration technology, as it was presented in this work and possibly with the adaptations discussed at the end of chapter 6, may be very useful. At a laboratory level, it is important to have a technology that makes it possible to realise new device ideas, without needing the complicated processing involved with monolithic integration technologies. For such applications it is mainly important to keep the devices as simple as possible. The additional processing required for passive alignment and the additional loss involved make that active alignment techniques are an obvious option.

For deciding if a hybrid integration technology employing only InP-based chips will also be useful for commercial applications, a complete yield and cost analysis incorporating all possible technologies will be required. However, based on the current success of Silicon bench hybrids, we believe that it is not impossible that also the kind of hybrid integration technology discussed here will be more successful than monolithically integrated technologies. In our opinion, spot size converters and passive alignment techniques will be indispensable for such applications.